Chair of Materials Physics

Doctoral Thesis

Microstructures and mechanical properties of CoCrFeNiAl-based high-entropy alloys

Zequn Zhang

June 2024

AFFIDAVIT

I declare on oath that I wrote this thesis independently, did not use any sources and aids other than those specified, have fully and truthfully reported the use of generative methods and models of artificial intelligence, and did not otherwise use any other unauthorized aids.

I declare that I have read, understood and complied with the “Good Scientific Practice” of the Montanuniversität Leoben.

Furthermore, I declare that the electronic and printed versions of the submitted thesis are identical in form and content.

Date 11.06.2024

Zequn Zhang

Signature Author
Zequn Zhang

This work was financially supported by the Austrian Science Fund (FWF, Y1236-N37), the National Natural Science Foundation of China (51871132), and the China Scholarship Council (CSC, 201906220226).

Erich Schmid Institute of Materials Science

Austrian Academy of Sciences

Jahnstraße 12

A-8700 Leoben

Acknowledgments

I would like to take this opportunity to thank all those people who have supported me over the past few years during my time as a doctoral student.

I am very grateful to my supervisor **Prof. Jürgen Eckert** for giving me this opportunity to study at ESI. His instruction and encouragement helped me a lot during the most tough period. Special thanks to **Dr. Christoph Gammer**, who took the time for countless conversations and discussions. His professional knowledge and patient guidance have given me a view toward research more scientifically and fully. His experience combined with thoughtful consideration and objections at the right time contributed significantly to the completion and success of this work.

I would like to thank my mentor **Prof. Christian Mitterer** for experiment support and for guidance in writing papers. Thanks are also given to **Prof. Kaikai Song**, **Dr. Anton Hohenwarter**, **Dr. Sergey Ketov**, **Dr. Stefan Wurster**, and **Dr. Oliver Renk** for the scientific discussions. Thank **Anton**, **Oliver**, and **Stefan** for the experiment design and test, which greatly improved the study content.

I gratefully acknowledge **Dr. Huaping Sheng**, **Dr. Zhuo Chen**, **Simon Fellner**, and **Yong Huang** for TEM characterization and analysis, **Dr. Megan J. Cordill** for the nanoindentation test, **Qi Xu**, and **Dr. Daniel Sopu** for MD simulations. Furthermore, I also would like to thank **Karl-Heinz Pichler** for synthesizing the thin films, and **Philipp Hoebenreich**, and **Peter Kutlesa** for assistance with metallographic sample preparation and HPT experiment. Thank all the other technicians for their help.

In the end, I would like to thank my parents **Minglan Ai** and **Kequan Zhang**. Over the past four years, they have supported me unswervingly in my life and research abroad.

Abstract

High-entropy alloys (HEAs) open a new field to explore and develop high-performance materials among the center area of multi-component phase diagrams. The chemical composition selection affects the microstructure, and a proper selection can bring unexpected property optimization than the rule of mixtures. This thesis is to study the influence of Al on the microstructure evolution of CoCrFeNi HEA at different temperatures and to design an AlCoCrFeNi-based HEA with enhanced mechanical properties through microstructure adjustment.

The first part focuses on the reactive diffusion behavior of the Al/CoCrFeNi diffusion couple under isothermal and isochronal annealing conditions. At temperatures below 1373 K, the major products of the reaction are intermetallic compounds as the process is enthalpy-dominated. Formation of the phases with lower energy than the disordered solid solution state causes the decomposition of the HEA. At and above 1373 K, entropy contribution to the system energy plays a more important role. Al diffuses toward the HEA matrix to form a more disordered state. The strong bonding tendency of Al and Ni indirectly induces new phases and causes the uphill diffusion of Ni toward the Al side in the fully disordered state.

The second part studies the response of AlCoCrFeNi-based eutectic HEA (EHEA) to high-pressure torsion (HPT). Introducing numerous defects causes the fragmentation of the lamellar structure through dislocation multiplication and arrangement. Fragmentation initiates close to the interface due to stress concentration and gradually evolves into the grain boundary. The soft face-centered cubic (Fcc) phase develops misorientation faster than the ordered body-centered cubic (B2) phase. With the increase of shear strain, a high number of nanograins form with the disordering of the B2 phase to Bcc phase, and the remaining Bcc lamellae evolve into vortex clusters. The structural change leads to a significant strengthening of the material. Both the yield strength and ultimate strength are enhanced by a factor of around two with certain ductility remaining.

By utilizing a wide thermal stability range of Al,Ni-rich B2 phase and Co,Cr,Fe-rich Fcc phase during reactive diffusion, the final part studies the structural optimization of an EHEA to enhance mechanical properties. The lamellar microstructure of an EHEA is adjusted to an equiaxed grain structure through a combination of HPT and annealing. As a result, the yield strength is improved from 703 MPa to 1199 MPa without reducing ductility. Detailed characterization of the deformation process shows that it has a Lüders-type deformation followed by a work hardening stage. High-angle

grain boundaries and phase boundaries act as sources for dislocations and block the dislocation transfer. The dual-phase structure avoids the necking in the early stage while the soft Fcc phase blocks the expansion of microcracks for the B2 phase. This provides a guideline for designing alloys with enhanced mechanical properties without dependence on loading direction.

Kurzfassung

Hochentropielegierungen (HEAs) eröffnen ein neues Forschungsfeld zur Erkundung und Entwicklung hochleistungsfähiger Materialien im zentralen Bereich mehrkomponentiger Phasendiagramme. Die Auswahl der chemischen Zusammensetzung beeinflusst die Mikrostruktur, und eine geeignete Auswahl kann eine unerwartete Optimierung der Materialeigenschaften im Vergleich zur Mischungsregel bringen. Diese Arbeit zielt darauf ab, den Einfluss von Al auf die Mikrostrukturentwicklung von CoCrFeNi HEA bei verschiedenen Temperaturen zu untersuchen und eine AlCoCrFeNi-basierte HEA durch Mikrostrukturanpassung mit verbesserten mechanischen Eigenschaften zu entwerfen.

Der erste Teil konzentriert sich auf das reaktive Diffusionsverhalten des Al/CoCrFeNi-Diffusionspaares unter isothermen und isochronen Glühbedingungen. Bei Temperaturen unter 1373 K sind die Hauptprodukte der Reaktion intermetallische Verbindungen, da der Prozess von der Enthalpie dominiert wird. Die Bildung von Phasen mit niedrigerer Energie als der ungeordnete Festkörperlösungszustand führt zur Zersetzung der HEA. Bei und über 1373 K spielt der Entropiebeitrag zur Systemenergie eine wichtigere Rolle. Al diffundiert zur HEA-Matrix, um einen stärker ungeordneten Zustand zu bilden. Die starke Bindungstendenz von Al und Ni induziert indirekt neue Phasen und verursacht die bergauf gerichtete Diffusion von Ni in Richtung der Al-Seite im vollständig ungeordneten Zustand.

Der zweite Teil untersucht die Reaktion der AlCoCrFeNi-basierten eutektischen HEA (EHEA) auf Hochdrucktorsion (HPT). Die Einführung zahlreicher Defekte führt zur Fragmentierung der lamellaren Struktur durch Dislokationsvervielfachung und -anordnung. Die Fragmentierung beginnt in der Nähe der Grenzfläche aufgrund von Spannungskonzentration und entwickelt sich allmählich zum Korngrenzgebiet hin. Die weiche kubisch-flächenzentrierte (Fcc)-Phase entwickelt schneller eine Fehlorientierung als die geordnete kubisch-raumzentrierte (B2)-Phase. Mit zunehmender Scherbeanspruchung bilden sich eine große Anzahl von Nanokörnern durch die Entmischung der B2-Phase zur Bcc-Phase, und die verbleibenden Bcc-Lamellen entwickeln sich zu Wirbelcluster. Die strukturelle Veränderung führt zu einer signifikanten Stärkung des Materials. Sowohl die Streckgrenze als auch die Zugfestigkeit werden um einen Faktor von etwa zwei erhöht, wobei eine gewisse Verformbarkeit erhalten bleibt.

Durch die Nutzung eines breiten thermischen Stabilitätsbereichs der aluminium- und

nickelreichen B2-Phase sowie der kobalt-, chrom- und eisenreichen Fcc-Phase während der reaktiven Diffusion untersucht der letzte Teil die strukturelle Optimierung der EHEA zur Verbesserung der mechanischen Eigenschaften. Die lamellare Mikrostruktur der EHEA wird durch eine Kombination aus HPT und Glühen zu einer äquiaxedischen Kornstruktur angepasst. Dadurch wird die Streckgrenze von 703 MPa auf 1199 MPa verbessert, ohne die Verformbarkeit zu verringern. Eine detaillierte Charakterisierung des Verformungsprozesses zeigt, dass es sich um eine Lüders-artige Verformung handelt, gefolgt von einer Verfestigungsstufe. Hohe Winkelkorn- und Phasengrenzen dienen als Quellen für Dislokationen und blockieren den Dislokationstransfer. Die dualphasige Struktur vermeidet das Einschnüren in der Frühphase, während die weiche Fcc-Phase die Ausbreitung von Mikrorissen für die B2-Phase blockiert. Dies bietet eine Richtlinie für das Design von Legierungen mit verbesserten mechanischen Eigenschaften ohne Abhängigkeit von der Belastungsrichtung.

Acronyms and Abbreviations

HEA	High-entropy alloy
EHEA	Eutectic high-entropy alloy
XRD	X-ray diffraction
Fcc, fcc	Face-centered cubic
Bcc, bcc	Body-centered cubic
B2	Ordered body-centered cubic
$L1_2$	Ordered face-centered cubic
SEM	Scanning electron microscope
BSE	Backscattered electron
EDS	Energy-dispersive X-ray spectroscopy
EBSD	Electron backscattering diffraction
FIB	Focused ion beam
TEM	Transmission electron microscopy
STEM	Scanning transmission electron microscopy
HRTEM	High-resolution transmission electron microscopy
BF	Bright-field
DF	Dark-field
SAED	Selected area electron diffraction
NBD	Nanobeam electron diffraction
DSC	Differential scanning calorimetry
GNDs	Geometrically necessary dislocations
HPT	High-pressure torsion
SPD	Severe plastic deformation
EDM	Electro-discharge machining
LAGB	Low-angle grain boundary
HAGB	High-angle grain boundary
PB	Phase boundary
DIC	Digital image correlation

Contents

1 Introduction

The concepts of HEAs and equiatomic multicomponent alloys were put forward in 2004 by Yeh et al. [1] and Cantor et al. [2]. Unlike traditional design strategies of alloys focusing on the corners of the phase diagram (Fig 1.1), the novel concept emphasizes the exploration of the center or near center area for the multiple components phase diagrams. This opens up a new world to explore alloys with a vast compositional space. Based on the Gibbs phase rule, the number of phases P in thermodynamic equilibrium at constant pressure can be given by the following equation [3]:

$$P = N - F + 1 \quad , \quad (1)$$

where N is the number of components and F is the degree of freedom. For a given system, the potential number of phases is within the range 1 to N+1 by restricting the degree of freedom F from maximum F=N to minimum F=0, and the addition of components increases the maximum phase number in the thermodynamic equilibrium.

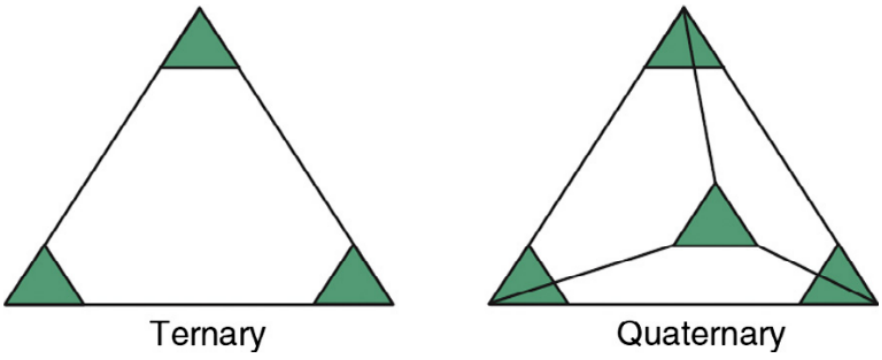

Fig. 1.1 Schematic ternary and quaternary alloys put forward by Cantor, green areas close to the corner in two phase diagrams are relatively well known but the center white areas are less well known [4].

Due to the multicomponent configuration, a hyper-dimensional composition space is needed to study the phase diagram for HEAs. This requires a significant effort. To understand the phase evolution of HEAs, Laurent-Brocq et al. [5] studied the microstructure of equimolar CrMnFeCoNi HEA. A fcc solid solution is stable at high temperatures and the phase diagram at elevated temperatures is analogous to a completely miscible pseudobinary alloy CrFeCo–MnNi. Cooling rate influences the microstructure due to the variant liquidus and solidus temperature of CrFeCo and MnNi systems. Jones et al. [6] investigated phase equilibria of an $Al_{0.5}$CrFeCoNiCu HEA, and it was found that a solid-state single phase does not exist and the configurational entropy contributes less than the

enthalpic one to the Gibbs energy. By substituting the composing elements of CoCrFeMnNi HEA with Ti, Mo, V, and Cu, multiple phases were formed in all but the base CoCrFeMnNi alloy without changing the ideal molar configurational entropy. Hence the enthalpy and non-configurational entropy contribution to the phase stability cannot be ignored [7]. In addition to experimental observations, simulations were also utilized to predict the phase formation of HEAs. Ma et al. [8] found the phase stability predicted by CALPHAD (CALculation of PHAse Diagrams) simulations yielding good agreement with experiment results for $Fe_xMn_{62-x}Ni_{30}Co_6Cr_2$ HEAs. Through finite-temperature ab initio methods, they furthermore found that the contribution to the phase stability from other entropy terms (i.e., vibrational, electronic, and magnetic ones) also needs to be considered [9]. Using CALPHAD simulations, Zhang et al. [10] suggested that the highest ideal molar configurational entropy does not necessarily give the lowest Gibbs energy, and most of the single-phase solid solution structures in HEAs were obtained due to the fast cooling during the casting process. Santodonato et al. [11] captured the temperature- and composition-dependent phase evolution in Al-containing HEAs through the high-throughput Monte Carlo method.

As mentioned above, high-throughput simulations and extensive experiments can predict and evaluate the phase stability of multicomponent systems. However, the real phase evolution process cannot be visualized with those methods. To capture the phase evolution of HEAs and evaluate the underlying thermodynamic and kinetic effects, **Publication I** and **Publication II** focus on the reactive diffusion of a CoCrFeNi/Al diffusion couple. By controlling the annealing conditions, these two papers demonstrate that a high ideal molar configurational entropy does not stabilize the disordered solid solution phase. Instead, the mixing enthalpy between the atomic pairs has a significant influence on the phase evolution. The enthalpy contribution cannot be neglected even when the system comes to a fully disordered state at elevated temperatures. Finally, surface modification can be realized through a proper combination of film deposition and annealing processes. The B2 phase which is rich in Al and Ni is thermally stable under a wide temperature range and hardens the free side of the CoCrFeNi/Al diffusion couple as demonstrated in publication II. Therefore, the present work also presents an attractive workflow for improving material properties via controlled surface modification.

The Al,Ni-rich B2 phase hardens the surface of Co,Cr,Fe-rich Fcc phase during reactive diffusion. If the B2 phase can be introduced into the Fcc matrix, a strengthening behavior can be expected on the macroscopic scale. As a natural composite, EHEAs from CoCrFeNiAl system have attracted lots

of attention in recent years. The alternatively distributed Fcc/$L1_2$ and B2 lamellae triggers a back-stress strengthening mechanism [12][13]. It is expected that the mechanical properties of EHEAs can be further optimized by tuning the microstructure. **Manuscript III** is devoted to the microstructure evolution of the $AlCoCrFeNi_{2.1}$ EHEA during HPT. The multiphase structure affects the defect distribution and misorientation evolution during severe plastic deformation and therefore controls the final mechanical properties. Saturated microstructure refinement is realized after a shear strain γ of 24. Restriction of dislocation activity in the achieved structure results in a high yield strength of 1.75 GPa with a failure strain of 5%. **Manuscript IV** reports that controlling both, the phase distribution and the interface structure allows to strongly improve the mechanical properties of the $AlCoCrFeNi_{2.1}$ EHEA. HPT is applied to the EHEA to realize microstructural refinement. During a subsequent annealing treatment, recrystallization and grain growth occur in the Fcc and B2 phases, and the original lamellar microstructure changes to an equiaxed grain microstructure. The introduction of a large number of HAGBs and PBs on the one hand provides a high-density of nucleation sites for defects. On the other hand it blocks the dislocation transmission. The localized softening resistance avoids the necking, and the intrinsic microcrack-arresting mechanism of the achieved two-phase structure effectively improves the overall fracture resistance, leading to an optimized combination of strength and ductility.

2 Background and motivation

2.1 Definition of high-entropy alloys

Since the discovery of HEAs, several definitions have been put forward [14][15]. The most common one is based on the composition ratio: An alloy consists of several principal elements with the concentration ranging from 5 to 35 at.% (atomic percentage). Another common one is based on the concept of entropy. For an ideal solid solution (random occupation of atoms on each lattice), the total configurational molar entropy $^{mix}S_m^{ideal}$ is given by the following equation:

$$^{mix}S_m^{ideal} = -R\sum_i x_i \ln(x_i) \quad , \quad (2)$$

where R is the gas constant and x_i is the atom fraction of element i. An alloy with $^{mix}S_m^{ideal}$ higher than $1.61R$ can be defined as an HEA. It should be noted that not all the multicomponent alloys are ideal solid solutions. Atoms in some alloys occupy specific lattices and cause the formation of intermetallic compounds. Therefore, this definition is based on the ideal case. These two definitions bring different composition spaces for HEAs. For example, a five-element HEA based on the first definition can have a configurational entropy of $1.36R$ (for an alloy with 5% A, 5% B, 20% C, 35% D, and 35% E), which is smaller than the one required from the second definition. As a compromise, alloys with smaller configurational entropy, such as quaternary equimolar alloys ($^{mix}S_m^{ideal} = 1.39R$), are also generally considered to be HEAs [16].

2.2 Four 'core effects'

Based on the early investigation of HEAs, Yeh [17] summarized four 'core effects' for HEAs: the high entropy effect; the lattice distortion effect; the sluggish diffusion effect, and the 'cocktail' effect. Three of them are hypotheses based on experiment results and the 'cocktail' effect describes the properties of HEAs.

2.2.1 The high entropy effect

The high entropy effect proposes that multicomponent systems may favor the formation of solid solutions instead of intermetallic compounds due to the high contribution of ideal molar configurational entropy to the total energy. Molar Gibbs energy G_m for a phase is given by [14]

$$G_m = \sum_i x_i(G_i) + {}^{mix}G_m^{ideal} + {}^{e}G_m \, , \quad (3)$$

The first term on the right side is the sum of Gibbs energy of the i elemental constituents. $^{mix}G_m^{ideal}$ is the ideal molar Gibbs energy of mixing. $^{e}G_m$ is the excess molar Gibbs energy. This term is

composed of excess enthalpy and entropy terms. To emphasize the difference between enthalpy and entropy of solid solution and intermetallic compound phases, the contribution from the term $\sum_i x_i(G_i)$ is removed for expedience considering pure elements are used as the standard states. ${}^{mix}G_m^{ideal}$ is

$$ {}^{mix}G_m^{ideal} = {}^{mix}H_m^{ideal} + {}^{mix}S_m^{ideal} \times T, \quad (4) $$

where T is the absolute temperature. ${}^{mix}H_m^{ideal} = 0$. Therefore, the molar Gibbs energy G_m can be written as follows:

$$ G_m = {}^{e}G_m + {}^{mix}S_m^{ideal} \times T, \quad (5) $$

Even though the ideal molar configurational entropy increases with increasing number of components, the terms from excess molar Gibbs energy contribution (i.e. non-ideal interactions of atoms and excess configurational entropy, atomic vibrations, magnetic moments, and electronic effects) cannot be ignored. Miracle et al. [14] analyzed the total entropy of binary liquid alloys and suggested that excess entropy terms can reach twice the value of ${}^{mix}S_m^{ideal}$. It is also found that some single solid-solution phase HEAs are metastable. Precipitates form after annealing [18]. The potential reasons for this phenomenon could be: 1. The excess molar Gibbs energy ${}^{e}G_m$ plays a more important role than the ideal one ${}^{mix}G_m^{ideal}$ in determining molar Gibbs energy of the system. By replacing the individual elements one at a time in the CoCrFeMnNi alloy, Otto et al. [7] found that configurational entropy does not always dominate the phase composition. 2. The time for the system to reach the equilibrium state is insufficient. Up to now, most single-phase HEAs were prepared by casting. The fast-cooling rate could keep the high-temperature phase in the microstructure. The annealing treatment or service for a certain length of time may promote the precipitation of the second phase [6][10][19].

2.2.2 The sluggish diffusion effect

Due to the multicomponent configuration of HEAs, migration of atoms and vacancies are confined by the surrounding atoms with various interatomic potentials, and the lattice diffusion is believed to be ‘sluggish’. Limited by the complex diffusion behavior, investigations of diffusion in HEAs are rare. The bulk tracer diffusion method revealed that the temperature dependence of bulk diffusion in single-phase CoCrFeNi and CoCrFeMnNi HEAs follows the Arrhenius behavior and the diffusion does not always become slower when the number of elements increases. The Co diffusivity is higher in CoCrFeMnNi than in CoCrFeNi alloys above a certain temperature [20]. The difference

in diffusion rates of substitutional solutes from a dilute solid solution $Co_2Cr_2Fe_2Mn_2Ni_{92}$ to a $Co_{20}Cr_{20}Fe_{20}Mn_{20}Ni_{20}$ alloy is within one order of magnitude at 1373 K. This phenomenon still follows general rules for substitutional diffusion in Fcc metals and it does not require 'sluggish' diffusion [21]. It should be noted that different standards to evaluate the diffusion ability (under an absolute temperature or under a homologous temperature) also influence the conclusion [20][22]. Dash et al. [23] evaluated the diffusion coefficient of all the components in the CoCrFeNi HEA. The proposed pseudo-binary and pseudo-ternary diffusion couple methods give a reasonable estimation of diffusion behavior in the HEA.

2.2.3 The lattice distortion effect

It is believed that elements with different atomic sizes within HEA lattices cause lattice distortion. The lattice site displacement is affected by the atom occupying that site and the types of atoms in the local environment [14]. As shown in Fig. 2.1, the distortion effect results in an intensity decrease of the X-ray diffraction peaks which is comparable to the intensity decrease from thermal effects [24]. In addition to this, lattice distortion is claimed to increase hardness and reduce electrical and thermal conductivity [17]. By adding V to CoNi alloy, the medium-entropy alloy with a single Fcc phase shows a yield strength of 1 GPa. This is attributed to the significant fluctuation of atomic bond distance due to the V element [25]. Similarly, the addition of Zr in NbTaTiV HEA broadens the distribution of first to fifth nearest neighbors interatomic distances and enhances the yield strength from 1240 MPa to 1520 MPa [26].

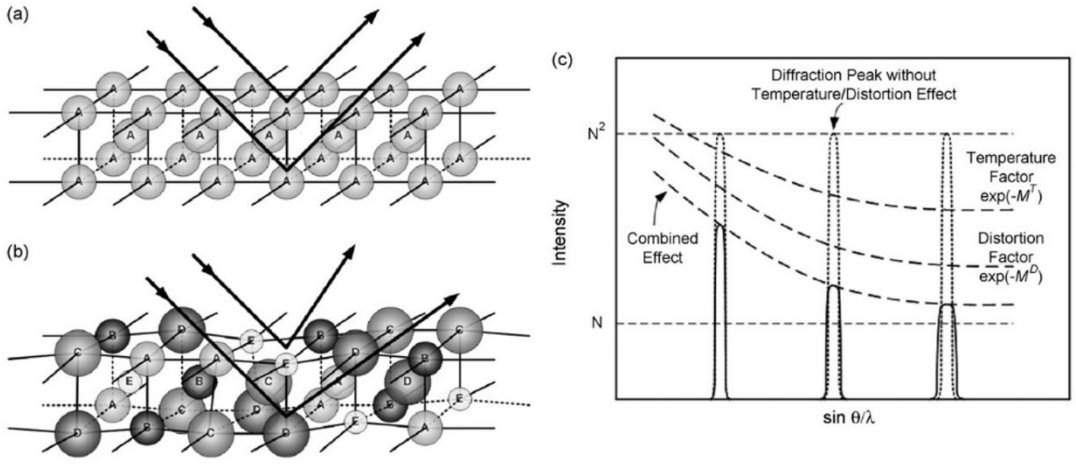

Fig. 2.1 Yeh et al. [24] proposed a schematic diagram of the influence of intrinsic lattice distortion of multicomponent configuration on Bragg diffraction: (a) Ideal lattice with each site being occupied by the same atoms; (b) Distorted lattice with varying sized atoms randomly occupying each site; (c)

An illustration of the impact of temperature and lattice distortion on the XRD intensity.

2.2.4 The 'cocktail' effect

Instead of an overlay of properties from the individual element, the 'cocktail' effect emphasizes the synergistic mixture. The result is unpredictable and it could be better than the sum of the individual contributions. As shown in Fig 2.2, the increase of soft Al content in $Al_xCoCrFeNi$ alloy promotes the formation of an Al,Ni-rich Bcc phase, which enhances lattice distortion and improves the hardness [27][28]. The 'cocktail' effect gives many possibilities to HEAs. It brings unexpected results and the huge composition space provides large discoverable new materials for application.

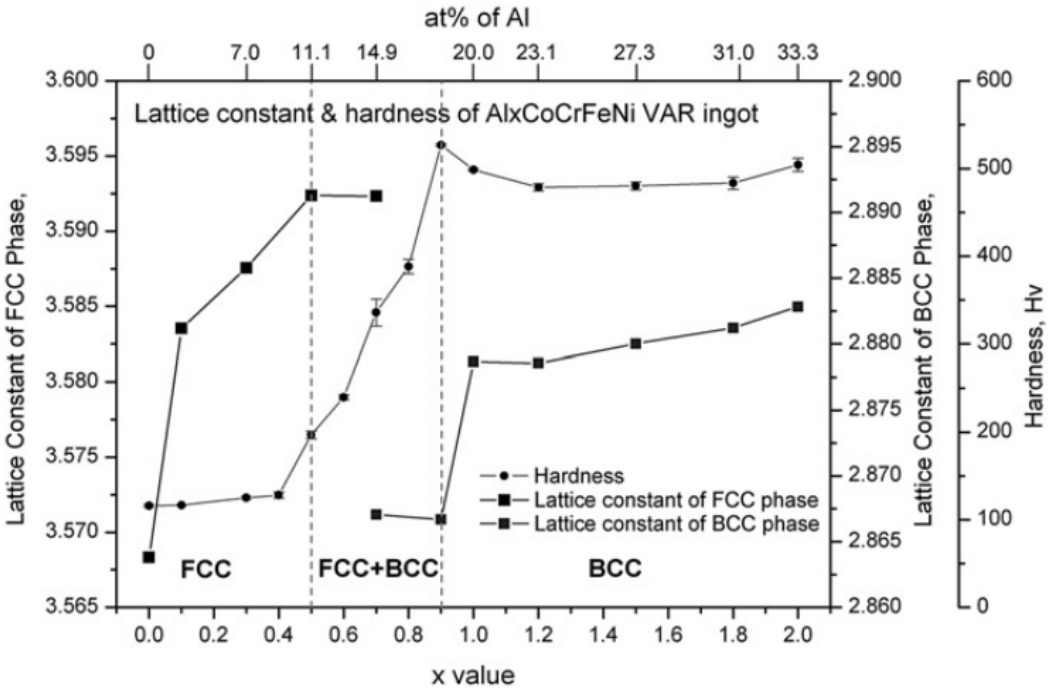

Fig. 2.2 The change of lattice constant and hardness of $Al_xCoCrFeNi$ alloys with increasing Al content [28].

2.3 Microstructures and mechanical properties

The mechanical property of alloys is always the central focus of scientific research. In this section, the relationship between microstructures and mechanical properties in HEAs reported in the literature is reviewed with a focus on tensile properties.

The components of alloys work as the 'brick' to build the material. They strongly affect the microstructure, the elastic property, the plastic deformation behavior, etc. Compared to conventional alloys, single-phase HEAs are expected to show a higher solid solution strengthening because of the dissolution of a large number of components with different sizes in the matrix. The Bcc CrMoNbV HEA exhibits high compression strength [29]. The high strength (more than 1000 MPa) is retained

even at elevated temperatures (up to 1273 K). This is related to the strong solute-pinning effect. The addition of Al in an Fcc CoCrFeMnNi alloy causes large distortion around Al. It blocks dislocation slip and results in high strength [30]. The interstitial C element in a Fcc $Fe_{40.4}Ni_{11.3}Mn_{34.8}Al_{7.5}Cr_6$ alloy increases the lattice friction stress and causes a transition from wavy slip to planar slip due to the decrease in stacking fault energy, leading to the improvement of yield strength and a high degree of strain hardening [31].

Similar to traditional alloys, Fcc phase HEAs show good ductility but low strength while Bcc phase HEAs exhibit high strength and low ductility [4]. For Fcc-structured HEAs, different preparation or processing methods are utilized to strengthen the material while retaining the ductility. Through partial recrystallization, a good combination of ductility and strength can be realized by heterogeneous structure design [32][33]. This will be discussed in detail in the next section. Moreover, the dominant deformation mechanism plays an important role for mechanical properties. Twinning-induced plasticity and transformation-induced plasticity can be realized by a composition adjustment that decreases the stacking fault energy. As a result, a good strength-ductility synergy can be achieved [34][35].

Generally, precipitates or second phases are introduced to block the dislocation movement. He et al. [36] introduced nano-scaled coherent precipitates in Fcc-based HEAs by controlling the overall valence electron concentration. The yield strength is enhanced by 670 MPa due to coherency strengthening and ordering strengthening coming from precipitates. Yang et al. [37] showed that after a combination of cold-rolling and annealing, three types of precipitates are present in a Fcc-structured HEA. Multiple deformation mechanisms are activated and the back-stress strengthening is realized due to a high volume fraction of interfaces [37].

2.4 Heterogeneous microstructure design

Materials with heterogeneous microstructures exhibit an excellent combination of strength and ductility. This is attributed to back-stress strengthening induced by strain gradients [38]. The deformation of heterogeneous microstructures can be separated into three stages (Fig. 2.3). In the first stage, both hard and soft domains deform elastically. Once deformation enters the second stage, the soft domains start to yield while the hard domains are still in the elastic deformation regime. The restriction of the hard domains causes limited dislocation activity in the soft domains. Since the strain should be continuous across the interface, strain gradients appear in the soft domains close to the

interface. During this process, GNDs are created in the soft domains to adjust the strain gradient and to keep the deformation compatibility between the two domains [39][40]. Due to the generation of GNDs, long-range stress (back stress) is exerted, which works in the opposite direction to the applied stress in the soft domains (Fig. 2.4). The back stress hampers dislocation movement within the soft domains, which strengthens the soft domains and finally improves the global yield strength. With increasing deformation, the degree of stress concentration increases due to the pile-up of GNDs at the interface. The hard domains begin yielding to adjust the stress concentration. This causes an overall yielding event in which both domains are plastically deformed together, resulting in the end of the second stage. However, the soft domains undertake a larger strain than the hard domains, leading to strain partitioning in the third stage. Because of a larger plastic strain in the soft domains, the hard domains endure a higher fraction of flow stress than the soft domains, leading to stress partitioning. As a result, the strain gradient appears at the interface to adjust both the stress and strain partitioning, and the resultant back stress improves the strain hardening capacity.

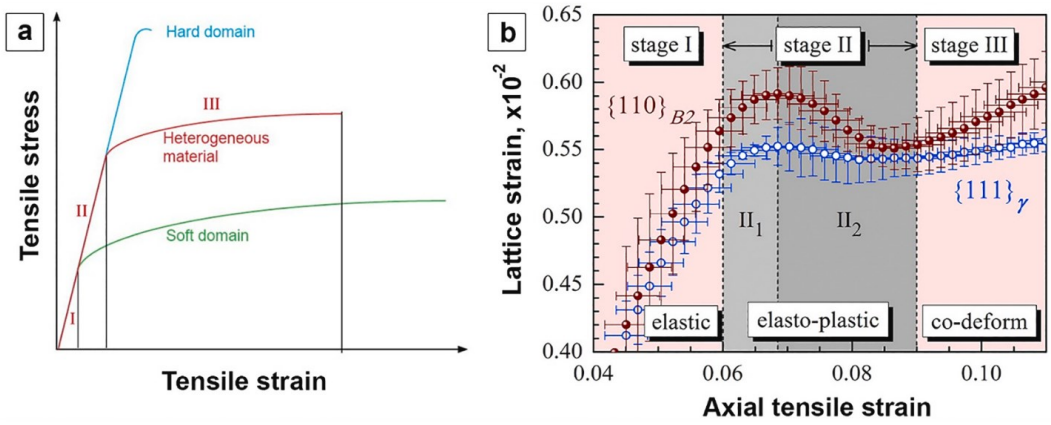

Fig. 2.3 (a) A schematic proposed by Wu et al. [41] showing the three deformation stages and the tensile property of materials with heterogeneous microstructures. (b) The lattice strain of the soft domains (γ phase) and the hard domains (B2 phase) of the high specific strength steel Fe-16Mn-10Al-0.86C-5Ni during three stages [42].

Both the yield strength and strain hardening capacity are improved in heterogeneous microstructures. This leads to a good combination of strength and ductility. Based on this strategy, several microstructures have been designed, such as gradient structure [43-46], heterogeneous lamella structure [47-49], single-phase heterogeneous grain structure [33][50][51], multiphase heterogeneous grain structure [52-54] and heterogeneous eutectic lamellar structure [12][55-57].

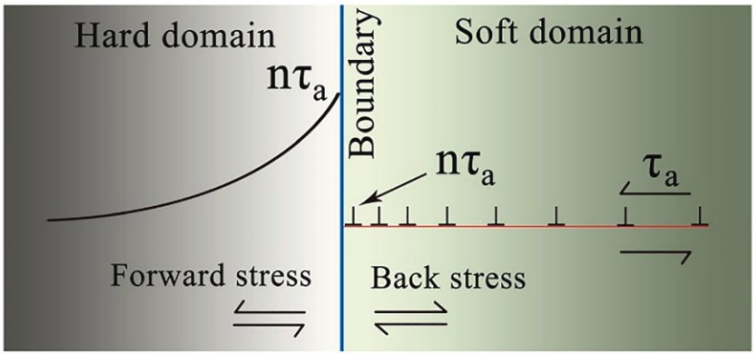

Fig. 2.4 A schematic showing the generation of back stress in a soft domain and forward stress in a hard domain due to the stress concentration at the boundary [58].

2.4.1 Back stress calculation

The back stress plays a crucial role during deformation for heterogeneous microstructures. To quantify the contribution, Cottrell [59], Kulman-Wilsdorf, and Laird [60] estimated the back stress σ_b based on the hysteresis loop during a loading-unloading-reloading test (Fig. 2.5). The back stress is obtained from the following equation:

$$\sigma_b = \frac{\sigma_{u0}+\sigma_u}{2}, \quad (6)$$

where σ_{u0} is the initial unloading stress and σ_u is the unloading yield stress. Equation (6) was modified by Dickson et al. [61] by considering the thermal component of the flow stress to avoid the overestimation. Recently, Yang et al. [62] proposed a similar equation where the calculated back stress shows less scattering compared to other equations. It assumes that the frictional stress σ_f is a constant during the whole unloading-reloading process and back stress remains unchanged with unloading before the unloading yield point C (marked in Fig. 2.5). During unloading, a quasi-elastic segment AB occurs due to the stress relaxation [61] or viscous flow [63][64]. It is followed by an elastic segment BC with an effective unloading Young's modulus E_u. Once the stress is lower than the unloading yield stress σ_u at the unloading yield point C, the applied stress and the frictional stress σ_f are overcome by the back stress σ_b to make the dislocations glide inversely. At point C, it gives:

$$\sigma_b = \sigma_u + \sigma_f, \quad (7)$$

During the reloading, an elastic segment EF with an effective reloading Young's modulus of E_r occurs following a quasi-elastic segment DE. After the reloading yield point F, the applied stress overcomes the back stress σ_b and the frictional stress σ_f to drive the dislocation movement forward. At point F, it gives:

$$\sigma_r = \sigma_b + \sigma_f, \quad (8)$$

Solving equations (7) and (8) gives the back stress:

$$\sigma_b = \frac{\sigma_r + \sigma_u}{2}, \quad (9)$$

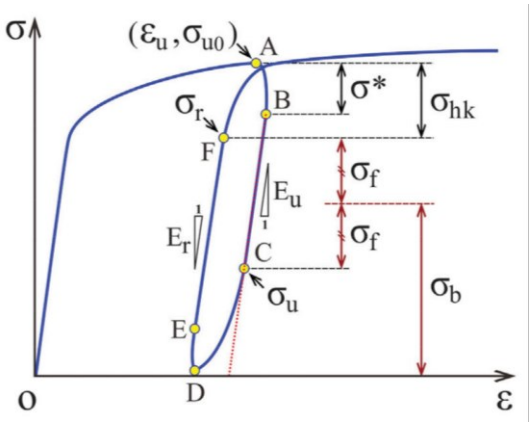

Fig. 2.5 A schematic showing the unloading–reloading loop. σ_u represents unload yielding stress; σ_r represents reload yielding stress; σ_b represents back stress; σ_f represents frictional stress, E_u represents effective unloading Young's modulus and E_r represents effective reloading Young's modulus [62].

2.4.2 Eutectic lamellar structure

As one of the heterogeneous microstructures, the eutectic lamellar structure has attracted lots of attention. Using only a proper composition selection, the lamellar structure can be easily created by a traditional casting process. Moreover, it is found that an appropriate structure adjustment can further tailor the mechanical properties. Through a combination of cold rolling and annealing, the microstructure shows a two-stage hierarchical constraint effect and a self-generated microcrack-arresting mechanism. This strengthens the $AlCoCrFeNi_{2.1}$ EHEA lamellar structure without loss of ductility [12]. By directional solidification, a tensile elongation of 50% with a yield strength of 670 MPa is realized in $Al_{19}Fe_{20}Co_{20}Ni_{41}$ EHEA with a herringbone microstructure. The dynamic strain-hardened feature induces crack buffering, which avoids catastrophic failure [13]. During laser metal deposition, microstructures can be optimized by controlling the direction of heat flow. The $AlCoCrFeNi_{2.1}$ EHEA prepared by this technique shows mechanical anisotropy and a good combination of tensile strength and ductility is realized when tested along the deposition direction. The fine lamellar structure provides more phase boundaries to block the crack propagation and this is thought to be the reason for the good strain-hardening ability [65].

2.5 A brief introduction to HPT

HPT is one of the severe plastic deformation methods. The high hydrostatic pressure during processing enables applying very high shear strain to the material without fracture. By the dynamical grain refinement process, the grain size of a bulk material can be reduced to the nanoscale. Fig. 2.6 (a) shows the schematic of the quasi-constrained HPT process. A sample is compressed between two anvils and shear strain is induced by the rotation of the lower anvil. Fig. 2.6 (b) reveals the nanograin structure of CoCrFeNi HEA realized by HPT.

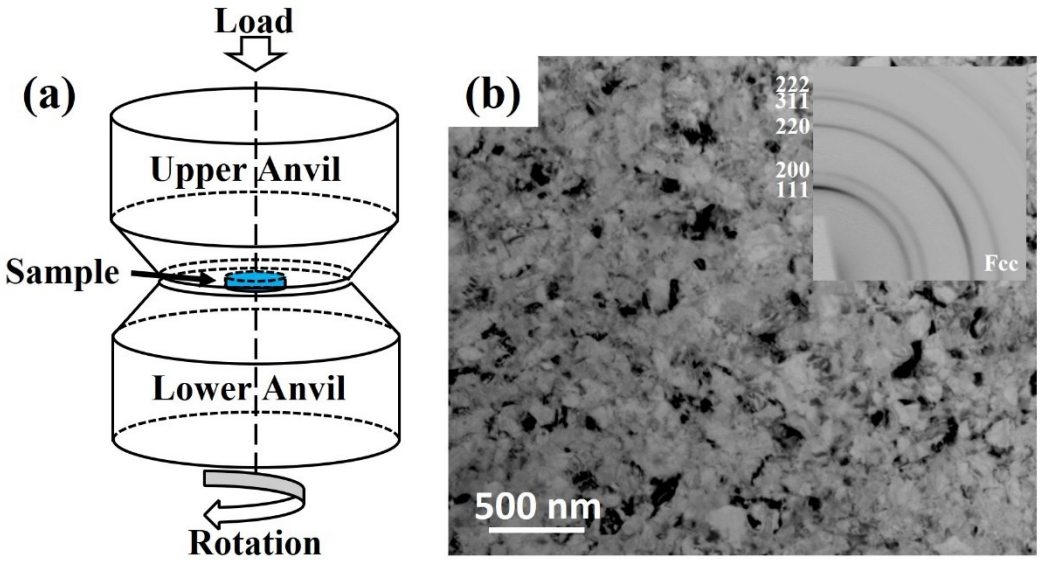

Fig. 2.6 (a) Schematic of the quasi-constrained HPT deformation. (b) TEM images showing the nanograin structure of CoCrFeNi HEA realized by HPT.

The ideal shear strain γ can be quantified by the following equation:

$$\gamma = \frac{2\pi rn}{t}, \quad (10)$$

where r is the specimen radius, t is the specimen thickness and n is the number of applied rotations. Ideally, the shear strain increases linearly along the radius direction from the center to the edge and hence results in an intrinsically heterogeneous strain throughout the disk. The deformation induced by the strain varies from area to area, which can be reflected by the change in mechanical properties. For materials with low stacking fault energies, perfect dislocations can easily split into Shockley partial dislocations with a certain separation width between partials. Cross slip is difficult, so materials show slow recovery rates. The hardness close to the periphery tends to be higher as a result of faster grain refinement in the early stage of straining. In the high purity Al with a high stacking fault energy, cross slip of dislocations results in grain refinement followed by very fast dynamic

recovery. A higher hardness measured initially in the central region is attributed to the dynamic recovery close to the edge part [66]. In both cases with increasing shear strain, a saturation is reached where the hardness reaches a uniform value throughout the entire disk [66]. For multiphase systems, the response difference of phases and the initial structural morphology can cause a high heterogeneity of the plastic flow and influence the structural evolution (Figure. 2.7). This can be seen in the Fe-Cu system [67], Cu-W system [68], Ni-Ag system [69], Fe-C system [70] and HEA system [71]. Generally, a homogeneous microstructure with saturated grain refinement is gradually developed throughout the specimen with the increase of strain. It is believed that the refinement process induced by defects, and recovery and the grain growth process induced by grain boundary migration reach a balance once a saturated state is realized. This may be the reason for the saturation of grain size during HPT.

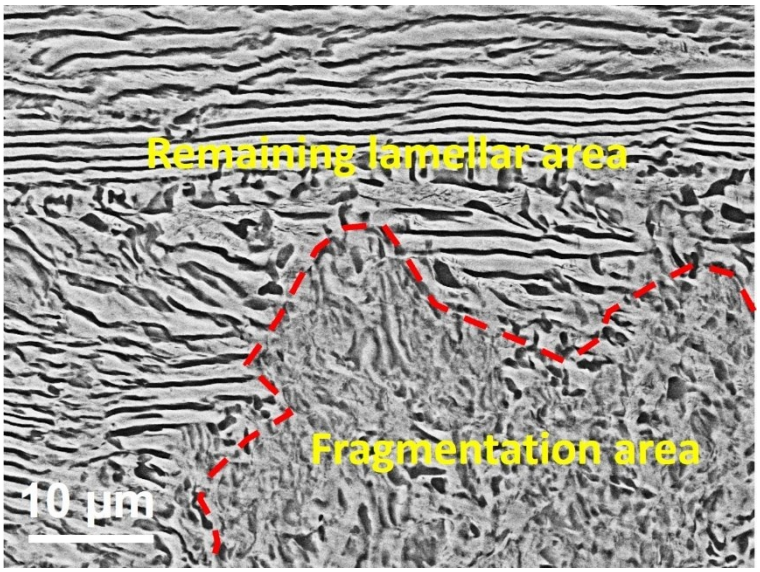

Figure. 2.7 Structural morphology of a lamellar EHEA after HPT of 1 rotation. Both the elongation and distortion feature of lamellae can be seen. The shear plane is horizontal.

Grain refinement occurs in different ways during HPT. For Bcc-structured alloys or Fcc-structured alloys with high stacking fault energies, the readily cross slip of dislocations leads to agglomeration of dislocations and formation of dislocation cell structures (Figure. 2.8) [72][73]. A high density of dislocations accumulates at cell boundaries while the cell interior is nearly defect-free, which leads to the misorientation between different domains and the formation of subgrain boundaries. The newly generated lattice dislocations are annihilated at subgrain boundaries which is accompanied by the increase of misorientation angle.

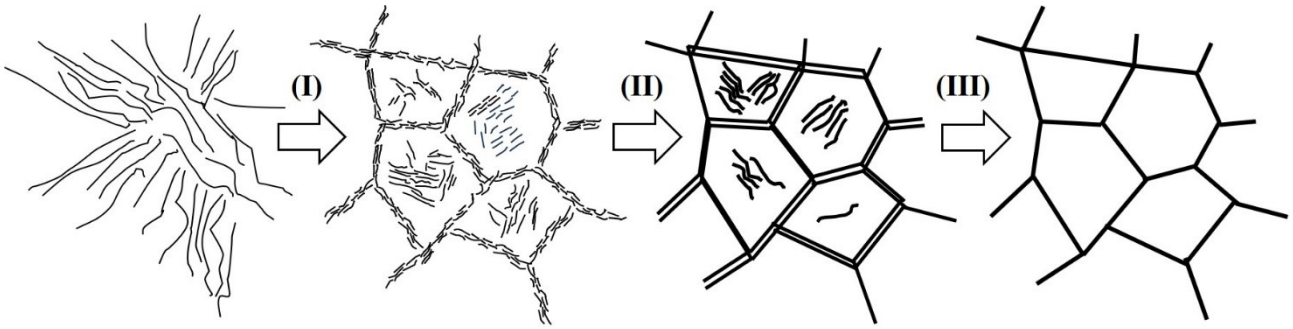

Figure. 2.8 A schematic put forward by Ito et al. [73], showing the dynamical grain refinement of pure Al during HPT. The process includes: (I) Accumulation of dislocations and the formation of subgrain boundaries. (II) Increase in misorientation angle and the absorption of dislocations at grain boundaries. (III) The balance between dislocation generation and absorption.

For Fcc alloys with low stacking fault energies, strain can be accommodated by partial dislocations, deformation twins and phase transformation during HPT. In the CoCrFeNi alloy, the matrix is fragmented into small domains separated by twins and nanobands. Further increase in strain causes the emission of secondary stacking faults and nanotwins from grain boundaries to the matrix which is accompanied by sub-grain rotation (Figure. 2.9). Schuh et al. [74] found that the interaction of different twinning variants forms blocks of twin lamellae, leading to grain refinement in the CoCrFeNiMn alloy.

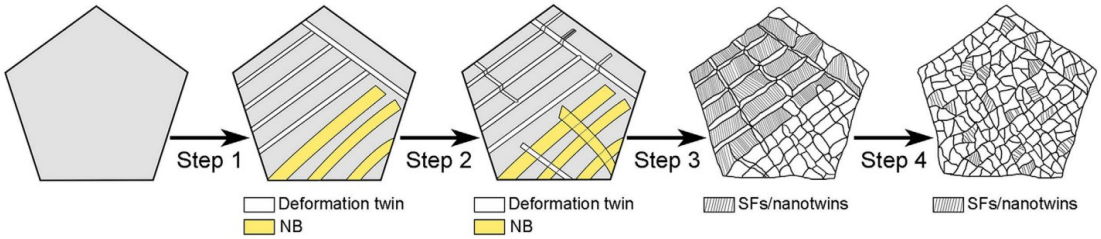

Figure. 2.9 A schematic showing the fragmentation process of a CoCrFeNi HEA during HPT [75].

The crystallographic orientation of alloys or metals is also affected by HPT. Most of the research focuses on Fcc-phase materials and a saturated texture typically is the shear texture. For Fcc alloy with high stacking fault energies, dislocation accumulation and rearrangement occur easily, leading to a change of texture [76]. Hafok et al. [77] investigated the texture evolution of Ni single crystal. It is found that the structure elements rotate into preferred orientations. Once a saturated refinement is realized, the texture is unchanged (Figure. 2.10). Similar behavior can also be found in the CoCuFeMnNi HEA [78]. While its intensity of texture at higher strain is weaker, which is attributed to the further grain fragmentation. For alloys with low stacking fault energy, the dissociated dislocations are hard to recombined for cross slip, which contributed to the delayed recovery process

and a stable texture at higher strain [79].

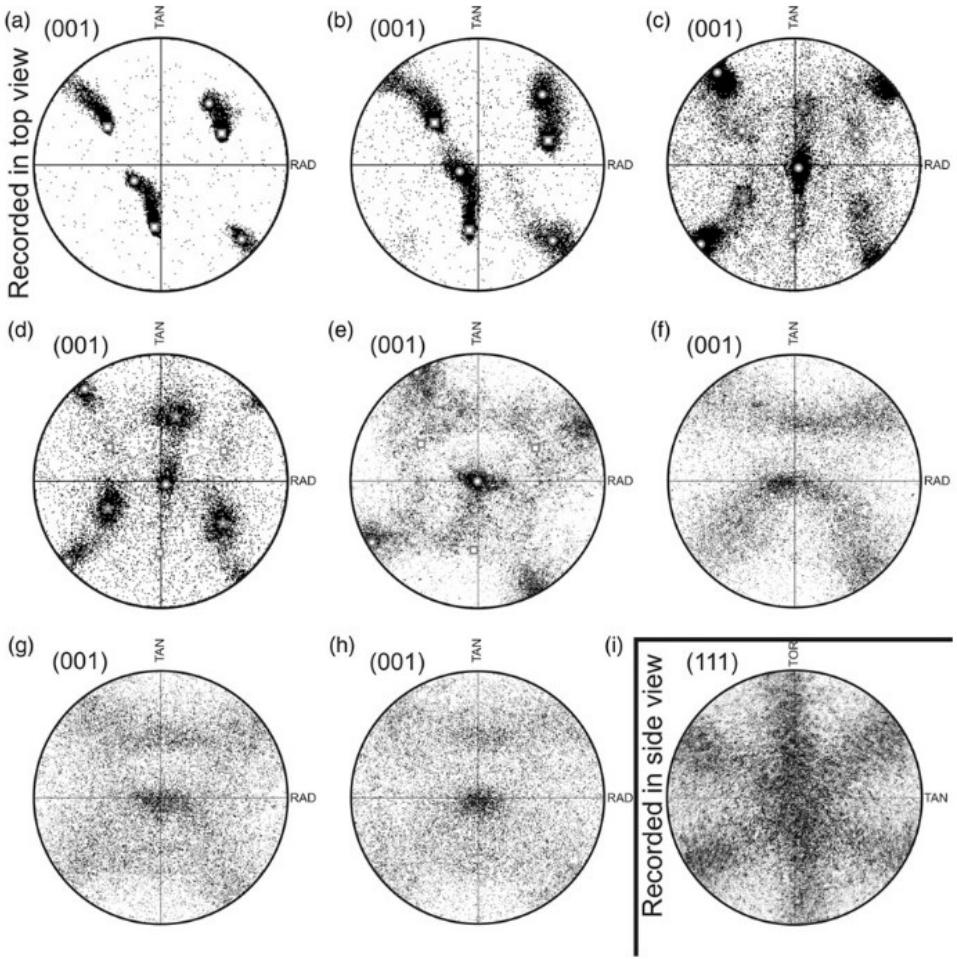

Figure. 2.10 Texture evolution of a nickel single crystal during HPT. White squares mark the initial orientation; white circles mark the first preferred orientation and white stars mark the second preferred orientation [77].

2.6 Motivation of this work

Although numerous studies have been conducted on HEAs, the structural evolution during reactive diffusion still lacks detailed investigation. In the first section of this thesis, a pure Al layer was deposited on a CoCrFeNi HEA by direct current magnetron sputtering without heating. This technique allows to attain physical bonding between bulk material and film without reaction. Then the diffusion couple was subjected to isothermal low-temperature and isochronous high-temperature annealing to investigate the structural evolution of the multicomponent system. In the second section of the thesis, the conclusions from the first section were used to optimize the microstructure of an EHEA to realize enhanced mechanical properties by a combination of HPT and annealing process, and the structural evolution of the EHEA during HPT was investigated.

3 Summary of the publications and manuscripts

Two papers have been published and two manuscripts are under review based on the objective of this work. All content is included in section 6 and a summary is provided below.

3.1 The phase transformation of CoCrFeNi/Al diffusion couple during reactive diffusion

In **PUBLICATION I**, reactive interdiffusion of a diffusion couple CoCrFeNi matrix/Al layer was carried out. The thickness of the Al film was selected to be 3μm based on the following consideration: The thickness is thin enough for the X-ray to penetrate to identify the potential phase transition on the HEA matrix side, and SEM equipped with an EDS detector can be utilized to characterize the structural and chemical changes during the diffusion process. By the combination of results obtained from XRD and SEM, the phase identification and structure evolution can be related. The results show that in the first diffusion stage (Fig. 3.1(a, b)), HEA components diffuse to the Al film, leading to the formation of a monoclinic Al_9Co_2 type phase (marked as T-Al_9Co_2). With the increase of annealing time, a hexagonal Al_5Co_2 type phase (marked as T-Al_5Co_2) starts to replace T-Al_9Co_2 along with the decomposition of the HEA matrix (Fig. 3.1(c, d)).

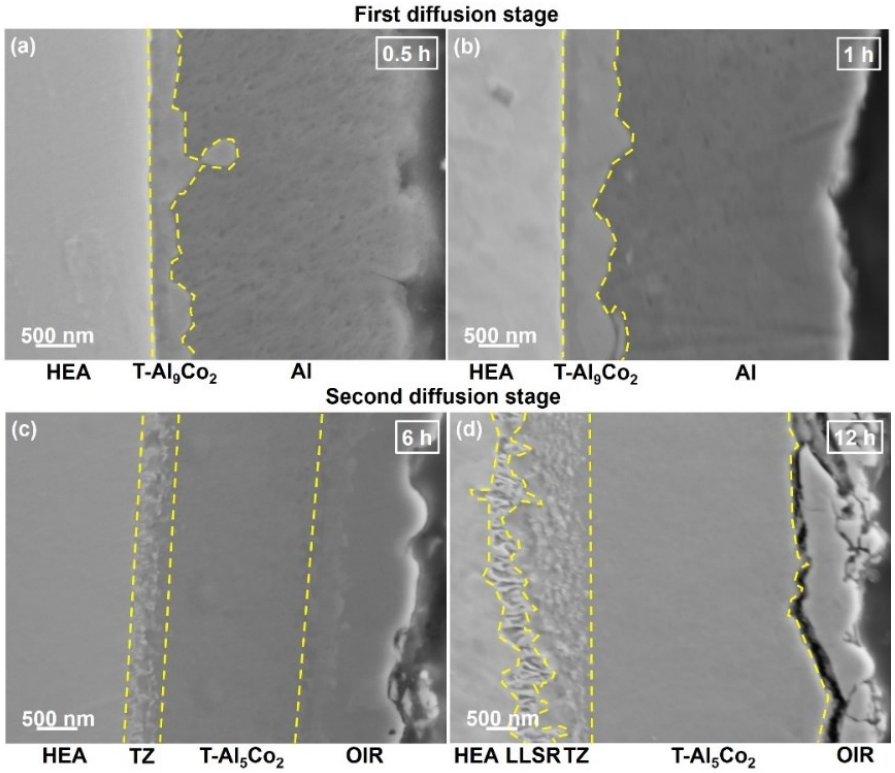

Figure. 3.1 Phase evolution of CoCrFeNi/Al diffusion couple during the isothermal annealing at 773 K for (a) 0.5 h, (b) 1 h, (c) 6 h and (d) 12 h. TZ, OIR, and LLSR indicate the transition zone, the oxide-influenced region, and the lamella-like structure region.

The diffusion direction is controlled by the chemical potential gradient in front of the interface. Under constant pressure and temperature, the molar Gibbs free energy is dominant (Fig. 3.2). In the first stage, T-Al_9Co_2 has lower Gibbs energy compared to the solid solution state, causing diffusion of the HEA component towards Al film. As the diffusion proceeds, a phase transformation from T-Al_9Co_2 to T-Al_5Co_2 phase initiates due to Gibbs free energy difference. The Gibbs free energy of the new phase appears to be even lower than the minimum energy of the Fcc solid solution. Therefore, the reactive diffusion process is accompanied by the decomposition of the HEA matrix.

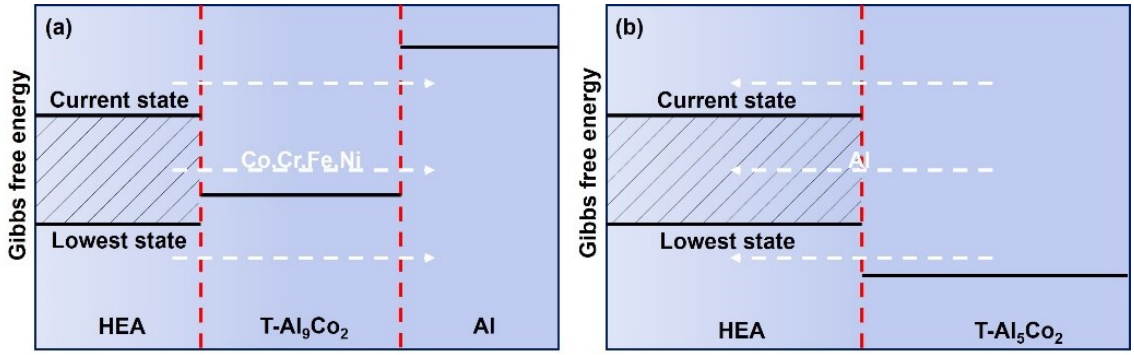

Figure. 3.2 Schematic showing the influence of Gibbs free energy difference of different phases on the diffusion process. (a) First diffusion stage and (b) Second diffusion stage.

PUBLICATION II focuses on the reactive process of a CoCrFeNi/Al diffusion couple during isochronous annealing at elevated temperatures. The energy contribution from the enthalpy part dominates the reaction below 1373 K, as the reaction products are ordered phases (Fig. 3.3(a, c, d)). While entropic contribution starts to play a more significant role at 1373 K, where diffusion of Al towards HEA initiates to form a more disordered state. This increases the lattice parameter of the HEA (Fig. 3.3(b)) and finally results in a single solid solution state (Fig. 3.3(f)). The preferred atomic bonding tendency cannot be fully ignored even in the fully disordered state, which is reflected by the uphill diffusion of Ni towards the Al film side.

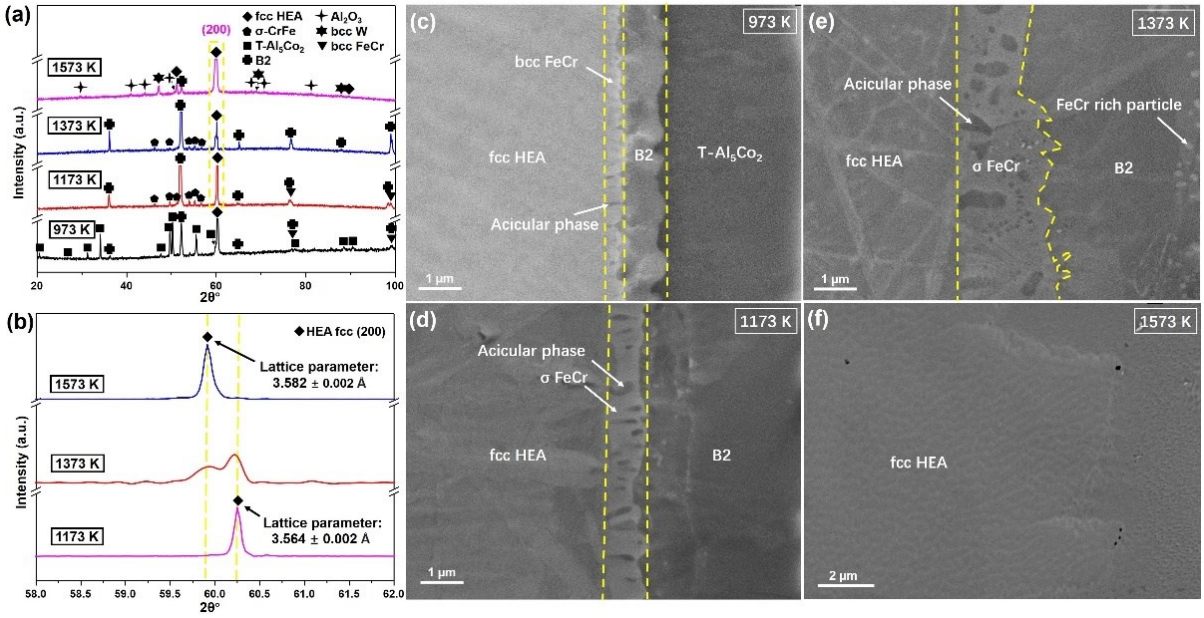

Figure. 3.3 Phase evolution and microstructure characterization of CoCrFeNi/Al diffusion couple after isochronous annealing at elevated temperatures. (a) XRD patterns of samples annealed at different temperatures. (b) Enlarged image of the HEA fcc peak (200) marked in (a). (c-f) SEM images of the interface area of samples annealed at 973 K (c), 1173 K (d), 1373 K (e), and 1573 K (f).

Surface modification can be realized through reactive diffusion. As shown in Fig. 3.4(a, c), the formation of intermetallic compounds on the film side at 1373 K leads to a sudden increase of hardness from the matrix to the film. In contrast to that, a continuous increase of hardness is realized for the sample annealed at 1573 K (Fig. 3.4(b, d)). This is attributed to the solid solution strengthening effect due to the up-hill diffusion of Ni toward the Al side.

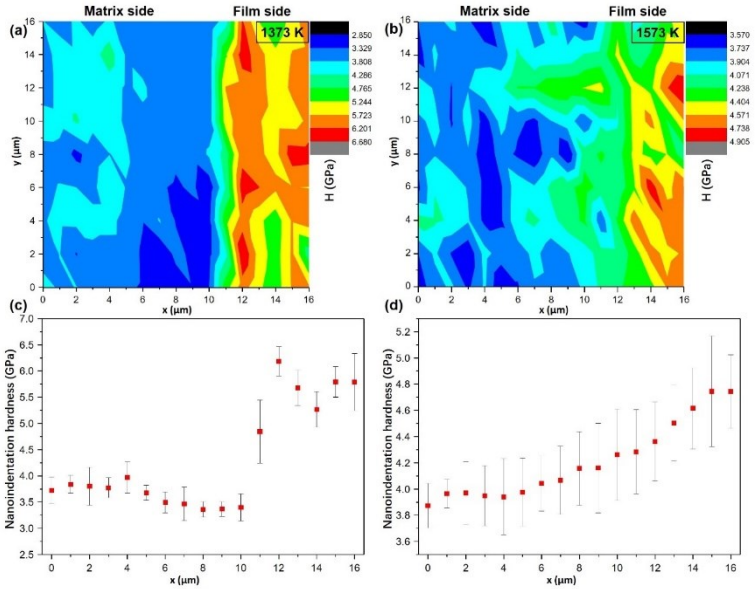

Figure. 3.4 Nanoindentation hardness maps of samples annealed at 1373 K (a) and 1573 K (b) and (c, d) corresponding hardness distribution from the matrix to the film side.

3.2 Structure evolution and mechanical properties of an EHEA during high-pressure torsion

As shown in section 2.4.2, the lamellar EHEAs have received lots of attention due to their ability to overcome the strength-ductility trade-off. However, their response to severe plastic deformation is still unclear. In **MANUSCRIPT III**, the structural evolution of an EHEA during HPT was investigated. It is found that the lamellar structure fragments into small domains due to the applied strain. Fragmentation occurs close to the interface as a result of stress concentration. Due to the different deformation resistance of Fcc and B2 phases, a faster grain refinement process occurs in the Fcc phase. The structural evolution can be reflected by changes in hardness as a function of shear strain (Fig. 3.5). The hardness increases as shear strain γ is applied. After a shear strain γ of 24, the hardness along with the grain refinement and dislocation density reach a saturated state. This is accompanied by the dissolution of Cr-rich nanoparticles and the disordering process of the B2 phase.

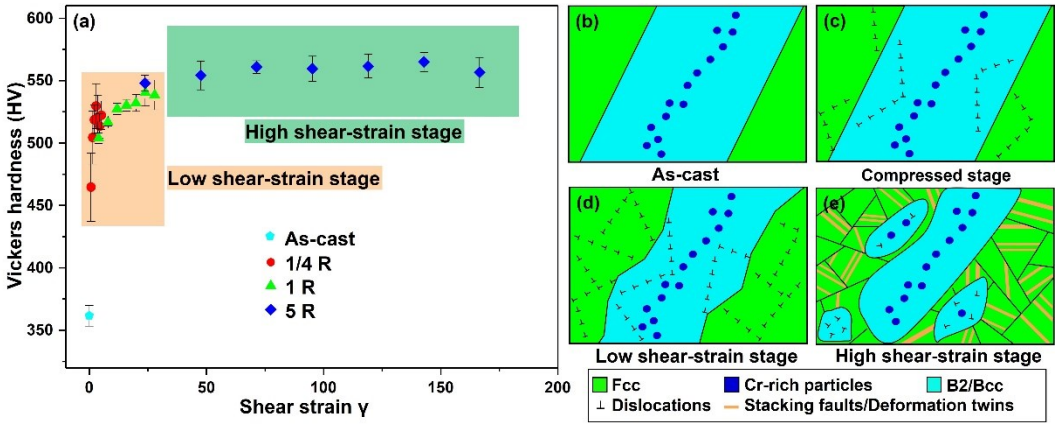

Figure. 3.5 (a) Variation of Vickers hardness as a function of shear strain γ. (b-e) Schematic diagrams showing the structure change of the EHEA during HPT. 1/4 R, 1 R and 5 R represent deformation by HPT for 1/4, 1 and 5 rotations respectively.

As a result of grain refinement and dislocation forest, both the yield strength and ultimate strength are enhanced by a factor of around two after HPT deformation, with some ductility remaining (Fig. 3.6). Even in nanograins, dislocation activity prevails. Introducing a high-volume fraction of grain boundaries, twining boundaries, and a high density of lattice defects during HPT reduces the mean free path of dislocations.

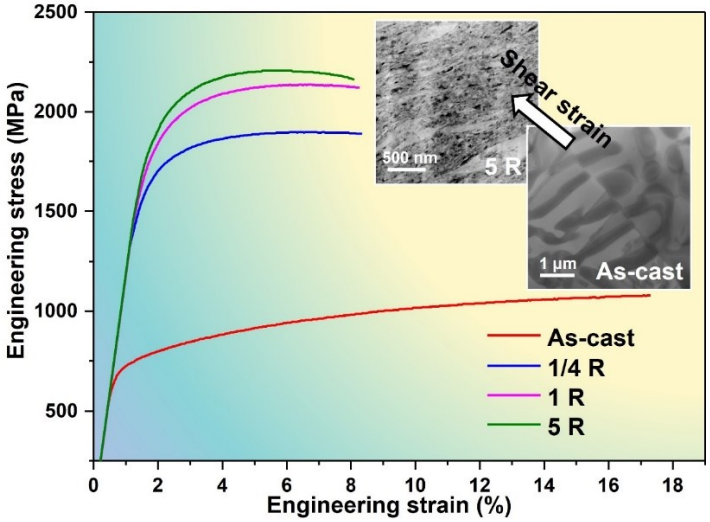

Figure. 3.6 Tensile properties of as-cast samples and HPT-deformed samples at room temperature. Inset shows the structure change from as-cast alloy to sample after HPT deformation of 5 rotations.

3.3 Optimizing mechanical properties of an EHEA through an equiaxed grain design

In **MANUSCRIPT IV,** recrystallization and grain growth of an EHEA are achieved through a combination of HPT and annealing. Through this process, an equiaxed dual-phase structure (EDPS) is formed, replacing the lamellar structure in the initial EHEA (Fig. 3.7). The interface deviates from the Kurdjumov-Sachs crystallographic orientation relationship with the generation of HAGBs.

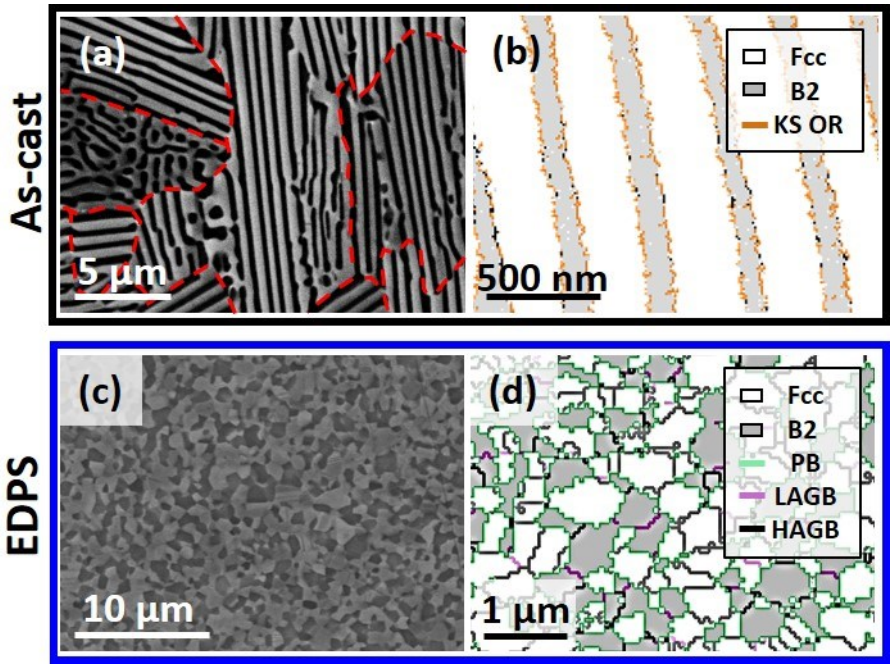

Figure. 3.7 (a) SEM-BSE image and (b) phase map of the as-cast lamellar structure. (c) SEM-BSE image and (d) phase map of the EDPS alloy. KS OR represents the Kurdjumov-Sachs crystallographic orientation relationship.

The structural transformation causes enhancement of strength without sacrificing ductility.

Fig. 3.8 shows the tensile and bending properties of the as-cast and EDPS alloys. The yield strength improves from 703 MPa of the as-cast alloy to 1199 MPa of the EDPS alloy. In contrast to the continuous strain hardening of the as-cast alloy, the plastic deformation of the EDPS alloy can be separated into three stages. After the yield-drop event, the stress gradually rises to a plateau. The last stage shows continuous work hardening until fracture. The strengthening is also reflected in the bending test. In two tested directions, the EDPS alloy shows higher flexural stress compared to the as-cast ones. The intrinsic microcrack-arresting mechanism blocks crack propagation. A high-volume fraction of PBs and HAGBs causes the strain gradient at the interface and the grain boundary, leading to the misorientation development and contributing to the high flow stress of the EDPS alloy.

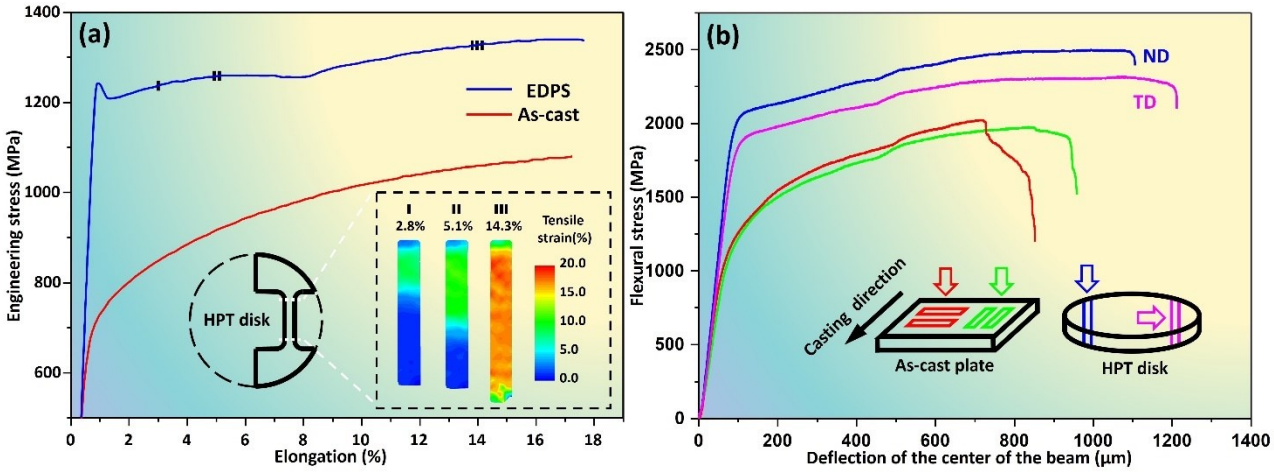

Figure. 3.8 Mechanical responses of the as-cast and EDPS alloys during (a) tensile and (b) three-point bending tests. Inset in (a) showing the schematic diagram of a tensile specimen machined from the HPT disk and strain maps of the gauge part during deformation. Inset in (b) shows the schematic diagram of bending beams machined from the as-cast plate and the HPT disk. Hollow arrows indicate the loading directions. ND and TD represent normal and transverse directions relative to the tensile specimen.

4 Conclusions

In this thesis, the reactive diffusion of a CoCrFeNi/Al diffusion couple has been systematically studied to understand the influence of Gibbs free energy on the phase evolution of the HEA and the potential to be applied for optimizing mechanical properties. To generate bulk samples with optimized properties, severe plastic deformation and annealing of a CoCrFeNiAl-based EHEA is used. The following main conclusions can be drawn from this work:

(i) A complex interdiffusion behavior occurs during isothermal annealing at 573 K. The diffusion process can be separated into two stages based on the molar Gibbs free energy in front of the interface. In the first stage, HEA components diffuse toward the Al film to form a T-Al_9Co_2 phase, which reduces the system energy. In the second stage, T-Al_9Co_2 phase transforms into T-Al_5Co_2 phase. The molar Gibbs free energy of the new phase appears to be lower than the lowest energy state of the disordered solid solution. Hence the formation of the new phase is accompanied by the decomposition of the HEA matrix.

(ii) Through isochronous annealing at elevated temperatures, the contribution of enthalpy and entropy to the total system energy is visualized by the reactive diffusion. At temperatures below 1373 K, intermetallic compounds form as a result of enthalpy-dominated phase evolution. At 1373 K, the entropy of mixing starts to play a more important role, where the diffusion of Al to the HEA matrix initiates at the microscale to form a more disordered state. Even in a fully disordered state, the contribution of enthalpy cannot be ignored as Ni shows up-hill diffusion to the Al side. By comparing the transition temperature from the ordered to the disordered state between the current system and some binary alloys, it is concluded that a high ideal configurational entropy does not stabilize the disordered state.

(iii) Utilizing the thermally stable region of the Al,Ni-rich B2 phase and Co,Cr,Fe-rich Fcc phase during reactive diffusion, a CoCrFeNiAl-based EHEA is selected for optimizing the mechanical properties by a combination of HPT and annealing. The applied strain during HPT leads to the fragmentation in the lamellar structure and the change of the morphology is strongly influenced by the orientation of the in-plane direction of the lamellae with respect to the shear plane. The fragmentation is accompanied by the disordering process of the B2 phase and the dissolution process of the Cr-rich nanoparticles. In areas with nanograins, dislocation-mediated deformation prevails. A high density of dislocations, grain boundaries and twinning

boundaries restrict dislocation activity. Consequently, a high-strength multiphase structure with retained ductility is obtained.

(iv) After HPT and annealing, recrystallization and grain growth occur for the Fcc and B2 phases. The microstructure transforms from the lamellar to an equiaxed one with a weak shear texture. The yield strength increases from 703 MPa to 1199 MPa without sacrificing ductility. During plastic deformation, the localized softening resistance avoids necking, and an intrinsic microcrack-arresting mechanism effectively improves the fracture resistance. Without introducing special structure alignment along the loading direction, a good combination of strength and ductility is realized through this structure design strategy.

5 Outlooks

Exploring new HEAs expands our knowledge of multicomponent systems. There is to date no full understanding of how the interaction between elements affects overall properties as the atomic configuration in HEAs is complex. Reactive diffusion provides a new route to handle this challenging question. By observing microstructure changes, the influence of element interaction on microstructures can be visualized. This helps to understand the origin and evolution of the structure of complex systems.

A combination of HPT and annealing allows to tune microstructures and mechanical properties significantly. This process can also be applied to other HEA systems. The properties can be artificially adjusted by controlling the recrystallization and grain growth.

Reactive diffusion provides guidance for designing multicomponent alloys with preferred structures. In combination with additive manufacturing, properties of the alloy can be constructed by proper element selection and choice of annealing process.

References

[1] J.W. Yeh, S.K. Chen, S.J. Lin, J.Y. Gan, T.S. Chin, T.T. Shun, C.H. Tsau, S.Y. Chang, Nanostructured high-entropy alloys with multiple principal elements: Novel alloy design concepts and outcomes, Adv. Eng. Mater. 6 (2004) 299–303.

[2] B. Cantor, I.T.H. Chang, P. Knight, A.J.B. Vincent, Microstructural development in equiatomic multicomponent alloys, Mater. Sci. Eng. A. 375–377 (2004) 213–218.

[3] B. Predel, M. Hoch, M. Pool, Phase diagrams and heterogeneous equilibria: a practical introduction, Springer Science & Business Media, 2013.

[4] Y. Zhang, T.T. Zuo, Z. Tang, M.C. Gao, K.A. Dahmen, P.K. Liaw, Z.P. Lu, Microstructures and properties of high-entropy alloys, Prog. Mater. Sci. 61 (2014) 1–93.

[5] M. Laurent-Brocq, A. Akhatova, L. Perrière, S. Chebini, X. Sauvage, E. Leroy, Y. Champion, Insights into the phase diagram of the CrMnFeCoNi high entropy alloy, Acta Mater. 88 (2015) 355–365.

[6] N.G. Jones, A. Frezza, H.J. Stone, Phase equilibria of an $Al_{0.5}$CrFeCoNiCu high entropy alloy, Mater. Sci. Eng. A. 615 (2014) 214–221.

[7] F. Otto, Y. Yang, H. Bei, E.P. George, Relative effects of enthalpy and entropy on the phase stability of equiatomic high-entropy alloys, Acta Mater. 61 (2013) 2628–2638.

[8] D. Ma, M. Yao, K.G. Pradeep, C.C. Tasan, H. Springer, D. Raabe, Phase stability of non-equiatomic CoCrFeMnNi high entropy alloys, Acta Mater. 98 (2015) 288–296.

[9] D. Ma, B. Grabowski, F. Körmann, J. Neugebauer, D. Raabe, Ab initio thermodynamics of the CoCrFeMnNi high entropy alloy: Importance of entropy contributions beyond the configurational one, Acta Mater. 100 (2015) 90–97.

[10] F. Zhang, C. Zhang, S.L. Chen, J. Zhu, W.S. Cao, U.R. Kattner, An understanding of high entropy alloys from phase diagram calculations, Calphad Comput. Coupling Phase Diagrams Thermochem. 45 (2014) 1–10.

[11] L.J. Santodonato, P.K. Liaw, R.R. Unocic, H. Bei, J.R. Morris, Predictive multiphase evolution in Al-containing high-entropy alloys, Nat. Commun. 9 (2018) 1–10.

[12] P.J. Shi, W.L. Ren, T.X. Zheng, Z.M. Ren, X.L. Hou, J.C. Peng, P.F. Hu, Y.F. Gao, Y.B. Zhong, P.K. Liaw, Enhanced strength–ductility synergy in ultrafine-grained eutectic high-entropy alloys by inheriting microstructural lamellae, Nat. Commun. 10 (2019) 1–8.

[13] P.J. Shi, R.G. Li, Y. Li, Y.B. Wen, Y.B. Zhong, W.L. Ren, Z. Shen, T.X. Zheng, J.C. Peng, X. Liang, P.F. Hu, N. Min, Y. Zhang, Y. Ren, P.K. Liaw, D. Raabe, Y.D. Wang, Hierarchical crack buffering triples ductility in eutectic herringbone high-entropy alloys, Science. 373 (2021) 912–918.

[14] D.B. Miracle, O.N. Senkov, A critical review of high entropy alloys and related concepts, Acta Mater. 122 (2017) 448–511.

[15] E.P. George, D. Raabe, R.O. Ritchie, High-entropy alloys, Nat. Rev. Mater. 4 (2019) 515–534.

[16] P. Sathiyamoorthi, J. Basu, S. Kashyap, K.G. Pradeep, R.S. Kottada, Thermal stability and grain boundary strengthening in ultrafine-grained CoCrFeNi high entropy alloy composite, Mater. Des. 134 (2017) 426–433.

[17] J.W. Yeh, Recent progress in high-entropy alloys, Ann. Chim. Sci. Des Mater. 31 (2006) 633–648.

[18] D.H. Lee, J.A. Lee, Y. Zhao, Z. Lu, J.Y. Suh, J.Y. Kim, U. Ramamurty, M. Kawasaki, T.G. Langdon, J. il Jang, Annealing effect on plastic flow in nanocrystalline CoCrFeMnNi high-entropy alloy: A nanomechanical analysis, Acta Mater. 140 (2017) 443–451.

[19] F. He, Z. Wang, Q. Wu, J. Li, J. Wang, C.T. Liu, Phase separation of metastable CoCrFeNi high entropy alloy at intermediate temperatures, Scr. Mater. 126 (2017) 15–19.

[20] M. Vaidya, K.G. Pradeep, B.S. Murty, G. Wilde, S. V. Divinski, Bulk tracer diffusion in CoCrFeNi and CoCrFeMnNi high entropy alloys, Acta Mater. 146 (2018) 211–224.

[21] J. Kottke, M. Laurent-Brocq, A. Fareed, D. Gaertner, L. Perrière, Ł. Rogal, S. V. Divinski, G. Wilde, Tracer diffusion in the Ni–CoCrFeMn system: Transition from a dilute solid solution to a high entropy alloy, Scr. Mater. 159 (2019) 94–98.

[22] M. Vaidya, S. Trubel, B.S. Murty, G. Wilde, S. V. Divinski, Ni tracer diffusion in CoCrFeNi and CoCrFeMnNi high entropy alloys, J. Alloys Compd. 688 (2016) 994–1001.

[23] A. Dash, N. Esakkiraja, A. Paul, Solving the issues of multicomponent diffusion in an equiatomic NiCoFeCr medium entropy alloy, Acta Mater. 193 (2020) 163–171.

[24] J.W. Yeh, S.Y. Chang, Y. Der Hong, S.K. Chen, S.J. Lin, Anomalous decrease in X-ray diffraction intensities of Cu-Ni-Al-Co-Cr-Fe-Si alloy systems with multi-principal elements, Mater. Chem. Phys. 103 (2007) 41–46.

[25] S.S. Sohn, A. Kwiatkowski da Silva, Y. Ikeda, F. Körmann, W. Lu, W.S. Choi, B. Gault, D. Ponge, J. Neugebauer, D. Raabe, Ultrastrong medium-entropy single-phase alloys designed via severe lattice distortion, Adv. Mater. 31 (2019) 1–8.

[26] C. Lee, Y. Chou, G. Kim, M.C. Gao, K. An, J. Brechtl, C. Zhang, W. Chen, J.D. Poplawsky, G. Song, Y. Ren, Y.C. Chou, P.K. Liaw, Lattice-distortion-enhanced yield strength in a refractory high-entropy alloy, Adv. Mater. 32 (2020) 1–9.

[27] C. Li, J.C. Li, M. Zhao, Q. Jiang, Effect of aluminum contents on microstructure and properties of $Al_xCoCrFeNi$ alloys, J. Alloys Compd. 504 (2010) 515–518.

[28] W.L.W.R. Wang, W.L.W.R. Wang, S.C. Wang, Y.C. Tsai, C.H. Lai, J.W. Yeh, Effects of Al addition on the microstructure and mechanical property of $Al_xCoCrFeNi$ high-entropy alloys, Intermetallics. 26 (2012) 44–51.

[29] R. Feng, B. Feng, M.C. Gao, C. Zhang, J.C. Neuefeind, J.D. Poplawsky, Y. Ren, K. An, M. Widom, P.K. Liaw, Superior high-temperature strength in a supersaturated refractory high-entropy alloy, Adv. Mater. 33 (2021) 1–9.

[30] J. Kumar, A. Linda, M. Sadhasivam, K.G. Pradeep, N.P. Gurao, K. Biswas, The effect of Al addition on solid solution strengthening in CoCrFeMnNi: Experiment and modelling, Acta Mater. 238 (2022) 118208.

[31] Z. Wang, I. Baker, Z. Cai, S. Chen, J.D. Poplawsky, W. Guo, The effect of interstitial carbon on the mechanical properties and dislocation substructure evolution in $Fe_{40.4}Ni_{11.3}Mn_{34.8}Al_{7.5}Cr_6$ high entropy alloys, Acta Mater. 120 (2016) 228–239.

[32] C.E. Slone, J. Miao, E.P. George, M.J. Mills, Achieving ultra-high strength and ductility in equiatomic CrCoNi with partially recrystallized microstructures, Acta Mater. 165 (2019) 496–507.

[33] S.W. Wu, G. Wang, Y.D. Jia, J. Yi, Q.J. Zhai, C.T. Liu, B.A. Sun, H.J. Chu, J. Shen, P.K. Liaw, T.Y. Zhang, Enhancement of strength-ductility trade-off in a high-entropy alloy through a heterogeneous structure, Acta Mater. 165 (2019) 444–458.

[34] Y. Deng, C.C. Tasan, K.G. Pradeep, H. Springer, A. Kostka, D. Raabe, Design of a twinning-induced plasticity high entropy alloy, Acta Mater. 94 (2015) 124–133.

[35] D.X. Wei, X. Li, J. Jiang, W. Heng, Y. Koizumi, W.M. Choi, B.J. Lee, H.S. Kim, H. Kato, A. Chiba, Novel Co-rich high performance twinning-induced plasticity (TWIP) and

transformation-induced plasticity (TRIP) high-entropy alloys, Scr. Mater. 165 (2019) 39–43.

[36] F. He, D. Chen, B. Han, Q. Wu, Z. Wang, S. Wei, D. Wei, J. Wang, C.T. Liu, J. jung Kai, Design of $D0_{22}$ superlattice with superior strengthening effect in high entropy alloys, Acta Mater. 167 (2019) 275–286.

[37] G. Yang, J.K. Kim, Hierarchical precipitates, sequential deformation-induced phase transformation, and enhanced back stress strengthening of the micro-alloyed high entropy alloy, Acta Mater. 233 (2022) 117974.

[38] P. Sathiyamoorthi, H.S. Kim, High-entropy alloys with heterogeneous microstructure: Processing and mechanical properties, Prog. Mater. Sci. 123 (2022) 100709.

[39] M.F. Ashby, The deformation of plastically non-homogeneous materials, Philos. Mag. 21 (1969) 37–41.

[40] D.A. Hughes, N. Hansen, D.J. Bammann, Geometrically necessary boundaries, incidental dislocation boundaries and geometrically necessary dislocations, Scr. Mater. 48 (2003) 147–153.

[41] X.L. Wu, Y.T. Zhu, Heterogeneous materials: a new class of materials with unprecedented mechanical properties, Mater. Res. Lett. 5 (2017) 527–532.

[42] M.X. Yang, F.P. Yuan, Q.G. Xie, Y.D. Wang, E. Ma, X.L. Wu, Strain hardening in Fe-16Mn-10Al-0.86C-5Ni high specific strength steel, Acta Mater. 109 (2016) 213–222.

[43] Y. Wei, Y. Li, L. Zhu, Y. Liu, X. Lei, G. Wang, Y. Wu, Z. Mi, J. Liu, H. Wang, H. Gao, Evading the strength-ductility trade-off dilemma in steel through gradient hierarchical nanotwins, Nat. Commun. 5 (2014) 1–8.

[44] K. Lu, Making strong nanomaterials ductile with gradients, Science. 345 (2014) 1455–1456.

[45] X.L. Wu, P. Jiang, L. Chen, J.F. Zhang, F.P. Yuan, Y.T. Zhu, Synergetic strengthening by gradient structure, Mater. Res. Lett. 2 (2014) 185–191.

[46] T.H. Fang, W.L. Li, N.R. Tao, K. Lu, Revealing extraordinary intrinsic tensile plasticity in gradient nano-grained copper, Science. 331 (2011) 1587–1590.

[47] X. Wu, M. Yang, F. Yuan, G. Wu, Y. Wei, X. Huang, Y. Zhu, Heterogeneous lamella structure unites ultrafine-grain strength with coarse-grain ductility, Proc. Natl. Acad. Sci. U. S. A. 112 (2015) 14501–14505.

[48] C. Zhang, C. Zhu, T. Harrington, K. Vecchio, Design of non-equiatomic high entropy alloys

with heterogeneous lamella structure towards strength-ductility synergy, Scr. Mater. 154 (2018) 78–82.

[49] C. Zhang, C. Zhu, K. Vecchio, Non-equiatomic FeNiCoAl-based high entropy alloys with multiscale heterogeneous lamella structure for strength and ductility, Mater. Sci. Eng. A. 743 (2019) 361–371.

[50] M. Yang, D. Yan, F. Yuan, P. Jiang, E. Ma, X. Wu, Dynamically reinforced heterogeneous grain structure prolongs ductility in a medium-entropy alloy with gigapascal yield strength, Proc. Natl. Acad. Sci. U. S. A. 115 (2018) 7224–7229.

[51] K. Ming, X. Bi, J. Wang, Strength and ductility of CrFeCoNiMo alloy with hierarchical microstructures, Int. J. Plast. 113 (2019) 255–268.

[52] Y.L. Zhao, T. Yang, Y. Tong, J. Wang, J.H. Luan, Z.B. Jiao, D. Chen, Y. Yang, A. Hu, C.T. Liu, J.J. Kai, Heterogeneous precipitation behavior and stacking-fault-mediated deformation in a CoCrNi-based medium-entropy alloy, Acta Mater. 138 (2017) 72–82.

[53] S. Shukla, D. Choudhuri, T. Wang, K. Liu, R. Wheeler, S. Williams, B. Gwalani, R.S. Mishra, Hierarchical features infused heterogeneous grain structure for extraordinary strength-ductility synergy, Mater. Res. Lett. 6 (2018) 676–682.

[54] P. Sathiyamoorthi, P. Asghari-Rad, J.M. Park, J. Moon, J.W. Bae, A. Zargaran, H.S. Kim, Exceptional cryogenic strength-ductility synergy in $Al_{0.3}$CoCrNi medium-entropy alloy through heterogeneous grain structure and nano-scale precipitates, Mater. Sci. Eng. A. 766 (2019) 138372.

[55] Y.P. Lu, X.Z. Gao, L. Jiang, Z.N. Chen, T.M. Wang, J.C. Jie, H.J. Kang, Y.B. Zhang, S. Guo, H.H. Ruan, Y.H. Zhao, Z.Q. Cao, T.J. Li, Directly cast bulk eutectic and near-eutectic high entropy alloys with balanced strength and ductility in a wide temperature range, Acta Mater. 124 (2017) 143–150.

[56] X. Gao, Y. Lu, B. Zhang, N. Liang, G. Wu, G. Sha, J. Liu, Y. Zhao, Microstructural origins of high strength and high ductility in an AlCoCrFe$Ni_{2.1}$ eutectic high-entropy alloy, Acta Mater. 141 (2017) 59–66.

[57] X. Jin, Y. Zhou, L. Zhang, X.Y. Du, B.S. Li, A new pseudo binary strategy to design eutectic high entropy alloys using mixing enthalpy and valence electron concentration, Mater. Des. 143 (2018) 49–55.

[58] Y. Zhu, X. Wu, Perspective on hetero-deformation induced (HDI) hardening and back stress, Mater. Res. Lett. 7 (2019) 393–398.

[59] A.H. Cottrell, D.L. Dexter, Dislocations and plastic flow in crystals, Am. J. Phys. 22 (1954) 242–243.

[60] D. Kuhlmann-Wilsdorf, C. Laird, Dislocation behavior in fatigue II. Friction stress and back stress as inferred from an analysis of hysteresis loops, Mater. Sci. Eng. 37 (1979) 111–120.

[61] J.I. Dickson, J. Boutin, L. Handfield, A comparison of two simple methods for measuring cyclic internal and effective stresses, Mater. Sci. Eng. 64 (1984) 7–11.

[62] M. Yang, Y. Pan, F. Yuan, Y. Zhu, X. Wu, Back stress strengthening and strain hardening in gradient structure, Mater. Res. Lett. 4 (2016) 145–151.

[63] B. Fournier, M. Sauzay, C. Caës, M. Noblecourt, M. Mottot, Analysis of the hysteresis loops of a martensitic steel. Part I: Study of the influence of strain amplitude and temperature under pure fatigue loadings using an enhanced stress partitioning method, Mater. Sci. Eng. A. 437 (2006) 183–196.

[64] B. Fournier, M. Sauzay, C. Caës, M. Mottot, M. Noblecourt, A. Pineau, Analysis of the hysteresis loops of a martensitic steel. Part II: Study of the influence of creep and stress relaxation holding times on cyclic behaviour, Mater. Sci. Eng. A. 437 (2006) 197–211.

[65] L.F. Huang, Y.N. Sun, N. Chen, H.W. Luan, G.M. Le, X. Liu, Y.Q. Ji, Y.P. Lu, P.K. Liaw, X.S. Yang, Y.Z. Zhou, J.F. Li, Simultaneously enhanced strength-ductility of $AlCoCrFeNi_{2.1}$ eutectic high-entropy alloy via additive manufacturing, Mater. Sci. Eng. A. 830 (2022) 142327.

[66] A.P. Zhilyaev, T.G. Langdon, Using high-pressure torsion for metal processing: Fundamentals and applications, Prog. Mater. Sci. 53 (2008) 893–979.

[67] A. Bachmaier, M. Kerber, D. Setman, R. Pippan, The formation of supersaturated solid solutions in Fe-Cu alloys deformed by high-pressure torsion, Acta Mater. 60 (2012) 860–871.

[68] I. Sabirov, R. Pippan, Formation of a W-25%Cu nanocomposite during high pressure torsion, Scr. Mater. 52 (2005) 1293–1298.

[69] A. Bachmaier, J. Keckes, K.S. Kormout, R. Pippan, Supersaturation in Ag-Ni alloy by two-step high-pressure torsion processing, Philos. Mag. Lett. 94 (2014) 9–17.

[70] F. Wetscher, R. Pippan, S. Sturm, F. Kauffmann, C. Scheu, G. Dehm, TEM investigations of the structural evolution in a pearlitic steel deformed by high-pressure torsion, Metall. Mater. Trans. A Phys. Metall. Mater. Sci. 37 (2006) 1963–1968.

[71] S. Taheriniya, F.A. Davani, S. Hilke, M. Hepp, C. Gadelmeier, M.R. Chellali, T. Boll, H. Rösner, M. Peterlechner, C. Gammer, S. V. Divinski, B. Butz, U. Glatzel, H. Hahn, G. Wilde, High entropy alloy nanocomposites produced by high pressure torsion, Acta Mater. 208 (2021) 116714.

[72] B. Schuh, B. Völker, J. Todt, N. Schell, L. Perrière, J. Li, J.P. Couzinié, A. Hohenwarter, Thermodynamic instability of a nanocrystalline, single-phase TiZrNbHfTa alloy and its impact on the mechanical properties, Acta Mater. 142 (2018) 201–212.

[73] Y. Ito, Z. Horita, Microstructural evolution in pure aluminum processed by high-pressure torsion, Mater. Sci. Eng. A. 503 (2009) 32–36.

[74] B. Schuh, F. Mendez-Martin, B. Völker, E.P. George, H. Clemens, R. Pippan, A. Hohenwarter, Mechanical properties, microstructure and thermal stability of a nanocrystalline CoCrFeMnNi high-entropy alloy after severe plastic deformation, Acta Mater. 96 (2015) 258–268.

[75] W. Wu, M. Song, S. Ni, J. Wang, Y. Liu, B. Liu, X. Liao, Dual mechanisms of grain refinement in a FeCoCrNi high entropy alloy processed by high-pressure torsion, Sci. Rep. 7 (2017) 1–13.

[76] Y. Liu, C. Lu, H. Wang, A.K. Tieu, B. Liu, Microstructure evolution, lattice rotation retardation and grain orientation fragmentation in commercial purity aluminium deformed by high pressure torsion, J. Mater. Res. Technol. 9 (2020) 6642–6654.

[77] M. Hafok, R. Pippan, High-pressure torsion applied to nickel single crystals, Philos. Mag. 88 (2008) 1857–1877.

[78] R. Sonkusare, K. Biswas, N. Al-Hamdany, H.G. Brokmeier, R. Kalsar, N. Schell, N.P. Gurao, A critical evaluation of microstructure-texture-mechanical behavior heterogeneity in high pressure torsion processed CoCuFeMnNi high entropy alloy, Mater. Sci. Eng. A. 782 (2020) 139187.

[79] H. Azzeddine, D. Bradai, T. Baudin, T.G. Langdon, Texture evolution in high-pressure torsion processing, Prog. Mater. Sci. 125 (2022) 100886.

6 Publication and manuscript list

6.1 Publications and manuscripts included in this thesis

Z. Q. Zhang, S. V. Ketov, S. Fellner, H. P. Sheng, C. Mitterer, K. K. Song, C. Gammer, J. Eckert, Reactive interdiffusion of an Al film and a CoCrFeNi high-entropy alloy, ***Mater. Des***. 216 (2022) 110530. DOI: 10.1016/j.matdes.2022.110530

Z. Q. Zhang, S. Fellner, S. Ketov, M. J. Cordill, H. P. Sheng, C. Mitterer, K. K. Song, C. Gammer, J. Eckert, Reactive interdiffusion of an Al film and a CoCrFeNi high-entropy alloy at elevated temperatures, ***Intermetallics***. 153 (2023) 107797. DOI: 10.1016/j.intermet.2022.107797

Z. Q. Zhang, S. Fellner, A. Hohenwarter, O. Renk, Y. Huang, Z. Chen, K. K. Song, C. J. Li, C. Gammer, J. Eckert, Microstructure evolution and mechanical properties of a lamellar $AlCoCrFeNi_{2.1}$ eutectic high-entropy alloy processed by high-pressure torsion, *submitted to* ***Mater. Sci. Eng. A***. *(under review)*

Z. Q. Zhang, Y. Huang, Q. Xu, S. Fellner, A. Hohenwarter, S. Wurster, K. K Song, C. Gammer, J. Eckert, Equiaxed microstructure design enables strength-ductility synergy in the eutectic high-entropy alloy, *submitted to* ***J. Mater. Res. Technol****. (under review)*

6.2 Publications not included in this thesis

[1] S. V. Ketov, Y. P. Ivanov, B. Putz, **Z. Q. Zhang**, J. Eckert, A. L. Greer, Atomic diffusivities in amorphous and liquid Cu-Zr: Kirkendall effects and dependence on packing density, ***Acta Mater***. 214 (2021) 116993. DOI: 10.1016/j.actamat.2021.116993

[2] X. M. Liu, Z. D. Kou, R. T. Qu, W. D. Song, Y. J. Gu, C. S. Zhou, Q. W. Gao, J. Y. Zhang, C. D. Cao, K. K. Song, V. Zadorozhnyy, **Z. Q. Zhang**, J. Eckert, Accelerating matrix/boundary precipitations to explore high-strength and high-ductile $Co_{34}Cr_{32}Ni_{27}Al_{3.5}Ti_{3.5}$ multicomponent alloys through hot extrusion and annealing, ***J. Mater. Sci. Technol***. 143 (2022) 62–83. DOI: 10.1016/j.jmst.2022.08.052

[3] X. D. Yuan, **Z. Q. Zhang**, Q. W. Gao, L. Zhou, K. K. Song, X. Y. Zou, D. Şopu, L. N. Hu, B. A. Sun, J. Eckert, Enhanced mechanical properties of $Zr_{65}Cu_{15}Ni_{10}Al_{10}$ bulk metallic glass by simultaneously introducing surface grooves and multiple shear bands, ***J. Mater. Res. Technol***. 21 (2022) 1490–1506. DOI: 10.1016/j.jmrt.2022.09.117

[4] M. Z. Zhang, K. Zhang, K. K. Song, X. Y. Zou, W. D. Song, K. F. Li, L. N. Hu, **Z. Q. Zhang**, J. Eckert, Enhanced mechanical performance of gradient-structured CoCrFeMnNi high-entropy alloys induced by industrial shot-blasting, ***Rare Met***. 42 (2022) 982–993. DOI: 10.1007/s12598-022-02164-1

[5] Y. Xing, C. J. Li, Y. K. Mu, Y. D. Jia, K. K. Song, J. Tan, G. Wang, **Z. Q. Zhang**, J. H. Yi, J. Eckert, Strengthening and deformation mechanism of high-strength CrMnFeCoNi high entropy alloy prepared by powder metallurgy, ***J. Mater. Sci. Technol***. 132 (2023) 119–131. DOI: 10.1016/j.jmst.2022.06.009

[6] S. L. Zhao, B. Jiang, K. K. Song, X. M. Liu, W. Y. Wang, D. K. Si, J. L. Zhang, X. Y. Chen, C. S. Zhou, P. P. Liu, D. Chen, **Z. Q. Zhang**, P. Ramasamy, J. L. Tang, W. Q. Lv, K. G. Prashanth, D. Şopu, J. Eckert, Machine learning assisted design of high-entropy alloys with ultra-high microhardness and unexpected low density, ***Mater. Des***. 238 (2024) 112634. DOI: 10.1016/j.matdes.2024.112634

[7] C. S. Zhou, Z. D. Kou, K. K. Song, J. H. Gong, P. P. Liu, Q. W. Gao, X. M. Liu, X. L. Han, **Z. Q. Zhang**, P. Ramasamy, L. N. Hu, J. Orava, J. Eckert, Evading strength-ductility trade-off dilemma in TRIP-assisted $Fe_{50}Mn_{30}Co_{10}Cr_{10}$ duplex high-entropy alloys via flash annealing and deep cryogenic treatments, ***Acta Mater***. 268 (2024) 119779. DOI: 10.1016/j.actamat.2024.119779

[8] X. M. Liu, K. K. Song, Z. D. Kou, J. H. Gong, X. Y. Chen, Q. W. Gao, H. Sun, P. P. Liu, R. T. Qu, L. N. Hu, **Z. Q. Zhang**, P. Ramasamy, Z. Q. Liu, Z. J. Zhang, F. Liu, Z. F. Zhang, J. Eckert, Synergistic grain boundary engineering for achieving strength-ductility balance in ultrafine-grained high-Cr-bearing multicomponent alloys, ***Int J Plasticity***. 177 (2024) 103992. DOI: 10.1016/j.ijplas.2024.103992

Publication I

Reactive interdiffusion of an Al film and a CoCrFeNi high-entropy alloy

Z. Q. Zhang[1,2], S. V. Ketov[1], S. Fellner[1,2], H. P. Sheng[1], C. Mitterer[4], K. K. Song[3], C. Gammer[1,*], J. Eckert[1,2,*]

[1]*Erich Schmid Institute of Materials Science, Austrian Academy of Sciences, Jahnstraße 12, 8700 Leoben, Austria*

[2]*Department of Materials Science, Montanuniversität Leoben, Jahnstraße 12, 8700 Leoben, Austria*

[3]*School of Mechanical, Electrical & Information Engineering, Shandong University, Wenhua Xilu 180, 264209 Weihai, China.*

[4]*Department of Materials Science, Montanuniversität Leoben, Franz-Josef-Straße 18, 8700 Leoben, Austria*

** Corresponding authors: christoph.gammer@oeaw.ac.at; juergen.eckert@unileoben.ac.at*

Abstract

Diffusion plays a significant role in phase formation and transformation in solid-state alloys. In order to determine the influence of element diffusion on the phase formation and transition behavior in a high-entropy alloy (HEA), a systematic study on the reactive diffusion of Al and a CoCrFeNi HEA was carried out. It is demonstrated that thermodynamic and kinetic effects play a coupled role in the phase evolution in the HEA, among which the thermodynamic effect governs the evolution of major phases. The diffusion direction of the elements is controlled by the Gibbs free energy gradient in front of the interface, while the sluggish diffusion effect does not play a dominant role during reactive diffusion. At an annealing temperature of 773 K, the enthalpy of mixing dominates the total energy and therefore has a significant impact on the phase evolution during reactive diffusion.

Keywords: Reactive diffusion, High-entropy alloy, Deposition, Phase evolution

1. Introduction

High-entropy alloys (HEAs) have attracted a lot of interest since the first report in 2004 by Cantor and Yeh [1,2]. In comparison to the conventional alloy design strategy based on one or two principal elements with minor additions of other elements, HEAs combine more than 4 or 5 principal elements

with equal or similar atomic ratios. This design strategy results in four core effects: high-entropy effect, sluggish diffusion effect, severe lattice-distortion effect and cocktail effect [3,4]. These core effects give HEAs some promising properties [5] such as high hardness [6,7] and strength [8,9], good thermal stability [10] and excellent corrosion resistance [11,12], etc.

One of the most important structural features of HEAs is the "high-entropy effect", which leads to the tendency to form simple solid solutions [4] with face-centered cubic (fcc), body-centered cubic (bcc) or hexagonal close-packed (hcp) structure [13–16] instead of multiple compounds or complex phases. However, several recent studies have debated the dominance of the configurational entropy in determining the phase stability of HEAs [15,17,18]. Based on phase diagram calculations, Zhang *et al.* [15] established that most of the HEAs reported in literature were prepared by casting and hence the major phases observed tend to be primary solidified solid solution phases. It was also pointed out that the precipitation of intermetallic phases during thermal exposure can be attributed to the significance of the enthalpy of phase formation in determining the phase equilibria [19]. Moreover, by introducing a large number of grain boundaries that serve as fast diffusion paths, phase decomposition was observed during annealing of severely deformed HEAs [20] and nanocrystalline single-phase CrMnFeCoNi alloy fabricated by thin film deposition decomposed after 1h annealing at 573 K [21]. Therefore, it is important to investigate the effect of atomic diffusion on the phase formation in HEAs. Several works have been performed to study the diffusion behavior of HEAs. Tsai *et al.* [22] proposed a pseudo-binary approach to investigate the interdiffusion behavior in HEAs. Vaidya *et al.* [23] investigated tracer diffusion of Co, Cr, Fe, and Mn in CoCrFeNi and CoCrFeMnNi HEAs, and found that, if the diffusion rate is compared at a given absolute temperature instead of the homologous temperature for the multicomponent alloys, diffusion is not at all sluggish. Besides, it was found that increasing the solute concentration while keeping the same elements does not inevitably induce 'sluggish' diffusion at a given temperature [24].

Due to the complex interaction between multiple elements, the investigation of reactive diffusion in HEAs is quite challenging. Only a few reports paid attention to the reactive diffusion behavior of HEAs. By joining $Al_{0.85}CoCrFeNi$ with a TiAl alloy, it was found that Ni and Co are more prone to diffuse from the HEA to TiAl than Cr and Fe. Moreover, new phases tend to form on the TiAl side, which was attributed to the sluggish diffusion effect in HEAs [25]. Li *et al.* [26] further studied the elemental diffusion behavior and mechanical properties of diffusion bonded joints between

$AlCoCrFeNi_{2.1}$ and a TiAl alloy. They found a penetration phenomenon and a convex structure formed in the diffusion zone, which results in an interlocking effect and thus enhances the strength of the resultant joint. They further joined the $AlCoCrFeNi_{2.1}$ HEA with a GH4169 superalloy and found that a layer of a fcc phase was formed near the base metal region of the HEA. As the bonding temperature increased, the fcc phase became broader accompanied by an enhancement of the joint shear strength [27]. Du *et al.* [28] bonded $Al_5(TiZrHfNb)_{95}$ with the Ti_2AlNb intermetallic compound and pointed out that the observed formation of Al_3Zr_5 is attributed to its lowest Gibbs energy for all the possible intermetallic compounds in the range of the welding temperature. By studying the microstructure and mechanical properties of diffusion bonded joints of the TC4 (Ti-6Al-4V) alloy and the $Al_5(HfNbTiZr)_{95}$ HEA, Peng *et al.* [29] found that the reactive zone can be separated into a zone with acicular titanium structures and a continuous solid solution reaction zone which inherited the orientation of the HEA matrix. The growth of all reaction zones was in a parabolic manner with increasing bonding temperature but the shear strength of the joints first increased and then decreased, which was attributed to insufficient bonding time and coarsening of grains, respectively.

To ensure true bonding, most of the reactive-diffusion studies in HEAs were carried out by bonding joints with a constant load applied for a certain time. Therefore, the information on the early stage of diffusion might be lost. Moreover, the creep behavior induced by the applied force might further complicate the diffusion process. Hence, systemic investigations of the reactive diffusion behavior of HEAs without an applied load are needed. In this paper, in order to better understand the influence of the reactive diffusion process on the phase evolution in HEAs and capture the diffusion behavior at different times, an Al film was deposited on a CoCrFeNi HEA, followed by isothermal annealing for different times. It is reported the CoCrFeNi HEA has a fcc structure showing excellent thermal stability without decomposition at elevated temperatures [10]. This can eliminate the effect of phase transformation in the HEA matrix on the interdiffusion behavior. Meanwhile, the CoCrFeNi system is a common prototype for 3d transition metal HEAs [4,30–32]. It was shown that the phase evolution from fcc to bcc phase is realized by the addition of Al to CoCrFeNi in conventional casting processes [33,34]. The study of reactive diffusion of CoCrFeNi with Al could thus provide guidance for the phase prediction and alloy design of HEAs. Moreover, Al atoms have a similar atomic radius as the current HEA components (within 15%). Based on the Hume-Rothery rules [35], it can be expected that the substitutional solid solution rule will be followed and that vacancy diffusion will be

the dominant diffusion mechanism. Hence, a more trackable investigation can be realized. Thus, CoCrFeNi and Al were chosen as the diffusion couple.

2. Materials and methods

The CoCrFeNi HEA with an equal atomic ratio was prepared by vacuum arc melting of nominal mixtures of the corresponding elements (purity ≥ 99.95%) and was remelted at least five times in a Ti-gettered high-purity argon atmosphere to ensure chemical homogeneity. The molten alloy was cast into a water-cooled Cu mold to form a plate with a width of 10 mm and a thickness of 2 mm. This was followed by homogenization annealing in a vacuum furnace (Xerion Xtube) at 993 ± 5 K for 1 h. The chamber was evacuated to $<5 \times 10^{-5}$ Pa before annealing.

For the sputter deposition of the Al films, the CoCrFeNi plate was cut into slices (length of ~ 3.5 mm, width of ~ 1.5 mm). The surfaces to be coated were prepared by mechanical grinding using 500 to 4000 FEPA grit size SiC abrasive planar papers, followed by a final polish with conventional aluminum oxide polishing suspension (OPS). Next, the substrates were loaded into the vacuum chamber of the magnetron sputter deposition system (FHR. Line. 600 V) and plasma cleaned for ~16 min using Ar ions to remove surface residues. In order to realize the diffusion process on the micron scale and characterize it conveniently, an Al film with thickness of 3 μm was deposited by direct current magnetron sputtering of a planar Al target (size 600 × 125 mm) at a power of 3500 W. The base pressure of the chamber before deposition was 3.4×10^{-4} Pa. No external heating was applied to the grounded substrate holder. The argon flow rate was set to 300 sccm and a pressure of 4.5×10^{-1} Pa was maintained during deposition. After deposition, the samples were isothermally vacuum annealed at 773 ± 5 K for 0.5, 1, 6, and 12 h, respectively. The pressure was maintained below 1.8×10^{-3} Pa during annealing.

After annealing, X-ray diffraction (XRD, Co-Kα radiation) patterns were obtained using a Bruker D2 phaser diffractometer at a scan rate of 1.04°/min. A scanning electron microscope (SEM-LEO1525, Zeiss) equipped with back-scattered electron (BSE) and energy-dispersive X-ray spectroscopy (EDS) units was used to determine the structure and elemental composition of the samples. For in-depth investigation of the phase evolution, transmission electron microscopy (TEM) was used to identify tiny crystals and the phase distribution of the specimens annealed at 773 K for 12 h. Cross-sectional TEM specimens from the interface were prepared by in-situ lift-out in a dual-beam focused ion beam

(Zeiss Auriga Laser FIB system) with an OmniProbe nanomanipulator. TEM images, diffraction patterns and scanning TEM (STEM) images were obtained using a JEOL JEM-2200FS equipped with EDS.

3. Results

An excellent thermal stability of the HEA matrix is a necessary prerequisite for the further reactive diffusion investigations. XRD patterns of as-cast and homogenized CoCrFeNi samples are presented in Fig. 1(a). Both samples retain a single-phase fcc structure. The differences in the peak intensities can be explained by slight texture variations of as-cast samples. However, texture does not affect the jump frequency and interatomic distance in cubic metals [36]. Therefore, potential grain re-orientation during reactive diffusion, caused by texture, cannot affect the bulk diffusion behavior in the HEA matrix. Fig. 1(b) shows the grain morphology of the homogenized alloy, revealing that the matrix is primarily composed of coarsened columnar-like grains with sizes of hundreds of micrometers.

Reactive diffusion behavior during low-temperature isothermal annealing

To understand the relationship between reactive diffusion and phase transition, HEA samples with deposited Al films (HEA/Al) were subjected to thermal diffusion experiments at 773 K. The phase evolution after different annealing times can be seen in the XRD patterns shown in Fig. 2(a). Initially only two fcc phases are present corresponding to the HEA matrix and the Al layer. The (200) peak of the fcc HEA is retained for all samples, demonstrating the thermal stability of the HEA matrix during annealing at 773 K. After annealing for 0.5 h, a monoclinic Al_9Co_2 phase is formed, marked as T-Al_9Co_2. After 1 h annealing, its volume fraction increases, as shown by the relative increase of the diffraction peaks. After 6 hours of annealing, the peaks corresponding to the fcc Al phase are no longer visible, indicating that Al has completely reacted with the elements of the HEA. The amount of T-Al_9Co_2 phase decreased and a new phase is formed. According to the XRD results, the new phase has a $P6_3/mmc$ space group which is isotypic to hexagonal Al_5Co_2 and Al_5FeNi. This phase is indicated as T-Al_5Co_2. After annealing for 12 h, the T-Al_9Co_2 phase has fully disappeared along with an increase in the amount of T-Al_5Co_2 phase. In addition, a disordered bcc phase is formed.

The structure evolution of the reaction area during annealing is shown in the SEM images in Figs.

2(b-f). It can be seen that all the interfaces formed during annealing show uneven features, which can be attributed to a faster diffusion along grain boundaries. From the inset of Fig. S1(c), the growth of a newly formed intermetallic compound along the grain boundary between two Al crystals can be seem. The SEM images of the as-deposited Al surface (Fig. 1(c)) and cross-sectional view (inset in Fig. S1(b)) reveal that the columnar Al crystals have a broad size distribution below 2 μm. The change of Al crystal morphology after annealing for 0.5 h demonstrates that grain growth occurred during annealing. This indicates that the grain growth in Al in combination with an anisotropic distribution of grain boundaries at the interface affect the diffusion rates and the nucleation and growth of new phases, which further influences the morphology of the interface. Fig. 2(b) reveals that sputter deposition results in good physical bonding without gaps between the HEA and the as-deposited Al layer. Annealing for 0.5 h (Fig. 2(c)) results in the diffusion of the HEA components towards the Al film, while no detectable diffusion of Al towards the HEA can be found. This is confirmed by the formation of new T-Al_9Co_2 crystals growing into the Al layer. Additionally, EDS analyses were performed to study the chemical distribution (see Table 1). Due to the dynamic diffusion process, the chemical composition for the same crystal phase can vary slightly in different scanning areas (±5 at.%). Therefore, each phase was measured at least three times, and the mean composition is shown along with the standard deviation (see supplementary Fig. S2 for the locations from which the EDS results were obtained). The results show that all four HEA matrix components are evenly distributed in the T-Al_9Co_2 phase, which can be explained by the substitution of Cr, Ni, and Fe for the Co lattice sites. In fact, the $Al_9(Fe,Ni)_2$ phase exists in the ternary Al-Fe-Ni system and it is isomorphous with Al_9Co_2 and $Al_9(Co,Ni)_2$ [37]. Annealing for 1 h leads to growth and coarsening of the T-Al_9Co_2 grains along with the formation of a spatially anisotropic diffusion front with separated T-Al_9Co_2 grains (see Fig. 2(d)). The corresponding EDS mapping results (cf. Table 1) shows faster diffusion of Cr into the Al layer. Since the surface of HEAs for deposition were mechanically polished to a mirror-like surface prior to the deposition process, the formation of Cr-oxide before annealing can be excluded. Cr reacts with Al and possibly forms monoclinic $Al_{13}Cr_2$ in front of the T-Al_9Co_2 layer (see Fig. S2(b)). However, due to its small amount, it is hard to detect by XRD. After 6 h of annealing (Fig. 2(e)), the pure Al film has vanished. Meanwhile, T-Al_5Co_2 gradually substitutes T-Al_9Co_2 and becomes the dominant phase on the film side. The diffusion zone near the free side becomes divided into two distinct zones (Fig. 2(e)). According to the EDS results shown in Fig. S3(d), a higher concentration

of Al and O can be found in the region near the free side, while the interior layer is rich in Cr and O, which could be attributed to oxidation; the strong oxygen signal in the HEA matrix is caused by the overlapping photon energy range between O and the HEA component Cr (~0.53 Kev of O Kα, ~0.57 Kev of Cr Lα). By studying the isothermal oxidation behavior of $CoCrFeNiAl_{0.5}$, Doleker *et al*. [38] found that Al, followed by Cr, react with oxygen to form an oxide scale, which leads to the selective depletion of elements close to the oxide scale, which further influences the element distribution of the free-surface side. This is similar to the present results of Fig. 2(e), revealing an oxide-influenced region. Moreover, a transition zone with a non-defined border between HEA and T-Al_5Co_2 in this region can be found. A closer examination of this area shows that the HEA phase decomposed at the interface. A similar phenomenon has also been found in previous reports [26,39]. In the present work, this can be interpreted as a second diffusion stage, where the HEA matrix starts to decompose and the growth of an Al-containing compound towards the HEA initiates. Annealing for 12 h leads to further growth of the T-Al_5Co_2 phase towards the HEA (Fig. 2(f)). Between the transition layer and the HEA matrix, a lamella-like structure region (LLSR) appears, where acicular bright and dark phases are distributed alternately. In addition, voids and cracks form at the free side of the film in the oxide influenced region. By studying the oxidation behavior of a CoCrFeMnNi HEA, Vilémová *et al.* [40] concluded that the formation of pores near the oxide scale during oxidation is attributed to the outward diffusion of Mn. A similar phenomenon observed in the present work is probably due to the outward diffusion of Al and Cr to form the oxide scale, leading to the appearance of voids. The accumulation of voids and the oxidation results in the formation of a porous brittle structure near the surface.

In order to identify the phase distribution in the LLSR region, detailed TEM investigations were carried out at the nanoscale. Fig. 3 shows a bright field (BF) STEM image, a selected area diffraction pattern (SAED) and the corresponding EDS map for the sample annealed for 12 h. From the dark field (DF) image (Fig. 3(b)) and the SAED patterns (Fig. 3(c)), it can be concluded that the lamella structure is composed of bcc phases, corresponding to the bcc phase found by XRD. The EDS mapping shows that the layers are composed of a Cr-rich or a (Fe, Co)-rich phase. Moreover, the up-hill diffusion of Ni and to some extent Co is clearly visible in the transition zone.

4. Discussion

4.1 Thermodynamic and kinetic analysis of the phase transition behavior during isothermal

annealing

The phase stability can be described by the Gibbs free energy. The most stable phases possess the lowest free energy under given conditions and concentrations of the consisting elements, which is visualized by the stable phase diagrams. For HEAs, consisting of multiple principal elements, it is almost impossible to construct their phase diagrams. However, as a first approximation, the reactive diffusion between the 3 μm Al layer and the HEA could be regarded as a semi-infinite pseudo-binary diffusion couple. It is therefore reasonable to use binary phase diagrams of Al with the HEA components to reflect the phase stability. According to the binary phase diagrams of Al with Co, Cr, Fe, Ni [41], and taking into account that Co, Cr, Fe and Ni diffuse to the Al side, we can expect the formation of Al_9Co_2, $Al_{13}Cr_2$, $Al_{13}Fe_4$ and Al_3Ni phases. The EDS results shown in Table 1 reveal a higher concentration of Cr in the Al layer as compared to other elements after a short diffusion time of 1 h. This indicates a higher diffusion coefficient of Cr in Al than for the other elements. Compared with the other potential intermetallic compounds, the formation of $Al_{13}Cr_2$ should be more preferable since already a relatively small addition of Cr to Al will result in the formation of $Al_{13}Cr_2$. In the experiments, however, only a small amount of $Al_{13}Cr_2$ (see Fig. S2(b)) was observed, while the major phase formed was T-Al_9Co_2, which can be explained by the fact that Co and Ni have more negative mixing enthalpy with Al than Cr (see Table 2). Therefore, Al tends to react with Co and Ni to form more stable phases. After annealing for 1 h, the content of Fe, Co and Ni in the T-Al_9Co_2 phase is higher than that of Cr (Table 1), suggesting that the formation of T-Al_9Co_2 will act as a barrier to the reactive diffusion of Al and HEA, and impede the further diffusion of Cr from the HEA towards Al. With further annealing, the T-Al_9Co_2 phase grows and gradually replaces Al. The depletion of Cr in the T-Al_9Co_2 phase and the continuous diffusion of the HEA components into the film cause a relative decrease of the Al content on the film side, which induces the formation of the T-Al_5Co_2 intermetallic compound. At the same time, Cr diffuses from the HEA matrix to T-Al_5Co_2. After annealing for 6 h, Co, Cr, Fe and Ni are relatively uniformly distributed in the T-Al_5Co_2 phase. It is interesting to note that only binary phases with simple structure were observed in the reaction zone, rather than complex multi-component phases.

During the first diffusion stage (< 6 h) no significant diffusion of Al into the HEA was observed. However, once T-Al_5Co_2 becomes the dominant phase in the Al layer, Al starts to diffuse from the film side into the HEA matrix, as can be seen from the broadening of the Al-containing region in Fig.

2(e) and Fig. S3(d). There are two possible reasons for this phenomenon: (i) From the perspective of kinetics, after homogenization annealing, the HEA contains only a few vacancies. The diffusion of the HEA components into the Al layer leads to an increase in vacancies close to the interface. These vacancies act as carriers for substitutional diffusion of Al towards the HEA. Therefore, after 6 h, the diffusion of Al into the HEA initiates. (ii) From the thermodynamic point of view, once a more stable phase compared with the HEA is formed on the film side, the reactive diffusion will go towards the HEA alloy side in order to lower the energy of the system. The diffusion of Al into the HEA observed here is accompanied by the decomposition of the HEA in the transition zone, proving that T-Al_5Co_2 has higher stability than the HEA. If kinetics would play a dominant role, vacancy formation and HEA component diffusion should proceed simultaneously, and a diffusion of Al to the HEA would be expected already after short diffusion times (< 6 h). Therefore, it is believed that thermodynamic effects dictate the diffusion direction. Because of the smaller crystal size on the film side, bulk and grain boundary diffusion will take place simultaneously. Still, the relatively homogenous element distribution in the intermetallic compounds formed at different times and their stable phase distribution at the interface (< 6 h) or film side (≥ 6 h) indicate that different diffusion processes do not affect the main conclusions of the present work. Finally, the strong bonding tendency of Ni, Co and Al at the interface, caused by their more negative mixing enthalpy, results in up-hill diffusion of Ni and some Co in the transition zone (as shown in Figs. 3(e-i)) and therefore indirectly leads to the formation of the lamellar-like bcc phases. The staggered formation of Cr-rich and (Fe, Co)-rich layers may be due to complex multicomponent interactions at the interface. Due to the variance of the phase composition and phase transformation during the reactive diffusion process, elements in different crystal configurations will have different interatomic potentials and thus different vibrational and jumping frequencies. As a result of this, the diffusion coefficients of different elements are hard to obtain. However, the coupled role of thermodynamic and kinetic effects during phase evolution in the HEA can be revealed through reactive interdiffusion.

4.2 Thermodynamic analysis of the diffusion direction

It is well known that the gradient of the chemical potential gives rise to the “internal” driving force for diffusion [42], which is also reflected by the up-hill diffusion found in the present work. Under the constant pressure and temperature applied during thermal diffusion, the Gibbs free energy

can be expressed as dominant chemical potential [43]. Therefore, diffusion proceeds in the direction of decreasing Gibbs free energy of the system. The Gibbs free energy G can be described by

$$G=H-TS \quad , \quad (1)$$

where H and S are the enthalpy and entropy of the system, respectively, and T is the absolute temperature. Although the entropy is composed of atomic configuration and excess entropy terms (atomic vibrations, magnetic moments and electronic effects), the excess entropic contributions are often similar or negligible as compared to the configurational one in ordered, segregated and solution phases [4,44,45]. Therefore, changes in atomic configuration represent the dominant entropy contribution to the total energy. For the CoCrFeNi HEA alloy in the present work, a single-phase fcc solid solution and an even element distribution are maintained in the HEA matrix during annealing. Therefore, it is reasonable to assume that a random solid solution state is sustained on the time scale of this study. For an ideal random solid solution phase, the contribution of the enthalpy to the change of Gibbs free energy is 0 and therefore the configurational entropy dominates the Gibbs free energy, which can be expressed as

$$S = -R \sum X_i \ln(X_i) \quad , \quad (2)$$

with the gas constant R and X_i as the atom fraction of element i. The schematic diagram for the change of the Gibbs free energy of the HEA phase as a function of Al content is shown in Fig. 4(a). Assuming that the added Al will be randomly distributed on the fcc HEA lattice sites and no phase transformation occurs, the minimum free energy for the five component alloy will be at 20 at.% of each element. Therefore, for short annealing times, a diffusion of Al into the HEA is expected to form a solid solution and reduce the system energy. However, this process can be either kinetically unfavorable or can be immediately accompanied by the formation of T-Al_9Co_2, which has a lower Gibbs energy compared to the solid solution state. The relatively low Gibbs free energy of T-Al_9Co_2 will enhance the diffusion of HEA components into the Al film (see schematic diagram in Fig. 4(b)). This explains why no apparent solution of Al in the fcc HEA phase was observed experimentally. With increasing diffusion of the HEA components into Al, based on forming sequence reflected by XRD (see Fig. 2(a)), the T-Al_5Co_2 phase starts to form due to its lower Gibbs free energy as compared to T-Al_9Co_2. Its Gibbs free energy appears to be even lower than the minimum energy of the fcc solid solution (see Fig. 4(a)). Therefore, the diffusion of Al from the film side towards the HEA to form T-Al_5Co_2 is more favorable, which is accompanied by the decomposition of the HEA (see schematic diagram in

Fig. 4(c)). This demonstrates that the Gibbs free energy dictates the diffusion direction, as detailed in Fig. 4. Instead of the formation of a disordered solid solution state, the major phases observed in the reactive area are ordered intermetallic compounds. This highlights the dominant role of enthalpy on determining the Gibbs free energy at the annealing temperature of 773 K.

5.Conclusions

Systematic investigations of the phase formation upon reactive diffusion between a CoCrFeNi HEA and an Al thin film were carried out. Kinetic and thermodynamic effects appear to play a coupled role in the reactive diffusion. The following results were established from the current study:

(1) Isothermal annealing at 773 K results in a complex interdiffusion behavior which can be separated into two stages. In the first stage (< 6 h) mainly the elements of the HEA diffuse to the Al film, without any visible diffusion of Al into the HEA. Although the diffusion rate of Cr in Al is higher as compared to the other HEA components, the formation of the metastable T-Al_9Co_2 phase is observed. This is attributed to the higher mixing enthalpy of Al with Co and Ni. Therefore, we have established that thermodynamics rather than kinetics determine the dominant phases and that the mixing enthalpy plays a significant role in the phase evolution during reactive diffusion.

(2) The second stage begins with the formation of the T-Al_5Co_2 phase (≥ 6 h), which appears to be more stable as compared to a fcc solid solution of Al with the HEA. At this stage, Al starts to diffuse towards the HEA which is accompanied by the transformation of the HEA into T-Al_5Co_2. The up-hill diffusion of Ni and Co to bond with Al at the interface indirectly results in the formation of lamellar bcc phases behind the interface.

(3) The diffusion direction in HEAs is closely related to the gradient of the chemical potential. Elements will diffuse towards the direction decreasing the system energy. Hence, it appears that the sluggish diffusion effect in HEAs does not play a dominant effect during reactive diffusion in the current system. The present work demonstrates that surface modification in HEAs can be realized through a combination of sputter deposition with annealing. Finally, the local structure can be controlled through proper combination of deposition elements and heat treatment.

Supplementary materials

Fig. S1 Phase identification and structural characterization of the as-deposited and annealed

samples with SEM-BSE mode.

Fig. S2 SEM images of locations where EDS point analysis were collected.

Fig. S3 Cross-section SEM images and corresponding EDS mapping results for different annealing times.

References

[1] B. Cantor, I.T.H. Chang, P. Knight, A.J.B. Vincent, Microstructural development in equiatomic multicomponent alloys, Mater. Sci. Eng. A. 375–377 (2004) 213–218.

[2] J.W. Yeh, S.K. Chen, S.J. Lin, J.Y. Gan, T.S. Chin, T.T. Shun, C.H. Tsau, S.Y. Chang, Nanostructured high-entropy alloys with multiple principal elements: Novel alloy design concepts and outcomes, Adv. Eng. Mater. 6 (2004) 299–303.

[3] Y. Zhang, T.T. Zuo, Z. Tang, M.C. Gao, K.A. Dahmen, P.K. Liaw, Z.P. Lu, Microstructures and properties of high-entropy alloys, Prog. Mater. Sci. 61 (2014) 1–93.

[4] D.B. Miracle, O.N. Senkov, A critical review of high entropy alloys and related concepts, Acta Mater. 122 (2017) 448–511.

[5] W. Zhang, P.K. Liaw, Y. Zhang, Science and technology in high-entropy alloys, Sci. China Mater. 61 (2018) 2–22.

[6] O.N. Senkov, S. V. Senkova, C. Woodward, Effect of aluminum on the microstructure and properties of two refractory high-entropy alloys, Acta Mater. 68 (2014) 214–228.

[7] P.F. Yu, L.J. Zhang, H. Cheng, H. Zhang, M.Z. Ma, Y.C. Li, G. Li, P.K. Liaw, R.P. Liu, The high-entropy alloys with high hardness and soft magnetic property prepared by mechanical alloying and high-pressure sintering, Intermetallics. 70 (2016) 82–87.

[8] P. Shi, W. Ren, T. Zheng, Z. Ren, X. Hou, J. Peng, P. Hu, Y. Gao, Y. Zhong, P.K. Liaw, Enhanced strength–ductility synergy in ultrafine-grained eutectic high-entropy alloys by inheriting microstructural lamellae, Nat. Commun. 10 (2019) 1–8.

[9] J.Y. He, H. Wang, H.L. Huang, X.D. Xu, M.W. Chen, Y. Wu, X.J. Liu, T.G. Nieh, K. An, Z.P. Lu, A precipitation-hardened high-entropy alloy with outstanding tensile properties, Acta Mater. 102 (2016) 187–196.

[10] M. Vaidya, K. Guruvidyathri, B.S. Murty, Phase formation and thermal stability of CoCrFeNi and CoCrFeMnNi equiatomic high entropy alloys, J. Alloys Compd. 774 (2019) 856–864.

[11] Y.L. Chou, Y.C. Wang, J.W. Yeh, H.C. Shih, Pitting corrosion of the high-entropy alloy $Co_{1.5}CrFeNi_{1.5}Ti_{0.5}Mo_{0.1}$ in chloride-containing sulphate solutions, Corr. Sci. 52 (2010) 3481–3491.

[12] Y.F. Kao, T.D. Lee, S.K. Chen, Y.S. Chang, Electrochemical passive properties of $Al_xCoCrFeNi$ (x = 0, 0.25, 0.50, 1.00) alloys in sulfuric acids, Corr. Sci. 52 (2010) 1026–1034.

[13] C. Ng, S. Guo, J. Luan, S. Shi, C.T. Liu, Entropy-driven phase stability and slow diffusion kinetics in an $Al_{0.5}CoCrCuFeNi$ high entropy alloy, Intermetallics. 31 (2012) 165–172.

[14] O.N. Senkov, S. V. Senkova, D.B. Miracle, C. Woodward, Mechanical properties of low-density, refractory multi-principal element alloys of the Cr-Nb-Ti-V-Zr system, Mater. Sci. Eng. A. 565 (2013) 51–62.

[15] F. Zhang, C. Zhang, S.L. Chen, J. Zhu, W.S. Cao, U.R. Kattner, An understanding of high entropy alloys from phase diagram calculations, CALPHAD. 45 (2014) 1–10.

[16] Y.J. Zhao, J.W. Qiao, S.G. Ma, M.C. Gao, H.J. Yang, M.W. Chen, Y. Zhang, A hexagonal close-packed high-entropy alloy: The effect of entropy, Mater. Des. 96 (2016) 10–15.

[17] F. Otto, Y. Yang, H. Bei, E.P. George, Relative effects of enthalpy and entropy on the phase stability of equiatomic high-entropy alloys, Acta Mater. 61 (2013) 2628–2638.

[18] S. Praveen, B.S. Murty, R.S. Kottada, Alloying behavior in multi-component AlCoCrCuFe and NiCoCrCuFe high entropy alloys, Mater. Sci. Eng. A. 534 (2012) 83–89.

[19] N.G. Jones, A. Frezza, H.J. Stone, Phase equilibria of an $Al_{0.5}CrFeCoNiCu$ high entropy alloy, Mater. Sci. Eng. A. 615 (2014) 214–221.

[20] B. Schuh, F. Mendez-Martin, B. Völker, E.P. George, H. Clemens, R. Pippan, A. Hohenwarter, Mechanical properties, microstructure and thermal stability of a nanocrystalline CoCrFeMnNi high-entropy alloy after severe plastic deformation, Acta Mater. 96 (2015) 258–268.

[21] Y.J. Li, A. Savan, A. Kostka, H.S. Stein, A. Ludwig, Accelerated atomic-scale exploration of phase evolution in compositionally complex materials, Mater. Horizons. 5 (2018) 86–92.

[22] K.Y. Tsai, M.H. Tsai, J.W. Yeh, Sluggish diffusion in Co-Cr-Fe-Mn-Ni high-entropy alloys, Acta Mater. 61 (2013) 4887–4897.

[23] M. Vaidya, K.G. Pradeep, B.S. Murty, G. Wilde, S. V. Divinski, Bulk tracer diffusion in CoCrFeNi and CoCrFeMnNi high entropy alloys, Acta Mater. 146 (2018) 211–224.

[24] J. Kottke, M. Laurent-Brocq, A. Fareed, D. Gaertner, L. Perrière, Ł. Rogal, S. V. Divinski, G.

Wilde, Tracer diffusion in the Ni–CoCrFeMn system: Transition from a dilute solid solution to a high entropy alloy, Scr. Mater. 159 (2019) 94–98.

[25] Y. Lei, S.P. Hu, T.L. Yang, X.G. Song, Y. Luo, G.D. Wang, Vacuum diffusion bonding of high-entropy $Al_{0.85}CoCrFeNi$ alloy to TiAl intermetallic, J. Mater. Process. Technol. 278 (2020) 116455.

[26] P. Li, S. Wang, Y. Xia, X. Hao, H. Dong, Diffusion bonding of $AlCoCrFeNi_{2.1}$ eutectic high entropy alloy to TiAl alloy, J. Mater. Sci. Technol. 45 (2020) 59–69.

[27] P. Li, H. Sun, S. Wang, Y. Xia, H. Dong, G. Wen, H. Zhang, Diffusion bonding of $AlCoCrFeNi_{2.1}$ eutectic high entropy alloy to GH4169 superalloy, Mater. Sci. Eng. A. 793 (2020) 139843.

[28] Y.J. Du, J.T. Xiong, F. Jin, S.W. Li, L. Yuan, D. Feng, J.M. Shi, J.L. Li, Microstructure evolution and mechanical properties of diffusion bonding $Al_5(TiZrHfNb)_{95}$ refractory high entropy alloy to Ti_2AlNb alloy, Mater. Sci. Eng. A. 802 (2021) 1–9.

[29] Y. Peng, J. Li, J. Shi, S. Li, J. Xiong, Microstructure and mechanical properties of diffusion bonded joints of high-entropy alloy $Al_5(HfNbTiZr)_{95}$ and TC4 titanium alloy, J. Mater. Res. Technol. 11 (2021) 1741–1752.

[30] J. Wang, T. Guo, J. Li, W. Jia, H. Kou, Microstructure and mechanical properties of non-equilibrium solidified CoCrFeNi high entropy alloy, Mater. Chem. Phys. 210 (2018) 192–196.

[31] W.R. Wang, W.L. Wang, S.C. Wang, Y.C. Tsai, C.H. Lai, J.W. Yeh, Effects of Al addition on the microstructure and mechanical property of $Al_xCoCrFeNi$ high-entropy alloys, Intermetallics. 26 (2012) 44–51.

[32] C.M. Lin, H.L. Tsai, Evolution of microstructure, hardness, and corrosion properties of high-entropy $Al_{0.5}CoCrFeNi$ alloy, Intermetallics. 19 (2011) 288–294.

[33] W.R. Wang, W.L. Wang, J.W. Yeh, Phases, microstructure and mechanical properties of $Al_xCoCrFeNi$ high-entropy alloys at elevated temperatures, J. Alloys Compd. 589 (2014) 143–152.

[34] C. Li, J.C. Li, M. Zhao, Q. Jiang, Effect of aluminum contents on microstructure and properties of $Al_xCoCrFeNi$ alloys, J. Alloys Compd. 504 (2010) 515–518.

[35] W.D. Callister Jr, D.G. Rethwisch, Materials Science and Engineering - An Introduction 10th Edition, John Wiley & Sons, Hoboken, 2018.

[36] A. Paul, T. Laurila, V. Vuorinen, S. V. Divinski, Thermodynamics, diffusion and the kirkendall effect in solids, Springer, Switzerland, 2014.

[37] L. Bendersky, Orientation relationship between precipitated $Al_9(Fe, Ni)_2$ phase and α-aluminum, Metall. Trans. A. 16 (1985) 683–686.

[38] K.M. Doleker, A. Erdogan, S. Zeytin, Laser re-melting influence on isothermal oxidation behavior of electric current assisted sintered CoCrFeNi, $CoCrFeNiAl_{0.5}$ and $CoCrFeNiTi_{0.5}Al_{0.5}$ high entropy alloys, Surf. Coatings Technol. 407 (2021) 126775.

[39] P. Li, J. Li, J. Xiong, F. Zhang, L. Liang, Investigations on interface microstructure and strength properties of dissimilar tin bronze/superalloy diffusion bonded joints, Sci. Eng. Compos. Mater. 22 (2015) 511–515.

[40] M. Vilémová, K. Illková, Š. Csáki, F. Lukáč, H. Hadraba, J. Matějíček, Z. Chlup, J. Klečka, Thermal and Oxidation Behavior of CoCrFeMnNi Alloy with and Without Yttrium Oxide Particle Dispersion, J. Mater. Eng. Perform. 28 (2019) 5850–5859.

[41] T.B. Massalski, J.L. Murray, L.H. Bennet, Binary alloy phase diagrams: Volume 1, ASM Int, Metals Park, Ohio, 1986.

[42] P. Shewmon, Diffusion in solids, Springer, Berlin Heidelberg, 2016.

[43] W.F Huebner, W.D Barfield, Opacity, Springer, New York, 2014.

[44] A. Van de Walle, G. Ceder, The effect of lattice vibrations on substitutional alloy thermodynamics, Rev. Mod. Phys. 74 (2002) 11–45.

[45] D.J.M. King, S.C. Middleburgh, A.G. McGregor, M.B. Cortie, Predicting the formation and stability of single phase high-entropy alloys, Acta Mater. 104 (2016) 172–179.

[46] A. Takeuchi, A. Inoue, Classification of bulk metallic glasses by atomic size difference, heat of mixing and period of constituent elements and its application to characterization of the main alloying element, Mater Trans. 46 (2005) 2817–2829.

CRediT authorship contribution statement

Zequn Zhang: Writing – original draft, Investigation, Data Curation. **Sergey V. Ketov:** Writing - Review & Editing. **Simon Fellner:** Writing - Review & Editing, Investigation. **Huaping Sheng:** Resources. **Christian Mitterer:** Writing - Review & Editing, Resources. **Kaikai Song:** Writing - Review & Editing. **Christoph Gammer:** Writing - Review & Editing, Supervision. **Jürgen Eckert:**

Writing - Review & Editing, Supervision.

Acknowledgements

The authors gratefully acknowledge the financial support from the China Scholarship Council (CSC, Grant No. 201906220226). Additional supports from the Austrian Science Fund (FWF) (Y1236-N37) and the National Natural Science Foundation of China (51871132) are acknowledged. We thank K.-H. Pichler for synthesizing the thin films, C. Freitag for assistance with metallographic sample preparation, and A. Hohenwarter and S. Wurster for technical support with the SEM investigations and F. Spieckermann for stimulating discussions.

Tables

Table 1. Chemical composition (in at.%) analyzed by EDS/SEM (mean composition ± standard deviation).

Annealing time	Phase constitution	Al	Co	Cr	Fe	Ni
0.5 h	fcc HEA	0.3 ± 0.2	26.6 ± 0.4	22.5 ± 0.4	24.7 ± 0.2	26.0 ± 0.3
	fcc Al	99.3 ± 0.1	0.2 ± 0.1	0.3 ± 0.0	0.0 ± 0.0	0.2 ± 0.1
	T-Al_9Co_2	78.0 ± 0.5	5.6 ± 0.2	5.5 ± 0.5	5.4 ± 0.2	5.5 ± 0.1
1 h	fcc HEA	0.2 ± 0.2	26.1 ± 0.4	23.1 ± 0.7	24.3 ± 0.4	26.4 ± 0.5
	fcc Al	97.1 ± 2.0	0.1 ± 0.2	2.6 ± 1.4	0.1 ± 0.3	0.1 ± 0.1
	T-Al_9Co_2	79.3 ± 4.2	6.0 ± 1.4	1.2 ± 0.5	5.3 ± 1.1	8.2 ± 1.8
6 h	fcc HEA	0.1 ± 0.1	26.4 ± 0.4	23.3 ± 0.5	24.0 ± 0.4	26.3 ± 0.5
	T-Al_5Co_2	66.8 ± 2.4	8.5 ± 1.0	8.8 ± 0.3	8.1 ± 1.1	7.8 ± 1.1
12 h	fcc HEA	0.0 ± 0.0	26.6 ± 0.4	22.2 ± 0.5	24.6 ± 0.6	26.6 ± 0.3
	T-Al_5Co_2	66.4 ± 0.8	8.9 ± 0.4	8.3 ± 0.6	8.4 ± 0.5	8.0 ± 0.7

Table 2. The mixing enthalpies of the atomic pairs between each element of the present alloy (KJ/mole) [46].

Elements	Al	Co	Cr	Fe	Ni
Al	-	-19	-10	-11	-22
Co	-	-	-4	-1	0
Cr	-	-	-	-1	-7
Fe	-	-	-	-	-2
Ni	-	-	-	-	-

Figures

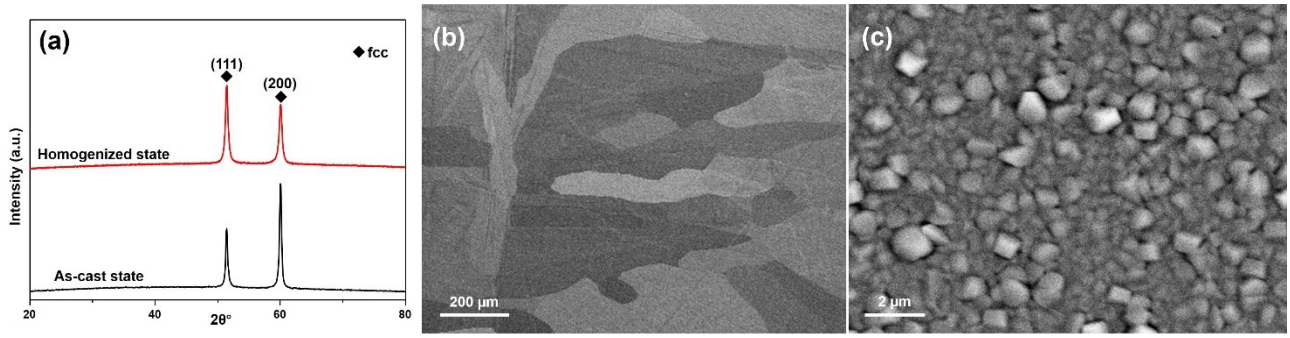

Fig. 1 Phase analysis and structural characterization of the HEA matrix and deposited samples. (a) XRD patterns of as-cast and homogenized alloys. (b) SEM image of the alloy after homogenization annealing (973 K for 1 h) and of the surface morphology after thin film deposition (c).

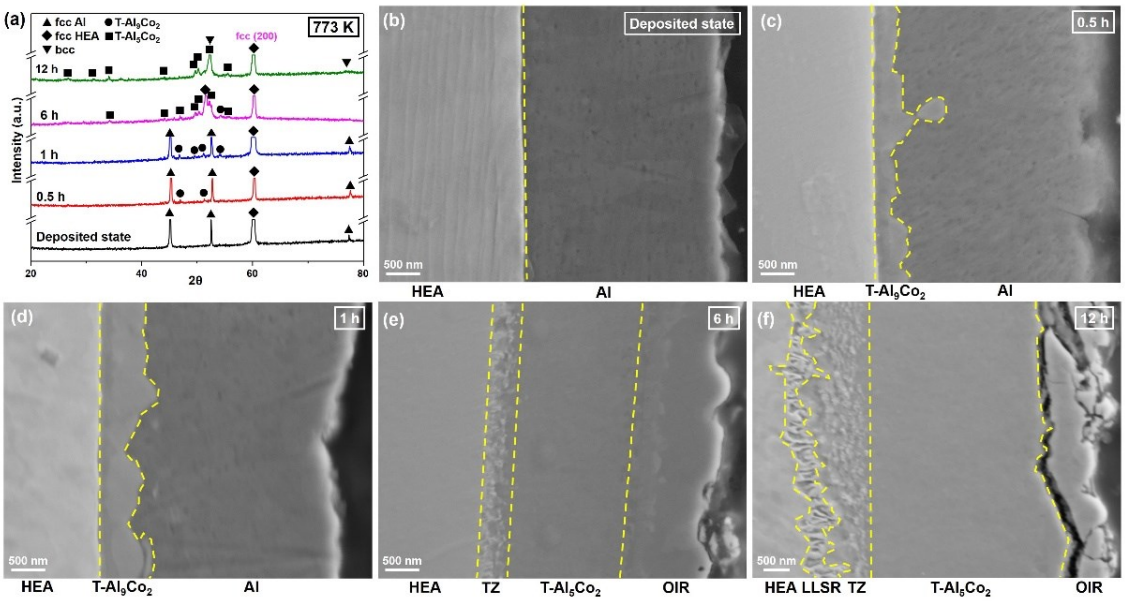

Fig. 2 Phase identification and structural characterization of the as-deposited and annealed samples. (a) XRD patterns as a function of annealing time. For a better visibility, the strongest XRD peaks

are cut to reveal the smaller ones. (b-f) SEM images from the reactive zone of as-deposited (b), 0.5 h (c), 1 h (d), 6 h (e) and 12 h (f) annealed samples (the dashed-yellow lines are drawn to indicate interfaces). TZ and OIR indicate the transition zone and the oxide-influenced region respectively, whereas LLSR stands for the lamella-like structure region.

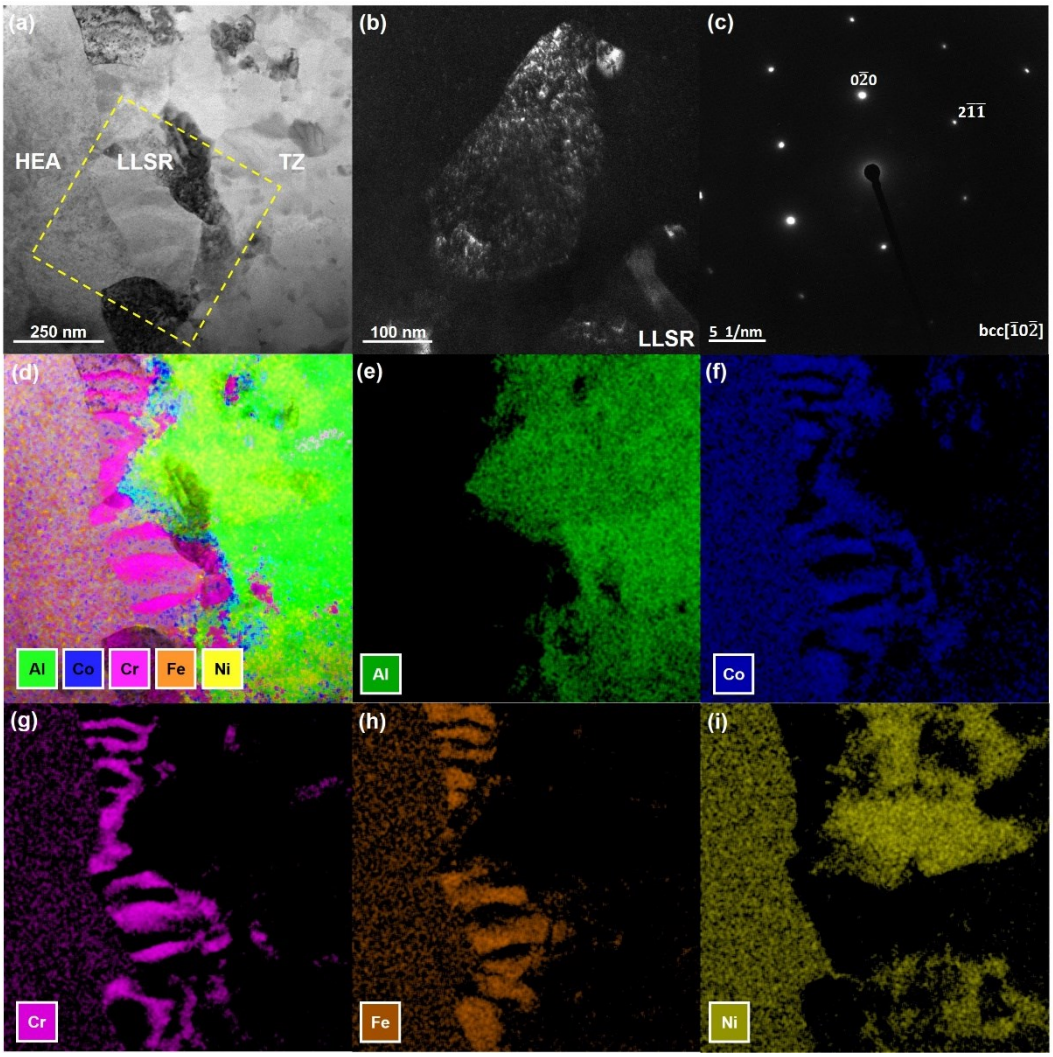

Fig. 3 Phase identification and element distribution of the lamella-like structure in the sample annealed at 773 K for 12 h. (a) BF-STEM image of the interface; (b) DF-TEM image of the lamella-like structure region (LLSR) marked in (a) and corresponding SAED pattern (c); Overview of the EDS results (d) and individual element distribution of Al (e), Co (f), Cr (g), Fe (h) and Ni (i).

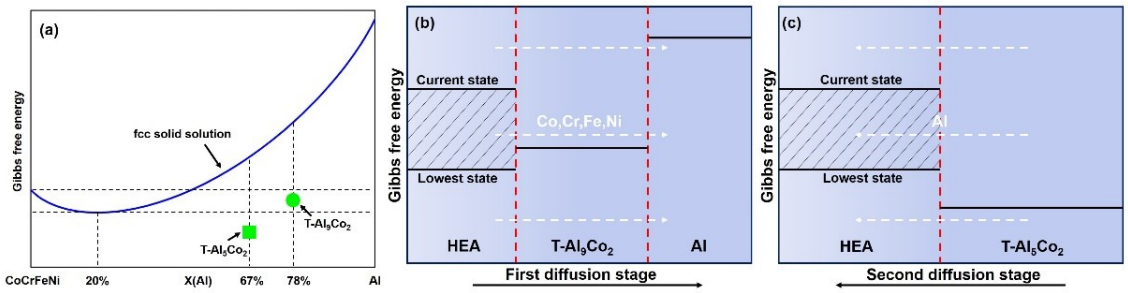

Fig. 4 Schematic diagrams of the Gibbs free energy of the different phases and its impact on diffusion direction. (a) Gibbs free energy of the CoCrFeNi-Al system at 773 K. (b-c) Diffusion direction dependence of the Gibbs free energy in the first stage (b) and the second stage (c).

Supplementary materials

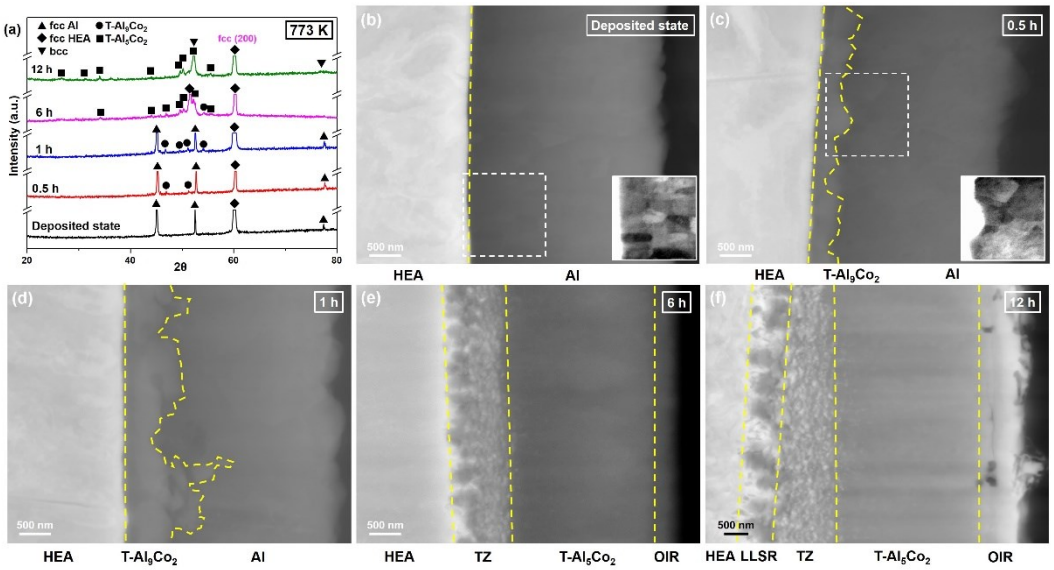

Fig. S1 Phase identification and structural characterization of the as-deposited and annealed samples with SEM-BSE mode. (a) XRD patterns as a function of annealing time. (b-f) BSE images from the reactive zone of as-deposited (b), 0.5 h (c), 1 h (d), 6 h (e) and 12 h (f) annealed samples (the dashed-yellow lines are drawn to indicate interfaces). To visualize the grain morphology in the Al layer inserts with boosted contrast are shown in (b) and (c) that correspond to the areas marked with rectangles.

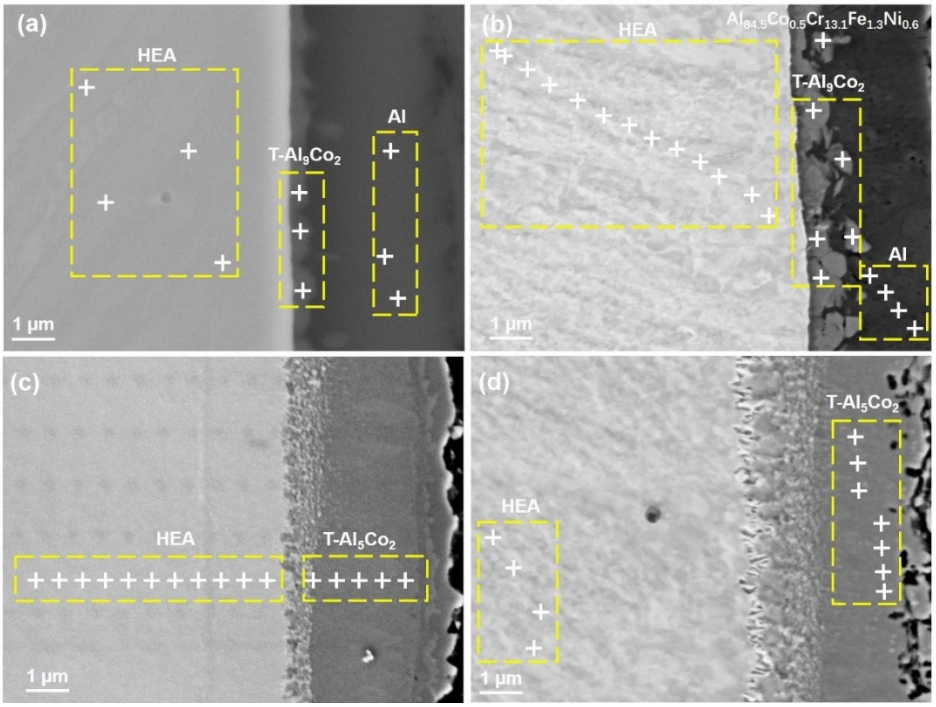

Fig. S2 SEM images of locations where EDS point analysis were collected. (a-d) samples annealed at 773 K for 0.5 h (a), 1 h (b), 6 h (c) and 12 h (d). The white phase that corresponds to $Al_{13}Cr_2$ intermetallic compound after 773 K annealing for 6 h is also marked in image (b).

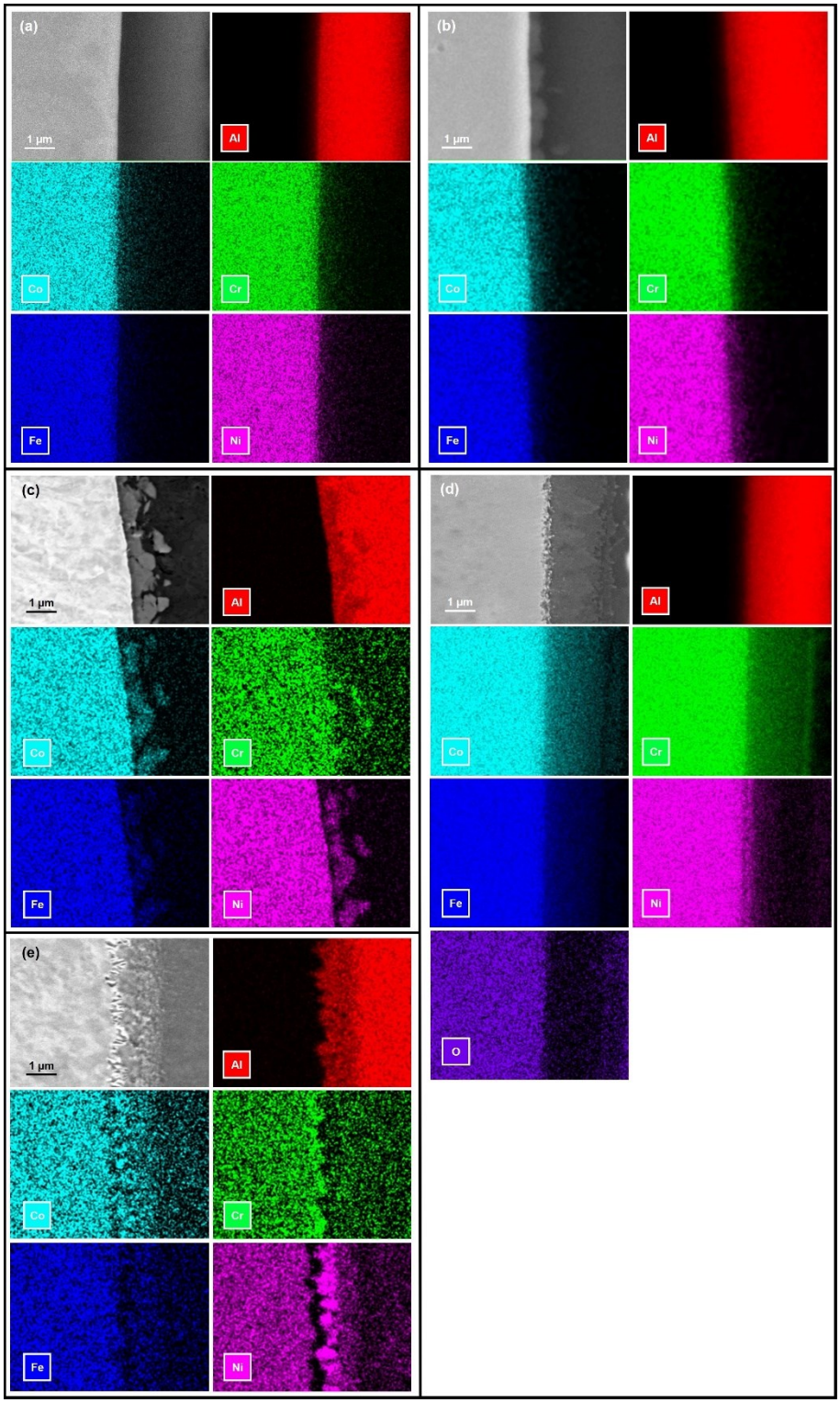

Fig. S3 Cross-section SEM images and corresponding EDS mapping results for different times. (a) as-deposited state. (b-e) samples annealed at 773K for 30 min (b), 1 h(c), 6 h(d) and 12 h(e). To determine the oxide-influenced region, the oxygen distribution after annealing for 6 h is also shown here.

Publication II

Reactive interdiffusion of an Al film and a CoCrFeNi high-entropy alloy at elevated temperatures

Zequn Zhang [a,b,*], Simon Fellner [a,b], Sergey Ketov [a], Megan J. Cordill [a], Huaping Sheng [a], Christian Mitterer [c], Kaikai Song [d], Christoph Gammer [a,*], Jürgen Eckert [a,b,*]

[a] *Erich Schmid Institute of Materials Science, Austrian Academy of Sciences, Jahnstraße 12, 8700 Leoben, Austria^^*

[b] *Department of Materials Science, Montanuniversität Leoben, Jahnstraße 12, 8700 Leoben, Austria*

[c] *Department of Materials Science, Montanuniversität Leoben, Franz-Josef-Straße 18, 8700 Leoben, Austria*

[d] *School of Mechanical, Electrical & Information Engineering, Shandong University, Wenhua Xilu 180, 264209 Weihai, China.*

[*] *Corresponding authors:*

zequn.zhang@stud.unileoben.ac.at; christoph.gammer@oeaw.ac.at; juergen.eckert@unileoben.ac.at

Abstract

The phase evolution of alloys is closely related to atomic diffusion. The influence of reactive diffusion on phase formation in high-entropy alloys (HEAs) is however still unclear. The present work systematically investigates the phase evolution of a multicomponent CoCrFeNi/Al diffusion couple through isochronous-reactive interdiffusion experiments. This provides a direct way to study the influence of enthalpy and entropy on the phase formation and element diffusion behavior. At temperatures below 1173 K, the enthalpy contribution dominates the total energy, leading to the formation of intermetallic compounds. When the temperature is in the range of 1173 - 1573 K, the entropy of mixing starts to play a more important role. This causes diffusion of Al towards the HEA without phase transformation, forming a more disordered state on the microscale. Even after the system reaches a disordered state, the enthalpy contribution cannot be totally ignored, which is reflected by the uphill diffusion of Ni towards Al. This demonstrates the combined effects of entropy and enthalpy on the phase formation in HEAs at elevated temperatures. Considering the homologous

temperature for different equimolar alloys reveals that a multicomponent configuration does not stabilize the disordered state, while the mixing enthalpies between atomic pairs have a large impact on the transition temperature from ordered to disordered state. Finally, it is shown that surface modification of the HEA can be realized through a combination of film deposition and annealing processes. Compared to the HEA matrix, the formation of intermetallic compounds results in a hard surface layer. After the system becomes disordered, the higher hardness of the film side compared to the matrix can be attributed to the lattice distortion induced by Al.

Keywords: Reactive diffusion, High-entropy alloy, Film deposition, Phase evolution, Surface Modification

1. INTRODUCTION

The phase composition in multi-principal element or high-entropy alloys has long been an open issue. Unlike traditional binary or ternary alloys, the multi-element constitution with different physical properties and the complex interaction between atoms makes the prediction of phase composition in HEAs more challenging. It is believed that the high configurational entropy in such alloy systems renders the disordered solid solution state more favorable, i.e., face-centered cubic (fcc), body-centered cubic (bcc) or hexagonal close-packed (hcp) solid solutions discovered in most of the HEAs [1–3]. However, it has been questioned whether the high-entropy effect stems from the fact that the solid solution phase constituting most HEAs is retained from rapid liquid quenching instead of being stable by itself [4]. Probably due to deep diffusion traps induced by the heterogeneous interatomic interactions of the different atoms, the movement of atoms to more favorable positions is "sluggish" [5–9]. Therefore, phase evolution to a more stable phase is kinetically restricted. In fact, HEAs that are initially single-phase after solidification tend to transform into intermetallic phases when annealed at intermediate temperatures [10–12].

To explore the phase constitution in HEAs, many investigations have been conducted. By increasing the amount of Al in CoCrFeNi, a phase transition from the fcc disordered state to a duplex bcc structure was realized [13,14]. This is attributed to the finite solid solution limit of Al in the fcc phase and the more negative enthalpy of mixing between Al and Ni, leading to the formation of new phases. Similar investigations have also been performed for other systems [15–17]. Moreover, the

intrinsic phase evolution in HEAs is also widely realized through thermal treatment, thereby overcoming the diffusion barrier to reach an equilibrium state [10,18–20]. By severe plastic deformation, a large amount of non-equilibrium grain boundaries serve as nucleation sites for thermally stable phases due to the fast diffusion kinetics in nano-crystalline materials [11,12,21]. In general, it is found that several factors can be related to the phase stability in HEAs, such as valance electron concentration (VEC), atomic size difference, mixing enthalpy and entropy, etc. [22–25]. However, the real phase transition process cannot be captured using these methods. Recently, a more intuitive view on phase evolution has been realized by diffusion coupling of HEAs with other alloys [26–29]. Element diffusion and consequently phase formation during the reactive process are captured. This opens up a new way to study the phase composition of HEAs. It should be noted however, that constant loading and long annealing times are needed in order to realize a truly physical bonding of the diffusion couples. The initial diffusion process of elements is therefore hardly accessible. Meanwhile, the creep behavior of the alloy, induced by the constant loading during bonding, might further complicate the reaction process. In fact, the annihilation of voids generated during the bonding process is attributed to the influence of high-temperature creep [29].

A pragmatic way to determine the phase constitution in HEAs during the diffusion process, without the influence from external factors, is to realize physical bonding between the diffusion couple before reactive diffusion. Hence in this paper, an Al film was deposited on the CoCrFeNi substrate by sputter deposition. The similar atomic radii of Al and the HEA components (smaller than 15% size mismatch) favor the formation of a substitutional solid solution according to the Hume-Rothery rules [30], and vacancy diffusion will be the dominant diffusion mechanism. Hence, a more directly interpretable investigation can be realized. Moreover, the CoCrFeNi HEA with disordered fcc structure shows excellent thermal stability without decomposition at elevated temperatures [20,31]. This can eliminate the potential influence of phase transformation in the HEA matrix on the interdiffusion behavior. Besides, by choosing CoCrFeNi/Al as the diffusion couple, a potential phase transition from fcc to bcc phase may be realized, as observed with the addition of Al to the CoCrFeNi system. This could lead to a gradient structure distribution as it is widely applied for surface modification [32,33].

2. EXPERIMENTAL DETAILS

The CoCrFeNi HEA with equal atomic ratio was prepared by vacuum arc melting of nominal mixtures of the constituent elements (purity ≥ 99.95%) and was remelted at least five times in a Ti-gettered high-purity argon atmosphere to ensure chemical homogeneity. The molten alloy was cast into a water-cooled Cu mold to form a 10 mm (width) × 100 mm (length) × 2 mm (thickness) plate. This was followed by homogenization annealing in a vacuum furnace (Xerion Xtube) at 993 ± 5 K for 1 h. The chamber was evacuated to $< 5 \times 10^{-5}$ Pa before annealing.

For the sputter deposition of the Al films, the CoCrFeNi plate was cut into slices (length of ~ 3.5 mm, width of ~ 1.5 mm). The surfaces to be coated were prepared by mechanical grinding using 500 to 4000 FEPA grit size SiC abrasive planar papers, followed by a final polish with conventional aluminum oxide polishing suspension (OPS). Next, the substrates were loaded into the vacuum chamber of the magnetron sputter deposition system (FHR.Line.600-V) and plasma cleaned for ~16 min using argon ions to remove surface residues. An Al film with thickness of 3 μm was deposited by direct current magnetron sputtering of a planar Al target (size 600 × 125 mm^2) at a power of 3500 W. The base pressure of the chamber before deposition was 3.4×10^{-4} Pa. No external heating was applied to the grounded substrate holder. The argon flow rate was set to 300 sccm and a pressure of 4.5×10^{-1} Pa was maintained during deposition. For isochronous annealing, a high cooling rate under vacuum condition is required in order to retain the phases that are stable at high temperature. A custom-made induction annealing device was used for this procedure. A schematic diagram for the induction annealing is shown in Fig. S1(a). A bulk tungsten (W) block was put below the sample for the conduction of induction heating. The temperature during annealing was followed with a Series QKTRD 1475 optical sensor (Dr. Georg Maurer GmbH) above the sample. The isochronous annealing was performed at 973 K, 1173 K, 1373 K and 1573 K for 10 min with a fluctuation of ± 5 K, then with a cooling rate of 390 ± 40 K/min under the protection of argon.

After annealing, X-ray diffraction patterns (XRD) (Co-Kα radiation) were obtained using a Bruker D2 phaser diffractometer. A scanning electron microscope (SEM-LEO1525, Zeiss) equipped with energy-dispersive X-ray spectroscopy (EDS) was used to determine the structure and elemental composition of the samples. Due to the formation of acicular and particle-like grains within reactive zone, a combination of EDS map with point analysis were used to identify element distribution and composition for each phase. The melting event of the as-cast HEA and the range of phase transformation temperature of the diffusion couple were examined by high-temperature differential

scanning calorimetry (DSC 404 F1 Pegasus, Netzsch) at a heating rate of 0.17 K/s. For in-depth investigation of the phase evolution, transmission electron microscopy (TEM) was used, allowing to identify tiny crystals and the phase distribution of the specimens annealed at 1373 K and 1573 K. Cross-sectional TEM specimens from the interface were prepared by in-situ lift-out in a dual-beam focused ion beam system (Zeiss Auriga Laser FIB) with an OmniProbe nanomanipulator. TEM images and diffraction patterns were obtained using a JEOL JEM-2200FS microscope.

For samples annealed at 1373 K and 1573 K, Vickers micro-hardness measurements were conducted with a Buehler (Micromet 5104) microhardness tester using a load of 300 g and a dwell time of 15 s. To understand the influence of reactive diffusion on the hardness distribution of these two samples, additional nanoindentation experiments were performed using a Bruker TS77 Select and a well-calibrated Berkovich tip on polished cross-sections of the samples. Scanning of the sample surface with the tip was used to position mapping matrices as close to the surface as possible. Mapping matrices of 20 × 20 with 1 μm spacing and a maximum load of 500 μN were performed on both samples and included imaging with the tip before and after mapping. The load of 500 μN and indent spacing of 1 μm were chosen to ensure no overlapping of the plastic zones that may interfere with the measurements. The maximum displacement of the indents was between 30 - 60 nm, depending on the phase. All load-displacement curves were analyzed with the well-known and accepted Oliver-Pharr method [34] to evaluate the hardness. At these low displacements, the well-known indentation size effect [35, 36] is most likely present resulting in higher hardness values due to the mechanical polishing.

3. RESULTS

3.1. Phase stability of the HEA matrix

An excellent phase stability of the HEA matrix at the expected temperature and time of the diffusion annealing treatment is a necessary condition for the further reactive diffusion investigation. Fig. 1(a) compares the XRD patterns of CoCrFeNi that was homogenized-annealed and annealed at the highest temperature of 1573 K for 10 min (denoted as “annealed state”). The results clearly show the phase stability. The differences in the peak intensities can be explained by slight random texture variations throughout the as-cast samples. However, due to the isotropic nature of the cubic fcc lattice, the jump frequency of atoms to all neighboring vacancy sites should be the same. The probable grain

boundary motion and accompanied grain re-orientation, caused by texture, were shown not to affect the bulk tracer diffusion contribution [37]. In addition, the XRD pattern (see Fig. 1(a)) shows that the as-deposited sample is composed of two fcc phases, corresponding to the HEA matrix and the Al layer.

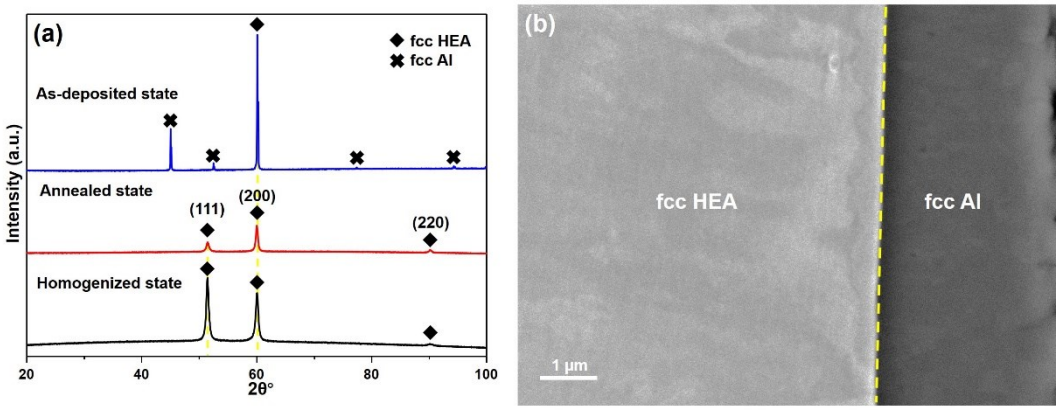

Fig. 1. Phase analysis and structural characterization of the HEA matrix and as-deposited sample. (a) XRD patterns of the homogenized and annealed (1573 K for 10 mins) HEA matrix and of the as-deposited sample. (b) SEM image of the interface of the as-deposited sample (the dashed-yellow line is drawn to indicate interface).

3.2. Reactive diffusion behavior during isochronous annealing at elevated temperatures

Fig. 1(b) shows a cross-sectional SEM image of the as-deposited sample. A good physical bonding without gaps between the HEA and the as-deposited Al layer is realized. To understand the relationship between reactive diffusion and phase evolution, diffusion couples were subjected to thermal diffusion experiments. Fig. 2(a) displays the XRD patterns after isochronous annealing at elevated temperatures. The (200) peak of the fcc HEA is retained for all samples, further demonstrating the excellent thermal stability of the HEA matrix. After annealing at 973 K for 10 min, the peaks corresponding to fcc Al disappeared. It indicates that the Al film has fully reacted with the elements from the HEA matrix. Three new phases can be found: disordered bcc, ordered bcc and a hexagonal phase that is isotypic to Al_5Co_2 and Al_5FeNi. This phase is marked as T-Al_5Co_2. It should be pointed out that a similar phase constitution was found after annealing at 773 K for 12 h [38]. Much faster diffusion kinetics at elevated temperature results in faster growth of each phase. When the annealing temperature reaches 1173 K and 1373 K, the T-Al_5Co_2 phase is no longer visible in the XRD patterns (Fig. 2(a)). Instead, the tetragonal intermetallic σ phase forms. It has been reported that the hard and brittle σ phase consisting mostly of Cr and Fe forms in the temperature range of 773 to 1248 K in CrFeNi-based HEAs through ordinary annealing processes [39–42].

By combining the XRD and EDS results (Fig. 2, Fig. 3 and Fig. S2) it can be concluded that the σ phase should be a FeCr rich phase forming at the interface. In the following it will be named as σ FeCr. At 973 K, due to similar d-spacings of B2 and bcc phases (~2.876 ± 0.002 Å, similar to the result from [13]), XRD peaks of B2 and bcc are overlapped. The formation of σ FeCr is accompanied by the disappearing of the bcc FeCr phase. This indicates that the precursor of σ FeCr should be the bcc FeCr phase formed between 973 K and 1173 K. Moreover, splitting of the B2 and bcc peaks at 1173 K is observed. Fast diffusion of elements at this temperature and the formation of the σ phase that is rich in Cr and Fe result in elemental segregation and, hence, in the difference of the d-spacings of the two phases. A further increase of the annealing temperature to 1573 K causes the σ phase to fully disappear leaving only fcc phase behind. In addition, a small fraction of Al_2O_3 and a diffraction peak corresponding to bcc W can be observed. The latter can be explained by fast surface diffusion from the W block below the specimen (see the schematic diagram Fig. S1). To know the distribution of W, an EDS map scan for the free side of specimen annealed at 1573 K is shown in Fig. S3. Due to the formation of Al_2O_3 layer closing to the free side, diffusion of W toward the diffusion couple is effectively hindered. Finally, Fig. 2(b) shows an enlarged image of the (200) peak corresponding to the fcc HEA matrix. With increasing annealing temperature, the peak shifts towards lower angles, which can be attributed to the severe lattice distortions during the diffusion process.

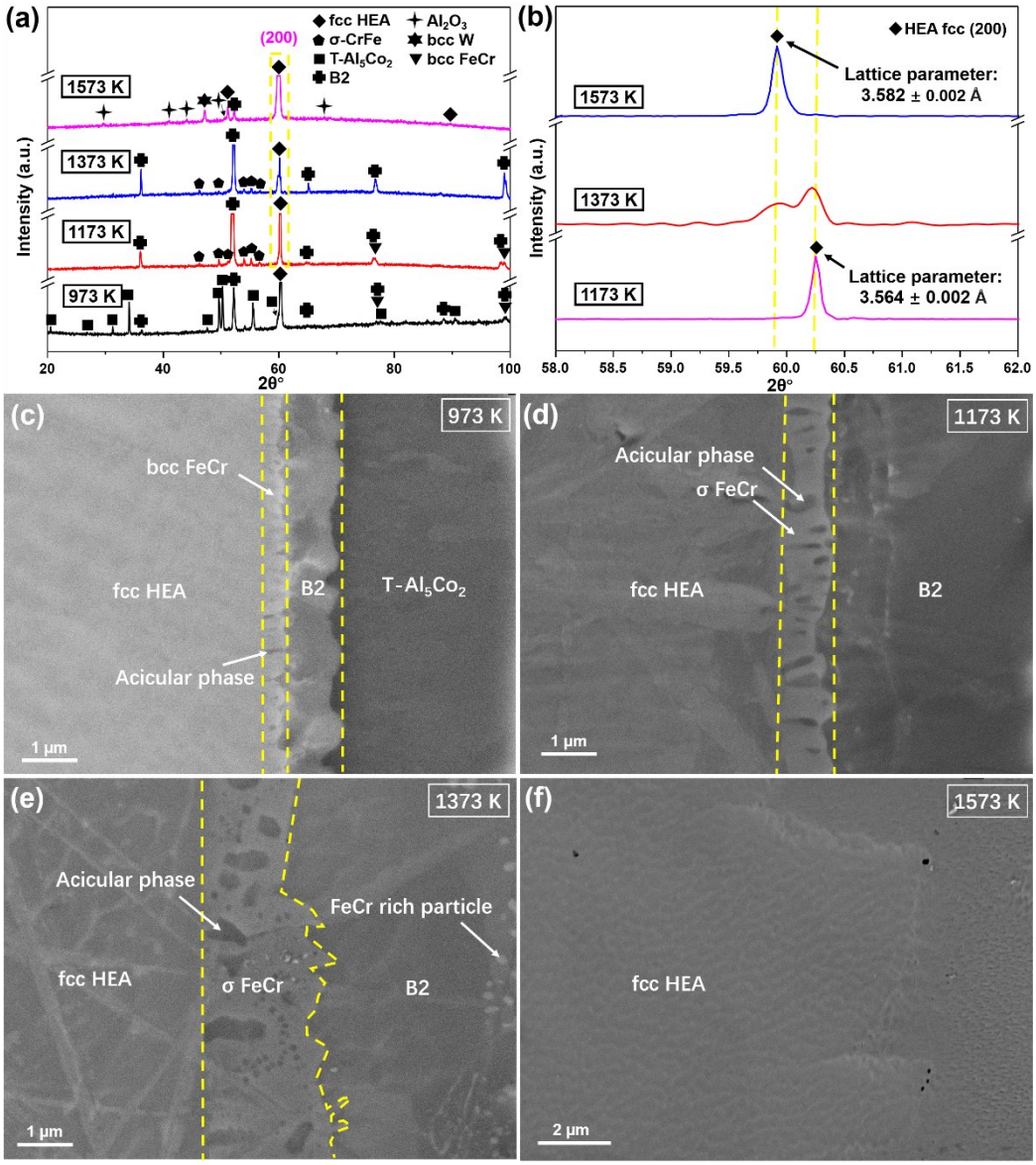

Fig. 2. Phase identification and structural characterization of samples after isochronous annealing at elevated temperatures. (a) XRD patterns as a function of annealing temperature. For a better visibility, the strongest XRD peaks are cut to reveal the smaller ones. (b) Enlarged area around the fcc HEA matrix peak ((200) plane) recorded at temperatures from 1173 K to 1573 K. (c-f) SEM images from the reactive area of samples annealed at 973 K (c), 1173 K (d), 1373 K (e) and 1573 K (f) (the dashed-yellow lines are drawn to indicate interfaces).

SEM images of the reaction region of different isochronous annealing states are displayed in Figs. 2(c-f). For the sample annealed at 973 K (Fig. 2(c)), the film side has transformed into T-Al_5Co_2 with a B2 phase growing towards it. A smaller amount of FeCr rich bcc phase, appearing bright in the SEM images (Fig. 2(c) and Fig. 3(a)) can be found between HEA matrix and B2 phase. A closer examination of this area shows an acicular phase forming at the interface (see dark phase marked by

an arrow in Fig. 2(c)). Based on the EDS mapping results (Fig. 3(a)), the acicular phase is a AlNi rich phase. Further increase of the annealing temperature to 1173 K induces a phase transition from bcc FeCr to σ-FeCr and further growth of the acicular phase. Meanwhile, the T-Al_5Co_2 phase on the film side is fully replaced by the B2 phase. Through investigation of the formation of the σ phase in stainless steels, Hsieh and Wu [43] pointed out that when Cr diffuses from the Cr rich δ-ferrite (bcc) phase to form the σ phase, a Cr depletion region will be formed simultaneously. This might explain the source for further growth and nucleation of a AlNi rich phase in the present work. Therefore, the broadening of this area during further annealing can be expected. Moreover, Cr does not diffuse much into Al; instead, it reacts with Fe and pushes Al out. The precipitated Al reacts with Ni and the concentration gradient in front of the interface finally results in the formation of the acicular phase in this area. A similar mechanism of the formation of acicular phase can also be expected for the sample annealed at 973 K. After annealing at 1373 K, the bcc FeCr phase has fully transformed to the σ FeCr phase. The σ layer broadens accompanied with further nucleation and growth of the dark acicular phase. Besides, a smaller number of white FeCr rich particles inside the B2 phase that are far away from the interface are formed (see Fig. 2(e) and Fig. S2(d)). Finally, annealing at 1573 K results in a disordered fcc solid solution state throughout the entire sample. Since diffusion involves the formation of new phases at the interface and the process of diffusional exchange of atoms across the interface, it is named “reactive interdiffusion”.

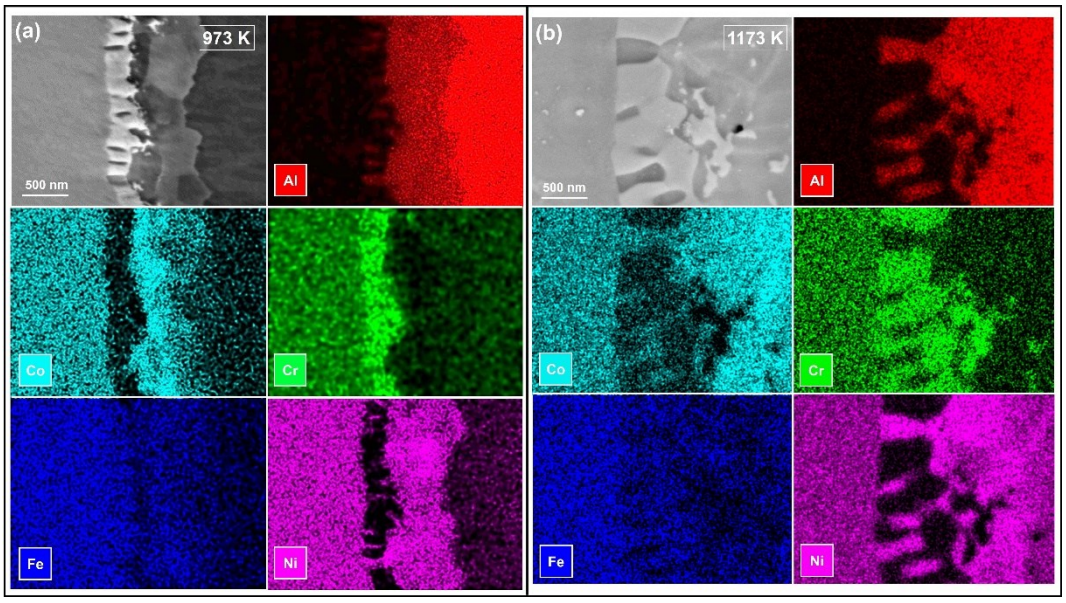

Fig. 3. Cross-section SEM images and corresponding EDS mapping results of samples annealed at (a) 973 K and (b) 1173 K.

Table 1. Chemical composition (in at.%) analyzed by EDS/SEM (mean composition ± standard deviation).

Annealing temperature	Phase constitution	Al	Co	Cr	Fe	Ni
973 K	fcc HEA	0.2 ± 0.3	26.1 ± 0.5	24.3 ± 1.0	25.3 ± 0.3	24.2 ± 0.9
	T-Al_5Co_2	63.0 ±2.4	9.7 ± 1.8	8.3 ± 0.7	9.1 ± 1.2	9.8 ± 1.4
	bcc FeCr	18.1 ± 3.6	17.8 ± 0.4	27.5 ± 1.4	23.4 ± 1.1	13.2 ± 0.7
	B2	48.4 ± 3.2	15.6 ± 1.0	9.5 ± 1.9	11.9 ±0.7	14.6 ± 0.6
1173 K	fcc HEA	0.2 ± 0.4	26.0 ± 0.8	25.0 ± 1.5	25.2 ± 0.4	23.7 ± 1.0
	B2	49.3 ± 3.2	13.5 ± 2.3	9.1 ± 2.6	14.7 ± 0.7	13.5 ± 1.8
	σ FeCr	1.6 ± 0.6	16.7 ± 0.5	45.5 ± 0.7	30.9 ± 0.5	5.4 ± 0.9
	Acicular phase	20.5 ± 3.5	16.1 ± 0.4	18.5 ± 3.8	16.3 ± 2.2	28.6 ± 2.8
1373 K	fcc HEA	2.9 ± 2.4	23.8 ± 1.3	27.5 ± 1.1	25.6 ± 0.7	20.3 ± 2.5
	B2	32.8 ± 3.3	20.9 ± 2.0	8.0 ± 2.2	12.6 ± 0.9	25.7 ± 3.1
	σ FeCr	2.4 ± 0.5	18.6 ± 0.7	42.9 ± 1.2	31.9 ± 0.5	4.2 ± 0.4
	Acicular phase	27.6 ± 1.4	19.3 ± 0.4	8.4 ± 1.7	12.6 ± 0.9	32.1 ± 0.8
	FeCr rich particles	16.2 ± 1.6	16.2 ± 2.5	31.0 ± 1.3	27.2 ± 1.1	9.5 ± 1.0
1573 K	fcc HEA	6.7 ± 0.7	23.3 ± 0.2	24.9 ± 0.3	24.0 ± 0.4	21.1 ± 0.2
	fcc film	9.8 ± 0.5	23.3 ± 0.5	19.3 ± 1.4	20.9 ± 0.2	26.8 ± 0.7

* Each phase was measured at least three times, and the mean composition is shown along with the standard deviation (see supplementary Fig. S4 for the locations from which the EDS results were obtained).

In order to confirm the tiny phases and prove the disordered state of the samples annealed at 1373 and 1573 K, TEM bright-field (BF), scanning transmission electron microscope (STEM) images, nanobeam electron diffraction (NBD) and selected area diffraction (SAED) patterns are given in Fig. 4. Fig. 4(a) shows the analysis of the interface region of the sample annealed at 1373 K. It reveals the presence of an AlNi rich phase inside σ FeCr, which is identified as B2 phase. Fig. 4(b) shows the film side of the sample. As concluded from the diffraction patterns, the major phase is a B2 phase, while the contained particle phase is a FeCr rich bcc phase. As shown in Fig. 4(c, d) for the sample annealed at 1573 K, both the HEA matrix and the film side exhibit a fcc solid solution. These results further confirm the phase prediction based on XRD and SEM results, and exclude the presence of

other phases at the nanoscale.

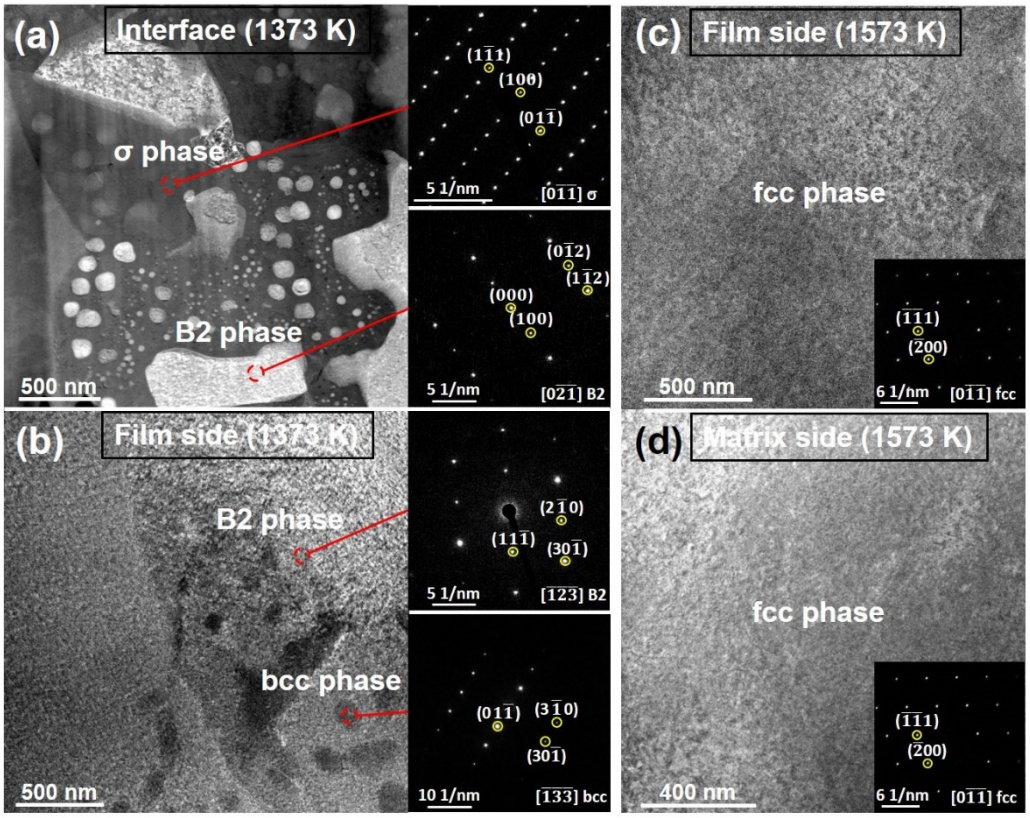

Fig. 4. Phase identification for the samples annealed at 1373 K (a, b) and 1573 K (c, d). (a) STEM image of the interface of a sample annealed at 1373 K; the NBD and SAED patterns on the right side were obtained from the major and acicular phases at the interface; (b) BF-TEM image of the film side, the SAED patterns on the right side were obtained from the matrix and particle phases; BF-TEM images and corresponding SAED patterns of sample annealed at 1573 K for the film side (c) and HEA matrix (d).

3.3. Hardness evolution during diffusion experiments

To determine the influence of different phase constitution on the mechanical behavior of the diffusion couple, samples annealed at 1373 K and 1573 K were subjected to hardness measurements. The Vickers hardness of the HEA matrix of the two samples is 126.6 ± 5.4 HV, which correlates well to previous reports [44–46]. It can be seen from the nanoindentation maps (Figs. 5(a-b)) made along polished cross-sections of the reaction areas that a higher hardness of the film side is realized through the thermal diffusion process in both samples. However, for samples annealed at 1373 K, the corresponding hardness distribution (Figs. 5(c-d)) shows a discontinuous hardness distribution with an increase in average hardness from 3.8 ± 0.3 GPa on the matrix side to 5.7 ± 0.5 GPa on the film side. The highest hardness of 6.2 ± 0.3 GPa is achieved at the interface area where the σ phase and

B2 (AlNi rich) phase coexist. Samples annealed at 1573 K on the other hand show a continuous hardness gradient with a slight increase of the hardness from the film side to the matrix (3.9 ± 0.2 GPa to 4.7 ± 0.5 GPa).

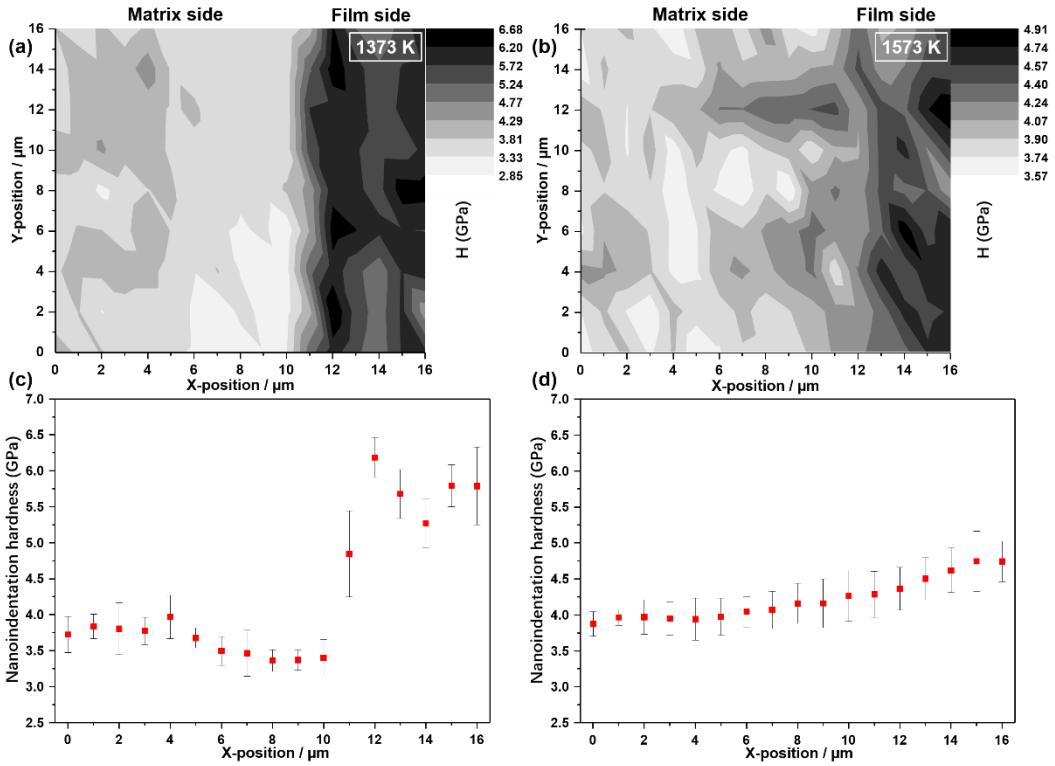

Fig. 5. Hardness maps of samples annealed at 1373 K (a) and 1573 K (b) (note the difference in scales), and (c-d) corresponding hardness distribution from the matrix side to the film (the error bars represent the standard deviation of indents in each column).

4. DISCUSSION

4.1. Thermodynamic and kinetic analysis of the phase transition behavior during isochronous annealing

At elevated temperatures, atoms have higher vibrational frequency facilitating vacancy jumps. This results in a more complex interaction between kinetics and thermodynamics and phase evolution behavior. The stability of each phase is described by its Gibbs energy, which consists of contributions from both enthalpy and entropy. The Gibbs free energy is a function of temperature for a line compound, a function of temperature and composition for a disordered solution, and a function of temperature, composition and site fraction for an ordered intermetallic phase with homogeneity range. The chemical potential gradient gives rise to the driving force for diffusion. Under the constant pressure and temperature applied during heat treatment, the Gibbs free energy per mole can be

expressed as dominant chemical potential. For the substitutional diffusion system, the particle number remains constant during diffusion. Therefore, diffusion proceeds in the direction of decreasing Gibbs free energy of the system. Even though the timescale may not be sufficient to reach equilibrium, it can be expected that the energy difference drives the reaction process. During annealing at 973 K, the reaction between HEA and Al takes place much faster since the annealing temperature exceeds the melting point of Al. Due to faster diffusion kinetics in liquid phase, the diffusion of HEA components toward the Al film is accelerated. To decrease the free energy of the diffusion zone, new solid phases are formed with the phase boundary moving towards the Al film. The faster diffusion kinetics disappears once Al is completely replaced by new phases with solid-solid interdiffusion. Based on the distribution of phases in the reaction area, it is expected that T-Al_5Co_2 is formed first, and the reaction in the diffusion zone transforms into solid-solid reaction. The continuous interdiffusion process causes a relative decrease of the Al content in the area close to the initial interface and finally leads to the phase transition from T-Al_5Co_2 to B2 phase. With increasing annealing time, B2 further grows towards T-Al_5Co_2. Meanwhile, the FeCr rich phase evolves to the σ FeCr phase. In literature it was shown that when a binary alloy containing Fe and Cr with almost equal atomic ratios is annealed at 773 K for 44 days, the σ-FeCr phase is formed and when it is annealed above 1103 K, the σ FeCr phase will transform to a bcc phase [47]. In the present case, however, both the formation temperature and the stable temperature range of the σ FeCr phase are higher than what is predicted by the binary phase diagram. The higher formation temperature can be explained by insufficient annealing time. It is expected that by longer heat treatment at 973 K the σ phase can also be formed. A further increase of temperature provides a higher reaction rate. Considering the similar chemical composition of the σ phase at 1173 K and 1373 K, it is believed that an equilibrium element distribution is realized in the σ phase. According to the Co-Cr binary phase diagram [48], addition of Co can stabilize σ phase at high temperatures. Therefore, the observed high stability of the σ phase should be caused by the large solubility of Co within it (see table 1). After further annealing at 1573 K, only fcc solid solution remains. It can be foreseen that, with the increase of temperature, the relative contribution of entropy to the Gibbs energy will increase and, hence, a more disordered solid solution state of the system can be expected. Actually, most of the HEAs investigated up to now were obtained by casting the alloy melts into molds. Thus, the high temperature stable phases, mostly solid solution structures, were captured. The XRD patterns magnified around $2\theta = 60°$ of samples annealed

at 1173 and 1573 K (Fig. 2(b)) show a shift of the fcc (200) peak to smaller diffraction angles with increasing temperature, evidencing an increase of the interplanar spacing. However, a transition state can be found at 1373 K. The lattice parameters calculated from the peak positions are shown in Fig. 2(b). A value of 3.564 ± 0.002 Å is obtained at 1173 K, which correlates well with the literature [49], and it increases to 3.582 ± 0.002 Å at 1573 K. The left hand shoulder shown at 1373 K can be explained by the diffusion of Al towards the HEA, which distorts the lattice further and increases the lattice parameter. The diffusion of Al towards the HEA to form a more disordered state also demonstrates that the disordered state is more stable than any intermetallic compounds at and above this temperature. Therefore, the entropy contribution to the Gibbs free energy becomes dominant. The composition of the B2 phase varies for different temperatures, which might be due to the substitution of elements. Actually, the B2 phase is found in the binary FeCo, FeCr, AlFe, AlNi and AlCo systems [50–54]. The additional contribution of the ideal entropy from mixing elements and the negative mixing enthalpy among the components might result in a stable state of B2 under a large temperature range. To determine the temperature range of phase transformations caused by the reactive diffusion, DSC measurements (see Fig. 6) were performed on a diffusion couple. During the first run, a prolonged heat-release region ranging from 838 K to 1377 K can be seen. Due to the continuous phase evolution, the exothermic processes are overlapped. However, one can still see the dominant role of enthalpy in the system energy in this stage as the phase transformation is accompanied by a heat release during the long-range ordering process in the reaction zone. No obvious heat-releasing event can be seen during further temperature increase or during the second heating, since the system enters the disordered state and no reaction occurs. In contrast to the DSC curve of the HEA matrix (see Fig. S5), melting starts earlier in the case of the of diffusion couple. This should relate to insufficient diffusion time. Even if the system enters a fully disordered state, the inhomogeneous distribution of components results in different melting points of different areas. The solution treatment of the HEA with Al having a low melting point causes an earlier melting event.

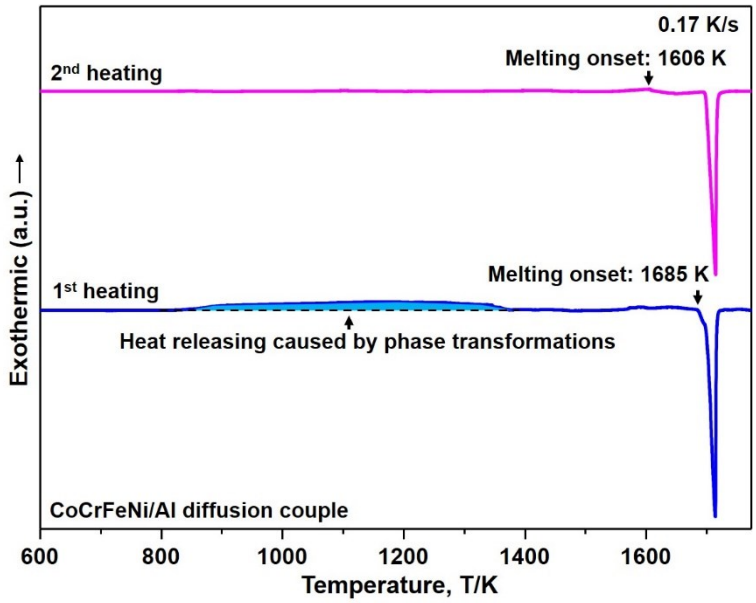

Fig. 6. DSC curve of the CoCrFeNi/Al diffusion couple. In addition to the melting event, an exothermic heat flow caused by phase transformation can be observed during the first heating run.

Table 2. Mixing enthalpies of binary alloys at an equi-atomic composition obtained from Miedema's model (KJ/mole) [55].

Elements	Al	Co	Cr	Fe	Ni
Al	-	-19	-10	-11	-22
Co	-	-	-4	-1	0
Cr	-	-	-	-1	-7
Fe	-	-	-	-	-2
Ni	-	-	-	-	-

4.2. Formation of σ phase, a hint for the indirect influence of the mixing enthalpy

The σ phase can be found in many Fe-Cr alloy systems [43,56,57]. It often serves as a hard secondary phase in HEAs that is introduced through annealing due to its higher hardness than the HEA matrix [41,58,59]. However, its formation mechanism is still unclear. Kitchingman [60] pointed out that the formation of the σ phase requires the bcc phase exhibiting partial long range order along the $[11\bar{1}]$ plane prior to the transformation. For the HEA investigated here, the excellent phase stability is confirmed by the current experiments and along with previous reports [20,31]. However, the addition of Al induces the formation of σ phase that lacks Al. Therefore, in the present case the σ phase is indirectly triggered by the HEA/Al reaction. At 973 K, the Gibbs free energy is dominated by the enthalpy. The more negative enthalpy of Al and Ni results in their preferred bonding tendency

to form new phases. The up-hill diffusion of Ni to the film side results in its depletion behind the reaction area where Fe and Cr accumulate and bond together to form the bcc phase. With increasing temperature, the FeCr rich bcc phase further transforms to the σ phase.

4.3. Phase composition of HEAs

Even though the annealing time might not be sufficient to form the equilibrium phases, it is still possible to observe the corresponding isomorphous compounds in the binary phase diagrams. By calculating the relative effects of enthalpy and entropy on the phase stability in equiatomic high-entropy alloys, Otto et al. [25] found that any elements that are prone to form phases when alloyed as binary pairs will also be found in the microstructure of the five-component alloy. It is therefore believed that the binary phase diagrams of the HEA components can provide a guide for predicting the phase formation in HEAs and that the mixing enthalpy between the components might play a dominant role on the formation of intermetallic compounds in HEAs.

4.4. Multicomponent configuration: Stabilization of high entropy phases?

The Gibbs free energy of mixing ΔG_{mix} for a solution can be written as the following:

$$\Delta G_{mix} = \Delta H_{mix} - T\Delta S_{mix} \quad , \quad (1)$$

where ΔH_{mix} and ΔS_{mix} are the enthalpy and entropy of mixing respectively, and T is the absolute temperature. The mixing of entropy ΔS_{mix} can be further described by:

$$\Delta S_{mix} = \Delta S_C^{Id} + \Delta S_{mix}^{Ex} \quad , \quad (2)$$

where ΔS_C^{Id} represents ideal chemical configurational entropy of mixing and ΔS_{mix}^{Ex} represents excess entropy of mixing. For an ideal solution, the contribution to Gibbs free energy is only from ideal configurational entropy.

It is believed that the high configurational entropy in HEAs favors the formation of a single-phase solid solution over alloys with intermetallic phases [2,61,62]. The CoCrFeNi/Al system analyzed in the present work is used to identify the contribution of the multicomponent configuration on the disordered state. Therefore, this multicomponent system is compared to the composed binary alloys with equal-atomic ratios. The homologous temperature is widely used to compare the atom diffusion ability in different alloy systems to understand the multicomponent configuration on the atomic diffusion ability [31,63,64]. With this criterion, the difference of diffusion ability of elements in different systems (caused by difference in vibration and movability frequency due to the difference in temperature with respect to the melting points) can be effectively compensated. Therefore, the

homologous temperature, namely the ratio of the "order-disorder" transition temperature (T_T) to the melting points (T_m) is chosen as the criterion to reflect the tendency to form a disordered state. The solidus temperatures are chosen as melting points in the estimates of the homologous temperatures. The specific choice of either solidus, liquidus or peak temperature of the melting event does not affect the main conclusions of the present paper. To determine the influence of enthalpy, the mixing enthalpies of different binary alloys at an equi-atomic composition are shown in Table 2. For CoCrFeNi and CoCrFeNi/Al investigated here, to reveal the bonding tendency of different atom pairs, the simple assumption is used that the mixing enthalpy is the average value of the composing atom pairs. Phase transitions from ordered to disordered state in different equal-atomic ratio alloys together with the CoCrFeNi/Al system are summarized in Table 3, and the relationship between homologous temperatures and mixing enthalpies is shown in Fig. 7.

Table 3. Phase transition from ordered to disordered state in different equal-atomic ratio alloys. To determine the configurational entropy influence on the transition behavior, the additional magnetic contribution from ferromagnetic to paramagnetic transition is neglected for the FeNi alloy. L and FM indicate liquid phase and ferromagnetic phase respectively. For CoCrFeNi/Al system, the melting point of equal-atomic ratio AlCoCrFeNi alloy obtained from [19] was used.

Alloy	Transformation	H_{mix}	T_m (K)	T_T (K)	T_H	Ref
CoCr	fcc+bcc→bcc+L	-4	1670	1670	1	[48]
CoFe	B2→bcc	-1	1750	1005	0.57	[65]
CoNi	Stable fcc	0	1469	< 273 K	< 0.19	[66]
CrFe	σ→bcc	-1	1805	1066	0.59	[66]
CrNi	fcc+bcc→bcc+L	-7	1618	1618	1	[67]
FeNi	fcc_{FM}+α-Fe→fcc_{FM}	-2	1713	652	0.38	[68]
AlNi	-	-22	1892	-	-	[66]
AlCo	-	-19	1913	-	-	[66]
AlFe	B2+L→L+bcc	-11	1583	1583	1	[66][69]
AlCr	βAl_8Cr_5+bcc→bcc+L	-10	1593	1593	1	[66][70]
CoCrFeNi	Stable fcc	-2.5	1698	< 273 K	< 0.16	This work
CoCrFeNi/Al	B2+σ→fcc	-7.7	1635	1173-1373	0.72-0.84	[19]+This work

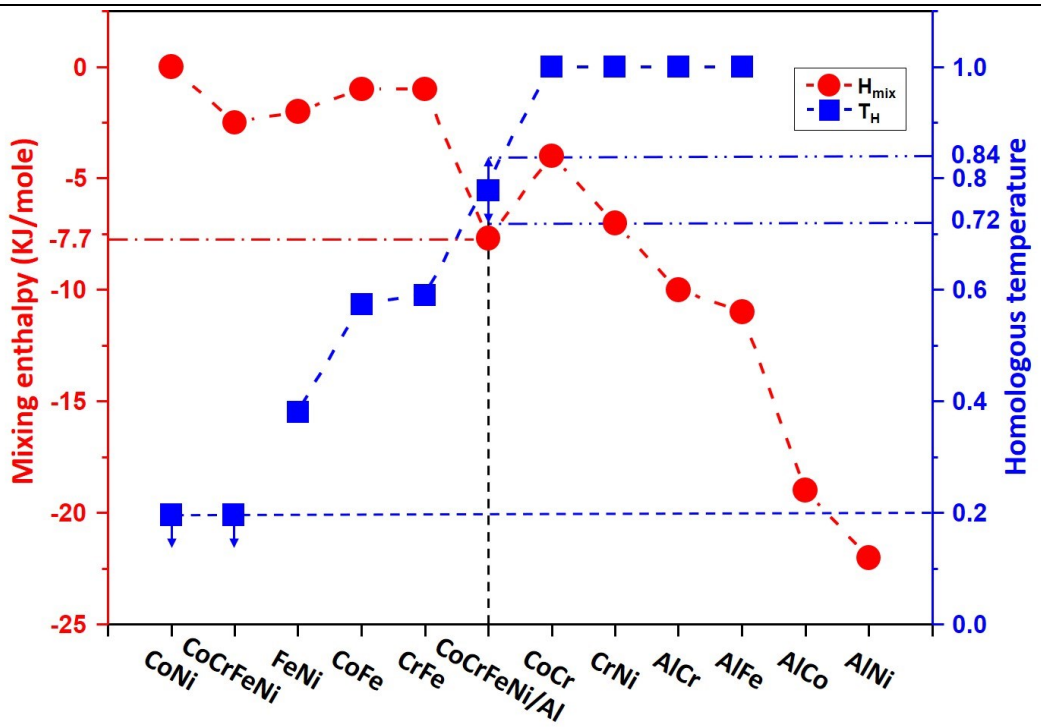

Fig. 7. Comparison of the homologous temperatures (TH) of different equal-atomic ratio alloys transforming from ordered to disordered state along with the mixing enthalpies of the composing atom pairs. Due to the stable disordered states of the CoNi and CoCrFeNi systems at room temperature, their homologous temperatures are marked as less than 0.2.

For the CoCrFeNi system, the fcc disordered state is sustained from room temperature up to the melting point, which has also been confirmed in several reports [20,31,71]. Hence, it shows a low homologous temperature that is comparable to the CoNi system. In contrast, due to the dynamic transformation process for the CoCrFeNi/Al system, the transition temperature is in the range of 1173 K to 1373 K. Thus, T_H is in the range of 0.72-0.84. Its homologous temperature is higher than for several of the binary alloy systems. Therefore, it is believed that the multi-component configuration does not stabilize the disordered solid solution state. Even after the system transforms to disordered state, the uphill diffusion of Ni in the reaction region occurs (see the intensity contrast of Ni on film side compared with HEA side in Fig. S2(e)), which cannot be explained merely by the contribution from ideal configurational entropy of mixing. Based on the equation (1) and (2), such an uphill diffusion behavior should be related to the excess Gibbs energy contribution from mixing enthalpy and/or excess entropy of mixing. Considering the strong bonding tendency of Al with Ni from 973 K to 1173 K, the uphill diffusion should be related to the additional contribution from mixing enthalpy. In order to demonstrate the strong Al-Ni bonding tendency, a sample was additionally annealed at

1573 K for 30 min. The SEM and corresponding EDS mapping results are shown in Fig. S2(f). Clearly uphill diffusion of Ni to the Al side can be seen. Therefore, it appears that the enthalpy contribution to the phase evolution cannot be ignored even in the disordered state at temperatures that are close to the onset-melting point of the HEA (93% of the HEA onset melting point, see Fig. S5 marked with a red arrow). In general, a gradual trend can be found, that is, the more negative the mixing enthalpy between the components, the higher the homologous order-to-disorder transformation temperature. The deviation of the CoCrFeNi/Al system might be due to additional atomic interactions and the unequal atomic ratio configuration during the dynamic diffusion process. The general trend reflected here should be related to the relative contribution of enthalpy and entropy to the free energy of the system. With a small mixing enthalpy between atom pairs, atoms have a similar bonding tendency to the different kinds of elements since their contribution to the total energy from heat release of the different bonds is similar. There is no preferential bonding tendency of atoms. Therefore, the atoms tend to randomly distribute in the lattice sites and a disordered state can be expected as is the case of the CoNi and CoCrFeNi systems shown here. However, for atom pairs with a relatively more negative mixing enthalpy, their bonding is beneficial for the energy reduction of the system. In such a system, the atoms have a tendency to preferentially bond, so higher transition temperatures and homologous temperatures are found, as for example in the case of CoCr, CrNi, AlCr and CrFe binary equal atomic ratio alloys. For the binary alloys AlCo and AlNi, the large negative mixing enthalpy between the atom pairs causes the solid-state transition temperature to disappear. Hence, no homologous temperature can be found based on their binary phase diagrams. Therefore, it can be concluded that the composing elements play a significant role in the phase stability of HEAs. Of special importance is the mixing enthalpy between atom pairs, which will influence the phase transition temperature and also indirectly influences the formation of other phases, such as in the present case of the uphill diffusion of Ni to bond with Al resulting in the formation of the bcc FeCr phase.

4.5. Surface modification of HEAs through combination of film deposition and thermal diffusion

It is well known that dislocations are the main carriers of plastic deformation in large-grained crystals. Compared with the ductile fcc HEA matrix that is composed of closely-packed atoms providing easier-operated slip systems, the larger Burgers vectors of the ordered phases hinder dislocation movement, making intermetallic phases harder but more brittle [1,72]. For the samples

annealed at 1373 K, the hard surface side can be attributed to the formation of intermetallic compounds. A closer examination of its hardness map (Fig. 5(a)) shows a heterogeneous hardness distribution within the film side. Since the grain sizes of the B2 and bcc precipitates are comparable to the size of the indents, the heterogeneous hardness distribution can be attributed to effects of grain boundaries and the different hardness of the B2, σ and bcc phases. The refinement of grain size increases the hardness by introducing of large number of grain boundaries as barriers for the dislocation movement. The area close to the interface shows a relatively higher hardness, which should be caused by the formation of the hard σ phase together with fine B2 grains in this area. Similar mechanism can also be expected for the area close to the free side, where B2 and fine-grained bcc phases coexists. For the sample annealed at 1573 K, a lower overall hardness that continuously increases towards the surface is measured. At this temperature, only the fcc solid solution state remains; however, the uphill diffusion of Ni to bond with Al is still to be considered. This results in a diffusion influenced zone in the matrix (see Fig. S2(e-f)), where a higher amount of Fe, Cr, Co and a smaller amount of Ni is found. Since only the fcc disordered state is sustained and the grain size is rather large at this temperature (see in Fig. 4(c-d) and Fig. S6(b)), the potential reason for the hardening behavior can be attributed to solid solution strengthening. As seen from Fig. 2(b), the diffusion of Al towards the HEA further increases the lattice parameter and the lattice distortion. Compared with the HEA which is homogenously composed of four elements, the stronger tendency of Ni to bond with Al on the film side results in a larger distortion in this area compared with the diffusion influence zone and the HEA matrix. The local higher stress fields, induced by the lattice distortion, restrict dislocation propagation and, hence, lead to a higher hardness on the film side.

5. CONCLUSIONS

Through reactive interdiffusion of CoCrFeNi/Al, a systematic investigation of the phase evolution in this multicomponent system was carried out. In contrast to studies of the phase evolution based on the addition of elements method, reactive interdiffusion provides more details about the influence of enthalpy and entropy on the phase formation and element diffusion behavior. This gives a direct way to study the phase evolution in the multi-component system and provides guidance to design single-phase disordered HEAs with high thermal stability. The following conclusions can be drawn from the present study:

(1) At temperatures below 1373 K, the enthalpy dominates the total energy, resulting in the formation of intermetallic compounds. Entropy of mixing starts to play a dominant role at a temperature of 1373 K, where on the microscale the diffusion of Al towards the HEA without phase transformation to form a more disordered state initiates.

(2) The mixing enthalpy still significantly influences the phase evolution at elevated temperatures. The strong tendency of Al to react with Ni induces the formation of a bcc FeCr phase behind the interface that later transforms to the σ phase. The contribution of enthalpy cannot be ignored even when the system reaches the disordered state, as shown by the uphill diffusion of Ni towards Al. Hence, the effects of entropy and enthalpy on the phase constitution in HEAs need to be both considered even at elevated temperatures.

(3) Comparing the homologous temperatures of different equal-atom ratio alloys reveals that the multicomponent configuration does not stabilize the disordered state. Instead, the mixing enthalpy between atom pairs has the strongest impact on the transition temperature from ordered to disordered state. The more negative the mixing enthalpy between the components, the higher the homologous order-disorder transformation temperature. This can be attributed to the relative contribution of enthalpy and entropy to the free energy of the system. Therefore, to design single phase disordered HEAs with excellent thermal stability, elements need to be considered that have mixing enthalpies between atom pairs close to 0.

(4) Surface modification of HEAs can be realized through the combination of film deposition and annealing. For the samples annealed at 1373 K and 1573 K, the formation of a hard surface layer is attributed to the formation of intermetallic compounds and more severe lattice distortion on the film side, respectively. It is believed that such a design strategy can also be applied to other HEA systems and the required properties can be realized through an appropriate combination of film deposition components and annealing process.

Acknowledgements

The authors gratefully acknowledge the financial support from the Austrian Science Fund (FWF): Y1236-N37 and the National Natural Science Foundation of China (51871132). Additional support from the China Scholarship Council (CSC, Grant No. 201906220226) is acknowledged. We thank K.-H. Pichler for synthesizing the thin films, C. Freitag for assistance with metallographic sample

preparation, A. Hohenwarter and S. Wurster for technical support with the SEM investigations, F. Spieckermann, P. Ramasamy and A. Xia for stimulating discussions.

References

[1] Y. Zhang, T.T. Zuo, Z. Tang, M.C. Gao, K.A. Dahmen, P.K. Liaw, Z.P. Lu, Microstructures and properties of high-entropy alloys, Prog. Mater. Sci. 61 (2014) 1–93.

[2] D.B. Miracle, O.N. Senkov, A critical review of high entropy alloys and related concepts, Acta Mater. 122 (2017) 448–511.

[3] Y.J. Zhao, J.W. Qiao, S.G. Ma, M.C. Gao, H.J. Yang, M.W. Chen, Y. Zhang, A hexagonal close-packed high-entropy alloy: The effect of entropy, Mater. Des. 96 (2016) 10–15.

[4] F. Zhang, C. Zhang, S.L. Chen, J. Zhu, W.S. Cao, U.R. Kattner, An understanding of high entropy alloys from phase diagram calculations, Calphad Comput. Coupling Phase Diagrams Thermochem. 45 (2014) 1–10.

[5] K.Y. Tsai, M.H. Tsai, J.W. Yeh, Sluggish diffusion in Co-Cr-Fe-Mn-Ni high-entropy alloys, Acta Mater. 61 (2013) 4887–4897.

[6] J.W. Yeh, Physical metallurgy of high-entropy alloys, Jom. 67 (2015) 2254–2261.

[7] J.W. Yeh, Alloy design strategies and future trends in high-entropy alloys, Jom. 65 (2013) 1759–1771.

[8] E.J. Pickering, N.G. Jones, High-entropy alloys: a critical assessment of their founding principles and future prospects, Int. Mater. Rev. 61 (2016) 183–202.

[9] O.N. Senkov, S.L. Semiatin, Microstructure and properties of a refractory high-entropy alloy after cold working, J. Alloys Compd. 649 (2015) 1110–1123.

[10] F. He, Z. Wang, Q. Wu, J. Li, J. Wang, C.T. Liu, Phase separation of metastable CoCrFeNi high entropy alloy at intermediate temperatures, Scr. Mater. 126 (2017) 15–19.

[11] B. Schuh, F. Mendez-Martin, B. Völker, E.P. George, H. Clemens, R. Pippan, A. Hohenwarter, Mechanical properties, microstructure and thermal stability of a nanocrystalline CoCrFeMnNi high-entropy alloy after severe plastic deformation, Acta Mater. 96 (2015) 258–268.

[12] B. Schuh, B. Völker, J. Todt, N. Schell, L. Perrière, J. Li, J.P. Couzinié, A. Hohenwarter, Thermodynamic instability of a nanocrystalline, single-phase TiZrNbHfTa alloy and its impact on the mechanical properties, Acta Mater. 142 (2018) 201–212.

[13] T. Yang, S. Xia, S. Liu, C. Wang, S. Liu, Y. Zhang, J. Xue, S. Yan, Y. Wang, Effects of Al addition on microstructure and mechanical properties of $Al_xCoCrFeNi$ High-entropy alloy, Mater. Sci. Eng. A. 648 (2015) 15–22.

[14] W.R. Wang, W.L. Wang, S.C. Wang, Y.C. Tsai, C.H. Lai, J.W. Yeh, Effects of Al addition on the microstructure and mechanical property of $Al_xCoCrFeNi$ high-entropy alloys, Intermetallics. 26 (2012) 44–51.

[15] O.N. Senkov, S. V. Senkova, D.B. Miracle, C. Woodward, Mechanical properties of low-density, refractory multi-principal element alloys of the Cr-Nb-Ti-V-Zr system, Mater. Sci. Eng. A. 565 (2013) 51–62.

[16] Y.J. Zhou, Y. Zhang, Y.L. Wang, G.L. Chen, Solid solution alloys of $AlCoCrFeNiTi_x$ with excellent room-temperature mechanical properties, Appl. Phys. Lett. 90 (2007) 181904-2.

[17] J. Chen, P. Niu, Y. Liu, Y. Lu, X. Wang, Y. Peng, J. Liu, Effect of Zr content on microstructure and mechanical properties of AlCoCrFeNi high entropy alloy, Mater. Des. 94 (2016) 39–44.

[18] V. Soni, B. Gwalani, O.N. Senkov, B. Viswanathan, T. Alam, D.B. Miracle, R. Banerjee, Phase stability as a function of temperature in a refractory high-entropy alloy, J. Mater. Res. 33 (2018) 3235–3246.

[19] W.R. Wang, W.L. Wang, J.W. Yeh, Phases, microstructure and mechanical properties of $Al_xCoCrFeNi$ high-entropy alloys at elevated temperatures, J. Alloys Compd. 589 (2014) 143–152.

[20] M. Vaidya, K. Guruvidyathri, B.S. Murty, Phase formation and thermal stability of CoCrFeNi and CoCrFeMnNi equiatomic high entropy alloys, J. Alloys Compd. 774 (2019) 856–864.

[21] H. Shahmir, J. He, Z. Lu, M. Kawasaki, T.G. Langdon, Evidence for superplasticity in a CoCrFeNiMn high-entropy alloy processed by high-pressure torsion, Mater. Sci. Eng. A. 685 (2017) 342–348.

[22] S. Guo, C. Ng, J. Lu, C.T. Liu, Effect of valence electron concentration on stability of fcc or bcc phase in high entropy alloys, J. Appl. Phys. 109 (2011) 103505-2.

[23] S. Guo, C.T. Liu, Phase stability in high entropy alloys: Formation of solid-solution phase or amorphous phase, Prog. Nat. Sci. Mater. Int. 21 (2011) 433–446.

[24] M.H. Tsai, A.C. Fan, H.A. Wang, Effect of atomic size difference on the type of major intermetallic phase in arc-melted $CoCrFeNi_x$ high-entropy alloys, J. Alloys Compd. 695 (2017)

1479–1487.

[25] F. Otto, Y. Yang, H. Bei, E.P. George, Relative effects of enthalpy and entropy on the phase stability of equiatomic high-entropy alloys, Acta Mater. 61 (2013) 2628–2638.

[26] Y.J. Du, J.T. Xiong, F. Jin, S.W. Li, L. Yuan, D. Feng, J.M. Shi, J.L. Li, Microstructure evolution and mechanical properties of diffusion bonding $Al_5(TiZrHfNb)_{95}$ refractory high entropy alloy to Ti_2AlNb alloy, Mater. Sci. Eng. A. 802 (2021) 1–9.

[27] Y. Lei, S.P. Hu, T.L. Yang, X.G. Song, Y. Luo, G.D. Wang, Vacuum diffusion bonding of high-entropy $Al_{0.85}CoCrFeNi$ alloy to TiAl intermetallic, J. Mater. Process. Technol. 278 (2020) 116455.

[28] Y. Peng, J. Li, J. Shi, S. Li, J. Xiong, Microstructure and mechanical properties of diffusion bonded joints of high-entropy alloy $Al_5(HfNbTiZr)_{95}$ and TC4 titanium alloy, J. Mater. Res. Technol. 11 (2021) 1741–1752.

[29] P. Li, H. Sun, S. Wang, Y. Xia, H. Dong, G. Wen, H. Zhang, Diffusion bonding of $AlCoCrFeNi_{2.1}$ eutectic high entropy alloy to GH4169 superalloy, Mater. Sci. Eng. A. 793 (2020) 139843.

[30] W.D. Callister Jr, D.G. Rethwisch, Materials Science and Engineering - An Introduction 10th Edition, John Wiley & Sons, Hoboken, 2018.

[31] M. Vaidya, S. Trubel, B.S. Murty, G. Wilde, S. V. Divinski, Ni tracer diffusion in CoCrFeNi and CoCrFeMnNi high entropy alloys, J. Alloys Compd. 688 (2016) 994–1001.

[32] L.J. Zhang, Z.K. Jiang, M.D. Zhang, J.T. Fan, D.J. Liu, P.F. Yu, G. Li, R.P. Liu, Effect of solid carburization on the surface microstructure and mechanical properties of the equiatomic CoCrFeNi high-entropy alloy, J. Alloys Compd. 769 (2018) 27–36.

[33] S. Chen, X. Chen, L. Wang, J. Liang, C. Liu, Laser cladding FeCrCoNiTiAl high entropy alloy coatings reinforced with self-generated TiC particles, J. Laser Appl. 29 (2017) 012004.

[34] W.C. Oliver, G.M. Pharr, An improved technique for determining hardness and elastic modulus using load and displacement sensing indentation experiments, J. Mater. Res. 7 (1992) 1564–1583.

[35] S.J. Bull, On the origins and mechanisms of the indentation size effect, Zeitschrift Fuer Met. Res. Adv. Tech. 94 (2003) 787–792.

[36] N.K. Mukhopadhyay, P. Paufler, Micro- and nanoindentation techniques for mechanical

characterisation of materials, Int. Mater. Rev. 51 (2006) 209–245.

[37] A. Paul, T. Laurila, V. Vuorinen, S. V. Divinski, Thermodynamics, diffusion and the kirkendall effect in solids, Springer, Switzerland, 2014.

[38] Z.Q. Zhang, S.V. Ketov, S. Fellner, H.P. Sheng, C. Mitterer, K.K. Song, C. Gammer, J. Eckert, Reactive interdiffusion of an Al film and a CoCrFeNi high-entropy alloy, Mater. Des. 216 (2022) 110530.

[39] H. Shahmir, T. Mousavi, J. He, Z. Lu, M. Kawasaki, T.G. Langdon, Microstructure and properties of a CoCrFeNiMn high-entropy alloy processed by equal-channel angular pressing, Mater. Sci. Eng. A. 705 (2017) 411–419.

[40] A. Munitz, S. Salhov, S. Hayun, N. Frage, Heat treatment impacts the micro-structure and mechanical properties of AlCoCrFeNi high entropy alloy, J. Alloys Compd. 683 (2016) 221–230.

[41] S.T. Chen, W.Y. Tang, Y.F. Kuo, S.Y. Chen, C.H. Tsau, T.T. Shun, J.W. Yeh, Microstructure and properties of age-hardenable $Al_xCrFe_{1.5}MnNi_{0.5}$ alloys, Mater. Sci. Eng. A. 527 (2010) 5818–5825.

[42] C.W. Lin, M.H. Tsai, C.W. Tsai, J.W. Yeh, S.K. Chen, Microstructure and aging behaviour of $Al_5Cr_{32}Fe_{35}Ni_{22}Ti_6$ high entropy alloy, Mater. Sci. Technol. (United Kingdom). 31 (2015) 1165–1170.

[43] C.-C. Hsieh, W. Wu, Overview of intermetallic sigma phase precipitation in stainless steels, ISRN Metall. 2012 (2012) 1–16.

[44] W.R. Wang, W.L. Wang, S.C. Wang, Y.C. Tsai, C.H. Lai, J.W. Yeh, Effects of Al addition on the microstructure and mechanical property of $Al_xCoCrFeNi$ high-entropy alloys, Intermetallics. 26 (2012) 44–51.

[45] J. Wang, T. Guo, J. Li, W. Jia, H. Kou, Microstructure and mechanical properties of non-equilibrium solidified CoCrFeNi high entropy alloy, Mater. Chem. Phys. 210 (2018) 192–196.

[46] Y.F. Kao, T.J. Chen, S.K. Chen, J.W. Yeh, Microstructure and mechanical property of as-cast, -homogenized, and -deformed $Al_xCoCrFeNi$ ($0 \leq x \leq 2$) high-entropy alloys, J. Alloys Compd. 488 (2009) 57–64.

[47] S. Novy, P. Pareige, C. Pareige, Atomic scale analysis and phase separation understanding in a thermally aged Fe-20 at.%Cr alloy, J. Nucl. Mater. 384 (2009) 96–102.

[48] K.P. Gupta, The Co-Cr-Mo (cobalt-chromium-molybdenum) system, J. Phase Equilibria Diffus. 26 (2005) 87–92.

[49] Y. Qiu, S. Thomas, D. Fabijanic, A.J. Barlow, H.L. Fraser, N. Birbilis, Microstructural evolution, electrochemical and corrosion properties of $Al_xCoCrFeNiTi_y$ high entropy alloys, Mater. Des. 170 (2019) 107698.

[50] A.A. Maradudin, Kinetics of short-range and long-range B2 ordering in FeCo, Phys. Rev. B. 44 (1995) 9805–9811.

[51] S.L. Qiu, Magnetic structure in ordered FeCr, Phys. Rev. B. 60 (1999) 56–59.

[52] A. Fraczkiewicz, A.S. Gay, M. Biscondi, On the boron effect in FeAl (B2) intermetallic alloys, Mater. Sci. Eng. A. 258 (1998) 108–114.

[53] R.D. Noebe, R.R. Bowman, M. V. Nathal, Physical and mechanical properties of the B2 compound NiAl, Int. Mater. Rev. 38 (1993) 193–232.

[54] F. Stein, C. He, N. Dupin, Melting behaviour and homogeneity range of B2 CoAl and updated thermodynamic description of the Al-Co system, Intermetallics. 39 (2013) 58–68.

[55] A. Takeuchi, A. Inoue, Classification of bulk metallic glasses by atomic size difference, heat of mixing and period of constituent elements and its application to characterization of the main alloying element, Mater. Trans. 46 (2005) 2817–2829.

[56] J. Wang, S. Liu, X. Han, Study on σ phase in Fe–Al–Cr alloys, Metals. 9 (2019) 1–10.

[57] B.F.O. Costa, G. Le Caër, J.M. Loureiro, V.S. Amaral, Mechanically induced phase transformations of the sigma phase of nanograined and of coarse-grained near-equiatomic FeCr alloys, J. Alloys Compd. 424 (2006) 131–140.

[58] M.H. Tsai, H. Yuan, G. Cheng, W. Xu, W.W. Jian, M.H. Chuang, C.C. Juan, A.C. Yeh, S.J. Lin, Y. Zhu, Significant hardening due to the formation of a sigma phase matrix in a high entropy alloy, Intermetallics. 33 (2013) 81–86.

[59] M.H. Tsai, K.Y. Tsai, C.W. Tsai, C. Lee, C.C. Juan, J.W. Yeh, Criterion for sigma phase formation in Cr- and V-Containing high-entropy alloys, Mater. Res. Lett. 1 (2013) 207–212.

[60] W.J. Kitchingman, The atomic mechanism of the body-centred cubic to σ-phase transformation, Acta Crystallogr. Sect. A. 24 (1968) 282–286.

[61] J.W. Yeh, S.K. Chen, S.J. Lin, J.Y. Gan, T.S. Chin, T.T. Shun, C.H. Tsau, S.Y. Chang, Nanostructured high-entropy alloys with multiple principal elements: Novel alloy design

concepts and outcomes, Adv. Eng. Mater. 6 (2004) 299–303.

[62] J. Yeh, S. Chen, J. Gan, S. Lin, T. Chin, Formation of simple crystal structures in Cu-Co-Ni-Cr-Al-Fe-Ti-V alloys with multiprincipal metallic elements, Metall. Mater. Trans. A. 35 (2010) 2533–2536.

[63] J. Kottke, M. Laurent-Brocq, A. Fareed, D. Gaertner, L. Perrière, Ł. Rogal, S. V. Divinski, G. Wilde, Tracer diffusion in the Ni–CoCrFeMn system: Transition from a dilute solid solution to a high entropy alloy, Scr. Mater. 159 (2019) 94–98.

[64] M. Vaidya, K.G. Pradeep, B.S. Murty, G. Wilde, S. V. Divinski, Bulk tracer diffusion in CoCrFeNi and CoCrFeMnNi high entropy alloys, Acta Mater. 146 (2018) 211–224.

[65] T. Sourmail, Near equiatomic FeCo alloys: Constitution, mechanical and magnetic properties, Prog. Mater. Sci. 50 (2005) 816–880.

[66] T.B. Massalski, J.L. Murray, L.H. Bennet, Binary alloy phase diagrams: Volume 1, ASM Int. Metals Park, Ohio, 1986.

[67] K.P. Gupta, The Cr-Ni-Zr (chromium-nickel-zirconium) system, J. Phase Equilibria Diffus. 31 (2010) 191–193.

[68] G. Cacciamani, A. Dinsdale, M. Palumbo, A. Pasturel, The Fe-Ni system: Thermodynamic modelling assisted by atomistic calculations, Intermetallics. 18 (2010) 1148–1162.

[69] K. Han, I. Ohnuma, R. Kainuma, Experimental determination of phase equilibria of Al-rich portion in the Al–Fe binary system, J. Alloys Compd. 668 (2016) 97–106.

[70] H. Okamoto, Al-Cr (Aluminum-Chromium), J. Phase Equilibria Diffus. 29 (2008) 112–113.

[71] F. Zheng, G. Zhang, X. Chen, X. Yang, Z. Yang, Y. Li, J. Li, A new strategy of tailoring strength and ductility of CoCrFeNi based high-entropy alloy, Mater. Sci. Eng. A. 774 (2020) 138940.

[72] T.H. Courtney, Mechanical Behavior of Materials. 2. ed., Waveland Press, Long Grove, 2000.

Supplementary materials

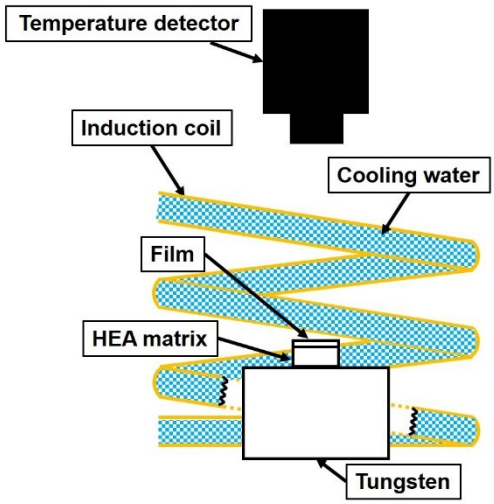

Fig. S1. Schematic diagram of the heating device used for isochronous annealing.

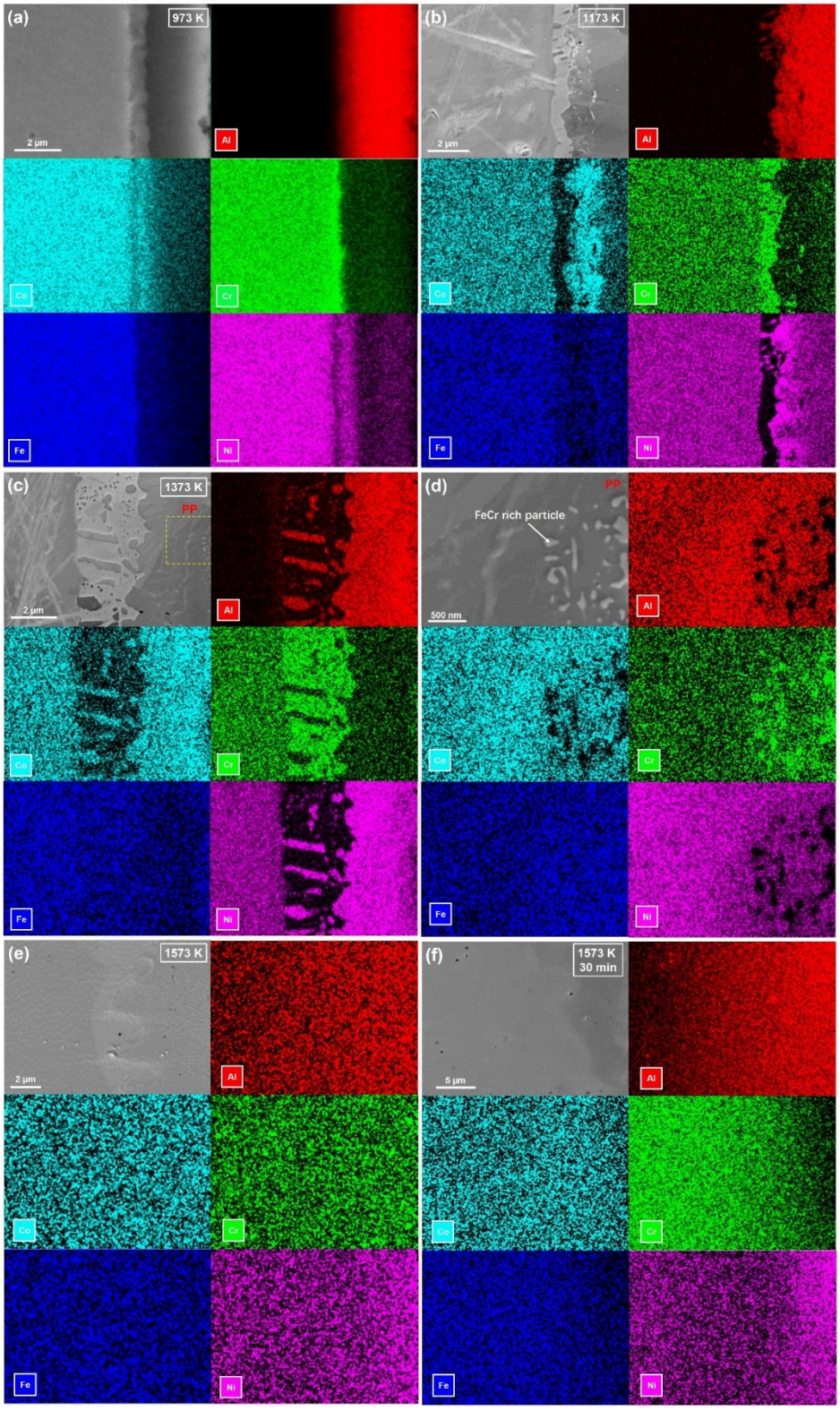

Fig. S2. Cross-section SEM images and corresponding EDS maps for different temperatures. Samples annealed at 973 K (a), 1173 K (b), 1373 K (c), 1573 K (e). The particle phase (PP) region marked in (c) is further magnified in (d) together with the corresponding EDS maps. To compare the effect of enthalpy on the diffusion process, the EDS maps for the sample annealed at 1573 K for 30 min are shown in (f).

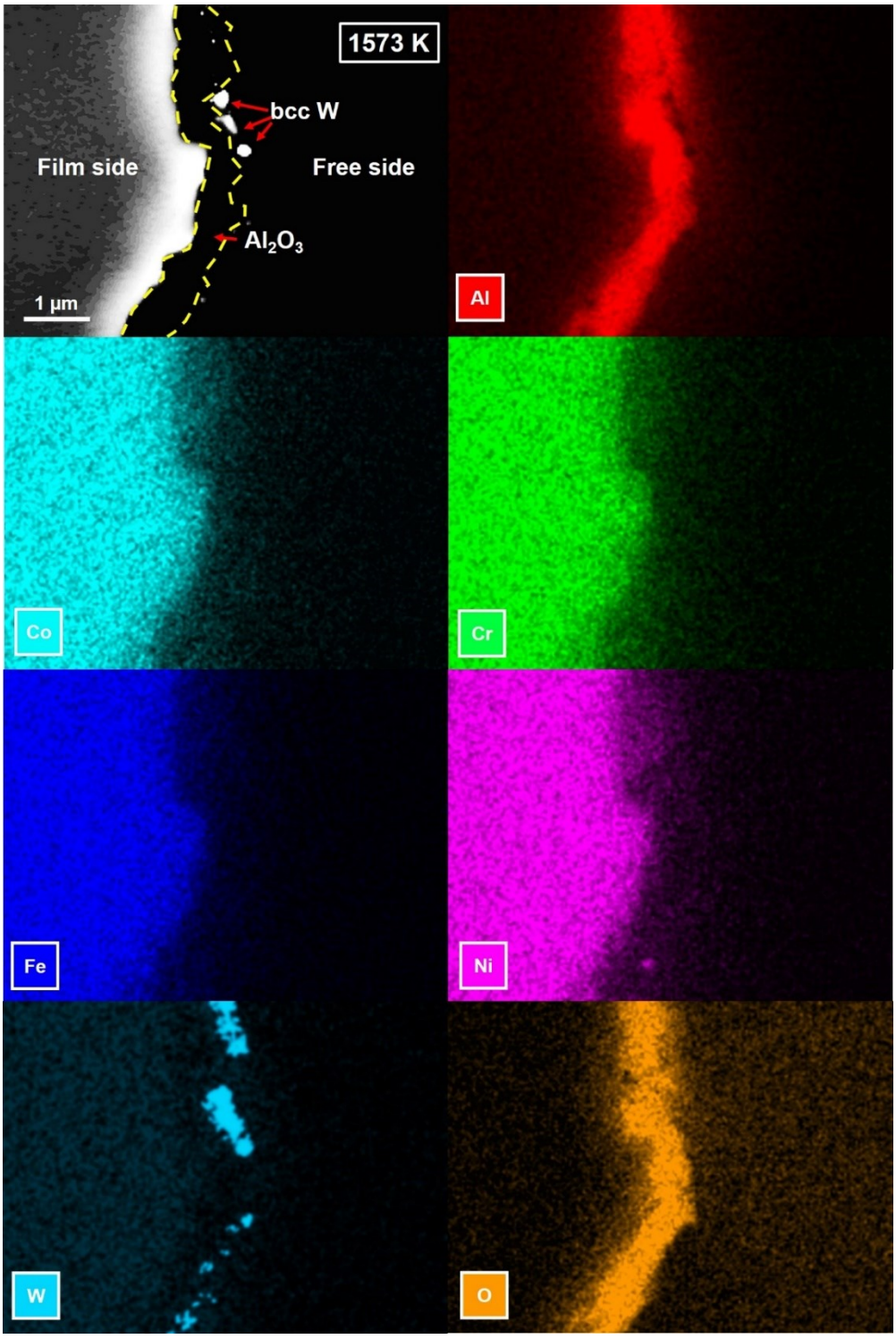

Fig. S3. Cross-section SEM image of the free side of specimen annealed at 1573 K for 10 min and corresponding Al, Co, Cr, Fe, Ni, W and O EDS maps. Due to the large atomic number difference between film and Al_2O_3 layer, the Al_2O_3 appears to be darker. While the W with high atomic number on the free side is brighter than the film (the dashed-yellow lines are drawn to indicate interfaces).

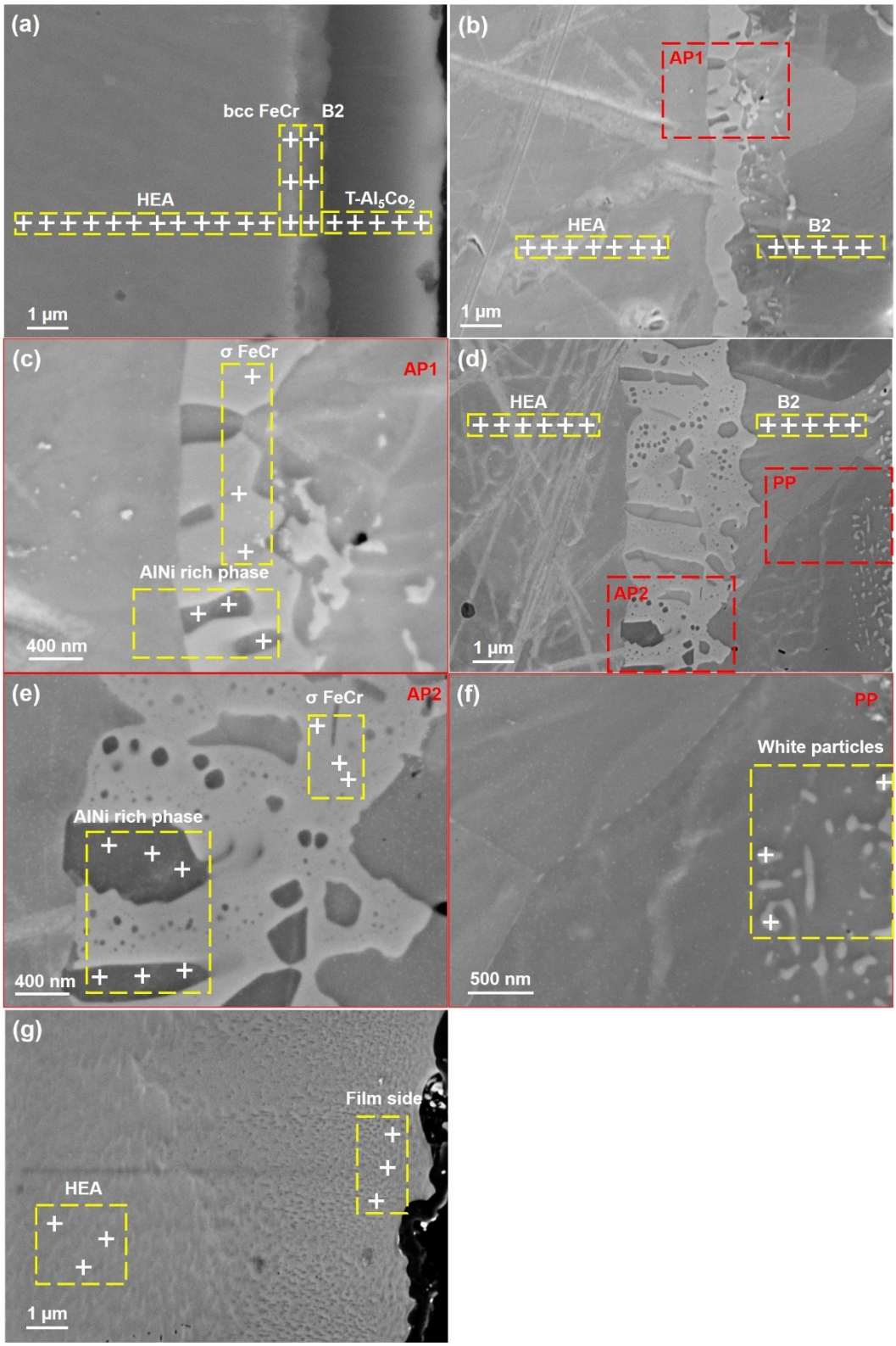

Fig. S4. SEM images of the locations where EDS point analysis was carried out for samples annealed at 973 K (a), 1173 K (b), 1373 K (d) and 1573 K (g). (c) represents the acicular phase (AP1) area marked in (b). (e) and (f) represent the acicular phase (AP2) area and the particle phase (PP) area marked in (d).

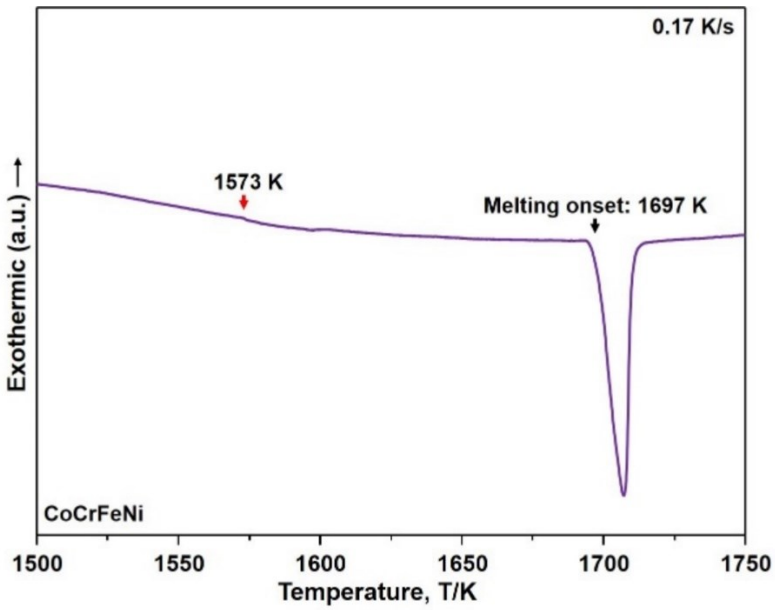

Fig. S5. DSC curve of the as-cast HEA. The red arrow indicates the highest heating temperature for the diffusion experiment.

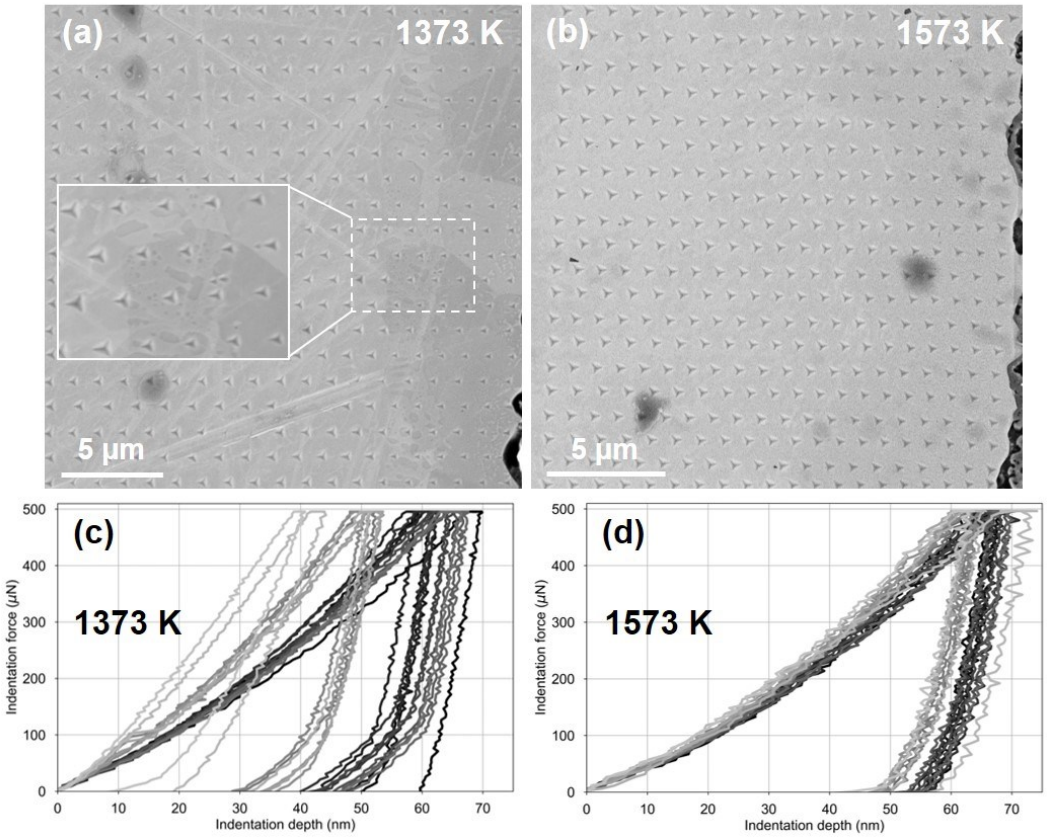

Fig. S6. SEM images of the nanoindentation map area of the samples annealed at 1373 K (a) and 1573 K (b). Exemplary load-displacement curves for the 1373 K (c) and 1573 K (d) samples.

Manuscript III

Microstructure evolution and mechanical properties of a lamellar $AlCoCrFeNi_{2.1}$ eutectic high-entropy alloy processed by high-pressure torsion

Zequn Zhang [a,b,*], Simon Fellner [b], Anton Hohenwarter [a], Oliver Renk [a], Yong Huang [b], Zhuo Chen [b], Kaikai Song [c], Caiju Li [d], Christoph Gammer [b,*], Jürgen Eckert [a,b]

[a] Department of Materials Science, Montanuniversität Leoben, Jahnstraße 12, 8700 Leoben, Austria.

[b] Erich Schmid Institute of Materials Science, Austrian Academy of Sciences, Jahnstraße 12, 8700 Leoben, Austria.

[c] School of Mechanical, Electrical & Information Engineering, Shandong University, 264209 Weihai, China.

[d] Faculty of Materials Science and Engineering, Kunming University of Science and Technology, 650093 Kunming, China.

[*] Corresponding authors:

zequn.zhang@stud.unileoben.ac.at; christoph.gammer@oeaw.ac.at

Abstract

High-pressure torsion (HPT) was applied to a lamellar eutectic high-entropy alloy (EHEA) to study the effect of severe plastic deformation (SPD) on the composite structure and mechanical properties. We found that the existence of multiple phases affects defect distribution and the fragmentation process during HPT. Structural evolution shows orientation dependence with respect to the shear plane, which finally leads to a refined multiphase structure with nanograins and vortex clusters after a shear strain γ of 24. In nanograins, dislocation-mediated deformation prevails. The high density of grain boundaries, forest dislocations, and the generation of deformation twins restrict dislocation movement. As a result, an EHEA with a yield strength of 1.75 GPa, an excellent tensile strength of 2.20 GPa, and an appreciable failure strain of 5 % is realized. Our results demonstrate that structural evolution of the EHEA during the HPT deformation is significantly affected by the initial structure and plastic flow behavior of phases. SPD on the multiphase structure is a suitable route for designing

high-strength yet ductile alloys.

Keywords: Eutectic high-entropy alloys, Severe plastic deformation, Structure evolution, Mechanical properties, Grain refinement

1. Introduction

High-entropy alloys (HEAs) have received worldwide attraction since their discovery in 2004 [1][2]. They are composed of more than four or five principal elements with equal or similar atomic ratios, which opens up a new world to explore alloys with a vast compositional space. By maximizing the contribution of configurational entropy to the molar Gibbs free energy, HEAs tend to form disordered solid solution phases. As a result, face-centered cubic (Fcc), body-centered cubic (Bcc) or hexagonal close-packed solid solutions are formed in most HEAs [3][4]. The unique design route brings promising properties to HEAs, such as excellent structural stability [5], good wear resistance [6] and high fracture resistance [7].

As one of the severe plastic deformation (SPD) methods, high-pressure torsion (HPT) can apply ultra-high strains in a controllable manner to metals or alloys at low homologous temperatures [8]. The introduction of shear strain during the HPT process causes fragmentation of the structure, which provides an approach to produce bulk ultrafine-grained or nanograined materials. The resulting structures can show outstanding mechanical and functional properties, such as high hardness [9], high fatigue strength [10], low coercivity [11], and high hydrogenation activity [12]. In recent years, HEAs were processed with HPT to investigate the thermal stability of high configurational entropy systems [13][14], the effect of alloying behavior on the mechanical property [15], the recrystallization and grain growth behavior of HEAs [16] and the joining of dissimilar materials [17-19]. etc. The final structure or property is closely related to structural evolution during HPT. In CoCrFeNi, the concurrent nanobands and deformation twins separate a grain into several segments and cause fragmentation [20]. In CoCrFeNiMn [13], the interaction of different twinning variants forms blocks of twin lamellae within grains, leading to grain refinement. Through the composition adjustment, Chandan et al. [21] found that transformation induced plasticity mechanism in $Fe_{40}Mn_{40}Co_{10}Cr_{10}$ transforms into dislocation slip-dominated deformation in $Fe_{35}Mn_{35}Co_{10}Cr_{10}Ni_{10}$ during HPT, and this is attributed to increased free energy of phase transformation with Ni addition. Kishore et al. [22] found that dislocation slip and twinning are dominant deformation mechanisms during HPT

processing of $Co_{33}Ni_{33}Cr_{19}Mn_{15}$ HEA.

Most of the research focuses on single-phase HEAs. The fragmentation of dual-phase or multiphase HEAs is less understood. Edalati et al. [23] studied the hardening behavior of dual-phase AlCrFeCoNiNb HEA during HPT. Extreme grain refinement to a grain size of 10 nm comes from the restriction of dynamic recrystallization due to the existence of the second phase. But the plastic flow difference of the two phases during fragmentation was not explained. Through HPT, gas atomized powders of CoCrFeMnNi and IN718 were joined [17]. The resulting lamellar composite is composed of nanograins with a vortex flow feature. This is believed to be caused by the local turbulence and shear strain vortices. Similar vortex-like structures are also reported in other multilayer materials processed by HPT [18][24]. Utilizing HPT, Son et al. [19] realized bonding between $AlCoCrFeNi_{2.1}$ and CoCrFeNi powders to design hierarchically heterogeneous microstructure. However, the applied strain needs to be high enough to realize physical bonding at the interface. The structural origin of nanostructure composites just after bonding was missed.

The goal of this study was to investigate the fragmentation behavior of an EHEA during HPT. With a natural composite structure, eutectic high-entropy alloys (EHEAs) show excellent strength-ductility synergy as a result of the heterogeneous eutectic lamellar structure [25-28]. The $AlCoCrFeNi_{2.1}$ EHEA was subjected to HPT deformation. The response of the soft and hard phases during HPT was investigated by structural characterization at multiple length scales. The resulting mechanical properties were tested via microhardness and tensile testing. The obtained results give a comprehensive overview of the microstructural evolution of a lamellar EHEA with complex phase composition during SPD and the related mechanical properties changes.

2. Experimental methods

2.1 Material processing

An EHEA ingot with a nominal composition of $AlCoCrFeNi_{2.1}$ (at.%) was prepared by vacuum arc melting of nominal mixtures of the constituent elements (purity ≥ 99.95%) and was remelted at least five times in a Ti-gettered high-purity argon atmosphere to ensure chemical homogeneity. The molten alloy was suction-cast into a 10 mm (width) × 100 mm (length) × 2 mm (thickness) water-cooled Cu mold. This was followed by homogenization annealing in a vacuum furnace (Xerion Xtube) at 1023 ± 5 K for 12 h. The chamber was evacuated to $< 5 \times 10^{-5}$ Pa before annealing.

For the HPT process, disks with a diameter of 8 mm and an initial thickness of 2 mm were machined from the cast plates using electro-discharge machining (EDM). This was followed by grinding with silicon carbide abrasive papers P280 (EFPA, The Federation of European Producers of Abrasives) to a reduction of the thickness to 1.9 mm. The disks were deformed using a quasi-constrained HPT system in anvils with a total groove depth of 0.5 mm at a nominal pressure of 6 GPa and a rotational speed of 0.6 rotations/min for 1/4, 1, and 5 rotations at room temperature. Because of the quasi-constrained setup in the current case, some material flowed out during deformation. To increase the friction between anvils and the disk and avoid slippage, the anvils were sandblasted before HPT. The samples after different deformation states are denoted as 1/4 R, 1 R, and 5 R according to the applied number of rotations during HPT deformation. The ideal shear strain γ of HPT processing can be calculated by,

$$\gamma = \frac{2\pi r n}{t} \quad , \quad (1)$$

where r is the sample radius, t is the sample thickness and n is the number of rotations [29]. Since the initial thickness was reduced by 43% - 65% during HPT, the thickness of samples after HPT was measured (1.08 mm for 1/4 R, 0.79 mm for 1 R, and 0.66 mm for 5 R) and were utilized in the calculation to mitigate the potential underestimation of strain values [30].

2.2 Phase analysis and microstructural characterization

The phase constitution of samples under different deformation states was analyzed by X-ray diffraction (XRD) (Co-Kα radiation) using a Bruker D2 phaser diffractometer at a scan rate of 1°/min. Microstructure and phase distribution were characterized with a scanning electron microscope (SEM, Zeiss Leo 1525) equipped with back-scattered electron (BSE), energy-dispersive X-ray spectroscopy (EDS) and electron backscatter diffraction (EBSD) units. For SEM observation the samples were ground mechanically using silicon carbide abrasive papers (P500-P4000) and then mechano-chemically polished with conventional aluminum oxide polishing suspension followed by vibrational polishing for 4 hours. By detecting Euler angles coming from each pixel, the orientation relationship of the phase boundary in the as-cast specimen was determined by EBSD using a Bruker eFlash FS detector and the result was analyzed and visualized by ATEX software with a tolerance angle of 5° [31].

2.3 Observation of the structural evolution using transmission electron microscopy

Further in-depth microstructure investigations were conducted by transmission electron

microscopy (TEM), allowing to identify phase constitution, interface information, and defect distribution of the undeformed state and the HPT-processed materials. The samples for TEM were taken from the as-cast specimen and HPT disks (1 R and 5 R), ground to 100 μm, subsequently punched into discs with a diameter of 3 mm and mechanically dimpled to ~ 30 μm, and finally thinned to electron transparency using a twin-jet electropolishing with a mixture of 90% ethanol and 10% perchloric acid (vol.%) at a voltage of 20 V and at -25°C. TEM images, diffraction patterns, and EDS results were obtained using a JEOL JEM-2200FS microscope equipped with an EDS unit, and the high-resolution TEM (HRTEM) images were obtained from JEOL JEM-2100F equipped with an image spherical aberration corrector. Due to misorientation development and grain refinement of samples during HPT, the standard indexed diffraction patterns for single crystals cannot be obtained. The identification of diffraction planes of the selected area electron diffraction (SAED) patterns was done by calculating the interplanar spacings.

2.4 Mechanical testing

For hardness testing the samples were ground and polished following the same procedure as for SEM observation without vibrational polishing. Vickers micro-hardness measurements were conducted with a Buehler microhardness tester (Micromet 5104) at a load of 1000 gf and a dwell time of 15 s. Tensile tests were performed with dog-bone specimens machined from a region 2 mm away from the HPT disk center by EDM having a gauge length of 2.5 mm and a square cross-section of ~ 0.36 mm^2. The tests were conducted at room temperature on a tensile Kammrath and Weiss testing machine with a strain rate of 1×10^{-3} s^{-1}. The tensile strain was directly measured on the sample surface by evaluating optical micrographs continuously taken throughout the tensile test. Images were taken using a stereomicroscope (Olympus SZx 16) equipped with a Canon EOS 600D camera at a frequency of 3 Hz. Intrinsic roughness and surface features served as reference points for calculating the displacements and recording strains. The starting point for image acquisition and the movement of the crosshead were synchronized to unambiguously link a particular image to a specific load point. The images were subsequently analyzed with the open software package GOM (Correlate 2016) to calculate the tensile strain. All tensile tests were repeated three times at least.

3. Results

3.1 Microstructure and phase composition of the as-cast EHEA

The morphology of the as-cast EHEA is shown in Fig. 1(a), displaying a lamellar structure with a colony size of ~ 10 μm. A needle-like phase can be occasionally seen within the grey lamellae (marked with white arrows). Combining the XRD pattern with the EBSD result (Figs. 1(b, c)), it can be proven that the grey lamellae with an average thickness of 570 nm are Fcc phase while the thinner black ones with an average thickness of 330 nm are ordered Body-centered cubic (B2) phase. Based on the analysis of ATEX software, the phase boundary between Fcc and B2 follows the Kurdjumov–Sachs crystallographic orientation relationship (KS-OR), i.e. {111} Fcc // {110} B2 and <110> Fcc // <111> B2. This correlates well with the results of pole figures (Fig. S1) and with previous research [32-34].

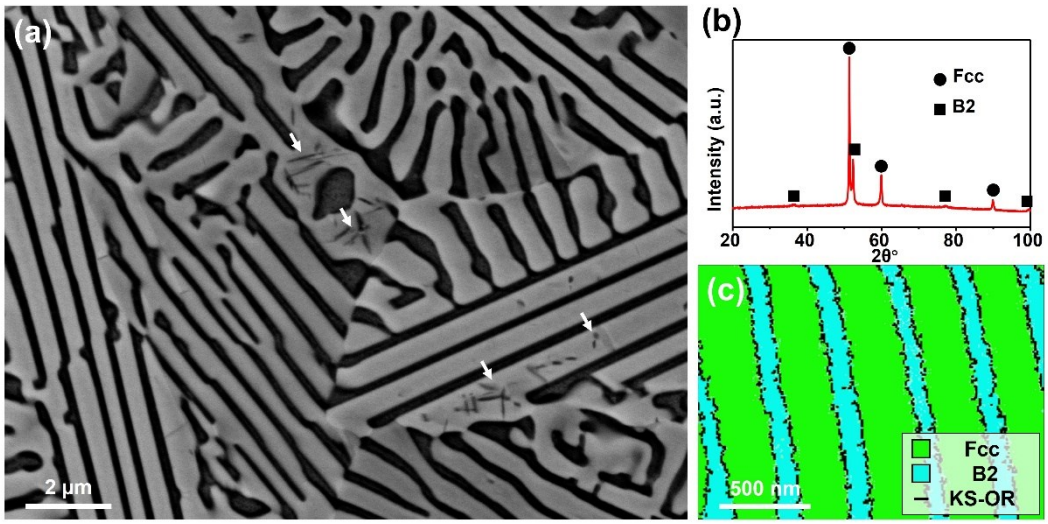

Fig. 1 Microstructure of the as-cast EHEA. (a) BSE-SEM image showing the lamellar structure. (b) The XRD pattern. (c) EBSD phase map of the lamellae, showing the KS-OR at the interfaces.

The scanning transmission electron microscopy (STEM) image and the EDS mapping results (Figs. 2(a-f)) show that the Fcc phase is rich in Co, Cr, and Fe, while the B2 phase is rich in Al and Ni. Based on the SAED pattern (inset in Fig. 2(a)), the needle-like phase is ordered Fcc phase ($L1_2$) and it is rich in Al and Ni. Moreover, high-density spherical nano-precipitates enriched in Cr exist in the center of the B2 lamellae. Both the $L1_2$ and the particle phases show a fully coherent interface with their matrix (Fig. 2(g-j)). Here the impact of the $L1_2$ phase on the microstructure evolution is neglected because of its very low volume fraction and inhomogeneous distribution within the Fcc phase.

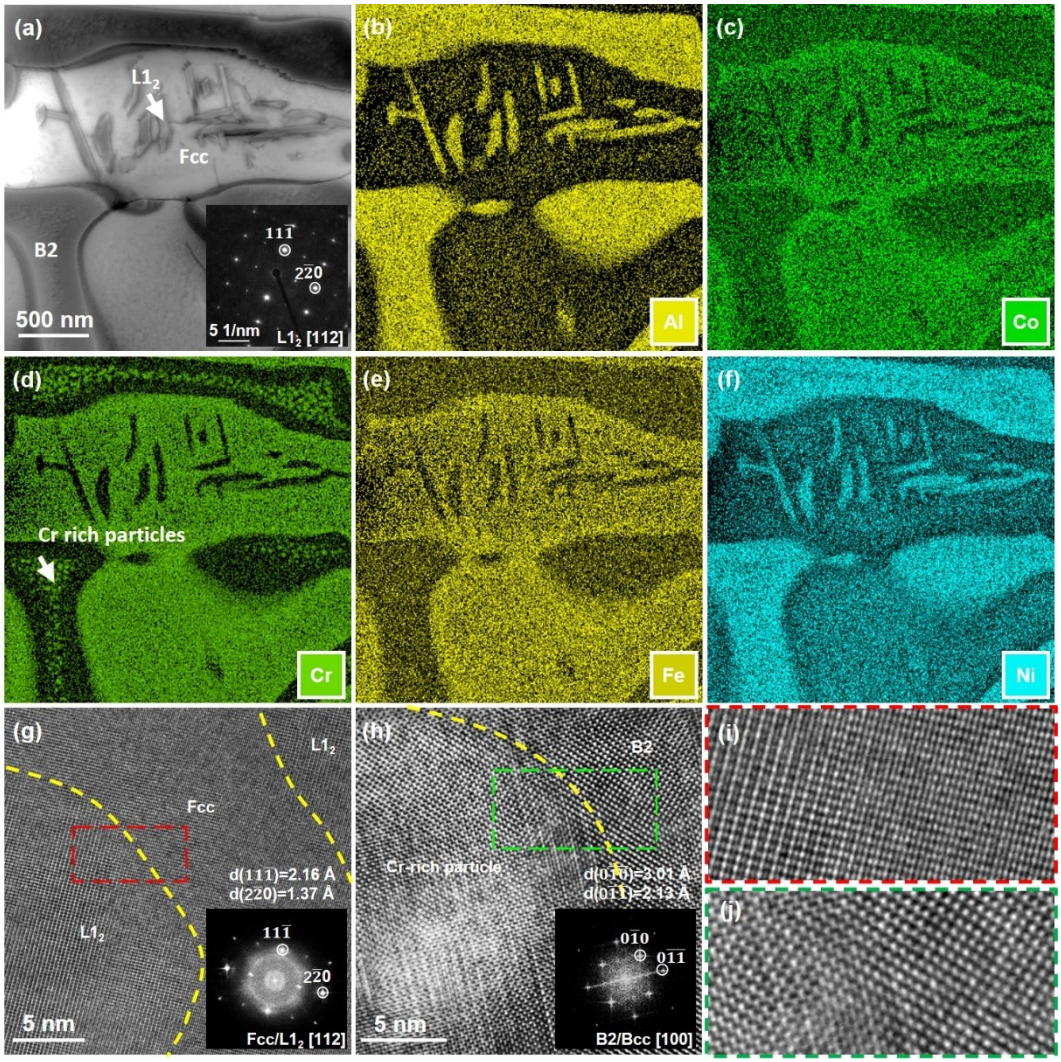

Fig. 2 (a) STEM image of the lamellar structure and corresponding element distribution map of (b) Al, (c) Co, (d) Cr, (e) Fe, and (f) Ni. HRTEM images of the needle phase area (g) and the particle phase area (h) within the Fcc and B2 lamella respectively, inset showing the Fast Fourier Transformations (FFTs) and the interplanar spacings calculated based on the FFTs. (i, j) The enlarged areas marked in (g) and (h).

3.2 Microstructure evolution of the EHEA during HPT processing

The XRD patterns of the as-cast alloy and samples after different deformation degrees are shown in Fig. 3(a). Due to the deformation gradient along the radial direction, slices from a constant radius (2 mm away from the HPT disk center) were machined for the XRD measurement. As a result of the change of the lattice parameter, microstrain, and structural refinement after SPD, all peaks of the Fcc phase shift to the left and show broadening [35]. After 1 rotation, the Fcc major peak 111 shows an asymmetric feature, which is caused by the overlap of the left-shifted and broadened B2 peak 110 with the Fcc peak together with the disordering process of the B2 to Bcc phase. This will be further

confirmed by detailed TEM characterization later.

SEM images of specimens after HPT are shown in Fig. 3(b-d). The imaging locations for 1/4 R, 1 R, and 5 R are 2 mm away from the center in the axial viewing direction with the corresponding shear strain γ of ~ 3, ~ 16, and ~ 95 based on equation (1). The shear plane is horizontal in all images. After a shear strain γ of ~ 3 (Fig. 3(b)), the initially parallel lamellae start to be bent with a large radius of curvature and some local fragmentation areas with lower contrast appear (marked with white arrows). Further deformation to γ ~ 16 (Fig. 3(c)) leads to the formation of two distinct regions. The lamellae that are initially parallel to the shear plane show less distortion but become elongated along the shear plane with some protrusion features (marked with yellow arrows) at the interface. These areas are defined as the remaining lamellar area. The lamellae showing large misorientation to the shear plane are distorted, forming fragmentation areas. In these areas, the two phases change their morphology, suggesting inhomogeneous plastic deformation during HPT. After a shear strain γ of ~ 95 (Fig. 3(d)), the black vortex areas (also seen in Fig. S2) are relatively homogeneously distributed in the matrix.

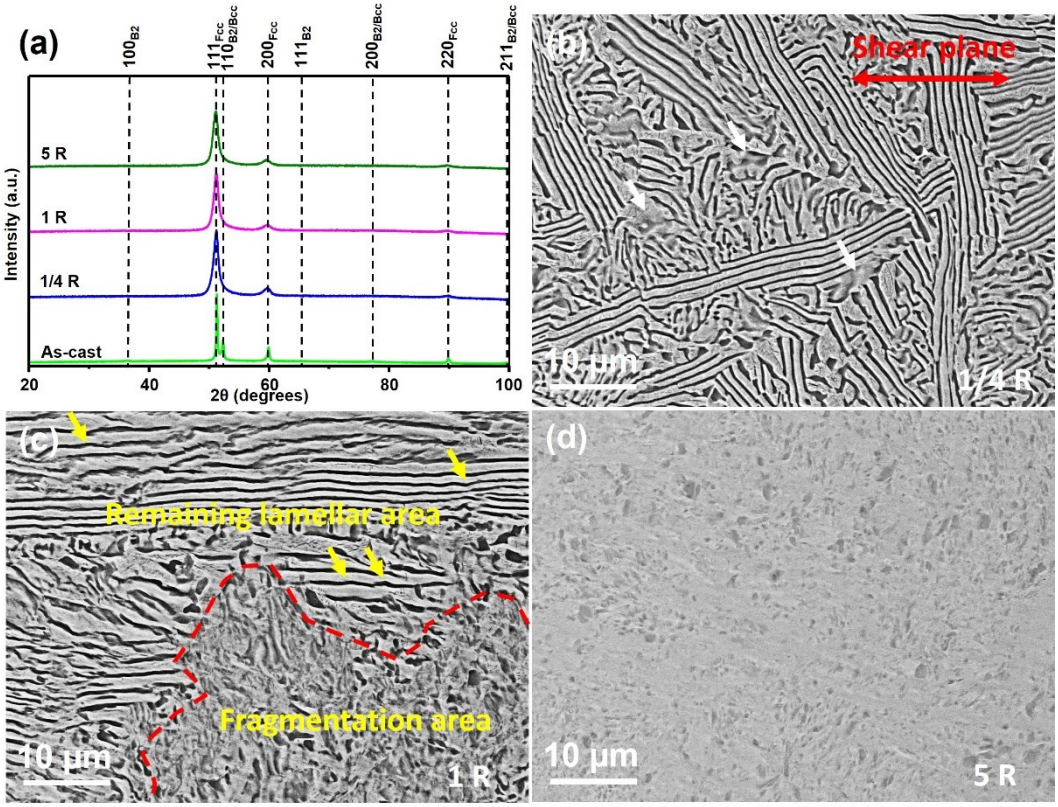

Fig. 3 Phase composition and morphology changes of the EHEA after HPT deformation. (a) XRD patterns of as-cast and HPT-deformed EHEA. SEM-BSE images of 1/4 R (b), 1 R (c), and 5 R (d).

3.3 TEM analysis of the microstructure evolution during HPT deformation

The in-depth TEM analyses were performed to understand the deformation mechanism during HPT. To capture the impact of compression deformation on the microstructure, an additional TEM sample was prepared that was only compressed in the HPT machine without any torsional straining (0 R), leading to a compressive strain of ~ 16%. For 0 R, the lamellar morphology remains intact (Fig. 4(a)). The bright-field (BF) images (Fig. 4(b, c)) show a high density of dislocations with wavy-slip features within both Fcc and B2 phases. The early stage of fragmentation of the two phases close to their interface can be seen in the dark-field (DF) image (Fig. 4(d)). The movement and re-arrangement of dislocations results in the formation of subgrain boundaries in lamellae and consequent fragmentation [20].

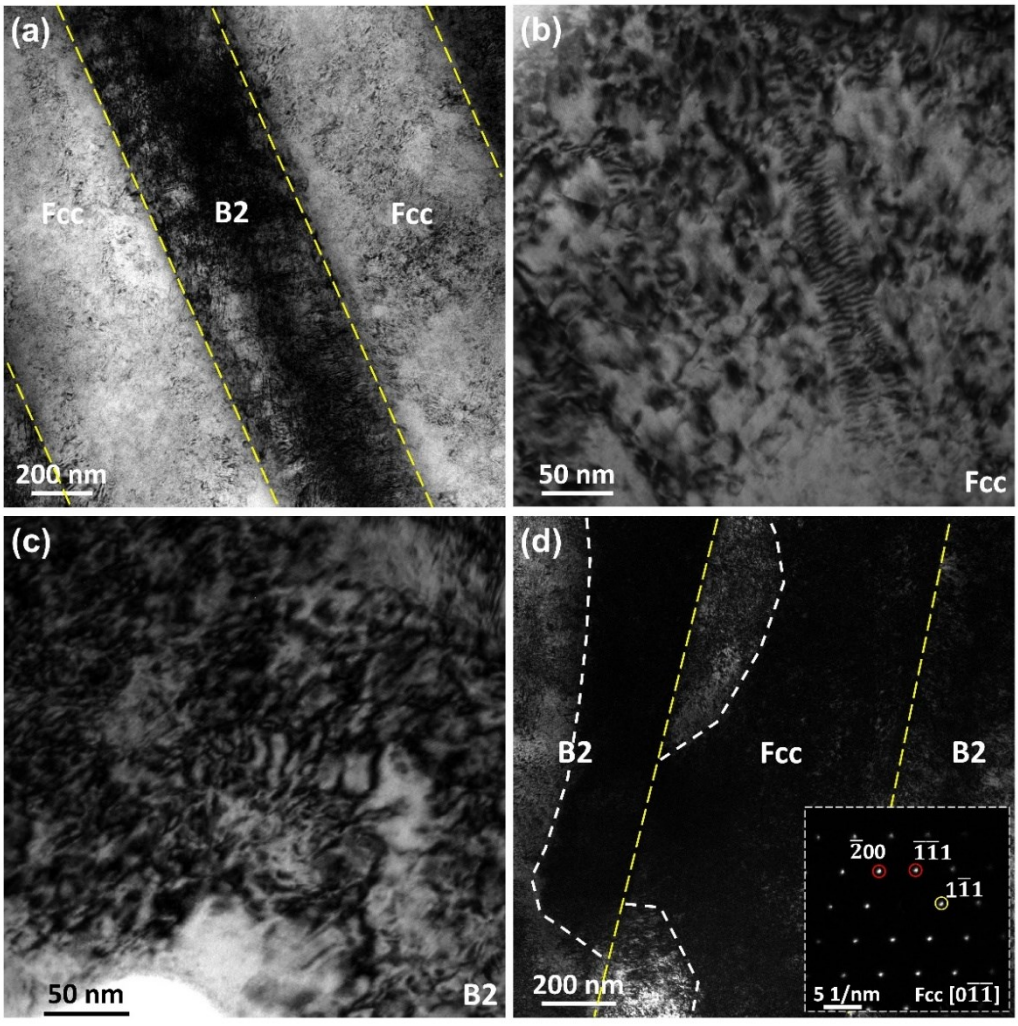

Fig. 4 TEM images of 0 R. (a) BF image showing the lamellar structure. BF images within a (b) Fcc lamella and a (c) B2 lamella. (d) DF image employing the $1\bar{1}1$ diffraction spot of the SAED pattern (marked with a yellow circle in the inset) for a Fcc lamella, revealing fragmentation close to the interface. Yellow dotted lines indicate the interfaces and the white dotted lines in (d) show the boundaries of different orientated domains.

After 1 R, the torsional straining causes a change in the morphology (Fig. 5(a)). The TEM specimen was taken from an area 2 mm away from the HPT disk center, corresponding to a shear strain γ of ~ 16. In the remaining lamellar area, a soft Fcc lamella subdivides into nanograins (Fig. 5(a)), which is also reflected by the diffraction ring feature of the SAED pattern (Fig. 5(b)). For the B2 phase, strain leads to misorientation inside a lamella, as revealed by the arc-shaped diffraction feature from the SAED pattern (Fig. 5(c)) and by the detailed TEM characterization (Fig. S3). Due to severe deformation, the long-range order of the B2 phase is undermined as 100 superlattice reflections of the SAED pattern show weak intensity (Fig. 5(c)). The DF-TEM image (Fig. 5(d)) using a 100 superlattice reflection indicates that only limited B2 phase exists. Some areas show the disappearance of 100 superlattice reflections (Fig. 5(e)). Hence the B2 phase transforms into a Bcc phase during the HPT process. Locally, the sample is transformed to a full fragmentation area showing nanocrystals (Fig. 5(f)) and stacking fault/deformation twin features (marked with white arrows in Fig. 5(g)). The rather blurry appearance of grains in the nanocrystalline state is typical for HPT-processed materials and is ascribed to the formation of non-equilibrium grain boundaries [30]. The SAED pattern (Fig. 5(h)) proves the full disappearance of the long-range order of the B2 phase. Meanwhile, the change of the lattice parameter due to the defect activities results in an overlap of 111_{Fcc} and 110_{Bcc} diffraction rings, which agrees well with XRD results (Fig. 3(a)).

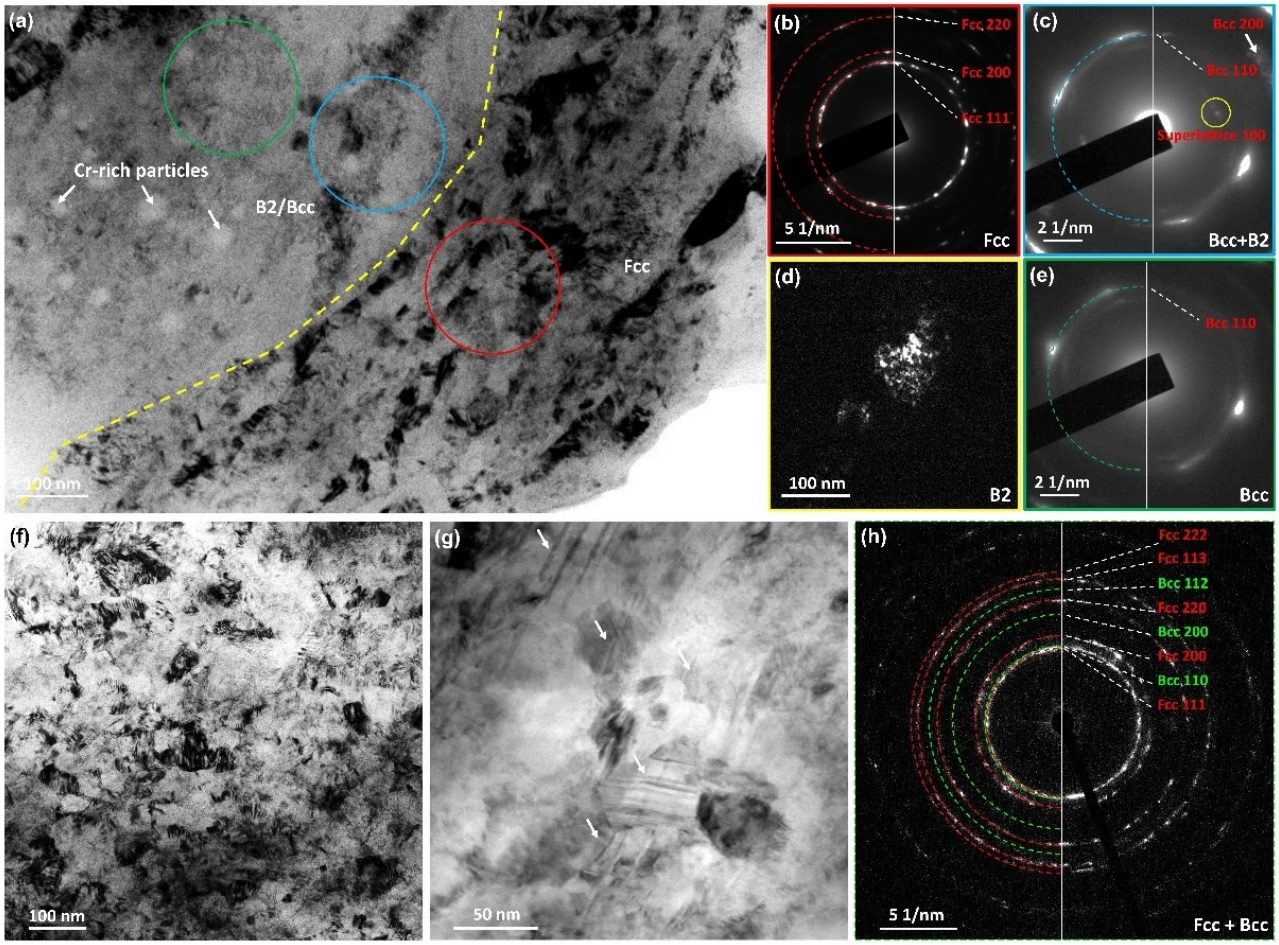

Fig. 5 TEM images from the EHEA after applying a shear strain γ of ~ 16. (a) BF image of a remaining lamellar area. Yellow dotted lines indicate the interface. White arrows mark Cr-rich particles. (b) SAED pattern of the Fcc phase. (c) SAED pattern of Bcc+B2 phases and (d) DF image of the B2 phase taken with a 100 superlattice reflection. The used superlattice reflection is marked with a yellow circle in (c). (e) SAED pattern of the Bcc phase. (f) BF image of a full fragmentation area. (g) An enlarged image of the full fragmentation area. (h) The SAED pattern of (f). Three circles marked in (a) are locations for SAED patterns shown in (b, c, e).

For the 5 R specimen, the lamellar structure cannot be found anymore with a shear strain γ ~ 95 (Fig. 6(a)). High-density nanograins show elongated features with a grain width of 40 ± 13 nm (Fig. S4). They are surrounded by Al, Ni-rich vortex areas with Cr-rich particles inside (Fig. 6(b-f)). Based on the analysis of the structure of 1 R and the composition difference between phases, it can be concluded that nanograins are composed of the Fcc and Bcc grains, and vortex-shaped areas originate from the remaining disordering B2 (Bcc) lamellae. The number of Cr-rich particles reduces as the size of the vortex decreases.

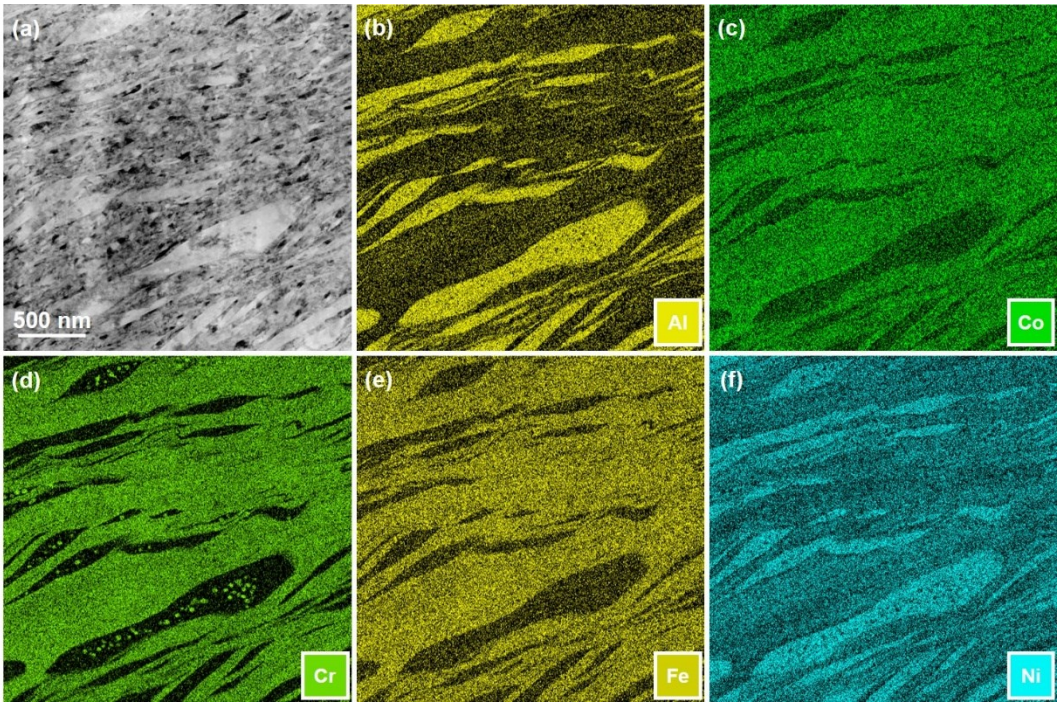

Fig. 6 (a) STEM image from the EHEA after applying a shear strain $\gamma \sim 95$ and corresponding element distribution maps of (b) Al, (c) Co, (d) Cr, (e) Fe, and (f) Ni.

3.4 Change of mechanical properties as a function of the applied strain

The evolution of hardness is presented in Fig. 7. The as-cast specimen has a hardness of 362 ± 8 HV (Fig. 7(a)). The hardness increases with the number of HPT rotations. Already after 1 rotation, the hardness at the periphery of the HPT disk tends to saturate. 5 rotations result in a broad hardness plateau along the radial direction with an average hardness of 557 ± 12 HV. This is also reflected by the hardness evolution as a function of shear strain (Fig. 7(b)). A saturation of hardness is realized after shear strain γ of 24.

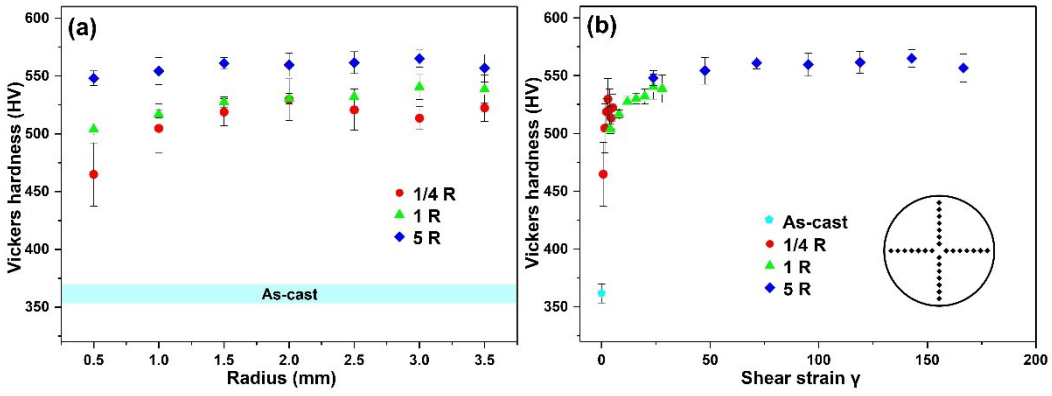

Fig. 7 Hardness of the as-cast and HPT-deformed EHEA. (a) Vickers hardness distribution along the radial direction of HPT disks as a function of the number of HPT rotations. (b) Vickers hardness evolution as a function of the shear strain (b). The hardness values were obtained by averaging

hardness values from four indents at an equivalent radial position. The standard deviation is indicated by the error bars. The inset in (b) shows the schematics of the indent distribution on an HPT disk.

The tensile stress-strain curves for the as-cast and HPT-deformed specimens are shown in Fig. 8(a). The as-cast sample shows a fracture strain of 15.6 ± 0.8 % with a yield stress $\sigma_{0.2}$ (at 0.2% offset) of 703.0 ± 23.6 MPa. The applied shear strain leads to a reduction of ductility and a strong increase of yield strength. After 5 rotations, the yield stress, tensile strength, and fracture strain are 1754.4 ± 18.4 MPa, 2201.9 ± 14.4 MPa and 5.0 ± 1.1 %, respectively. Fig. 8(b) shows the tensile properties of the specimens in the current work and literature results for various EHEAs and other high-strength HEAs, revealing that a high-strength EHEA with retained ductility is realized after the HPT process.

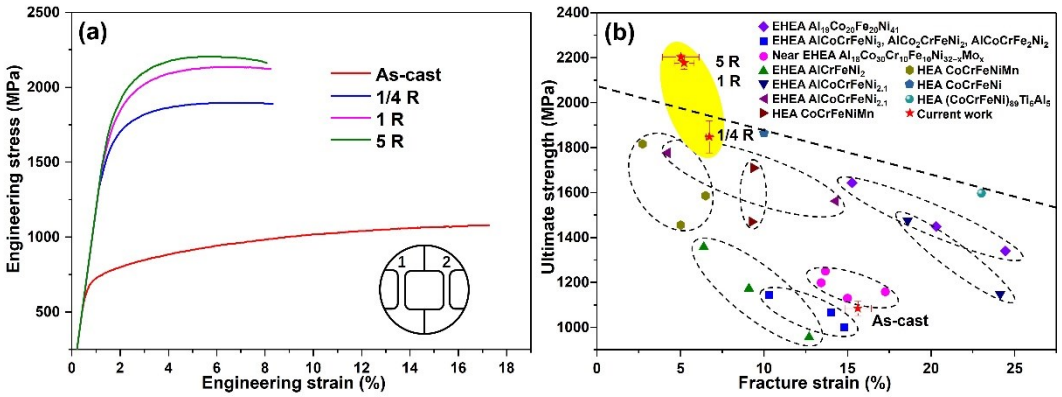

Fig. 8 Tensile performance of the as-cast and HPT-deformed EHEA specimens. (a) Engineering stress-strain curves. The inset shows a schematic of two tensile specimens machined from an HPT disk. (b) Tensile properties of the present results (star symbols) in comparison with previously reported high-strength HEAs and EHEAs [36-45]. Statistics of the fracture strain of [36, 38-43, 45] were estimated from the corresponding engineering stress-strain curves.

4. Discussion

4.1 Microstructural evolution during HPT

The microstructural evolution of the multiphase lamellar microstructure can be subdivided into three stages: compressed stage, low shear-strain stage ($\gamma < 24$), and high shear-strain stage ($\gamma > 24$). The details are discussed below.

4.1.1 Compressed stage

After compression, a large number of defects are introduced to accommodate the plastic deformation. The wavy-slip feature of dislocations within Fcc and B2 phases indicates the cross slip

behavior of screw dislocations, which boosts dislocation mobility. The rearrangement of dislocations forms sub-grain boundaries [46]. The individual phases of the EHEA experience a similar grain refinement process as single-phase HEAs [13][47]. However, the lamellar structure endows a heterogeneous deformation behavior. The fragmentation starts close to the interface as a result of a stress concentration. On the one hand, the strain incompatibility between two phases can introduce back and front stress within the Fcc and B2 phases respectively [28]. On the other hand, the interface serves as a barrier to dislocation movement [48][49]. Stress concentration occurs when dislocations pile up at the interface [50][51].

4.1.2 Low shear-strain stage ($\gamma < 24$)

As shear strain is applied, the hardness increases significantly due to the grain refinement process and the introduction of high-density dislocations. The lamellar morphology changes. Depending on the orientation of lamellae with respect to the shear plane of the HPT process, the resulting morphology can be classified into two types. In remaining lamellar areas where the lamellar in-plane direction is parallel to the shear plane, lamellae are elongated along the shear plane to accommodate the shear strain. The soft Fcc phase undergoes most deformation. The accumulation and rearrangement of dislocations separate the Fcc lamellae into small misorientation zones and finally develop into grain boundaries by absorption of dislocations [30][52][53]. Meanwhile, the severe deformation can induce dislocations in the B2 lamellae, leading to further fragmentation. During this process, mechanically-driven disordering breaks the periodically atomic binding and finally converts the ordered B2 into the Bcc phase. Destruction of the long-range order in intermetallic alloys during SPD was seen in Ni_3Al, Fe_3Al, FeAl and Cu_3Au systems [54-57]. Gliding dislocations carrying an antiphase boundary fault accumulate to form high-density antiphase boundary faults and antiphase boundary tubes, which leads to the disordering [57].

Lamellae that are not parallel to the shear plane are distorted and form fragmentation areas comprising a large number of nanograins. Depending on the deviation angle and plastic flow around, it can be expected that the straining state and straining degree of lamellae could be different, hence a difference in the distortion degree. Stacking faults/deformation twins in nanograins (Fig. 5(g)) indicate the activation of (a/6<112>) Shockley partial dislocations in the Fcc nanograins. To form a stacking fault, the critical shear stress required to move a leading partial should be smaller than the one to move a full dislocation. This is the precondition to forming a deformation twin. Since the cross

slip of dislocations is typically a feature for screw dislocations, the critical external shear stress to move a leading partial dislocation (τ_P) and a lattice screw dislocation (τ_L) can be obtained based on the model of the screw system using the following equations [58]:

$$\tau_P = \frac{1}{\cos(\alpha-30°)}\left[\frac{\sqrt{6}\gamma}{a} + \frac{Ga(4-v)}{8\sqrt{6}\pi(1-v)d}\ln\frac{\sqrt{2}d}{a}\right] \quad , \quad (2)$$

$$\tau_L = \frac{Ga}{2\sqrt{2}\pi(1-v)d\cos\alpha}\ln\frac{\sqrt{2}d}{a} \quad , \quad (3)$$

Moreover, the formation of a twin requires the emission of a second partial dislocation with the same Burgers vector as the first one on a slip plane adjacent to the first stacking fault. During this process, the trailing partial might glide on the stacking fault plane to erase the stacking plane. Hence, the critical twinning stress τ_{twin} should be lower than the one for the gliding of trialing partial τ_{trial} to nucleate a twin. Stresses needed to form the deformation twin and to move the trailing partial can be calculated by [58]:

$$\tau_{twin} = \frac{Ga(4-v)}{8\sqrt{6}\pi(1-v)d\cos(\alpha-30°)}\ln\frac{\sqrt{2}d}{a} \quad , \quad (4)$$

$$\tau_{trial} = \frac{1}{\cos(\alpha+30°)}\left[\frac{\sqrt{6}(8+v)Ga}{48\pi(1-v)d}\ln\frac{\sqrt{2}d}{a} - \frac{\sqrt{6}\gamma}{a}\right] \quad , \quad (5)$$

Here, the lattice parameter *a* is 3.580 Å, which is obtained from the XRD data for the 1 R sample. The measured composition of the Fcc nanograins in the full fragmentation area is $Al_{4.2}Co_{20.5}Cr_{23.1}Fe_{23.7}Ni_{28.5}$ (obtained from TEM EDS data). The stacking fault energy γ, shear modulus *G*, and Poisson's ratio *v* reported for CoCrFeNi (39.5 mJ/m^2, 103.25 GPa, and 0.286) are used for the calculations [59][60]. α is the angle between the dislocation line and external shear stress, and the α value that brings the lowest twinning nucleation stress (τ_c) is considered [58]. In the screw system, τ_c can be calculated by:

$$\tau_c = \frac{\gamma}{a}f(\alpha) \quad , \quad (6)$$

where

$$f(\alpha) = \frac{12\sqrt{2}\cos(\alpha-30°)}{\cos(\alpha)[(8+v)\cos(\alpha-30°)-(4-v)\cos(\alpha+30°)]} \quad , \quad (7)$$

Setting $df(\alpha)/d\alpha = 0$, we obtain the optimum $\alpha = 27.2°$. Putting all parameters into Eqs. (2), (3), (4) and (5), Fig. 9 shows the stresses required for different defects as a function of the grain size. Below a critical grain size d_c of 72 nm, the movement of a leading partial is more favorable than a full dislocation and the gliding of a twining partial requires lower stress than the one for a trial partial. Deformation twinning can be expected, and a high volume fraction of grain boundaries in the

nanograin state provides abundant nucleation sites for partial dislocations [61][62]. Due to the complex stress state and inhomogeneous deformation during HPT, the deformation mechanism might be different in different locations.

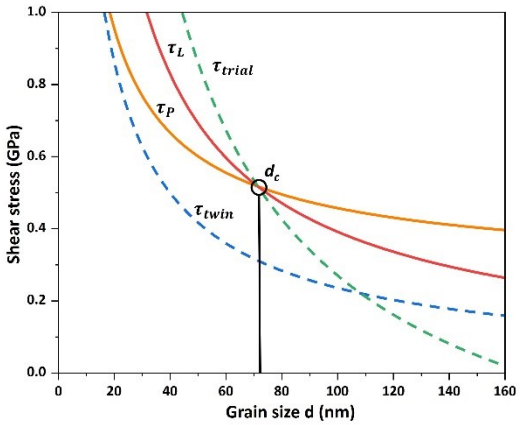

Fig. 9 The evolution of the critical stresses τ_L, τ_P, τ_{twin} and τ_{trial} as a function of grain size d for α = 27.2° in the Fcc phase.

4.1.3 High shear-strain stage (γ > 24)

After a shear strain γ of 24, the microstructural change only leads to the fluctuation of hardness. This reflects a saturation of grain refinement and defect density [29]. During this process, the remaining Bcc lamellae transform into vortex clusters. Pouryazdan et al. [63] discussed the formation of vortex in metallic multilayers under severe plastic deformation and it was found that mechanical instability is the overall mechanism for the microstructural evolution. A protrusion at the interface, either formed during casting or during the shear deformation, can be amplified to a vortex due to velocity perturbations induced by the development of vorticity. The inhomogeneous deformation during HPT causes the variance of straining state from area to area, which might also promote the formation of the vortex with different morphologies.

As can be seen in Fig. 6, a dissolution process is induced during HPT. The Cr-rich particles within the original B2 lamellae disappear in the thinner vortex area. Deformation-induced mixing was found for the SPD process in different materials, such as Cu-Ag, Cu-Zr, and Fe-Cu [64-67] etc. The origin of this phenomenon is still controversially discussed. The grain refinement process is accompanied by a considerable amount of enthalpy stored at the interface and at non-equilibrium grain boundaries, which might promote mechanical alloying [68]. Meanwhile, the shearing and interface roughing caused by transphase plastic deformation on more than one slip system provides material from the surrounding phase for the dissolving event [69]. Moreover, the diffusion-driven dissolution process

could also contribute to this process since the high density of defects in the nanostructure state could accelerate the dissolution [64].

Based on the discussion, the schematic illustrations of the structural evolution of the EHEA during HPT are shown in Fig. 10.

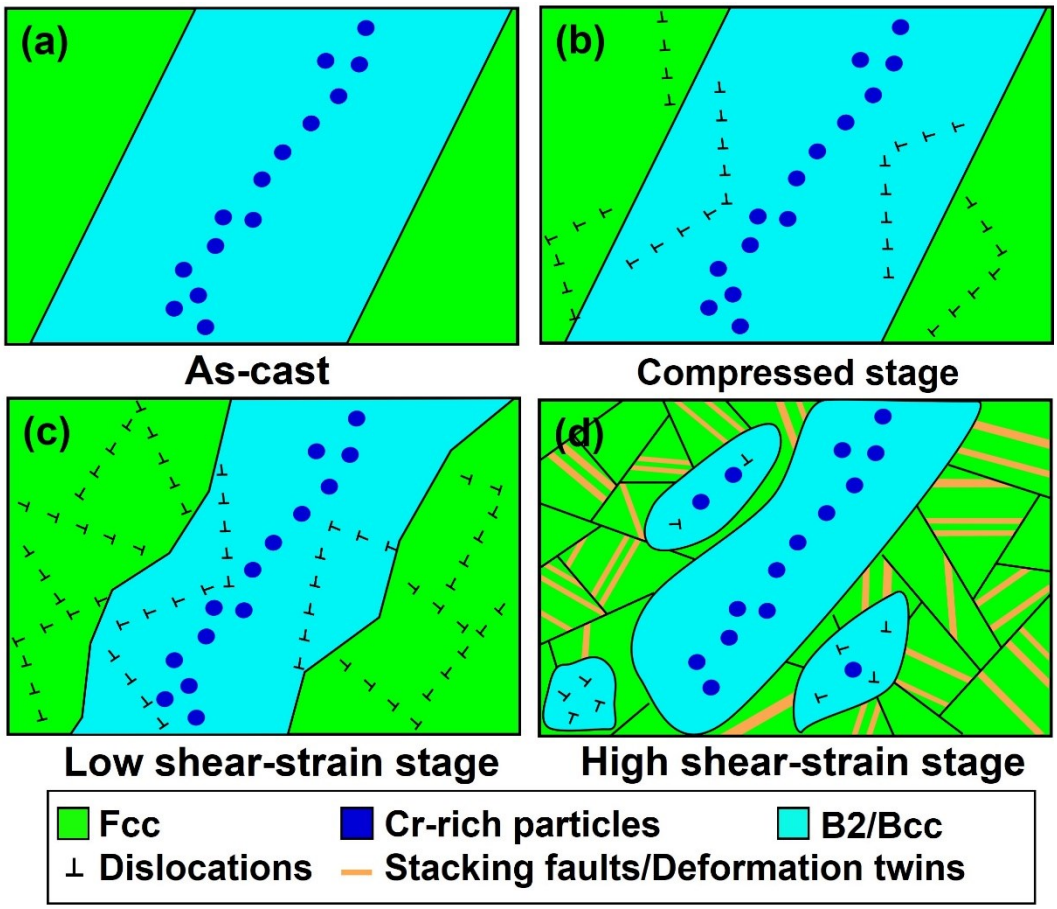

Fig. 10 Schematic illustrations showing the structural evolution of the EHEA from the as-cast alloy to the high shear-strain stage. Compression induces fragmentation close to the interface. With the introduction of the shear strain, defect multiplication and rearrangement cause misorientation development within the lamellar structure, the disordering of the B2 phase, and the dissolution process of the Cr-rich phase. Reduction of the grain size activates stacking faults/deformation twins in Fcc nanograins.

4.2 The origin of the high strength of EHEA after HPT

During HPT process, the dislocation-dominated grain refinement process and high density of dislocations improve the strength based on the Hall-Petch effect [70][71] and Taylor hardening [72]. The strengthening reaches saturation as reflected by a steady state hardness after a shear strain γ of 24. At this state, the softening coming from dynamic recovery [73] or recrystallization [74] reaches a

balance with hardening. Both the yield and ultimate strengths of 5 R are enhanced by a factor of around two compared to the as-cast state. Still, an appreciable ductility remains. For most of the single-phase metals or alloys, the nanocrystalline state achieved by HPT shows fracture or softening just after the yield event [14][75-77]. Instead, introducing the second phase can suppress grain boundary-mediated deformation mechanism in nanograins [29][78], which might restrict the necking behavior after the yielding event of the EHEA. As can be seen in Fig. 11, stacking faults and deformation twins are activated within a Fcc nanograin, and a high density of lattice dislocations exists in a Bcc nanograin. Therefore, it can be concluded that lattice defects still prevail even in nanograins. The nanograined structure restricts dislocation propagation due to the obstacle effect of a high-volume fraction of grain boundaries for Fcc and Bcc grains and additional twining boundaries for Fcc grains. Moreover, the dislocation forests reduce the mean free path of mobile dislocations within the lattice by generating entanglements and jogs. These finally lead to the high strength and certain ductility of the EHEA after HPT. Compared to single-phase HEAs, the structural evolution of multiphase lamellar EHEA during HPT is complex and is affected by the interface, response difference of phases, and phase distribution. HPT on multiphase HEAs provides a route to design high-strength HEAs with a certain ductility.

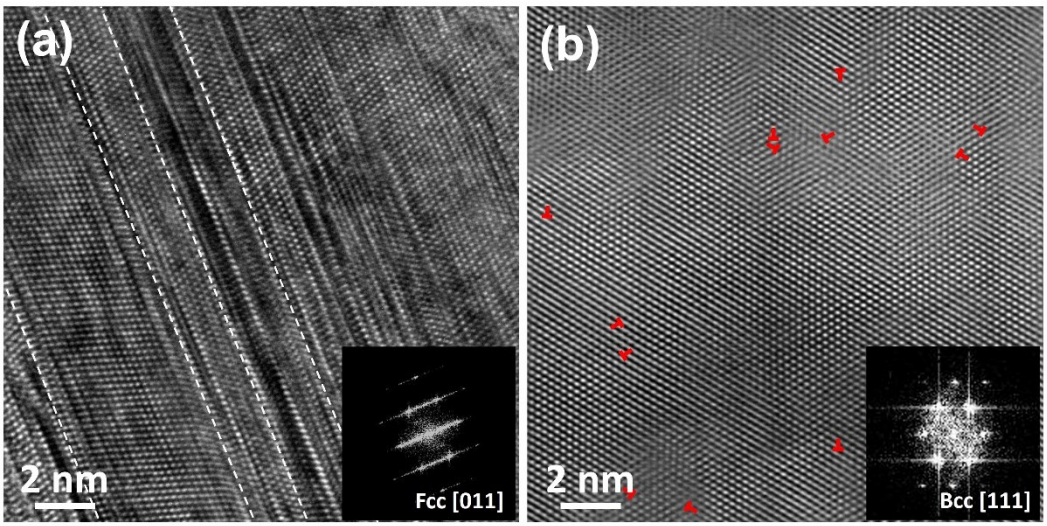

Fig. 11 Defect distribution of 5 R. HRTEM images of a Fcc nanograin (a) and a Bcc nanograin (b) with insets showing the FFTs. White lines in (a) indicate the coherent twining boundaries and red symbols in (b) show edge dislocations.

5. Conclusions

The structural evolution of the lamellar $AlCoCrFeNi_{2.1}$ (at.%) EHEA during HPT was studied.

The following conclusions can be drawn from the current work:

(i) The deformation of the EHEA during HPT can be divided into three stages. Firstly, by just applying high pressure, fragmentation occurs close to the interface as a result of stress concentration. When shear strain γ is applied and is smaller than 24, the morphology of the lamellar structure starts to change and the resulting structure is strongly influenced by the orientation of the in-plane direction of the lamellae with respect to the shear plane. The misorientation development and refinement process are faster in the Fcc phase than in the B2 phase. Defect activity causes disordering of the B2 phase. As a result of defect introduction and grain refinement, the hardness increases from 362 ± 8 HV to 557 ± 12 HV and the yield strength is improved with the loss of ductility.

(ii) When the shear strain γ is larger than 24, the structural refinement and the dislocation density reach the saturation stage. This is reflected by the saturation of hardness. A large number of full fragmentation areas develop and the remaining Bcc lamellae transform into vortex clusters due to the mechanical instability. This is accompanied by the dissolution process of the Cr-rich phase.

(iii) After 5 rotations of HPT deformation, the strength of the EHEA is significantly increased. Surprisingly, a fracture strain of 5% is sustained. Even in areas with nanograins, dislocation-mediated deformation prevails. Additionally, the grain refinement induces stacking faults and deformation twins in the Fcc phase. The high density of grain boundaries, forest dislocations, and twin boundaries restrict dislocation movement and cause ultrahigh strength with appreciable ductility. The current work demonstrates that the structural evolution of the lamellar EHEA during HPT is strongly affected by the interface, phase distribution and plastic flow behavior of phases. Through HPT processing on the EHEA, it is possible to design a refined multiphase structure with excellent strength.

Declaration of competing interest

The authors declare that they have no known competing financial interests or personal relationships that could have appeared to influence the work reported in this paper.

CRediT authorship contribution statement

Zequn Zhang: Conceptualization, Methodology, Investigation, Data curation, Writing - original draft. **Simon Fellner**: Investigation, Writing - review & editing. **Anton Hohenwarter**: Methodology, Investigation, Writing - review & editing. **Oliver Renk**: Methodology, Writing -

review & editing. **Yong Huang**: Investigation, Writing - review & editing. **Zhuo Chen**: Investigation, Writing - review & editing. **Kaikai Song**: Conceptualization, Writing - review & editing. **Caiju Li**: Methodology, Writing - review & editing. **Christoph Gammer**: Supervision, Writing - review & editing. **Jürgen Eckert**: Supervision, Writing - review & editing.

Acknowledgements

The financial support from the Austrian Science Fund (FWF): Y1236-N37 and the National Natural Science Foundation of China (51871132) are gratefully acknowledged. Additional support from the China Scholarship Council (CSC, Grant No. 201906220226) is acknowledged. We thank colleagues J. Keckes (Montanuniversität Leoben) for technical support with XRD investigations, P. Höbenreich (Erich Schmid Institute of Materials Science) for assistance with metallographic sample preparation, H. Felber and G. Felber (Erich Schmid Institute of Materials Science) for TEM sample preparation. Z.L. Zhang (Erich Schmid Institute of Materials Science) for technical support with the TEM investigations.

References

[1] B. Cantor, I.T.H. Chang, P. Knight, A.J.B. Vincent, Microstructural development in equiatomic multicomponent alloys, Mater. Sci. Eng. A. 375–377 (2004) 213–218.

[2] J.W. Yeh, S.K. Chen, S.J. Lin, J.Y. Gan, T.S. Chin, T.T. Shun, C.H. Tsau, S.Y. Chang, Nanostructured high-entropy alloys with multiple principal elements: Novel alloy design concepts and outcomes, Adv. Eng. Mater. 6 (2004) 299–303.

[3] E.P. George, D. Raabe, R.O. Ritchie, High-entropy alloys, Nat. Rev. Mater. 4 (2019) 515–534.

[4] Y.J. Zhao, J.W. Qiao, S.G. Ma, M.C. Gao, H.J. Yang, M.W. Chen, Y. Zhang, A hexagonal close-packed high-entropy alloy: The effect of entropy, Mater. Des. 96 (2016) 10–15.

[5] Y.D. Wu, Y.H. Cai, T. Wang, J.J. Si, J. Zhu, Y.D. Wang, X.D. Hui, A refractory $Hf_{25}Nb_{25}Ti_{25}Zr_{25}$ high-entropy alloy with excellent structural stability and tensile properties, Mater. Lett. 130 (2014) 277–280.

[6] J.M. Wu, S.J. Lin, J.W. Yeh, S.K. Chen, Y.S. Huang, H.C. Chen, Adhesive wear behavior of $Al_xCoCrCuFeNi$ high-entropy alloys as a function of aluminum content, Wear. 261 (2006) 513–519.

[7] B. Gludovatz, A. Hohenwarter, D. Catoor, E.H. Chang, E.P. George, R.O. Ritchie, A fracture-resistant high-entropy alloy for cryogenic applications, Science. 345 (2014) 1153–1158.

[8] A.P. Zhilyaev, T.G. Langdon, Using high-pressure torsion for metal processing: Fundamentals and applications, Prog. Mater. Sci. 53 (2008) 893–979.

[9] T. Müller, M.W. Kapp, A. Bachmaier, P. Felfer, R. Pippan, Ultrahigh-strength low carbon steel obtained from the martensitic state via high pressure torsion, Acta Mater. 166 (2019) 168–177.

[10] O. Renk, A. Hohenwarter, C. Gammer, J. Eckert, R. Pippan, Achieving 1 GPa fatigue strength in nanocrystalline 316L steel through recovery annealing, Scr. Mater. 217 (2022) 114773.

[11] S. Scheriau, M. Kriegisch, S. Kleber, N. Mehboob, R. Grssinger, R. Pippan, Magnetic characteristics of HPT deformed soft-magnetic materials, J. Magn. Magn. Mater. 322 (2010) 2984–2988.

[12] K. Edalati, E. Akiba, Z. Horita, High-pressure torsion for new hydrogen storage materials, Sci. Technol. Adv. Mater. 19 (2018) 185–193.

[13] B. Schuh, F. Mendez-Martin, B. Völker, E.P. George, H. Clemens, R. Pippan, A. Hohenwarter, Mechanical properties, microstructure and thermal stability of a nanocrystalline CoCrFeMnNi high-entropy alloy after severe plastic deformation, Acta Mater. 96 (2015) 258–268.

[14] B. Schuh, B. Völker, J. Todt, N. Schell, L. Perrière, J. Li, J.P. Couzinié, A. Hohenwarter, Thermodynamic instability of a nanocrystalline, single-phase TiZrNbHfTa alloy and its impact on the mechanical properties, Acta Mater. 142 (2018) 201–212.

[15] T. Keil, E. Bruder, M. Laurent-Brocq, K. Durst, From diluted solid solutions to high entropy alloys: Saturation grain size and mechanical properties after high pressure torsion, Scr. Mater. 192 (2021) 43–48.

[16] P.T. Hung, M. Kawasaki, J.K. Han, J.L. Lábár, J. Gubicza, Microstructure evolution in a

nanocrystalline CoCrFeNi multi-principal element alloy during annealing, Mater. Charact. 171 (2021).

[17] G.M. Karthik, P. Asghari-Rad, P. Sathiyamoorthi, A. Zargaran, E.S. Kim, T.S. Kim, H.S. Kim, Architectured multi-metal CoCrFeMnNi-Inconel 718 lamellar composite by high-pressure torsion, Scr. Mater. 195 (2021) 113722.

[18] S. Taheriniya, F.A. Davani, S. Hilke, M. Hepp, C. Gadelmeier, M.R. Chellali, T. Boll, H. Rösner, M. Peterlechner, C. Gammer, S. V. Divinski, B. Butz, U. Glatzel, H. Hahn, G. Wilde, High entropy alloy nanocomposites produced by high pressure torsion, Acta Mater. 208 (2021) 116714.

[19] S. Son, J. Lee, P. Asghari-Rad, R.E. Kim, H. Park, J. il Jang, W. Chen, Y.U. Heo, H.S. Kim, Hierarchically heterogeneous microstructure and mechanical behavior of the multi-materials prepared by powder severe plastic deformation, Mater. Res. Lett. 11 (2023) 915–924.

[20] W. Wu, M. Song, S. Ni, J. Wang, Y. Liu, B. Liu, X. Liao, Dual mechanisms of grain refinement in a FeCoCrNi high entropy alloy processed by high-pressure torsion, Sci. Rep. 7 (2017) 1–13.

[21] A.K. Chandan, K. Kishore, P.T. Hung, M. Ghosh, S.G. Chowdhury, M. Kawasaki, J. Gubicza, Effect of nickel addition on enhancing nano-structuring and suppressing TRIP effect in $Fe_{40}Mn_{40}Co_{10}Cr_{10}$ high entropy alloy during high-pressure torsion, Int. J. Plast. 150 (2022).

[22] K. Kishore, A.K. Chandan, P.T. Hung, S. Kumar, M. Kawasaki, J. Gubicza, On the enhanced hardening ability and plasticity mechanisms in a novel Mn-added CoCrNi medium entropy alloy during high-pressure torsion, J. Alloys Compd. 904 (2022).

[23] P. Edalati, A. Mohammadi, M. Ketabchi, K. Edalati, Ultrahigh hardness in nanostructured dual-phase high-entropy alloy AlCrFeCoNiNb developed by high-pressure torsion, J. Alloys Compd. 884 (2021) 161101.

[24] A. Mazilkin, V. Tavakkoli, O. Davydenko, Y. Beygelzimer, E. Boltynjuk, T. Boll, B. Straumal, B. Baretzky, Y. Estrin, R. Kulagin, Mechanisms of structural evolution of laminates with immiscible components under high-pressure torsion, Acta Mater. 269 (2024) 119804.

[25] X. Gao, Y. Lu, B. Zhang, N. Liang, G. Wu, G. Sha, J. Liu, Y. Zhao, Microstructural origins

of high strength and high ductility in an $AlCoCrFeNi_{2.1}$ eutectic high-entropy alloy, Acta Mater. 141 (2017) 59–66.

[26] L.F. Huang, Y.N. Sun, N. Chen, H.W. Luan, G.M. Le, X. Liu, Y.Q. Ji, Y.P. Lu, P.K. Liaw, X.S. Yang, Y.Z. Zhou, J.F. Li, Simultaneously enhanced strength-ductility of $AlCoCrFeNi_{2.1}$ eutectic high-entropy alloy via additive manufacturing, Mater. Sci. Eng. A. 830 (2022) 142327.

[27] P.J. Shi, R.G. Li, Y. Li, Y.B. Wen, Y.B. Zhong, W.L. Ren, Z. Shen, T.X. Zheng, J.C. Peng, X. Liang, P.F. Hu, N. Min, Y. Zhang, Y. Ren, P.K. Liaw, D. Raabe, Y.D. Wang, Hierarchical crack buffering triples ductility in eutectic herringbone high-entropy alloys, Science. 373 (2021) 912–918.

[28] P. Sathiyamoorthi, H.S. Kim, High-entropy alloys with heterogeneous microstructure: Processing and mechanical properties, Prog. Mater. Sci. 123 (2022) 100709.

[29] R. Pippan, S. Scheriau, A. Taylor, M. Hafok, A. Hohenwarter, A. Bachmaier, Saturation of fragmentation during severe plastic deformation, Annu. Rev. Mater. Res. 40 (2010) 319–343.

[30] R.Z. Valiev, R.K. Islamgaliev, I. V. Alexandrov, Bulk nanostructured materials from severe plastic deformation, 45 (2000) 103-189.

[31] B. Beausir, J.J. Fundenberger, Analysis tools for electron and X-ray diffraction, ATEX-software, Univ. Lorraine-Metz. 2017 (2017).

[32] T. Xiong, W. Yang, S. Zheng, Z. Liu, Y. Lu, R. Zhang, Y. Zhou, X. Shao, B. Zhang, J. Wang, F. Yin, P.K. Liaw, X. Ma, Faceted Kurdjumov-Sachs interface-induced slip continuity in the eutectic high-entropy alloy, $AlCoCrFeNi_{2.1}$, J. Mater. Sci. Technol. 65 (2021) 216–227.

[33] R.J. Vikram, B.S. Murty, D. Fabijanic, S. Suwas, Insights into micro-mechanical response and texture of the additively manufactured eutectic high entropy alloy $AlCoCrFeNi_{2.1}$, J. Alloys Compd. 827 (2020) 154034.

[34] X. Li, C. Jin, H. Li, X. Hao, K. Hua, X. Deng, H. Wang, Z. Wang, A combinatorial assessment of microstructure and mechanical properties in $AlCrCuFeNi_2V_x$ concentrated alloys, J. Alloys Compd. 906 (2022) 164304.

[35] G. Deng, X. Zhao, L. Su, P. Wei, L. Zhang, L. Zhan, Y. Chong, H. Zhu, N. Tsuji, Effect of high pressure torsion process on the microhardness, microstructure and tribological property

of Ti6Al4V alloy, J. Mater. Sci. Technol. 94 (2021) 183–195.

[36] P.J. Shi, W.L. Ren, T.X. Zheng, Z.M. Ren, X.L. Hou, J.C. Peng, P.F. Hu, Y.F. Gao, Y.B. Zhong, P.K. Liaw, Enhanced strength–ductility synergy in ultrafine-grained eutectic high-entropy alloys by inheriting microstructural lamellae, Nat. Commun. 10 (2019) 1–8.

[37] X. Jin, Y. Zhou, L. Zhang, X.Y. Du, B.S. Li, A new pseudo binary strategy to design eutectic high entropy alloys using mixing enthalpy and valence electron concentration, Mater. Des. 143 (2018) 49–55.

[38] Z.S. Yang, Z.J. Wang, Q.F. Wu, T. Zheng, P.R. Zhao, J.K. Zhao, J.Y. Chen, Enhancing the mechanical properties of casting eutectic high entropy alloys with Mo addition, Appl. Phys. A Mater. Sci. Process. 125 (2019) 1–6.

[39] X. Jin, J. Bi, L. Zhang, Y. Zhou, X.Y. Du, Y.X. Liang, B.S. Li, A new $CrFeNi_2Al$ eutectic high entropy alloy system with excellent mechanical properties, J. Alloys Compd. 770 (2019) 655–661.

[40] T. Xiong, S.J. Zheng, J.Y. Pang, X.L. Ma, High-strength and high-ductility $AlCoCrFeNi_{2.1}$ eutectic high-entropy alloy achieved via precipitation strengthening in a heterogeneous structure, Scr. Mater. 186 (2020) 336–340.

[41] T. Bhattacharjee, I.S. Wani, S. Sheikh, I.T. Clark, T. Okawa, S. Guo, P.P. Bhattacharjee, N. Tsuji, Simultaneous strength-ductility enhancement of a nano-lamellar $AlCoCrFeNi_{2.1}$ eutectic high entropy alloy by cryo-rolling and annealing, Sci. Rep. 8 (2018) 1–8.

[42] Y.J. Kwon, J.W. Won, S.H. Park, J.H. Lee, K.R. Lim, Y.S. Na, C.S. Lee, Ultrahigh-strength CoCrFeMnNi high-entropy alloy wire rod with excellent resistance to hydrogen embrittlement, Mater. Sci. Eng. A. 732 (2018) 105–111.

[43] Y. Xie, T. Xia, D. Zhou, Y. Luo, W. Zeng, Z. Zhang, J. Wang, J. Liang, D. Zhang, A novel nanostructure to achieve ultrahigh strength and good tensile ductility of a CoCrFeNiMn high entropy alloy, Nanoscale. 12 (2020) 5347–5352.

[44] L. Zeng, L. Zeng, R. Gao, C. You, B. Liu, Achieving ultra-high strength in a face-centered-cubic FeCrCoNi high entropy alloy through dense nanotwins bundles structure prepared by cryo-rolling, Intermetallics. 148 (2022) 107638.

[45] Y. Qi, Y. Wu, T. Cao, L. He, F. Jiang, J. sun, $L2_1$-strengthened face-centered cubic high-entropy alloy with high strength and ductility, Mater. Sci. Eng. A. 797 (2020) 140056.

[46] B. Cantor, G.A. Chadwick, The tensile deformation of unidirectionally solidified Al-Al_3Ni and Al-Al_2Cu eutectics, J. Mater. Sci. 10 (1975) 578–588.

[47] P.F. Yu, H. Cheng, L.J. Zhang, H. Zhang, Q. Jing, M.Z. Ma, P.K. Liaw, G. Li, R.P. Liu, Effects of high pressure torsion on microstructures and properties of an $Al_{0.1}CoCrFeNi$ high-entropy alloy, Mater. Sci. Eng. A. 655 (2016) 283–291.

[48] R. Guo, P. Zhang, J. Pan, J. Xu, L. Liu, C. Zhang, L. Liu, Achieving prominent high-temperature mechanical properties in a dual-phase high-entropy alloy : A synergy of deformation-induced twinning and martensite transformation, Acta Mater. 264 (2024) 119591.

[49] Q. Li, L. Tian, X. Li, X. Deng, H. Wang, Sensitivity of reduction rate on the mechanical response of boron-doped $Fe_{50}Mn_{30}Co_{10}Cr_{10}$ high entropy alloy, J. Alloys Compd. 985 (2024) 174030.

[50] D. Hull, J.D. Bacon, Introduction to Dislocations, Elsevier Oxford, 2011.

[51] X. Liu, Z. Kou, R. Qu, W. Song, Y. Gu, C. Zhou, Q. Gao, J. Zhang, C. Cao, K. Song, V. Zadorozhnyy, Z. Zhang, J. Eckert, Accelerating matrix/boundary precipitations to explore high-strength and high-ductile $Co_{34}Cr_{32}Ni_{27}Al_{3.5}Ti_{3.5}$ multicomponent alloys through hot extrusion and annealing, J. Mater. Sci. Technol. 143 (2022) 62–83.

[52] Y. Ito, Z. Horita, Microstructural evolution in pure aluminum processed by high-pressure torsion, Mater. Sci. Eng. A. 503 (2009) 32–36.

[53] K. Wang, N.R. Tao, G. Liu, J. Lu, K. Lu, Plastic strain-induced grain refinement at the nanometer scale in copper, Acta Mater. 54 (2006) 5281–5291.

[54] C. Mangler, C. Gammer, H.P. Karnthaler, C. Rentenberger, Structural modifications during heating of bulk nanocrystalline FeAl produced by high-pressure torsion, Acta Mater. 58 (2010) 5631–5638.

[55] C. Gammer, C. Mangler, H.P. Karnthaler, C. Rentenberger, Anomalous re-ordering of Fe_3Al disordered by high pressure torsion deformation, Scr. Mater. 156 (2018) 90–94.

[56] C. Rentenberger, C. Mangler, S. Scheriau, R. Pippan, H.P. Karnthaler, TEM study of local disordering: A structural phase change induced by high-pressure torsion, Mater. Sci. Forum. 584-586 PA (2008) 422–427.

[57] C. Rentenberger, H.P. Karnthaler, Extensive disordering in long-range-ordered Cu_3Au

induced by severe plastic deformation studied by transmission electron microscopy, Acta Mater. 56 (2008) 2526–2530.

[58] Y.T. Zhu, X.Z. Liao, S.G. Srinivasan, E.J. Lavernia, Nucleation of deformation twins in nanocrystalline face-centered-cubic metals processed by severe plastic deformation, J. Appl. Phys. 98 (2005) 034319.

[59] M. Beyramali Kivy, M. Asle Zaeem, Generalized stacking fault energies, ductilities, and twinnabilities of CoCrFeNi-based face-centered cubic high entropy alloys, Scr. Mater. 139 (2017) 83–86.

[60] D. Wei, X. Li, S. Schönecker, J. Jiang, W.M. Choi, B.J. Lee, H.S. Kim, A. Chiba, H. Kato, Development of strong and ductile metastable face-centered cubic single-phase high-entropy alloys, Acta Mater. 181 (2019) 318–330.

[61] Z.W. Shan, L. Lu, A.M. Minor, E.A. Stach, S.X. Mao, The effect of twin plane spacing on the deformation of copper containing a high density of growth twins, Jom. 60 (2008) 71–74.

[62] L.H. Wang, P.F. Guan, J. Teng, P. Liu, D.K. Chen, W.Y. Xie, D.L. Kong, S.B. Zhang, T. Zhu, Z. Zhang, E. Ma, M.W. Chen, X.D. Han, New twinning route in face-centered cubic nanocrystalline metals, Nat. Commun. 8 (2017) 2142.

[63] M. Pouryazdan, B.J.P. Kaus, A. Rack, A. Ershov, H. Hahn, Mixing instabilities during shearing of metals, Nat. Commun. 8 (2017) 1611.

[64] Y. Ivanisenko, W. Lojkowski, R.Z. Valiev, H.J. Fecht, The mechanism of formation of nanostructure and dissolution of cementite in a pearlitic steel during high pressure torsion, Acta Mater. 51 (2003) 5555–5570.

[65] C. Suryanarayana, Mechanical alloying and milling, Prog. Mater. Sci. 46 (2001) 1–184.

[66] S. Ohsaki, S. Kato, N. Tsuji, T. Ohkubo, K. Hono, Bulk mechanical alloying of Cu – Ag and Cu / Zr two-phase microstructures by accumulative roll-bonding process, Acta Mater. 55 (2007) 2885–2895.

[67] A. Bachmaier, M. Kerber, D. Setman, R. Pippan, The formation of supersaturated solid solutions in Fe-Cu alloys deformed by high-pressure torsion, Acta Mater. 60 (2012) 860–871.

[68] G. Veltl, B. Scholz, H.D. Kunze, Amorphization of CuTa alloys by mechanical alloying, Mater. Sci. Eng. A. 134 (1991) 1410–1413.

[69] D. Raabe, S. Ohsaki, K. Hono, Mechanical alloying and amorphization in Cu-Nb-Ag in situ composite wires studied by transmission electron microscopy and atom probe tomography, Acta Mater. 57 (2009) 5254–5263.

[70] E.O. Hall, The deformation and ageing of mild steel: III Discussion of results, Proc. Phys. Soc. Sect. B. 64 (1951) 747–753.

[71] N.J. Petch, The cleavage strength of polycrystals, J. Iron Steel Inst. 174 (1953) 25–28.

[72] L.M. Brown, Constant intermittent flow of dislocations: Central problems in plasticity, Mater. Sci. Technol. (United Kingdom). 28 (2012) 1209–1232.

[73] O. Renk, A. Hohenwarter, S. Wurster, R. Pippan, Direct evidence for grain boundary motion as the dominant restoration mechanism in the steady-state regime of extremely cold-rolled copper, Acta Mater. 77 (2014) 401–410.

[74] K. Edalati, T. Fujioka, Z. Horita, Evolution of mechanical properties and microstructures with equivalent strain in Pure Fe processed by High Pressure Torsion, Mater. Trans. 50 (2009) 44–50.

[75] H. Shahmir, M. Nili-Ahmadabadi, A. Shafiee, M. Andrzejczuk, M. Lewandowska, T.G. Langdon, Effect of Ti on phase stability and strengthening mechanisms of a nanocrystalline CoCrFeMnNi high-entropy alloy, Mater. Sci. Eng. A. 725 (2018) 196–206.

[76] H. Shahmir, J. He, Z. Lu, M. Kawasaki, T.G. Langdon, Effect of annealing on mechanical properties of a nanocrystalline CoCrFeNiMn high-entropy alloy processed by high-pressure torsion, Mater. Sci. Eng. A. 676 (2016) 294–303.

[77] S. Praveen, J.W. Bae, P. Asghari-Rad, J.M. Park, H.S. Kim, Ultra-high tensile strength nanocrystalline CoCrNi equi-atomic medium entropy alloy processed by high-pressure torsion, Mater. Sci. Eng. A. 735 (2018) 394–397.

[78] Y. Li, D. Raabe, M. Herbig, P.P. Choi, S. Goto, A. Kostka, H. Yarita, C. Borchers, R. Kirchheim, Segregation stabilizes nanocrystalline bulk steel with near theoretical strength, Phys. Rev. Lett. 113 (2014) 1–5.

Supplementary materials

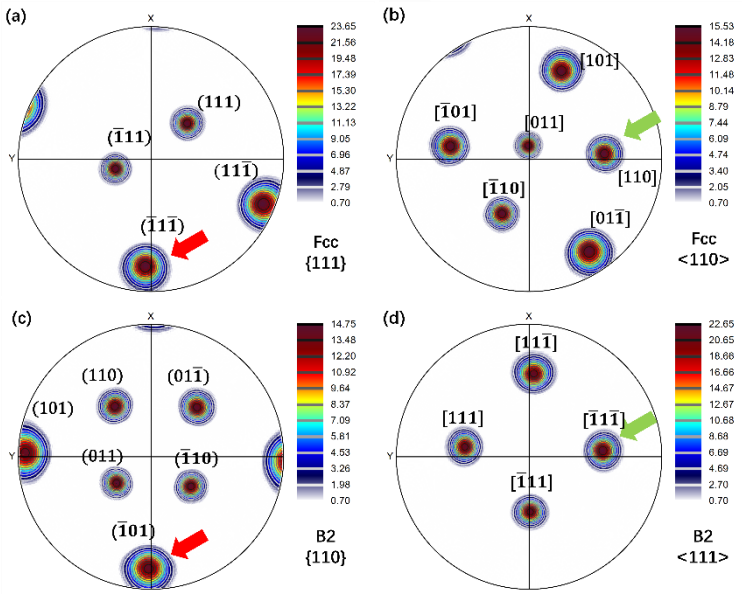

Fig. S1 (a, b) The {111} and <110> pole figures of Fcc lamellae and (c, d) the {110} and <111> pole figures of B2 lamellae under the same stage coordinate system. As indicated by the red arrows in (a, c) and green arrows in (b, d), $(\bar{1}1\bar{1})$ Fcc is parallel to $(\bar{1}01)$ B2 and [110] Fcc is parallel to $[\bar{1}1\bar{1}]$ B2.

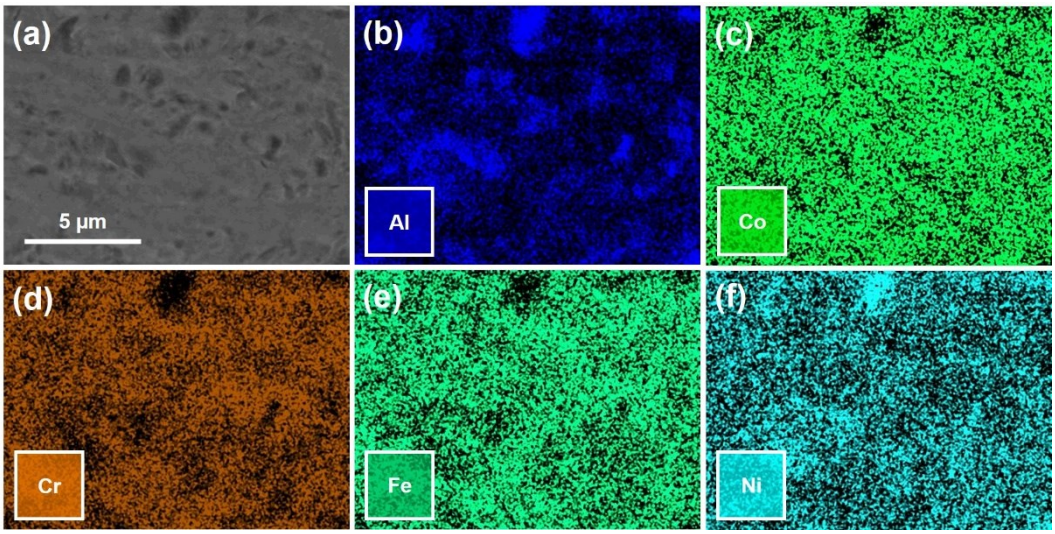

Fig. S2 (a) SEM image of 5 R with a shear strain $\gamma \sim 95$ and individual element distribution of (b) Al, (c) Co, (d) Cr, (e) Fe, and (f) Ni.

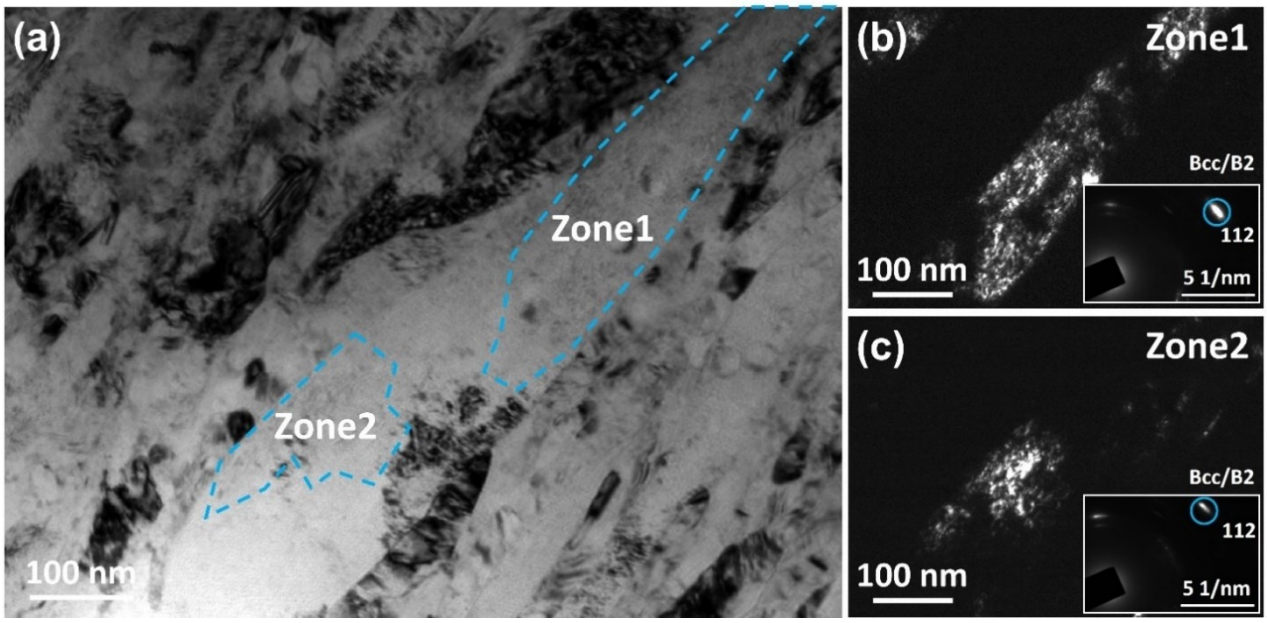

Fig. S3 (a) BF-TEM image of a remaining lamellar area of 1 R with a shear strain γ of ~ 16. (b, c) the DF-TEM images (using the 112 diffraction arcs of Bcc/B2 phase from the SAED patterns) of Zone 1 (b) and Zone 2 (c) in the remaining lamellar area marked in (a). The SAED patterns of Zone 1 and Zone 2 (inset in (b) and (c) respectively) show a misorientation of ~ 8° between two zones and a misorientation of ~3° within two zones.

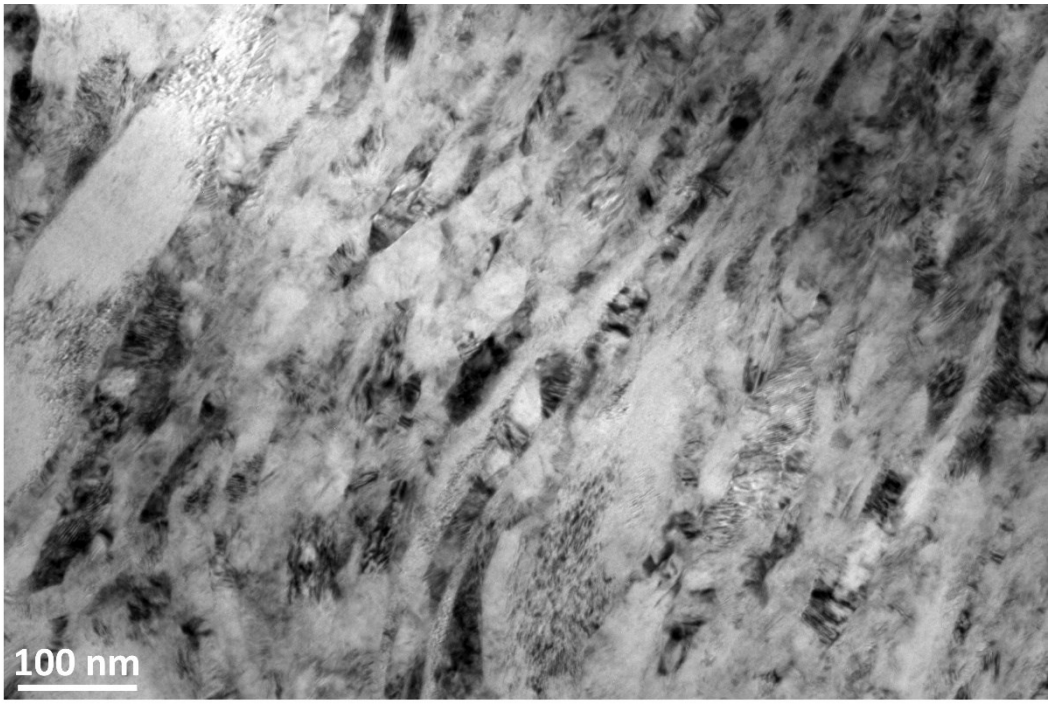

Fig. S4 BF-TEM image of 5 R with a shear strain γ ~ 95.

Manuscript IV

Equiaxed microstructure design enables strength-ductility synergy in the eutectic high-entropy alloy

Zequn Zhang [a,b,*], Yong Huang [a,b], Qi Xu [a,b], Simon Fellner [a,b], Anton Hohenwarter [a], Stefan Wurster [b], Kaikai Song [c], Christoph Gammer [b,*], Jürgen Eckert [a,b]

[a] Department of Materials Science, Montanuniversität Leoben, Jahnstraße 12, 8700 Leoben, Austria.

[b] Erich Schmid Institute of Materials Science, Austrian Academy of Sciences, Jahnstraße 12, 8700 Leoben, Austria.

[c] School of Mechanical, Electrical & Information Engineering, Shandong University, Wenhua Xilu 180, 264209 Weihai, China.

[*] Corresponding authors:

zequn.zhang@stud.unileoben.ac.at; christoph.gammer@oeaw.ac.at

Abstract

Eutectic high-entropy alloys (EHEAs) represent attractive candidate materials for overcoming the strength-ductility trade-off, which can be enhanced through the directional alignment of the lamellar structure along the loading direction. Here, we put forward a new route to optimize the strength-ductility synergy without orientation dependence. Through a combination of severe plastic deformation and annealing, we convert the initially lamellar structure into a dual-phase structure comprised of ultrafine equiaxed grains. The significant grain refinement improves the yield strength from 703 MPa to 1199 MPa without sacrificing any ductility. During deformation, the localized softening resistance of the achieved dual-phase microstructure avoids necking, and the intrinsic microcrack-arresting mechanism effectively improves the fracture resistance. Grain boundaries and phase boundaries provide nucleation sites for dislocations and restrict dislocation transfer while the strain incompatibility is accommodated by geometrically necessary dislocations. This work demonstrates that dual-phase alloys comprised of ultrafine equiaxed grains provide a pathway for strengthening without loss of ductility.

Keywords: High-entropy alloy; Structure design; Strength; Plastic deformation; Texture

1. Introduction

The design of materials with high strength and ductility is a central focus of engineering materials and has therefore attracted large scientific interest [1–5]. The typical carriers of plastic flow (dislocations) can be effectively blocked by, for example, precipitates, grain boundaries and lattice defects, resulting in a higher stress to maintain deformation. However, the high stress required to activate or transfer the plastic deformation in the high strength regime typically cause crack nucleation and growth, which finally leads to catastrophic failure and limited ductility.

The key strategy for retaining ductility while increasing strength is to enhance the strain-hardening ability to enable an increase in flow stress and delay plastic instability. Recently, high-entropy alloys (HEAs) that contain more than four principal elements in equal or near-equal atomic ratio, have opened up a new field exploring the central part of multicomponent alloy phase diagrams for use as high-performance alloys [6,7]. Among those, eutectic HEAs (EHEAs) with a regular lamellar dual-phase structure have great potential to break the strength-ductility trade-off. According to the theory of non-uniform plastic deformations from Ashby [8], the different responses of the soft and hard phases to deformation cause geometrically necessary dislocations (GNDs) at the interface to accommodate strain gradients and to maintain the deformation compatibility between the two phases. The back-stress exerted by the GNDs interferes with the defects and enhances the yield strength and the strain-hardening capacity [9,10]. Based on the concept of heterostructures in EHEAs, different design strategies are adopted, such as composition optimization [11] and alloying effects [12]. Moreover, it has been shown that the microstructure adjustment of EHEAs can further enhance their integrated tensile properties. Through the directional solidification, Shi et al. [13] found that the tensile elongation of $Al_{19}Fe_{20}Co_{20}Ni_{41}$ can be improved from 16% to 50% without sacrificing strength, which was attributed to the combined effects of aligned eutectic colonies and branched eutectic colonies, and the effective regime of buffering and blunting cracks. Similarly, an $AlCoCrFeNi_{2.1}$ EHEA produced by additive manufacturing shows a refined crystal structure with grains growing along the heat flow direction. A large number of phase boundaries work as a barrier for dislocation propagation and hence lead to an improved strength [14]. By tuning the morphology of lamellar arrangement via thermo-mechanical processing, mechanical properties can also be optimized [15,16]. Although the microstructure adjustment using these approaches enhances strength and ductility

simultaneously, it comes along with a pronounced mechanical anisotropy and hence limits their use in potential engineering applications [17,18].

Here, we report a route to enhance the strength-ductility synergy in EHEAs with a homogeneous microstructure design. Different from the traditional strategies, the original lamellar structure is converted into an equiaxed dual-phase structure (EDPS) to activate more sites for the defect nucleation. The mechanical properties of the eutectic structure are substantially enhanced by tailoring the microstructure at an ultrafine grain scale with softening resistance and crack growth resistance regimes.

2. Materials and Methods

2.1 Sample preparation

The EHEA ingot with a nominal composition of $AlCoCrFeNi_{2.1}$ (at.%) was prepared by vacuum arc melting of a nominal mixture of the constituent elements (purity ≥ 99.95%) and was remelted at least five times in a Ti-gettered high-purity Ar atmosphere to ensure chemical homogeneity. The molten alloy was suction-cast into a 10 mm (width) × 100 mm (length) × 2 mm (thickness) water-cooled Cu mold. This was followed by homogenization in a vacuum furnace (Xerion Xtube) at 1023 ± 5 K for 12 h. The chamber was evacuated to $< 5 \times 10^{-5}$ Pa before annealing.

For the high-pressure torsion (HPT) process, disks with a diameter of 8 mm and an initial thickness of 2 mm were machined from the as-cast plates using electric discharge machining, followed by grinding with P280 (FEPA, The Federation of European Producers of Abrasives) abrasive papers to a reduction of the thickness to 1.9 mm. The disks were deformed by HPT at a nominal pressure of 6 GPa and a rotational speed of 0.6 rotations/min for 5 rotations at room temperature. The HPT-processed disks were annealed at 1173 K for 10 min in atmosphere followed by water quenching.

2.2 Tensile test, bending test and microstructure characterization

Dog-bone shaped tensile specimens (gauge length of 2.5 mm, width and thickness of 600 μm) were machined from as-cast plates and EDPS disks in the region 2 mm away from the center of the HPT disk by electric discharge machining. Before testing, the sample surface was ground with P320 (FEPA) abrasive papers. Tensile tests were conducted at room temperature using a Kammrath and Weiss testing machine (tensile module) with a crosshead speed of 1×10^{-3} s^{-1}. The tensile strain was

directly measured on the sample surface by evaluating optical micrographs continuously taken throughout the tensile test. Images were taken using a stereomicroscope (Olympus SZx 16) equipped with a Canon EOS 600D camera at a frequency of 3 Hz. Intrinsic roughness and surface features perfectly served as reference points for calculating the displacements and recording strains. The starting point for image acquisition and the movement of the crosshead were synchronized to unambiguously link a particular image to a specific load point. The images were subsequently analyzed with the open software package GOM (Correlate 2016) to calculate the tensile strains. To obtain reproducible tensile properties, all tensile tests were repeated at least three times. For one EDPS specimen, digital image correlation (DIC) was used to measure the displacement on the tensile sample and generate local strain maps during deformation. Additional EDPS samples were polished with conventional aluminum oxide polishing suspension (OPS) and unloaded at different stages during tensile testing to analyze the deformation behavior. Beams (length of 7 mm, width and thickness of 600 μm) for three-point bending tests were machined from both as-cast plate and EDPS alloys. Bending tests were conducted at room temperature with a support span of 4.62 mm using a bending module from Kammrath and Weiss with a displacement control of 2.5 μm s^{-1}. The deflection of the beam center was measured with an extensometer (DD1, Hottinger Baldwin Messtechnik GmbH). Bending tests under each condition were repeated at least two times.

The phase constitution of as-cast and EDPS samples was analyzed by X-ray diffraction (XRD) with Co-Kα radiation using a Bruker D2 phaser diffractometer. Microstructural characterization and deformation analysis were carried out with a scanning electron microscope (SEM, LEO1525, Zeiss) equipped with a back-scattered electron (BSE) detector. The elemental composition, phase distribution, and crystallographic orientation relationship were determined from SEM (Tescan Magna) equipped with energy-dispersive X-ray spectroscopy (EDS, XFlash 6-60, Bruker) and electron backscatter diffraction (EBSD, eFlash^{FS}, Bruker) detectors. For SEM observation and EBSD analysis the samples were ground mechanically using silicon carbide abrasive papers and then mechano-chemically polished with OPS followed by vibrational polishing within OPS for 2 h. To evaluate the actual composition after annealing, EDS map scans were conducted in three areas of an annealed specimen. The composition is shown in Table S1, which correlates well with the nominal composition. A higher deviation of the Al concentration is probably caused by the higher vapor pressure resulting in a slightly larger loss during vacuum arc melting. The phase maps, orientation relationship, and

grain boundary statistics were analyzed using the ATEX [19] software with a pixel size of 25*25 nm^2. For the internal misorientation detection, the grain reference orientation deviation (GROD) maps were constructed by considering the deviation angle of pixels from the pixel with the best quality pattern within a grain, and the max misorientation of 5° was used to differentiate with the high-angle grain boundary. The aspect ratio smaller than 2.5 was used for the definition of equiaxed grains [20]. Further in-depth microstructure investigation was conducted using transmission electron microscopy (TEM), allowing to identification of the defect distribution. Samples for TEM analysis were taken from the as-cast and EDPS tensile specimens after deformation. They were first ground to 100 μm with a multiprep machine (Allied High Tech). Subsequently, the multiprep arm was set to wedging, upon which samples were further ground until a wedge was formed. In the end, they were ion polished with Ar^+ ions using a precision ion polishing system (GATAN-PIPS). TEM images and diffraction patterns were obtained using JEOL JEM-2200FS, operated at 200 kV. High-resolution (HR) TEM imaging was carried out using a JEOL JEM-2100F equipped with an imaging aberration corrector, operated at 200 kV.

2.3 Modeling

Molecular dynamics (MD) simulations were implemented by the Large-scale Atomic/Molecular Massively Parallel Simulator [21]. The embedded atom method potential developed by Farkas et al. was employed to describe the atomic interactions within the AlCoCrFeNi system [22]. Firstly, the $Al_{0.5}$CoCrFeNi HEA with a well-defined face-centered cubic (Fcc) structure was constructed with a simulation box $10a_0 \times 49a_0 \times 104a_0$ nm^3 containing 815360 atoms, where a_0 is the lattice constant equal to 0.35 nm. The atoms were randomly distributed in the Fcc lattice and periodic boundary conditions (PBCs) were applied in all three directions. The $Al_{0.5}$CoCrFeNi HEA sample with the high-angle Σ5(210) symmetrical tilt grain boundary (GB) was constructed with a simulation box $14a_0 \times 84a_0 \times 168a_0$ nm^3 containing 792792 atoms. The GB was built by joining two perfect crystals along (210) plane followed by static energy minimization. Then, the ordered body-centered cubic (B2) structure was represented by the AlNi alloy as the most composition contribution is from Al and Ni atoms (Table S2). The B2 sample was constructed with a simulation box $12a_0 \times 35a_0 \times 180a_0$ nm^3 containing 296640 atoms, where a_0 is the lattice constant equal to 0.29 nm. For the as-cast configuration, the crystallographic orientations of Fcc phase and B2 phase are x (-1 1 0), y (1 1 1), z

(1 1 -2) and x (-1 1 0), y (1 1 0), z (0 0 -1) to simulate the Kurdjumov-Sachs crystallographic orientation relationship (KS OR). Finally, the two different HEA configurations were constructed by embedding the B2 plate into the center of the Fcc and GB plates, respectively. The PBCs were applied in all three directions for all the samples.

To investigate the deformation behavior, these two HEA configurations were deformed at a constant engineering strain rate of 4×10^7 /s at room temperature along the z direction. The temperature of the systems was controlled at room temperature within an isothermal-isobaric ensemble, so that thermal effects can be eliminated. Prior to deformation, the samples were relaxed at zero pressure for 1 ns to reach an equilibrium state. The visualization software (OVITO) was used to perform the post-processing via common neighbor analysis and atomic strain to analyze the atomic-scale deformation mechanisms [23–26]. Shear strain is obtained by affine mapping of the simulation cell with "To reference" mapping option.

3. Results

3.1 Microstructure characterization

In the as-cast state, the $AlCoCrFeNi_{2.1}$ EHEA contains Fcc and B2 phases (Fig. 1(a)). The lamellar structure follows the KS OR at the interface (Figs. 1(b, c)). The colony size is ~ 7.5 μm with Fcc lamellae generally showing larger thickness than B2 ones (Fig. S1(a)). After HPT and annealing, the lamellar structure is converted into ultrafine equiaxed B2 and Fcc grains, yielding a EDPS (Figs. 1(d, e) and Fig. S1(b)). During HPT, grain refinement is caused by introducing and arranging a high density of defects. The nanocrystalline state after HPT provides fast diffusion kinetics for recrystallization and crystal growth during annealing [27]. The phase boundary characteristic deviates from the original KS OR with the generation of more than 85% high-angle grain boundaries. Moreover, ∑3 boundaries are seen in the Fcc phase for the EDPS alloy due to the formation of annealing twins (Fig. S2). The morphology and element analysis (Figs. 1(f-k) and Table S2) suggest that the Fcc phase is rich in Co, Cr and Fe, and the B2 phase is rich in Al and Ni.

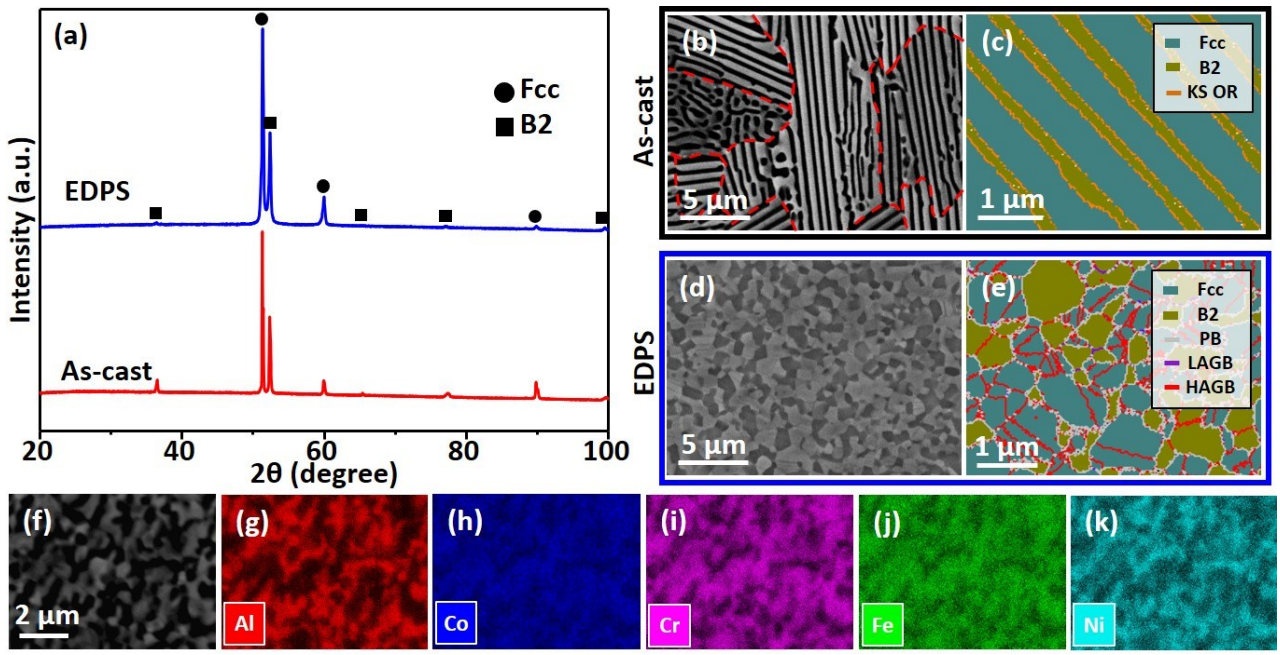

Fig. 1. Structural characterizations of the as-cast and EDPS alloys. (a) XRD patterns. (b) SEM-BSE image and (c) EBSD phase map of the as-cast specimen. (d) SEM-BSE image of the EDPS alloy. The Fcc phase is grey and the B2 phase is black. (e) EBSD phase map of the EDPS alloy. Misorientation angles of 5° and 15° were used to define the type of grain boundary. PB represents the phase boundary, LAGB represents the low-angle grain boundary and HAGB represents the high-angle grain boundary. (f) SEM image of the EDPS alloy and corresponding EDS element distribution maps of Al (g), Co (h), Cr (i), Fe (j) and Ni (k).

3.2 Mechanical testing

The structure transformation induced by HPT and annealing enhances the strength of the EDPS alloy significantly. Fig. 2(a) displays the engineering tensile stress-strain curves of as-cast and EDPS alloys measured at room temperature. Both specimens show similar ductility but remarkable strength differences. The yield stress $\sigma_{0.2}$ (0.2% offset) is improved from only 703 ± 24 MPa for the as-cast specimen to 1199 ± 35 MPa for the EDPS alloy, and the ultimate tensile strength (σ_{UTS}) is enhanced by 230 MPa. In contrast to the continuous work-hardening behavior of the as-cast alloy, the plastic deformation of the EDPS alloy can be separated into three stages. After the yield-drop event, the stress gradually rises to a plateau of ~1260 MPa. The last stage shows continuous work hardening until fracture.

The strain analysis for the EDPS sample (inset in Fig. 2(a)) reveals inhomogeneous plastic

deformation. The deformation initiates from one end of the specimen and gradually propagates toward the other end, suggesting Lüders-type deformation. The maximum local deformation inside the Lüders band reaches 11.7% when the global deformation is 5.1%. In the last stage, the Lüders band spreads across the whole sample with a work hardening behavior. The yield point phenomenon and Lüders band propagation are strongly affected by the grain size [28]. The inhomogeneous deformation by Lüders band propagation occurs as a consequence of sufficiently fine and defect scarce grains. Strain hardening induced by lattice dislocation storage and strain softening reach a balance and cause the spread of Lüders band [29]. Below a critical size, early necking restricts the propagation of the Lüders band due to the wide absence of dislocation storage for the hardening. This behavior can be found in pure aluminum with a grain size of 1 μm-4 μm and pure copper with a grain size of 0.5 μm-3 μm [30][31]. However, in the current case, the introduction of the second phase and high-volume ratio of boundaries restricts the softening of EDPS alloy with an average grain size of 0.29 μm.

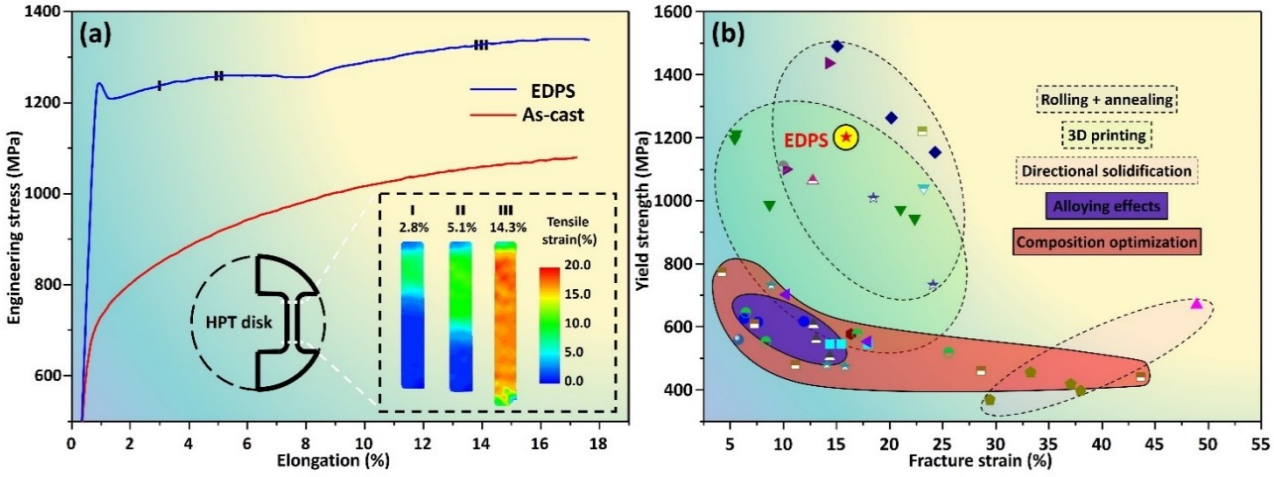

Fig. 2 Mechanical performance of the as-cast and EDPS alloys. (a) Engineering stress-strain curves of the as-cast and EDPS specimens; the inset shows the configuration of the tensile specimen machined from a disk specimen and the DIC strain maps for different elongation (marked with I, II and III in the deformation curve). (b) Tensile properties of the EDPS alloy in comparison with eutectic and near-eutectic HEAs processed with different methods [11-15, 32-45]. Data points within the area marked with dotted lines represent specimens with a directional microstructure. Fracture strains for [11–15, 33–43, 45] were evaluated from the corresponding engineering stress-strain curves.

Table 1 Room-temperature tensile mechanical properties of the as-cast and EDPS alloys

Samples	$\sigma_{0.2}$ (MPa)	σ_{UTS} (MPa)	Elongation to failure ε_f (%)
As-cast	703 ± 24	1083 ± 32	16.3 ± 0.8
EDPS	1199 ± 35	1313 ± 34	16.8 ± 1.7

3.3 Micro-morphology during deformation

For the as-cast alloy after fracture, cracks form along phase boundaries with an angle of ~45° to the tensile direction (Fig. 3(a)), which is accompanied with numerous parallel slip traces within the lamellar Fcc phase (Fig. 3(b)). Microcracks are also found occasionally along the boundary of eutectic colonies (Fig. 3(c)). The collective deformation within each colony causes a relatively flat surface after fracture. The fracture surface (Fig. 3(d)) shows that the soft Fcc phase is stretched, gradually becoming thinner, finally necking and forming parallel sharp lines. In contrast to that, a large number of microcracks nucleate at the phase boundaries of the hard B2 phase and propagate to the opposite phase boundary. Therefore, the failure of the as-cast alloy is mainly caused by the decohesion of the lamellar phase boundaries with specific orientations and the crack penetration through the lamella. For the EDPS alloy, after a smaller amount of straining (Fig. 3(e)), a smaller number of slip traces along a single active system within Fcc grains is observed in the Lüders band area and the orientation varies from one crystal to another. Further deformation causes an increase in density of slip traces (Fig. 3(f)). The movement of defects results in the formation of step features in Fcc grains and hence an uneven surface. Slip traces deflect once entering an annealing twin and a microcrack forms along the grain boundary of two grains. After deformation reaches the work-hardening stage, the density of the slip trace increases remarkably (Fig. 3(g)). Some grains contain slip traces on two non-parallel slip planes. Fig. 3(h) and Fig. 3(i) show that microcracks broaden with both transgranular and intergranular fracture modes for B2 grains. However, the surrounding Fcc crystals can effectively hinder further propagation of cracks. The fracture surface of the EDPS alloy (Fig. 3(j)) also exhibits a different morphology compared to the as-cast alloy. The micro-ductile fracture surface consists of dimples in the size range of a micrometer and larger which surround a B2 particle, respectively. Both two typical processes for void initiation, either by phase de-cohesion or the local failure of a second phase particle, are observed on the fractography. On the surface of some B2 particles a substructure with river patterns is clearly visible, which is a feature of the cleavage fracture of the body-centered

cubic structure failing in the lower shelf of the ductile to brittle transition [46]. Therefore this is a local transgranular fracture with primary cracks in the B2 phase. On the other hand, polyhedral structures with no specific substructures on the surface are observed for some B2 grains. In such cases the void is initiated by a de-cohesion process. The growth and coalescence of the void finally cause the micro-ductile fracture [47]. These behaviors correspond well with the features observed in the unloaded sample shown in Figs. 3(i). Hence, through structure transformation, the micro-crack expansion route transforms from phase boundaries in the as-cast alloy to grain boundaries of B2 grains and to the B2 interior for the EDPS alloy. The interconnection of cracks causes the final failure.

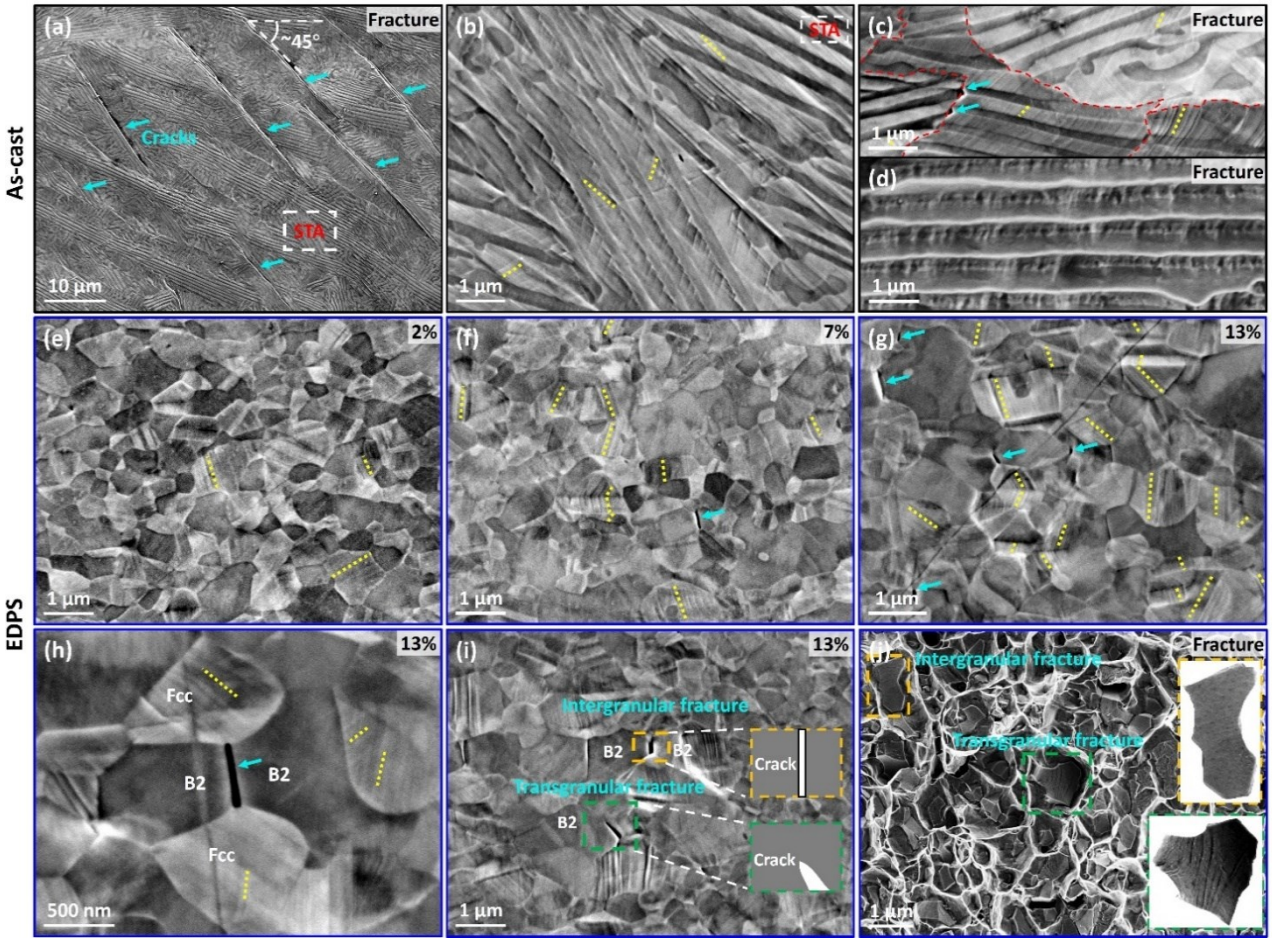

Fig. 3 Fracture mechanisms of the as-cast (a-d) and EDPS (e-j) alloys. (a) SEM images of the as-cast specimen after fracture and (b) slip trace area (STA) marked in (a). (c) Different directions of slip traces in eutectic colonies and the formation of microcracks on the colony boundary. (d) Fracture surface of the as-cast alloy, showing crack expansion from the phase boundary. (e-g) EDPS specimens unloaded after straining to ~2% (e), ~7% (f), and ~13% (g). (h) Restriction of crack growth by Fcc grains. (i) The formation of microcracks with both intergranular and transgranular modes. (j) Fracture surface of the EDPS alloy. The insets showing details of fracture morphologies of the B2 phase, both

the river patterns caused by the local failure of a B2 phase particle and the polyhedral structure with no specific substructure induced by the de-cohesion process of the B2 phase can be seen. The tensile direction is horizontal in all images except those showing fracture morphologies. Blue arrows show cracks and the yellow dotted lines show slip traces.

For both structures, slip traces are parallel to {111} planes (Fig. 4) due to dislocation gliding on the close-packed plane of the Fcc phase. The misorientation at the interface of the lamellar one shows only a slight change with some step features (Fig. 4(c)), which suggests that a small strain gradient is generated at the interface during deformation. In contrast, dislocation gliding at the EDPS causes significant misorientation change within grains (Fig. 4(d-f)). It should be noted that the diffraction pattern quality degrades as a result of increasing presence of dislocations and strain gradients within the specimen beam interaction volume, leading to signal loss near the triple junction and the interface for the EDPS.

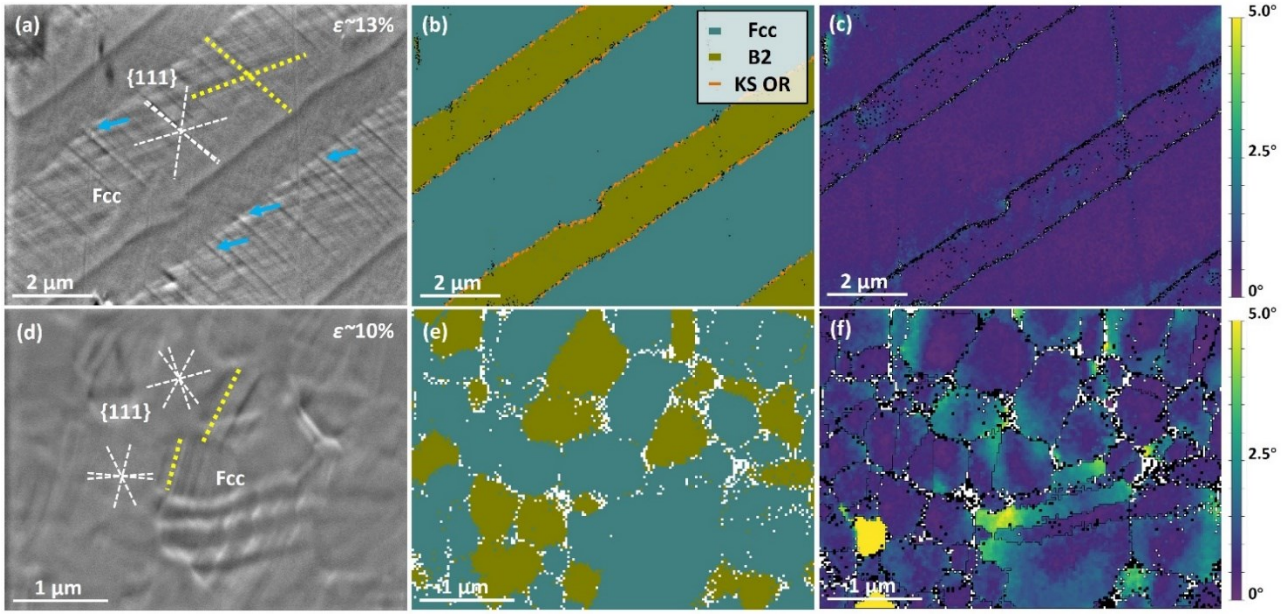

Fig. 4 Microstructure and misorientation of the as-cast and EDPS alloy. The local morphology of a tensile specimen unloaded at a local strain of ~13% for the as-cast (a) and ~10% for the EDPS alloy (d). Yellow dotted lines indicate the slip traces and white dotted lines represent calculated slip traces representing {111} planes of the Fcc phase according to the EBSD information. Blue arrows indicate step features at the interface. (b, e) Corresponding phase maps and (c, f) GROD maps of (a, d). The tensile direction is horizontal to the SEM image.

3.4 Analysis of the microstructure and crystallographic orientation

The EDPS sample exhibits an enhanced strength-ductility synergy compared with most EHEAs and near-eutectic HEAs (Fig. 2(b)). To improve the mechanical performance, in some EHEAs directional microstructure is introduced during preparation or post processing, such as directional solidification, additive manufacturing and a combination of cold rolling and annealing, etc. For EDPS, a dual-phase structure composed of equiaxed grains is sustained throughout the gauge part. The texture distribution of an EDPS tensile sample was evaluated to analyze the orientation of equiaxed grains. Due to the shear strain during the HPT process [48], the {111} pole figures in the middle position of the tensile specimen (Fig. 5(a)) show a weak shear texture (maximum intensity: 3.89). With the position changing from the middle of the gauge to the right part, the center axis of the shear texture rotates along the tangential direction of the HPT process to the left (Figs. 5(a-c)). As a result of weak texture and multiple slip systems [49], the distribution of the Schmid factor for full and partial dislocations for the Fcc system ({111}<110> and {111}<112> respectively) along the tensile direction is homogeneous for different positions (Figs. 5(d, e)). Similar results are also observed from the transverse direction (Fig. S3). Here the Schmid factor for the Fcc system is calculated following the consideration: 1. The Fcc phase undertakes the majority of plastic deformation and 2. Obvious dislocation activity is on close-packed planes for the Fcc system. The result indicates that the mechanical properties are enhanced through EDPS design compared to the lamellar structure, without introducing specific structure and crystallographic orientation along the tensile direction. To reveal that the enhanced mechanical properties are realized without dependence on loading direction, three-point bending tests were performed in both the as-cast state and for EDPS alloys along different directions (Fig. S4). In comparison to the as-cast alloy, the EDPS alloy shows higher flexural stress with the same deflection for different testing directions. Flexural stress tested along the normal direction is only slightly higher (< 9%) than the one tested along the transverse direction for the EDPS alloy, which is caused by the slight elongation feature of grains along elongation direction. This could introduce difference of phase and grain boundary density and affect the emission and blocking effects of boundaries to dislocations. It is expected that isotropic mechanical properties can be realized once the grain has spherical morphology.

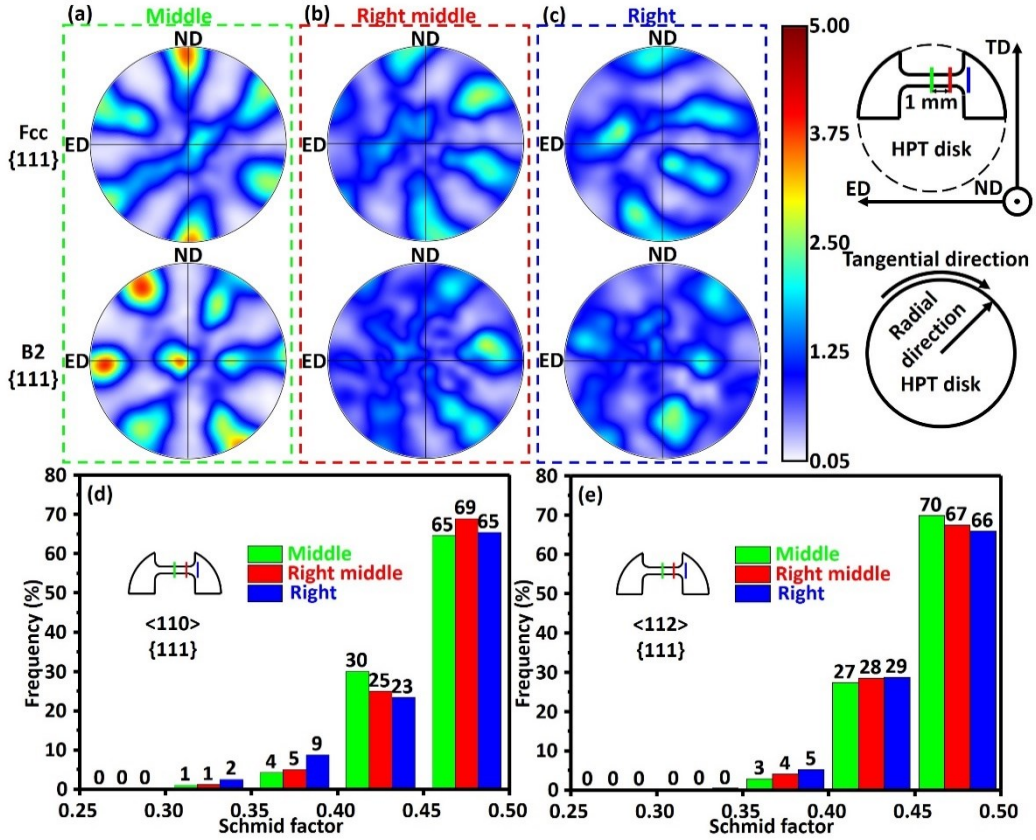

Fig. 5 Initial texture distribution along the elongation direction of the EDPS alloy observed from the normal direction. The {111} pole figures of the Fcc and B2 phases from (a) middle, (b) middle right, and (c) right position of a tensile specimen. The schematic diagrams on the right part show positions for EBSD scanning and definitions of the specimen coordinate (top) and the HPT coordinate (bottom); TD, ND, and ED represent Transverse Direction, Normal Direction, and Elongation Direction, respectively. More than 400 grains were counted for each map. Schmid factor distribution for (d) full and (e) partial dislocations for the Fcc system along the elongation direction from the middle, right middle, and right part of an EDPS tensile sample. The distance between the testing positions is 1 mm.

3.5 Nanostructure characterization

TEM characterizations provide more detail of the deformation mechanism for both the as-cast and the EDPS specimens (Fig. 6). For the as-cast alloy the propagation of a partial dislocation with Burgers vector 1/6 $[\bar{1}21]$ on a $(\bar{1}\bar{1}1)$ plane results in the formation of a stacking fault inside a Fcc lamella (Fig. 6(a)). In the Fcc phase with low stacking fault energy, the formation of Shockley partials can be caused by dissociation of perfect dislocations [49] or by emission from grain boundaries [50].

A large number of partial dislocations glide on {111} planes of the Fcc phase and dislocation entanglement occurs within the B2 phase (Figs. 6(b, c)). The interaction of partial dislocations from two close-packed systems causes the generation of a sessile dislocation [51][52], which impedes the movement of dislocations. The barrier effect of the phase boundary on the dislocation propagation and the interaction between defects within the lamellar Fcc and B2 phases causes continuous work-hardening behavior. In the EDPS alloy, dislocation activity is accompanied by grain misorientation development (Fig. 6(d)), which matches the EBSD result. Through gliding of partial dislocations (Fig. 6(e)), the Fcc phase undertakes the majority of deformation, while the dislocation entanglement and misorientation occur within the B2 phase (Fig. 6(f)).

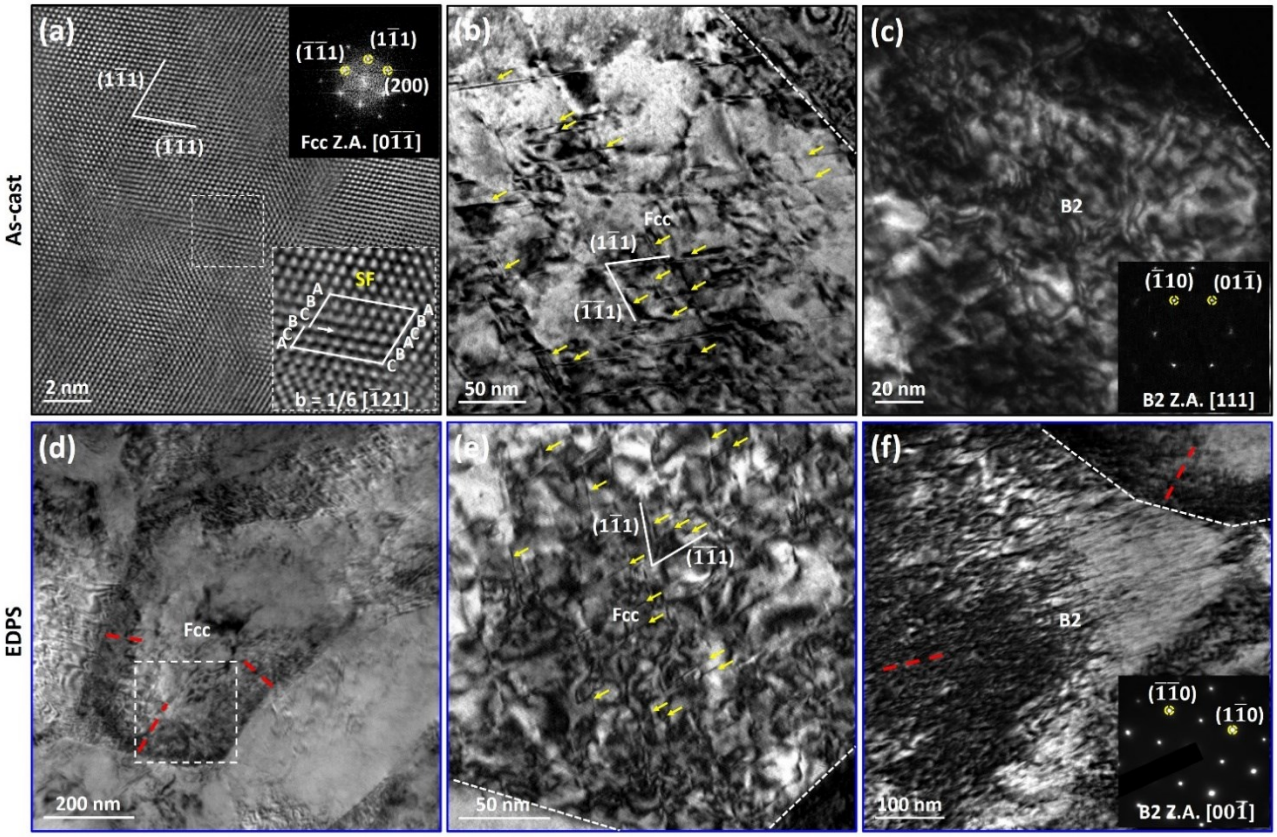

Fig. 6 Deformation mechanisms of as-cast and EDPS alloys. (a) HRTEM image of the as-cast alloy after fracture. Insets are the enlarged image of the marked area and the fast Fourier transformation image of the Fcc phase. SF represents the stacking fault. (b) Bight-field (BF) TEM image of the lamellar Fcc phase. (c) Dark-field (DF) TEM image of a B2 lamella. The inset is the selected area electron diffraction (SAED) pattern of the B2 phase. (d) BF TEM image of EDPS alloy after fracture. (e) BF TEM image of the area marked in (d). (f) BF TEM image of a B2 grain. The inset is the SAED pattern of the B2 phase. Stacking faults are marked by yellow arrows. Red dotted lines

indicate the misorientation development.

3.6 Structural simulation

The deformation mechanism agrees well with the results from MD simulations (Fig. 7). Gliding of a partial dislocation changes the stacking sequence of {111} planes, leading to the stacking fault in the Fcc lamella (Fig. 7(a)). For the EDPS alloy, partial dislocations are emitted from both grain and phase boundaries on different slip systems, and the HAGB blocks the dislocation transmission (Fig. 7(b)). The shear strain map of as-cast one shows that the strain is localized inside the stacking fault area with different strain levels and occasionally at the interface (Fig. 7(c)). The gliding of the second partial turns the stacking sequence back to Fcc one, leaving a high strain area (marked by the arrow in Fig. 7(e) and "A" label in Fig. 7(f). As a comparison, "B" in Fig. 7(f) indicates finishing of gliding of the second partial). In contrast, both grain boundaries and phase boundaries provide multiple dislocation nucleation sites in the EDPS alloy, contributing to a homogenous strain in the deformed area (Fig. 7(d)).

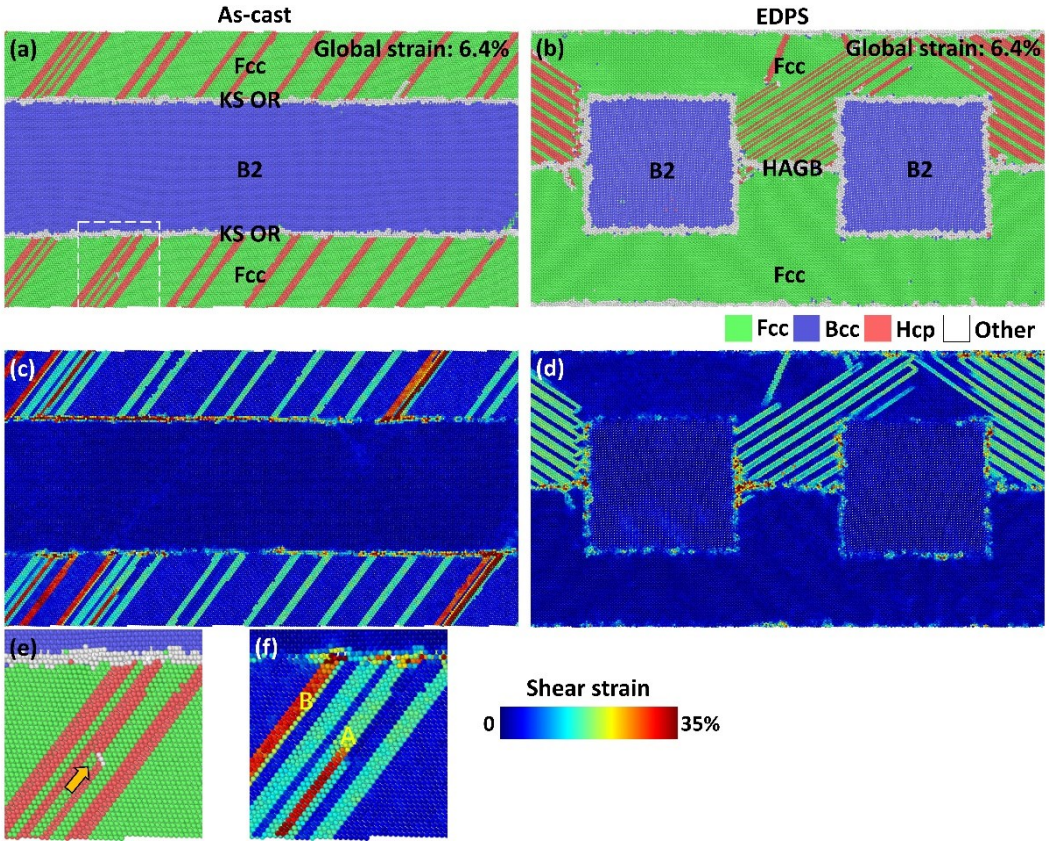

Fig. 7 Molecular dynamics simulation of the defect distribution. The structure of the (a) as-cast and (b) EDPS alloys for an identical global strain of 6.4%. The change of the stacking structure from

ABCABC… to ABABAB… type due to partial dislocation gliding is marked by the change of the color of atoms from green to red. (c, d) The corresponding shear strain distribution of (a, b). (e) The enlarged image of the area marked in (a) and the corresponding shear strain map (f), showing that the gliding of the second partial causes the disappearance of the stacking fault but with a higher shear stain. The initial dimensions of the two simulation boxes are $5\times30\times60$ nm^3.

4. Discussion

4.1 Origin of the high yield strength of the EDPS

Compared to the as-cast alloy, the EDPS shows an enhancement of yield strength of about 500 MPa through microstructure adjustment and the strength-ductility synergy is comparable to EHEAs with directional structure. To understand the high yield strength $\sigma_{0.2}$ of EDPS alloy, the contribution from several strengthening mechanisms is evaluated: frictional stress of the lattice (σ_f), grain refined strengthening (σ_g), solid solution strengthening (σ_s), and dislocation strengthening (σ_d). For recrystallized microstructures, the dislocation density is low and its contribution is ignored. The total contribution from the Fcc and B2 phases is calculated by the rule of mixture:

$$\sigma_{0.2}=f_{Fcc}[\sigma_f+\sigma_g+\sigma_s]_{Fcc}+f_{B2}[\sigma_f+\sigma_g]_{B2} \quad , \quad (1)$$

where f_{Fcc} and f_{B2} are the volume fraction of two phases and are 63% for the Fcc phase, and 37% for the B2 phase (from EBSD data). The frictional stress σ_f of Fcc and B2 phases are referred from the nearest reported composition: $Al_{0.3}$CoCrFeNi and AlNi alloys [53][54]. The σ_f of the Fcc phase was taken as 95 MPa and that of B2 as 120 MPa. In the current case, both grain and phase boundaries act as pinning points impeding dislocation propagation. The grain refinement strengthening is evaluated based on the Hall-Petch equation:

$$\sigma_g=K_y d^{-1/2} \quad , \quad (2)$$

where K_y is the Hall-Petch constant and d is the average grain size. The average grain size is 0.27 μm for the Fcc phase and 0.29 μm for the B2 phase (from EBSD data). K_y was taken as 823 and 155 MPa μm$^{1/2}$ for Fcc and B2 phases, respectively [53][54]. The grain size strengthening contribution was calculated as 1584 MPa for the Fcc phase and 288 MPa for the B2 phase. The solid solution strengthening comes from the impeding effect of the stress field of the solute atoms on dislocation movement in the Fcc phase. Since the high content of Ni compared with other components (from EDS data), Ni is regarded as the solvent and other elements work as solutes. The model of Gypen and

Deruyttere [55] for multi-component solid solution was considered:

$$\sigma_s = \left(\sum_i \left(k_i \cdot \sqrt{C_i}\right)^{1/n}\right)^n \quad , \quad (3)$$

where C_i is the atomic percentage of the solute. n is a constant and is taken as 1/2 to be consistent with the dependence on concentration in the Feltham equation [56][57][58]. k_i is the strengthening constants for element i and its value for Al, Co, Cr and Fe in Ni is taken as 225, 39, 337 and 153 MPa/(at.%)$^{1/2}$, respectively [58]. Including the composition of the Fcc phase into the equation, results in a contribution from solid solution strengthening of 181 MPa. Inputting all the strengthening values into equation (1), the total contribution is 1323 MPa. The calculated yield strength is slightly higher (9.4 %) than the real one, which can be attributed to the parameter difference between the referred systems and the real system and simplification of the phase boundary as the grain boundary. In general, the significant strengthening of the EDPS alloy mainly comes from the microstructural design of dual-phase equiaxed grains at an ultrafine grain scale, which enhances the Hall-Petch strengthening significantly.

4.2 Misorientation development during deformation

For the as-cast alloy, the continuous work-hardening process is typically attributed to the back-stress hardening. The strain gradient generated at the interface promotes the generation of GNDs, which blocks dislocations gliding and contributes to higher flow stress [9]. However, from the current results, the plastic deformation process only triggers limited misorientation changes at the interface with the interface relationship of some areas remaining (Fig. 4(a-c)). The step-like feature at the interface suggests the penetration of dislocations across the interface, which decreases the strain gradient. Hence, only limited GNDs are generated. Through molecular dynamics simulation, Wang et al. [59] found that the glide dislocation at the interface with KS OR can be trapped, and the consequent nucleation and glide of interfacial dislocation loops can trigger interface sliding. This correlates well with the simulation result (Fig. 7(c)) and might explain the loss of KS OR locally. For the EDPS alloy, deformation causes misorientation development within grains. As can be seen in Fig. 8, the misorientation angle increases from grain boundaries, phase boundaries and triple junctions to the interior of Fcc and B2 grain with the increase of strain and it shows the preferred direction within each grain. The introduction of grain boundaries and the break of KS OR at the interface effectively restricts the slip transmission [60]. The dislocation activity is confined within grains. The expression

of the strain-hardening rate as a function of the true strain is a typical way to show the stages of work hardening. Due to the plastic instability, the relationship cannot be visualized. However, the contribution to the strain hardening is expected from several aspects: 1. Grain boundaries and phase boundaries provide multiple nucleation sites to defects and hence the source for dislocation interaction. 2. To accommodate lattice curvatures, regions with non-zero net Burgers vectors are formed close to the interface. The long-range stress field increases the shear stress for statistically stored dislocations (SSDs) to move during the beginning of plastic deformation [8], which might provide strain hardening against rapid necking. 3. The short-range interaction of SSDs with GNDs confines the mean free path of gliding dislocations within the grain [61]. This strengthening increases with deformation as the misorientation gradually develops into the grain interior.

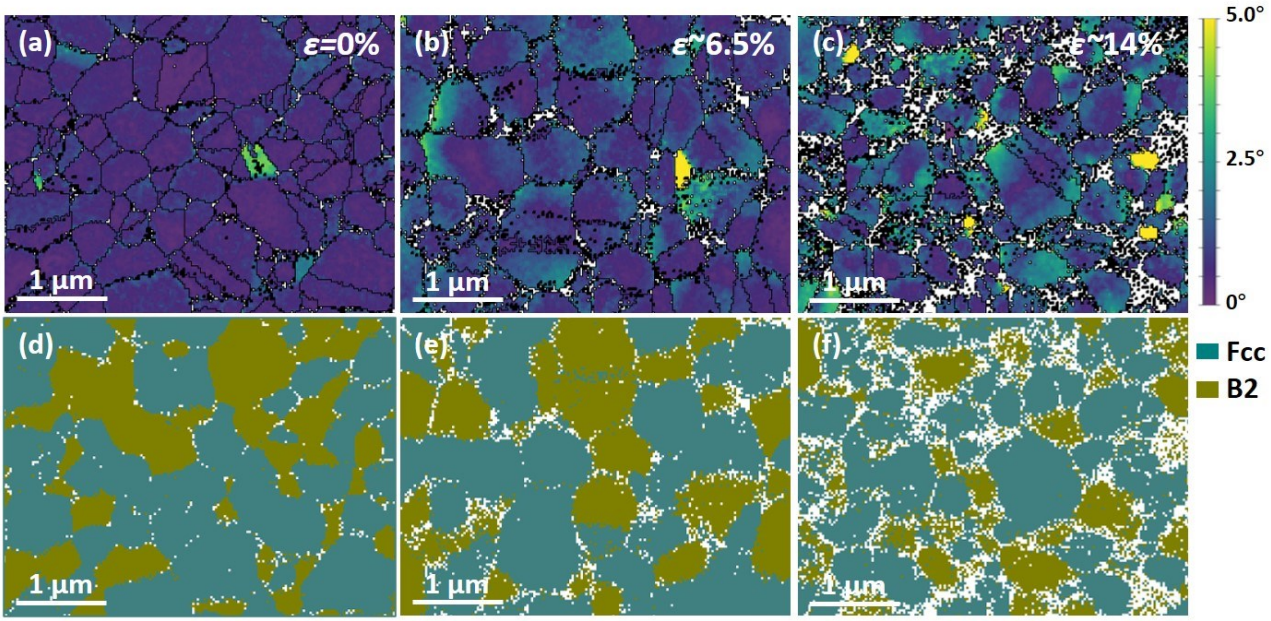

Fig. 8 Misorientation evolution of the EDPS alloy. GROD maps of a tensile specimen before tensile testing (a) and specimens unloaded at a local strain ε of ~6.5% (b) and ~14% (c), and the corresponding phase maps (d-f). The tensile direction is horizontal to all GROD maps.

4.3 Deformation process of EDPS

From these results, we can explain the deformation of EDPS alloy (Fig. 2(a)). During elastic deformation, grain boundary strengthening improves the yield strength significantly. This strengthening effect lasts up to the upper-yield point, where both phases start to yield. The release of mobile dislocations within grains in the elastic region close to the band front results in a decrease in stress required to maintain the applied strain rate and consequently leads to the observed yield drop

[62]. Dislocation rapidly multiplies within grains inside the Lüders band and extends with the increasing strain to occupy the entire gauge part. During Lüders-type deformation, plastic flow is mainly realized through dislocation gliding within Fcc crystals. Phase boundaries and grain boundaries provide multiple sites for defect generation. The plastic strain incompatibility under the high flow stress is accommodated by the generation of GNDs in both two phases, causing misorientation within grains. Due to the difference in crystallographic orientation and the local stress, the dislocation activity and misorientation development vary from one crystal to another. The plastic instability effectively spreads in the dual-phase structure. Stress concentration around the B2 phase on the one hand causes dislocation movement in the B2 phase. On the other hand, it triggers the formation of cracks along the grain boundary between B2 grains and towards their grain interior. However, the crack propagation is arrested by the surrounding Fcc grains, resulting in the formation of multiple microcracks with different orientations. The dislocation interaction and block effect of phase boundaries and grain boundaries to dislocation propagation finally contributes to the work-hardening in the third stage. The schematic diagram of the deformation process is shown in Fig. 9.

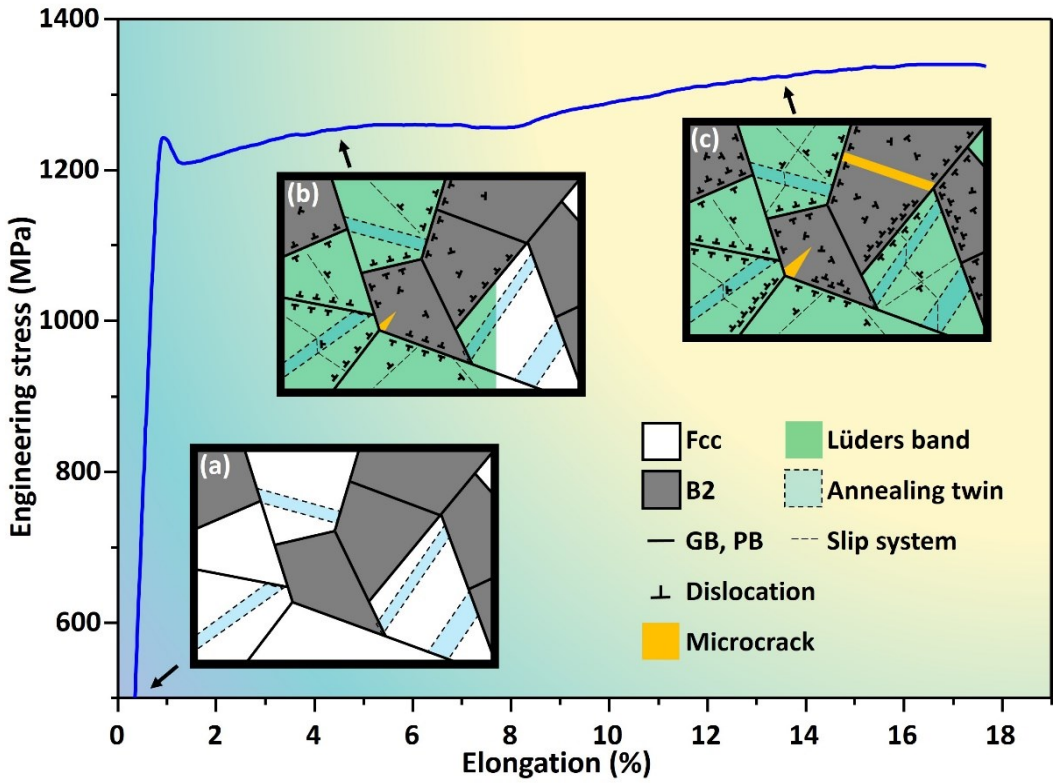

Fig. 9. Schematic of the deformation process of the EDPS. (a) Schematic representation of the morphology of two phases before deformation. (b) Defect distribution during the propagation of Lüders band. The Fcc phase undertakes the majority of deformation by dislocation gliding. The

non-uniform plastic deformation causes GNDs at the interface and the grain boundary. Stress concentration leads to the generation of the microcracks of the B2 phase. (c) Defect distribution during the work hardening stage. GNDs develop toward grain interior. Multiple slip systems are activated in the Fcc phase and both intergranular and transgranular fracture modes occur in the B2 phase. GB and PB represent the grain boundary and the phase boundary respectively.

5. Conclusions

In this study, we systematically investigated mechanical properties and deformation mechanism of the eutectic $AlCoCrFeNi_{2.1}$ alloy and proposed a unique route to realize a superior strength-ductility combination without orientation dependence. The lamellar structure of the alloy is tailored into a microstructure comprised of ultrafine equiaxed dual-phase grains by a combination of HPT and annealing. The EDPS alloy shows an increase in the yield and fracture strength without sacrificing ductility. The softening resistance and the intrinsic microcrack-arresting mechanism effectively improve the plastic deformation ability of the material under high stress, which is accompanied with the generation of GNDs at the grain and phase boundaries to accommodate the strain incompatibility. Such a structure design provides a promising guideline in synthesizing dual-phase material for engineering applications, with enhanced mechanical properties that are independent of the loading direction.

Acknowledgements

We thank Z. Chen and Z.L. Zhang for technical support with the TEM investigations, P. Höbenreich for assistance with metallographic sample preparation, and D. Şopu, O. Renk and J. Wang for valuable discussions. **Funding:** The authors gratefully acknowledge the financial support from the Austrian Science Fund (FWF): Y1236-N37 and the National Natural Science Foundation of China (51871132). Additional support from the China Scholarship Council (CSC, Grant No. 201906220226) is acknowledged.

References

[1] Y.M. Wang, T. Voisin, J.T. McKeown, J.C. Ye, N.P. Calta, Z. Li, Z. Zeng, Y. Zhang, W. Chen, T.T. Roehling, R.T. Ott, M.K. Santala, P.J. Depond, M.J. Matthews, A. V. Hamza, T. Zhu, Additively manufactured hierarchical stainless steels with high strength and ductility, Nat. Mater. 17

(2018) 63–70.

[2] K. Watanabe, T. Kawasaki, H. Tanaka, Structural origin of enhanced slow dynamics near a wall in glass-forming systems, Nat. Mater. 10 (2011) 512–520.

[3] Z.M. Li, K.G. Pradeep, Y. Deng, D. Raabe, C.C. Tasan, Metastable high-entropy dual-phase alloys overcome the strength-ductility trade-off, Nature. 534 (2016) 227–230.

[4] B. Gludovatz, A. Hohenwarter, D. Catoor, E.H. Chang, E.P. George, R.O. Ritchie, A fracture-resistant high-entropy alloy for cryogenic applications, Science. 345 (2014) 1153–1158.

[5] D. Raabe, C.C. Tasan, E.A. Olivetti, Strategies for improving the sustainability of structural metals, Nature. 575 (2019) 64–74.

[6] Y. Zhang, T.T. Zuo, Z. Tang, M.C. Gao, K.A. Dahmen, P.K. Liaw, Z.P. Lu, Microstructures and properties of high-entropy alloys, Prog. Mater. Sci. 61 (2014) 1–93.

[7] D.B. Miracle, O.N. Senkov, A critical review of high entropy alloys and related concepts, Acta Mater. 122 (2017) 448–511.

[8] M.F. Ashby, The deformation of plastically non-homogeneous materials, Philos. Mag. 21 (1969) 37–41.

[9] P. Sathiyamoorthi, H.S. Kim, High-entropy alloys with heterogeneous microstructure: Processing and mechanical properties, Prog. Mater. Sci. 123 (2022) 100709.

[10] X.L. Wu, Y.T. Zhu, Heterogeneous materials: a new class of materials with unprecedented mechanical properties, Mater. Res. Lett. 5 (2017) 527–532.

[11] Y.P. Lu, X.Z. Gao, L. Jiang, Z.N. Chen, T.M. Wang, J.C. Jie, H.J. Kang, Y.B. Zhang, S. Guo, H.H. Ruan, Y.H. Zhao, Z.Q. Cao, T.J. Li, Directly cast bulk eutectic and near-eutectic high entropy alloys with balanced strength and ductility in a wide temperature range, Acta Mater. 124 (2017) 143–150.

[12] X.H. Chen, W.Y. Xie, J. Zhu, Z.D. Wang, Y.L. Wang, Y.F. Ma, M. Yang, W.W. Jiang, H.W. Yu, Y.D. Wu, X.D. Hui, Influences of Ti additions on the microstructure and tensile properties of $AlCoCrFeNi_{2.1}$ eutectic high entropy alloy, Intermetallics. 128 (2021) 107024.

[13] P.J. Shi, R.G. Li, Y. Li, Y.B. Wen, Y.B. Zhong, W.L. Ren, Z. Shen, T.X. Zheng, J.C. Peng, X. Liang, P.F. Hu, N. Min, Y. Zhang, Y. Ren, P.K. Liaw, D. Raabe, Y.D. Wang, Hierarchical crack buffering triples ductility in eutectic herringbone high-entropy alloys, Science. 373 (2021) 912–918.

[14] Y.N. Guo, H.J. Su, H.T. Zhou, Z.L. Shen, Y. Liu, J. Zhang, L. Liu, H.Z. Fu, Unique strength-

ductility balance of $AlCoCrFeNi_{2.1}$ eutectic high entropy alloy with ultra-fine duplex microstructure prepared by selective laser melting, J. Mater. Sci. Technol. 111 (2022) 298–306.

[15] P.J. Shi, W.L. Ren, T.X. Zheng, Z.M. Ren, X.L. Hou, J.C. Peng, P.F. Hu, Y.F. Gao, Y.B. Zhong, P.K. Liaw, Enhanced strength–ductility synergy in ultrafine-grained eutectic high-entropy alloys by inheriting microstructural lamellae, Nat. Commun. 10 (2019) 1–8.

[16] I.S. Wani, T. Bhattacharjee, S. Sheikh, P.P. Bhattacharjee, S. Guo, N. Tsuji, Tailoring nanostructures and mechanical properties of $AlCoCrFeNi_{2.1}$ eutectic high entropy alloy using thermo-mechanical processing, Mater. Sci. Eng. A. 675 (2016) 99–109.

[17] Y. Kok, X.P. Tan, P. Wang, M.L.S. Nai, N.H. Loh, E. Liu, S.B. Tor, Anisotropy and heterogeneity of microstructure and mechanical properties in metal additive manufacturing: A critical review, Mater. Des. 139 (2018) 565–586.

[18] G.G. Yapici, I. Karaman, H.J. Maier, Mechanical flow anisotropy in severely deformed pure titanium, Mater. Sci. Eng. A. 434 (2006) 294–302.

[19] B. Beausir, J.J. Fundenberger, Analysis Tools for Electron and X-ray diffraction, ATEX-software, Univ. Lorraine-Metz. 2017 (2017).

[20] V.B. Biscuola, M.A. Martorano, Mechanical blocking mechanism for the columnar to equiaxed transition, Metall. Mater. Trans. A Phys. Metall. Mater. Sci. 39 (2008) 2885–2895.

[21] S. Plimpton, Fast parallel algorithms for short-range molecular dynamics, J. Comput. Phys. 117 (1995) 1–19.

[22] D. Farkas, A. Caro, Model interatomic potentials for Fe-Ni-Cr-Co-Al high-entropy alloys, J. Mater. Res. 35 (2020) 3031–3040.

[23] S. Mishra, K.V. Reddy, S. Pal, Impact of crystalline–amorphous interface on shock response of metallic glass $Al_{90}Sm_{10}$/crystalline Al nanolaminates, Appl. Phys. A Mater. Sci. Process. 127 (2021) 1–13.

[24] K.V. Reddy, C. Deng, S. Pal, Dynamic characterization of shock response in crystalline-metallic glass nanolaminates, Acta Mater. 164 (2019) 347–361.

[25] A. Stukowski, Visualization and analysis of atomistic simulation data with OVITO-the Open Visualization Tool, Model. Simul. Mater. Sci. Eng. 18 (2010) 015012.

[26] A. Stukowski, Structure identification methods for atomistic simulations of crystalline

materials, Model. Simul. Mater. Sci. Eng. 20 (2012).

[27] B. Schuh, F. Mendez-Martin, B. Völker, E.P. George, H. Clemens, R. Pippan, A. Hohenwarter, Mechanical properties, microstructure and thermal stability of a nanocrystalline CoCrFeMnNi high-entropy alloy after severe plastic deformation, Acta Mater. 96 (2015) 258–268.

[28] J. Wyrzykowski, M.W. Grabski, Lüders deformation in ultrafine-grained pure aluminium, Mater. Sci. Eng. 56 (1982) 197–200.

[29] O. Renk, R. Pippan, Anneal hardening in single phase nanostructured metals, Mater. Trans. 64 (2023) 1464–1473.

[30] C.Y. Yu, P.W. Kao, C.P. Chang, Transition of tensile deformation behaviors in ultrafine-grained aluminum, Acta Mater. 53 (2005) 4019–4028.

[31] Y.Z. Tian, S. Gao, L.J. Zhao, S. Lu, R. Pippan, Z.F. Zhang, N. Tsuji, Remarkable transitions of yield behavior and Lüders deformation in pure Cu by changing grain sizes, Scr. Mater. 142 (2018) 88–91.

[32] L.F. Huang, Y.N. Sun, N. Chen, H.W. Luan, G.M. Le, X. Liu, Y.Q. Ji, Y.P. Lu, P.K. Liaw, X.S. Yang, Y.Z. Zhou, J.F. Li, Simultaneously enhanced strength-ductility of $AlCoCrFeNi_{2.1}$ eutectic high-entropy alloy via additive manufacturing, Mater. Sci. Eng. A. 830 (2022) 142327.

[33] T. Bhattacharjee, I.S. Wani, S. Sheikh, I.T. Clark, T. Okawa, S. Guo, P.P. Bhattacharjee, N. Tsuji, Simultaneous strength-ductility enhancement of a nano-lamellar $AlCoCrFeNi_{2.1}$ eutectic high entropy alloy by cryo-rolling and annealing, Sci. Rep. 8 (2018) 1–8.

[34] X. Jin, Y. Zhou, L. Zhang, X.Y. Du, B.S. Li, A novel $Fe_{20}Co_{20}Ni_{41}Al_{19}$ eutectic high entropy alloy with excellent tensile properties, Mater. Lett. 216 (2018) 144–146.

[35] L. Wang, C.L. Yao, J. Shen, Y.P. Zhang, T. Wang, Y.H. Ge, L.H. Gao, G.J. Zhang, Microstructures and room temperature tensile properties of as-cast and directionally solidified $AlCoCrFeNi_{2.1}$ eutectic high-entropy alloy, Intermetallics. 118 (2020) 106681.

[36] H. Jiang, D.X. Qiao, W.N. Jiao, K.M. Han, Y.P. Lu, P.K. Liaw, Tensile deformation behavior and mechanical properties of a bulk cast $Al_{0.9}CoFeNi_2$ eutectic high-entropy alloy, J. Mater. Sci. Technol. 61 (2021) 119–124.

[37] X. Jin, Y. Zhou, L. Zhang, X.Y. Du, B.S. Li, A new pseudo binary strategy to design eutectic high entropy alloys using mixing enthalpy and valence electron concentration, Mater. Des.

143 (2018) 49–55.

[38] X. Jin, J. Bi, L. Zhang, Y. Zhou, X.Y. Du, Y.X. Liang, B.S. Li, A new $CrFeNi_2Al$ eutectic high entropy alloy system with excellent mechanical properties, J. Alloys Compd. 770 (2019) 655–661.

[39] X. Jin, Y.X. Liang, J. Bi, B.S. Li, Enhanced strength and ductility of $Al_{0.9}CoCrNi_{2.1}$ eutectic high entropy alloy by thermomechanical processing, Materialia. 10 (2020) 100639.

[40] S. Wang, Y. Li, D. Zhang, Y. Yang, S. Marwana Manladan, Z. Luo, Microstructure and mechanical properties of high strength $AlCoCrFeNi_{2.1}$ eutectic high entropy alloy prepared by selective laser melting (SLM), Mater. Lett. 310 (2022) 131511.

[41] Y.P. Lu, X.X. Wu, Z.H. Fu, Q.K. Yang, Y. Zhang, Q.M. Liu, T.X. Li, Y.Z. Tian, H. Tan, Z.M. Li, T.M. Wang, T.J. Li, Ductile and ultrahigh-strength eutectic high-entropy alloys by large-volume 3D printing, J. Mater. Sci. Technol. 126 (2022) 15–21.

[42] T. Xiong, S.J. Zheng, J.Y. Pang, X.L. Ma, High-strength and high-ductility $AlCoCrFeNi_{2.1}$ eutectic high-entropy alloy achieved via precipitation strengthening in a heterogeneous structure, Scr. Mater. 186 (2020) 336–340.

[43] P.J. Shi, Y.B. Zhong, Y. Li, W.L. Ren, T.X. Zheng, Z. Shen, B. Yang, J.C. Peng, P.F. Hu, Y. Zhang, P.K. Liaw, Y.T. Zhu, Multistage work hardening assisted by multi-type twinning in ultrafine-grained heterostructural eutectic high-entropy alloys, Mater. Today. 41 (2020) 62–71.

[44] S. Shukla, T.H. Wang, S. Cotton, R.S. Mishra, Hierarchical microstructure for improved fatigue properties in a eutectic high entropy alloy, Scr. Mater. 156 (2018) 105–109.

[45] Z.S. Yang, Z.J. Wang, Q.F. Wu, T. Zheng, P.R. Zhao, J.K. Zhao, J.Y. Chen, Enhancing the mechanical properties of casting eutectic high entropy alloys with Mo addition, Appl. Phys. A Mater. Sci. Process. 125 (2019) 1–6.

[46] J.H. Chen, R. Cao, Micromechanism of cleavage fracture of metals: a comprehensive microphysical model for cleavage cracking in metals, Elsevier Oxford, 2015.

[47] A. Pineau, A.A. Benzerga, T. Pardoen, Failure of metals I: Brittle and ductile fracture, Acta Mater. 107 (2016) 424–483.

[48] M. Hafok, R. Pippan, High-pressure torsion applied to nickel single crystals, Philos. Mag. 88 (2008) 1857–1877.

[49] D. Hull, J.D. Bacon, Introduction to Dislocations, Elsevier Oxford, 2011.

[50] L.H. Wang, P.F. Guan, J. Teng, P. Liu, D.K. Chen, W.Y. Xie, D.L. Kong, S.B. Zhang, T. Zhu, Z. Zhang, E. Ma, M.W. Chen, X.D. Han, New twinning route in face-centered cubic nanocrystalline metals, Nat. Commun. 8 (2017) 1–7.

[51] D. Geist, C. Gammer, C. Rentenberger, H.P. Karnthaler, Sessile dislocations by reactions in NiAl severely deformed at room temperature, J. Alloys Compd. 621 (2015) 371–377.

[52] Z. Chen, A. Chen, Q. Jia, Z. Xia, R. Li, C. Wang, J. Pan, Y. Shi, Investigation of microstructures and strengthening mechanisms in an N-doped Co-Cr-Mo alloy fabricated by laser powder bed fusion, Virtual Phys. Prototyp. 18 (2023).

[53] B. Gwalani, V. Soni, M. Lee, S.A. Mantri, Y. Ren, R. Banerjee, Optimizing the coupled effects of Hall-Petch and precipitation strengthening in a $Al_{0.3}$CoCrFeNi high entropy alloy, Mater. Des. 121 (2017) 254–260.

[54] J.D. Cotton, R.D. Noebe, M.J. Kaufman, The effects of chromium on NiAl intermetallic alloys: Part II. Slip systems, Intermetallics. 1 (1993) 117–126.

[55] L.A. Gypen, A. Deruyttere, Multi-component solid solution hardening - Part 1 Proposed model, J. Mater. Sci. 12 (1977) 1028–1033.

[56] Q. Tian, G. Zhang, K. Yin, W. Wang, W. Cheng, Y. Wang, The strengthening effects of relatively lightweight AlCoCrFeNi high entropy alloy, Mater. Charact. 151 (2019) 302–309.

[57] N.J. Harrison, I. Todd, K. Mumtaz, Reduction of micro-cracking in nickel superalloys processed by Selective Laser Melting: A fundamental alloy design approach, Acta Mater. 94 (2015) 59–68.

[58] H.A. Roth, C.L. Davis, R.C. Thomson, Modeling solid solution strengthening in nickel alloys, Metall. Mater. Trans. A Phys. Metall. Mater. Sci. 28 (1997) 1329–1335.

[59] J. Wang, R.G. Hoagland, J.P. Hirth, A. Misra, Atomistic modeling of the interaction of glide dislocations with “weak” interfaces, Acta Mater. 56 (2008) 5685–5693.

[60] J. Qiang, K. Tsuchiya, H. Diao, P.K. Liaw, Vanishing of room-temperature slip avalanches in a face-centered-cubic high-entropy alloy by ultrafine grain formation, Scr. Mater. 155 (2018) 99–103.

[61] Y. Mu, L. He, S. Deng, Y. Jia, Y. Jia, G. Wang, Q. Zhai, P.K. Liaw, C.T. Liu, A high-entropy alloy with dislocation-precipitate skeleton for ultrastrength and ductility, Acta Mater. 232 (2022) 117975.

[62] A. Lozinko, R. Gholizadeh, Y. Bin Zhang, U. Klement, N. Tsuji, O. V. Mishin, S. Guo, Evolution of microstructure and mechanical properties during annealing of heavily rolled $AlCoCrFeNi_{2.1}$ eutectic high-entropy alloy, Mater. Sci. Eng. A. 833 (2022) 142558.

Supplementary Materials

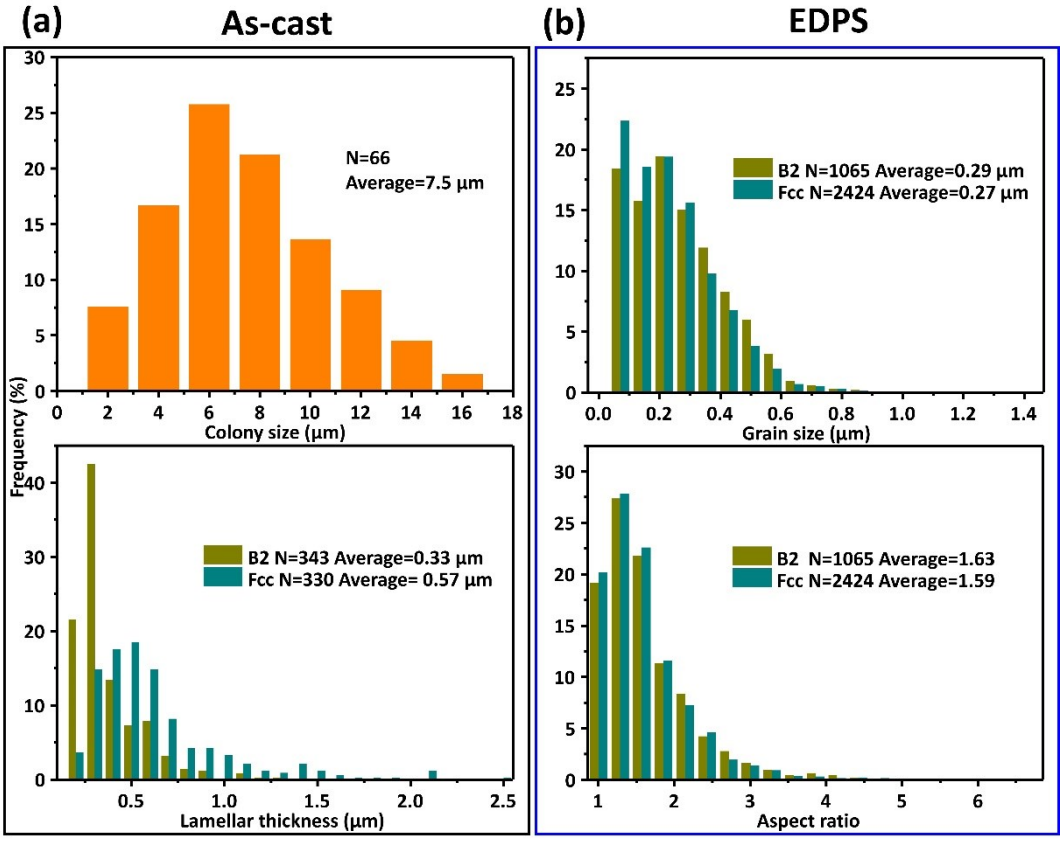

Fig. S1 Statistical information of eutectic colonies and grains in the as-cast and EDPS alloys. (a) Relative frequency of the colony size and the lamellar thickness within the as-cast alloy. (b) Relative frequency of grain size and aspect ratio within the EDPS alloy. The statistical information of both the lamellar structure and EDPS is summarized using a combination of results from SEM and EBSD data.

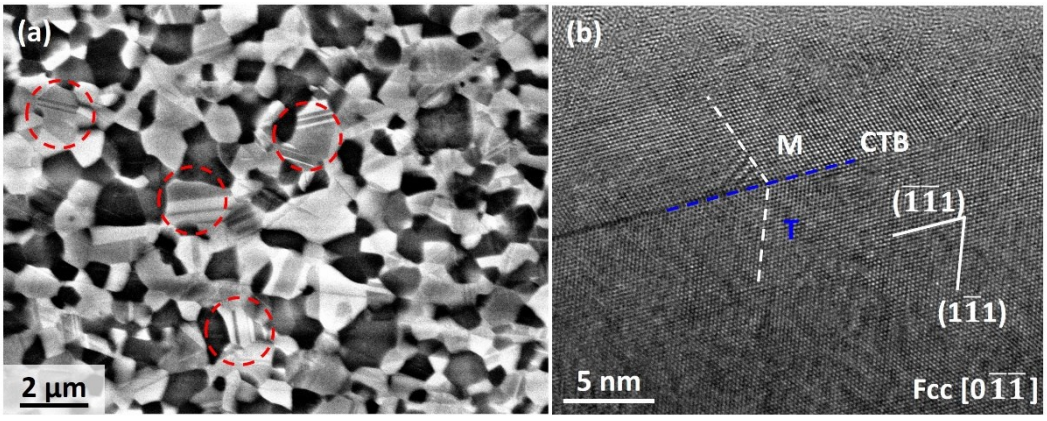

Fig. S2 Characterization of annealing twins in the EDPS alloy. (a) Distribution of twin boundaries in the EDPS alloy. Some regions containing annealing twins are marked by red dotted circles. (b) HRTEM image of a coherent twin boundary.

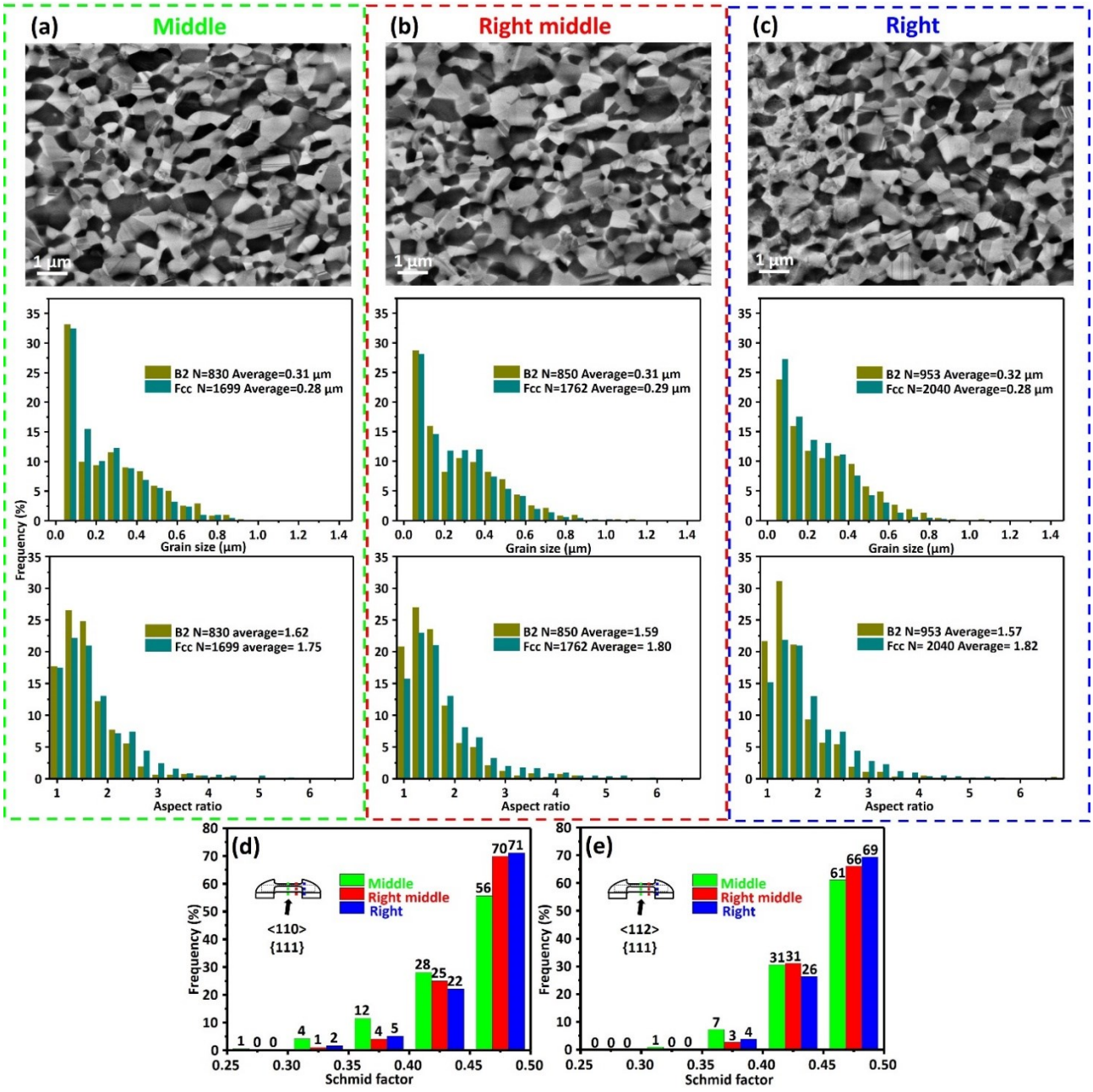

Fig. S3 The morphologies and statistical information of grains of the EDPS alloy observed from the transverse direction. The morphology, aspect ratio, and grain size along the tensile direction of middle (a), right middle (b), and right (c) parts. The tensile direction is horizontal to all BSE-SEM images. The corresponding Schmid factor distribution for (d) full and (e) partial dislocations for the Fcc system. The distance between testing positions was 1 mm.

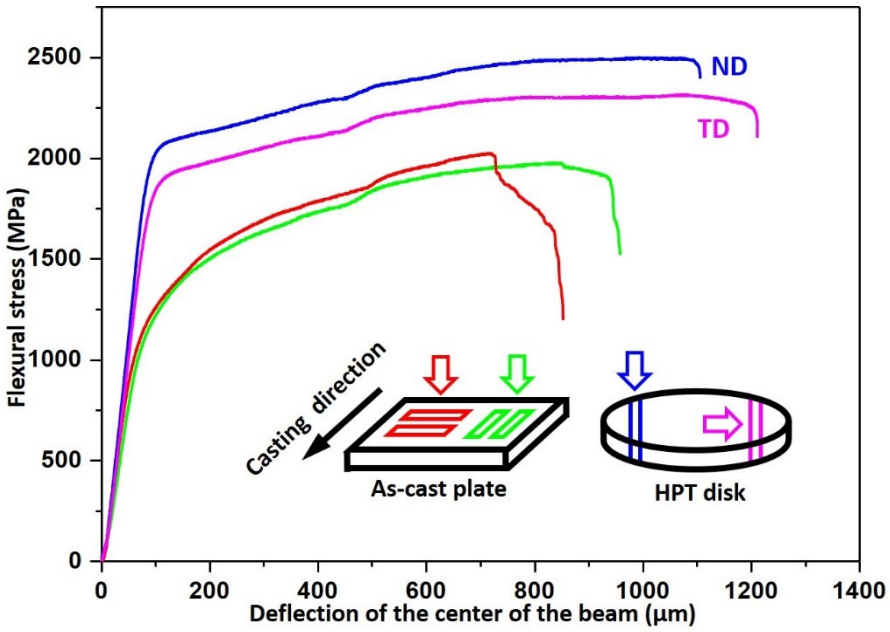

Fig. S4 Mechanical performance of the as-cast and EDPS alloys. Results of three-point bending test for as-cast and EDPS alloys. Four arrows of schematic diagrams indicate loading directions for beams machined from the as-cast alloy and from the EDPS alloy. TD and ND represent Transverse Direction and Normal Direction, respectively.

Table S1. Actual chemical composition (in at.%) of a specimen after annealing analyzed by EDS/SEM map scan (mean composition ± standard deviation).

Alloy	Al	Co	Cr	Fe	Ni
Annealed specimen	15.2 ± 3.8	16.9 ± 1.6	17.1 ± 1.7	16.9 ± 1.7	33.8 ± 1.7

Table S2. Chemical composition (in at.%) of the as-cast and EDPS alloys analyzed by EDS/SEM (mean composition ± standard deviation).

Alloy	phases	Al	Co	Cr	Fe	Ni
As-cast	Fcc	13.1 ± 0.5	17.6 ± 0.4	18.3 ± 0.4	17.7 ± 0.2	33.3 ± 0.3
	B2	22.0 ± 1.3	15.1 ± 0.5	14.3 ± 0.9	14.4 ± 0.9	34.2 ± 1.0
EDPS	Fcc	11.3 ± 0.8	18.9 ± 0.3	19.6 ± 0.3	18.7 ± 0.1	31.5 ± 0.5
	B2	25.0 ± 1.3	13.3 ± 0.6	11.5 ± 1.0	12.2 ± 0.6	38.1 ± 1.0